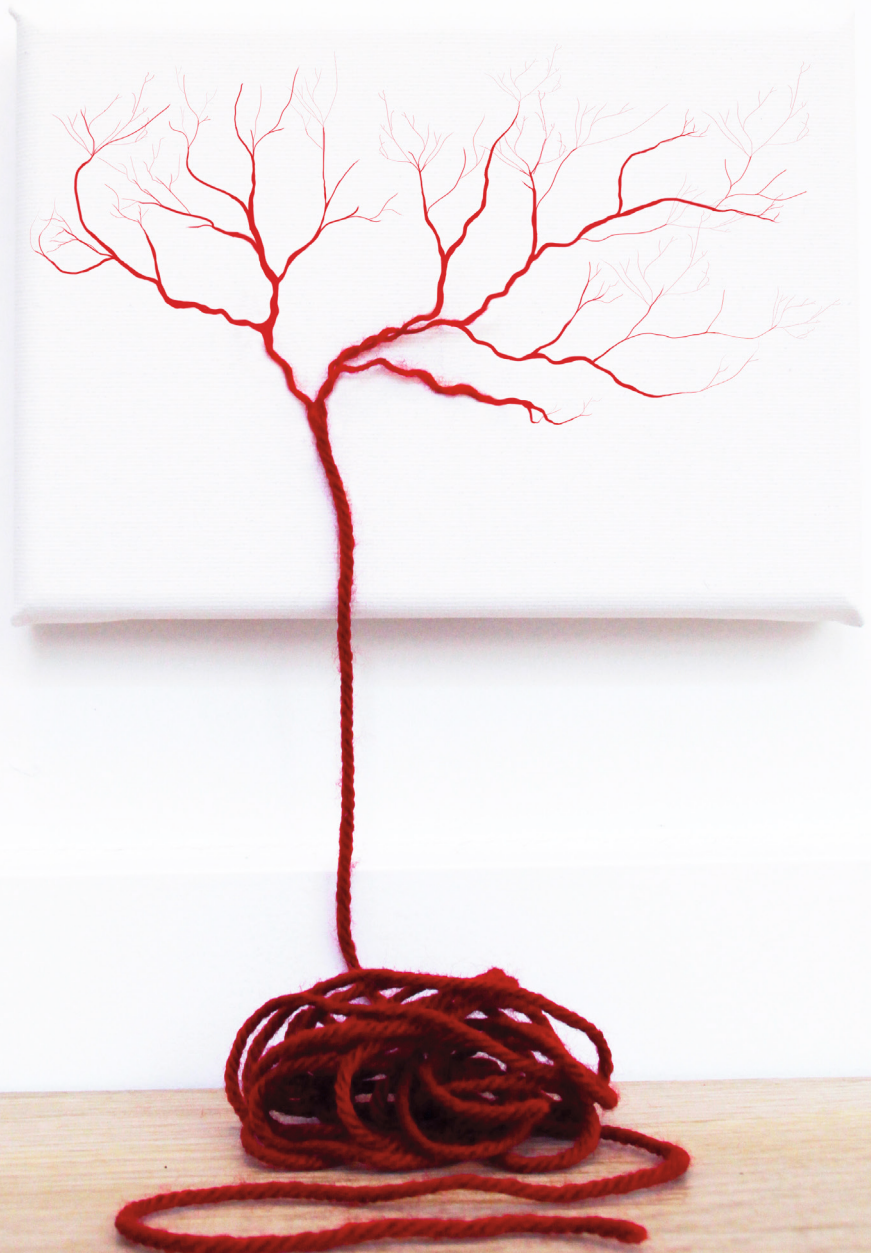


Building axons from formation to function

Feline W. Lindhout



Building axons

from formation to function

Feline W. Lindhout

ISBN: 978-94-6416-103-8

The studies described in this thesis were performed at the division of Cell Biology, Neurobiology and Biophysics at the Faculty of Science of the Utrecht University in Utrecht, the Netherlands.

Cover design: *Axon Thread* by Roos Lindhout & Feline Lindhout

Layout by Roos Lindhout

Printed by Ridderprint

Copyright © Feline Willeke Lindhout, 2020.

All rights reserved.

Building axons: from formation to function

Ontwikkeling van het axon: van formatie tot functie

(met een samenvatting in het Nederlands)

Proefschrift

ter verkrijging van de graad van doctor aan de Universiteit Utrecht
op gezag van de rector magnificus, prof.dr. H.R.B.M. Kummeling,
ingevolge het besluit van het college voor promoties in het openbaar te
verdedigen op woensdag 7 oktober 2020 des middags te 12.45 uur

door

Feline Willeke Lindhout

geboren op 18 oktober 1990 te Tilburg

Promotor: Prof. dr. C.C. Hoogenraad
Copromotor: Dr. H.D. Mac Gillavry

Voor Anke & Wim

Content

1. General introduction page 8

 2. Quantitative mapping of transcriptome and proteome dynamics during polarization of human iPSC-derived neuron page 30

 3. Centrosome-mediated microtubule remodeling during axon formation in human iPSC-derived neurons page 70

 4. VAP-SCRN1 interaction regulates dynamic endoplasmic reticulum remodeling and presynaptic function page 108

 5. General discussion page 148

 - & Addendum page 162
-

1.



General introduction

Feline W. Lindhout¹

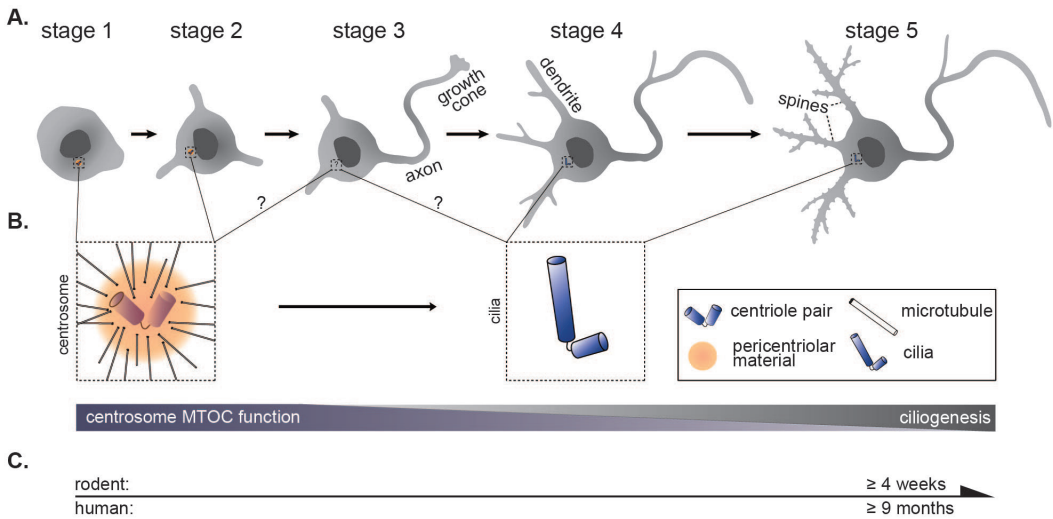
¹Cell Biology, Neurobiology and Biophysics, Department of Biology, Faculty of Science, Utrecht University, 3584 CH Utrecht, The Netherlands.

The human brain is populated by $\sim 10^{11}$ neurons that are highly interconnected to form complex neuronal networks (Azevedo et al. 2009; von Bartheld, Bahney, and Herculano-Houzel 2016). Neurons are compartmentalized into two morphologically, structurally and functionally distinct domains: the axonal and the somatodendritic domain. These different compartments give rise to intracellular polarity within neurons, thereby enabling the directional flow of information processing in neuronal networks. The axonal domain is a single process originating from the soma, and is characterized by its excessive length and narrow width. This extreme axon morphology is accompanied by large adaptations of axonal substructures, which play important roles in axon functioning. A key function of axons is facilitating firing of action potentials, electrical excitation waves generated at the beginnings of axons and further propagated along axonal membranes. The somatodendritic domain, comprised of the soma and multiple dendritic processes, receives and integrates input coming from axons of other neurons. In neuronal networks, information transmission occurs at highly specialized synaptic connections between the axon and the somatodendritic domains of different neurons. Synapses are subdivided into distinct specialized subdomains, thereby displaying that polarity is also observed at the synaptic level. Specifically, synapses contain a presynaptic site located on axons, a postsynaptic site located on dendrites, and a narrow synaptic cleft in between. In conclusion, axon formation and functioning are key for establishing and maintaining neuronal polarity, which is fundamental for information processing in neuronal networks. This thesis aims to identify and dissect new molecular processes that are important for axon formation and functioning. This chapter covers a broad and general introduction of the key topics presented in this thesis, and specific research questions are further laid out in their corresponding chapters (*Chapter 2, 3 and 4*).

Neurodevelopment

Developing neurons: insights from rodents

Important advances in understanding mammalian brain development come from a large body of work using rodent model systems. The development of the vertebrate brain begins with the folding and closing of a pseudostratified epithelial sheet, the neuroepithelium, thereby forming the neural tube (Kelava and Lancaster 2016). The neural tube, composed of neuroepithelial cells, undergoes lateral expansion to later generate various structures in the central nervous system. After the lateral expansion of the neural tube, the neuroepithelial cells transform into self-renewing radial glia cells (RGCs), which leads to the thickening of the neuronal tissue and thereby giving rise to the ventricular zone (VZ) (Bystron, Blakemore, and Rakic 2008). Asymmetric divisions of RGCs result in either newborn neurons or in intermediate progenitors (IPs), which populate the subventricular zone (SVZ) and later differentiate into neurons. The immature neurons migrate towards their target location, in a process known as neuronal delamination (Evsyukova, Plestant, and Anton 2013; Theveneau and Mayor 2012). As such, the six layers of the cerebral cortex are formed following an inside-out fashion, in which early-born neurons first form deeper layers followed by the formation of the more superficial layers. In developing brains, the process of neuronal migration highly coincides with axon formation and pathfinding of neurons (Noctor et al. 2004).

**Figure 1.****Neurodevelopment and centrosome functions**

A. Schematic overview of the five neurodevelopmental stages. Symmetric neurons with lamellipodia (stage 1) grow multiple non-polarized neurites (stage 2). A single neurite undergoes extensive growth (stage 3), the future axon, whereas the remaining neurites develop into dendrites (stage 4). Next, neurons undergo synaptogenesis and further mature (stage 5).

B. Centrosomes display different functions throughout neurodevelopment. Initially, centrosomes are important microtubule-organizing centers (MTOCs) (stage 1 and 2), and this function is declined as centrosomes transform into cilia during ciliogenesis (stage 4 and 5). This developmental transition occurs in stage 3 neurons, but the exact timing in relation to the process of axon formation is unknown.

C. Indication of the developmental timing from neurogenesis (stage 1) to mature neurons (stage 5) in rodents and humans. Data is based on transplanted human and mouse induced pluripotent stem cells (iPSC)-derived neurons in mouse brains (Espuny-Camacho et al. 2013; Maroof et al. 2013; Nicholas et al. 2013; Linaro et al. 2019).

Many studies using *in vitro* model systems greatly complemented our understanding of neurodevelopment, and particularly provided important insights in the underlying cell-intrinsic and molecular processes. Early studies in dissociated hippocampal and cortical rodent neurons in culture reported that newborn neurons proceed through five neurodevelopmental stages (Fig 1) (Dotti, Sullivan, and Banker 1988; Powell et al. 1997). In stage 1, neurons appear as round symmetric cells with dynamic lamellipodia and filopodia structures. In stage 2, neurons grow multiple processes of similar lengths containing dynamic growth cones. In stage 3 neurons, a symmetry break occurs as one of these processes shows extensive growth compared to the others, and will develop into an axon. Multiple studies showed that

this extensive growth relies on drastic changes in the local cytoskeleton of the future axon, which specifically employs microtubule stabilization and actin depolymerization (Yu and Baas 1994; Bradke and Dotti 1999; Geraldo et al. 2008; Witte, Neukirchen, and Bradke 2008; Neukirchen and Bradke 2011; Zhao et al. 2017). Accordingly, the formation of multiple axons is observed when inducing microtubule stabilization using pharmacological treatments in stage 2/3 neurons (Witte, Neukirchen, and Bradke 2008). The observed microtubule stabilization in growth cones is accompanied with increased local actin dynamics, further implying that a controlled interplay between these different cytoskeletal components is at play in developing axons (Zhao et al. 2017). In stage 4 neurons, the remaining neurites will transform in dendrites, and further mature as dendrites undergo extensive arborization. Finally, in stage 5, neurons will undergo synaptogenesis, which involves the formation of specialized synaptic connections between neurons. These synapses generally arise between axonal boutons, swellings along the axon shaft or terminals, and dendritic shafts or spines, typically mushroom-shaped protrusions at dendrites (Fig 2). These neurodevelopmental stages identified in *in vitro* rodent neurons largely coincide with neurodevelopment *in vivo*, thereby indicating that these developmental processes are mostly driven by cell-intrinsic mechanisms. In developing brains, the temporal coordination of the neuronal migration and transition through neurodevelopmental stages is steered by the structural organization and molecular composition of neuronal tissues (Stoeckli 2018). In conclusion, studies in rodent model systems reveal that the development of complex neuronal networks is orchestrated by cell-intrinsic neurodevelopmental stages, which are further guided by extracellular processes in highly organized neuronal structures.

Developing neurons: insights from humans

Most insights in neurodevelopmental processes come from studies using non-human model systems (e.g. rodents, zebrafish, flies, worms). Many basic principles of brain development are found to be conserved throughout evolution. However, the human brain also shows striking anatomical differences compared to other species. This is mostly highlighted by a larger cortex containing gyri and sulci, which is accompanied with increased cognitive functions in humans (Emery and Clayton 2005; Pollard et al. 2006). Humans and other larger-brained species (e.g. ferrets, sheep, cats, and apes) contain an additional cortical layer, the outer subventricular zone (oSVZ), which is populated by the primate-specific outer radial glia cells (oRGCs), a subtype of neuronal precursor cells (Fish et al. 2008; Fietz et al. 2010; Hansen et al. 2010; Reillo et al. 2011; Dehay, Kennedy, and Kosik 2015; De Juan Romero and Borrell 2015). Also at the single-cell level, there are similarities as well as profound differences between the development of human and non-human neurons. Similar to rodents, human neurons also proceed through the five neurodevelopmental stages that were first identified in dissociated rodent neuron cultures (Dotti, Sullivan, and Banker 1988; Powell et al. 1997; Lancaster et al. 2013) (*Chapter 2*). However, there are also human-specific morphologies observed in neurons, as marked by larger spine sizes and more complex dendritic arborization compared to non-human primates (Benavides-Piccione et al. 2002; Defelipe 2011).

Another particularly striking feature of human neurodevelopment, is the significant prolonged development of human neurons compared to non-human neurons (Fig 1). Multiple studies reported that human neurogenesis *in vitro* occurs at slower rates, as this process takes about 1 week when derived from mouse embryonic stem cells (ESCs) and more than 3 months when derived from human ESCs (Gaspard et al. 2008; Shi, Kirwan, and Livesey 2012; Espuny-Camacho et al. 2013). This is consistent with the observed neoteny of the human neocortex, as *in vivo* neurogenesis also takes about 1 week in mice and upon 120 days in humans (Sousa et al. 2017). Likewise, induced pluripotent stem cells (iPSC)-derived neuronal stem cell (NSC) cultures from mouse and human with the exact same culture conditions showed that neurogenesis was initiated after 2 days in mice and only after 3 weeks in humans (Espuny-Camacho et al. 2013). This protracted development in humans is also reported to occur during NSC expansion prior to neurogenesis, as human NSCs are subjected to significantly more cell cycles before they undergo neuronal differentiation (Espuny-Camacho et al. 2013). Remarkably, these temporal developmental differences are still observed when comparing more closely related species. Neurogenesis occurred at a significant slower phase in iPSC-derived cells derived from human and chimpanzee compared to those from macaque, consistent with *in vivo* development (Otani et al. 2016). Moreover, these and these temporal species-specific differences were even maintained in co-cultures of human and macaque neurons (Otani et al. 2016). Neurodevelopment of human and chimpanzee neurons is overall highly similar, however, human NSCs showed prolonged transition time between prometaphase and metaphase (Mora-Bermudez et al. 2016). Also at later neurodevelopmental stages, human neurons continue to mature at slower rates, as cortical neurons reach mature adult-like stages in years whereas this takes a few months in macaque neurons (Huttenlocher 1979; Huttenlocher et al. 1982; Somel et al. 2009; Petanjek et al. 2011; Liu et al. 2012). Moreover, transplanted human iPSC-derived neurons in chimera mouse brains take about 9-12 months to fully develop, whereas this takes about 4 weeks for mouse iPSC-derived neurons (Espuny-Camacho et al. 2013; Maroof et al. 2013; Nicholas et al. 2013; Linaro et al. 2019).

In summary, first insights begin to elucidate unique hallmarks of human neurodevelopment, however, the precise differences in neurodevelopment between human and other species remain largely unknown. This is mostly due to technical challenges, as access to living or post-mortem human brain tissues is limited. Nevertheless, with the development of neurons derived from human iPSCs it is now possible to overcome these limitations, and more insights in human-specific processes during neurodevelopment begin to emerge (Lancaster et al. 2013) (*Chapter 2 and 3*).

Axons: specialized structures and functions

Axon morphology

Axons are comprised of a unique morphology, marked by their excessive length and small diameter. These extreme axon lengths are necessary, as axons often need to reach long

distances to innervate target structures that are not in close proximity to their cell bodies. To illustrate this, axons can grow up to ~1 meter in humans, which is longer than the total size of most commonly used model organisms for neurodevelopmental studies (e.g. rodents, zebrafish, flies, worms) (Cavanagh 1984). These unique axon morphologies are accompanied with drastic adaptations of organelle structures and cytoskeletal organizations, such as the endoplasmic reticulum (ER) and the microtubule network. Additionally, axons are comprised of typical axon-specific structures, including an axon initial segment (AIS) and presynaptic boutons, to execute its function.

The axon initial segment

An essential component for axon structure and function is the AIS, a specialized compartment localized at the base of the axon that separates the axon from the somatodendritic domain. The AIS is thought to act as an important diffusion barrier that is indispensable for selective cargo transport, and is critical for neuronal polarity (Leterrier 2018). Another important function of the AIS is the generation and shaping of action potentials, which is facilitated by the local clustering of voltage-gated sodium and potassium channels (Kole et al. 2008). The highly organized AIS structure is formed by the coordinated assembly of specific proteins, including scaffolds (i.e. AnkyrinG), cytoskeletal components (i.e. Trim46), membrane-associated proteins and ion channels (i.e. voltage-gated sodium and potassium channels) (Leterrier 2018; Freal et al. 2019). New insights in the highly temporal controlled process of AIS assembly are presented in *Chapter 2*.

The axonal microtubule network

The unique microtubule cytoskeleton organization in axons is important for long-range transport, and drives axon specification and outgrowth (Neukirchen and Bradke 2011; Stuessi and Bradke 2011; van Beuningen and Hoogenraad 2016; Schelski and Bradke 2017). Microtubules are highly dynamic and polarized structures, typically built by 13 protofilaments that each contain α -tubulin and β -tubulin heterodimers (Mitchison 1993; Desai and Mitchison 1997). The axonal microtubule network is characterized by a uniform microtubule organization with all plus-ends oriented distal to the soma, a plus-end out orientation, which is highly conserved throughout species (Baas, White, and Heidemann 1987; Baas et al. 1988; Stepanova et al. 2003; Stone, Roegiers, and Rolls 2008; Goodwin, Sasaki, and Juo 2012; Maniar et al. 2011; Yau et al. 2016). This is distinctive from the microtubule organization in dendrites, which exhibits mixed orientations with ~50% plus-end and ~50% minus-end out microtubules in rodent and human neurons, and an uniform minus-end out organization in invertebrate neurons (Baas et al. 1988; Stepanova et al. 2003; Stone, Roegiers, and Rolls 2008; Goodwin, Sasaki, and Juo 2012; Maniar et al. 2011; Yau et al. 2016) (*Chapter 2*). These differences in the axonal and dendritic microtubule organization underlie polarized cargo transport and are therefore a key aspect of neuronal polarity and functioning. In stage 2 neurons, the microtubule cytoskeleton is similarly organized in all the multiple nonpolarized neurites, and is marked by mixed orientations of

~80% plus-end and ~20% minus-end out microtubules (Yau et al. 2016). Thus, during the transition of unpolarized neurons (stage 2) to polarized neurons (stage 3), the microtubule cytoskeleton drastically reorganizes in both axons and dendrites, and new insights underlying this process are presented in *Chapter 3*.

The axonal ER network

The ER is the largest organelle in neurons and other cell types. It is a highly dynamic structure that undergoes continuous remodeling, while the continuity of the structure remains intact. The ER network is composed of perinuclear ER sheets and peripheral ER tubules, which typically reflect rough and smooth ER, respectively. The rough ER contains ribosomes and is involved in protein translation. Instead, the smooth ER lacks ribosomes and does not contribute to protein translation, but acts as a key regulator of Ca^{2+} homeostasis, signaling, and lipid synthesis and delivery. Axons primarily contain smooth ER, and the structure of axonal smooth ER differs significantly from other smooth ER structures (Yalcin et al. 2017; Wu et al. 2017; Terasaki 2018). The unique axonal ER structure is characterized by thin ER tubules at the shaft, with 1 or 2 tubules per axon diameter, and local ER cisternae at presynaptic boutons (Yalcin et al. 2017; Wu et al. 2017; Terasaki 2018). The importance of the axonal ER network is illustrated by axon degeneration diseases (i.e. hereditary spastic paraplegia and amyotrophic lateral sclerosis) caused by mutations in generic ER proteins (Hazan et al. 1999; Zhao et al. 2001; Nishimura et al. 2004; Zuchner et al. 2006; Montenegro et al. 2012; Esteves et al. 2014; Yalcin et al. 2017). This includes proteins that facilitate ER tubule formation (e.g. atlastin-1, reticulon-2, receptor expression-enhancing protein 1 (REEP1), receptor expression-enhancing protein 2 (REEP2)) or act as ER receptor (vesicle-associated membrane protein(VAMP)-associated protein B (VAPB)) (Hazan et al. 1999; Zhao et al. 2001; Nishimura et al. 2004; Zuchner et al. 2006; Montenegro et al. 2012; Esteves et al. 2014; Yalcin et al. 2017). All these identified ER proteins are highly evolutionary conserved and essential for ER formation and function throughout different cell types. It remains largely unclear why the dysfunction of these important ER proteins is specifically associated with axonopathies. Nevertheless, it implies that the unique axonal ER structures, which are highly adapted to the extreme axonal morphologies, are particularly susceptible for structural ER perturbations. Accordingly, emerging evidence is starting to elucidate the implication of local ER structure and dynamics in axon function (Ozturk, O'Kane, and Perez-Moreno 2020) (*Chapter 4*).

Role of centrosomes in developing neurons

Transitions of neurodevelopmental stages, including axon formation, are accompanied with drastic changes in cell morphologies that are steered by large cytoskeletal remodeling (Neukirchen and Bradke 2011; Stiess and Bradke 2011; van Beuningen and Hoogenraad 2016; Schelski and Bradke 2017). A particularly important organizer of the cytoskeleton is the centrosome, the predominant microtubule-organizing center (MTOC) in cells. Although the precise role of centrosomes during specific neurodevelopmental processes is still

under debate, emerging evidence begins to elucidate the importance of centrosomes for development of neurons (Nano and Basto 2017; Meka, Scharrenberg, and Calderon de Anda 2020).

Centrosome composition and function

Centrosomes are small and non-membranous organelles localized at the cell center of most animal cells, where they act as the main MTOC (Fig 1). Centrosomes are composed of a pair of centrioles surrounded by a highly organized meshwork of more than 100 proteins, the pericentriolar material (PCM) (Karsenti et al. 1984; Bobinnec et al. 1998; Nigg and Raff 2009; Sonnen et al. 2012; Mennella et al. 2012). The centriole pair displays an orthogonal organization, where each individual centriole consists of nine sets of polymerized tubulin filaments (Anderson 1972). Most microtubules in cells are nucleated from γ -Tubulin Ring Complexes (γ TuRCs) embedded in the PCM, thereby giving rise to the characteristic radial microtubule networks in cells (Moritz et al. 2000). Thus, centrosomes play a key role in generating and organizing microtubule arrays in cells, by locally generating and anchoring microtubules at cell centers. In addition to their well-described MTOC function, centrosomes are also involved in other cellular processes, such as actin cytoskeleton organization, intracellular signaling and protein homeostasis (Conduit, Wainman, and Raff 2015; Farina et al. 2016; Vora and Phillips 2016). Moreover, in differentiating cells, centrioles gradually lose their function as MTOC as they transform and assemble into cilia, which lack γ TuRC complexes and typically mediate non-microtubule organizing functions (Figure 1) (Ishikawa and Marshall 2011). There are two types of cilia: motile cilia and primary cilia. In the brain, motile cilia are present in multi-ciliated ependymal cells, where they are important to direct the flow of cerebrospinal fluid (CSF) (Klos Dehring et al. 2013; Al Jord et al. 2014). Whilst primary cilia are essential signaling hubs in the brain, as they act as receptors for developmental signals such as sonic hedgehog (Shh) and Wnt (Shimogori et al. 2004; Simons et al. 2005; Corbit et al. 2005; Rohatgi, Milenkovic, and Scott 2007; Wallingford and Mitchell 2011; Taverna, Gotz, and Huttner 2014).

Role of centrosomes during axon formation and neurodevelopment

In neuronal stem cells and unpolarized neurons (stage 1 and 2), centrosomes still act as an MTOC, but they lose this function during further development (Fig 1) (Tsai and Gleeson 2005; Stiess et al. 2010; Meka, Scharrenberg, and Calderon de Anda 2020). From studies in dissociated rodent neuron cultures it was found that this process occurs during axon formation in stage 3 neurons, although the exact developmental timing is unclear (Stiess et al. 2010). Removing centrosomes in stage 3 neurons, thus when their MTOC functions are declined, did not affect further outgrowth of the specified axon (Stiess et al. 2010). Nevertheless, it is poorly understood if centrosomes play a role, possibly as MTOC, in the process of axon specification, and new insights in these processes are presented in *Chapter 3*. Previous studies showed that centrosome positioning was found to correlate with sites of newly emerging axons, which could hint for a possible functional role of centrosomes in

axon specification (Zmuda and Rivas 1998; de Anda et al. 2005). Also, the importance of centrosome function at early neurodevelopmental stages prior to axon formation begins to emerge. This is mostly illustrated by the increasing number of identified mutations in centrosome proteins that are causative for microcephaly in humans, a neurodevelopmental disorder marked by smaller brains and declined cognitive functions (Nano and Basto 2017). Multiple studies indicated that these reduced brain sizes upon centrosome dysfunction typically reflect an immature cortex, which is largely attributed to a reduction of the NSC pool at the ventricular zone (Nano and Basto 2017). In normal conditions, the developmental expansion of the NSC pool is accomplished by multiple rounds of symmetric cell divisions of NSCs, a process highly controlled by centrosome function and positioning (Taverna, Gotz, and Huttner 2014). With symmetric cell divisions of mammalian NSCs, the spindle pool and the cleavage plane are positioned perpendicular to the ventricular zone, resulting in two equal daughter cells that remain their NSC fate (Shitamukai and Matsuzaki 2012). Contrarily, asymmetric cell divisions of mammalian NSCs lead to neuronal differentiation of at least one of the daughter cells (Rhyu, Jan, and Jan 1994; Jan and Jan 1998; Liu et al. 2010; Knoblich 2010; Taverna, Gotz, and Huttner 2014). Malfunctioning centrosomes are accompanied with increased asymmetric cell divisions of NSCs during early development, resulting in premature neuronal differentiation and a decreased NSC pool (Lancaster et al. 2013; Nano and Basto 2017). However, it remains to be addressed if these prematurely differentiated neurons, despite centrosome dysfunction, can subsequently follow normal neurodevelopment and form functional axons. Notably, for unclear reasons, human neurodevelopmental disorders caused by dysfunctional centrosomes are often poorly recapitulated in other species. In fact, full centrosome removal in *Drosophila* did not reduce brain size, unlike observed with microcephaly in humans, and both centrosome dysfunction or centrosome amplification in *Drosophila* could lead to brain tumor formation (Basto et al. 2006; Basto et al. 2008; Castellanos, Dominguez, and Gonzalez 2008; Poulton, Cunningham, and Peifer 2017). Additionally, in mouse models the autosomal recessive primary microcephaly (MCPH) disorder often shows milder phenotypes compared to humans (Pulvers et al. 2010). Together, these studies indicate that centrosomes may display human-specific functions during neurodevelopment, thereby highlighting the relevance of investigating these processes in human neurons (*Chapter 3*).

Molecular mechanisms for presynaptic function

The synaptic vesicle cycle

Neuronal communication relies on Ca^{2+} -dependent neurotransmitter release at the active zone, a complex molecular compartment at the presynaptic membrane. The active zone is directly opposing the postsynaptic site that is enriched for neurotransmitter receptors, thereby facilitating efficient neurotransmission at synaptic contacts. Presynaptic boutons are densely packed with synaptic vesicles containing neurotransmitters. Release of these neurotransmitters occurs via a highly coordinated local recycling process known as the synaptic vesicle cycle, and the sequence of events during this process are well-described

(Fig 2) (Sudhof 2004; Rizzoli 2014). First, neurotransmitter uptake by synaptic vesicles is mediated by local transporters inserted in synaptic vesicle membranes. Second, the synaptic vesicles are recruited and docked to the presynaptic membrane at the active zone. Third, synaptic vesicles are primed at the active zone as they come in close proximity to the plasma membrane, which is critical to efficiently facilitate the subsequent exocytosis required for fast neurotransmission. Fourth, an incoming action potential drives the opening of voltage-gated Ca^{2+} channels at the active zone, resulting in a local Ca^{2+} influx. This is followed by Ca^{2+} -dependent exocytosis of synaptic vesicles primed at the active zone, a process mediated by Ca^{2+} sensor proteins that trigger the presynaptic release machinery. This leads to the release of the synaptic vesicle content into the synaptic cleft. The neurotransmitters will subsequently bind to receptors at the postsynaptic membrane to further transmit the signal. Meanwhile, the synaptic vesicle membrane is retrieved and refilled with neurotransmitters to replenish the local pool of synaptic vesicles at the axonal bouton, and to restore the presynaptic membrane after synaptic vesicle fusion. The local recycling of synaptic vesicles at single synapses is critical to facilitate fast and continuous neurotransmission.

The role of ER for presynaptic function

The distinctive axonal ER network forms unique structures at synapses, as recently uncovered by high resolution imaging studies (Wu et al. 2017; Yalcin et al. 2017). Specifically, at presynaptic boutons, the axonal ER tubules are organized into characteristic small cisternae and networks, localized near the plasma membrane opposite of the active zone (Wu et al. 2017; Yalcin et al. 2017). Similar to axonal ER, the presynaptic ER is exclusively comprised of ribosome-lacking smooth ER and likely carries out smooth ER functions (Yalcin et al. 2017; Wu et al. 2017; Terasaki 2018). Emerging evidence is starting to elucidate the importance of presynaptic ER for Ca^{2+} -induced neurotransmitter release (Skehel et al. 1995; Summerville et al. 2016; De Gregorio et al. 2017; de Juan-Sanz et al. 2017). In *Drosophila*, perturbed axonal ER structures, induced by loss of ER shaping proteins, is accompanied with significant decreased neurotransmitter release (Summerville et al. 2016; De Gregorio et al. 2017). In rodent neurons, neuronal transmission coincides with increased ER Ca^{2+} levels locally at presynaptic sites, and it is suggested that the presynaptic ER buffers Ca^{2+} to modulate presynaptic function (de Juan-Sanz et al. 2017). New insights in the role of presynaptic ER structure and dynamics in modulating the synaptic vesicle cycle are presented in *Chapter 4* and the findings of this chapter are discussed by others (Bezprozvanny and Kavalali 2020; Ozturk, O’Kane, and Perez-Moreno 2020).

Scope of this thesis

Axon formation and functioning are critical for establishing neuronal polarity and facilitating neurotransmission, respectively, which are both fundamental aspects of information processing in neuronal networks. This thesis aims to dissect molecular machineries important for axon formation and axon functioning, by using multi-disciplinary approaches

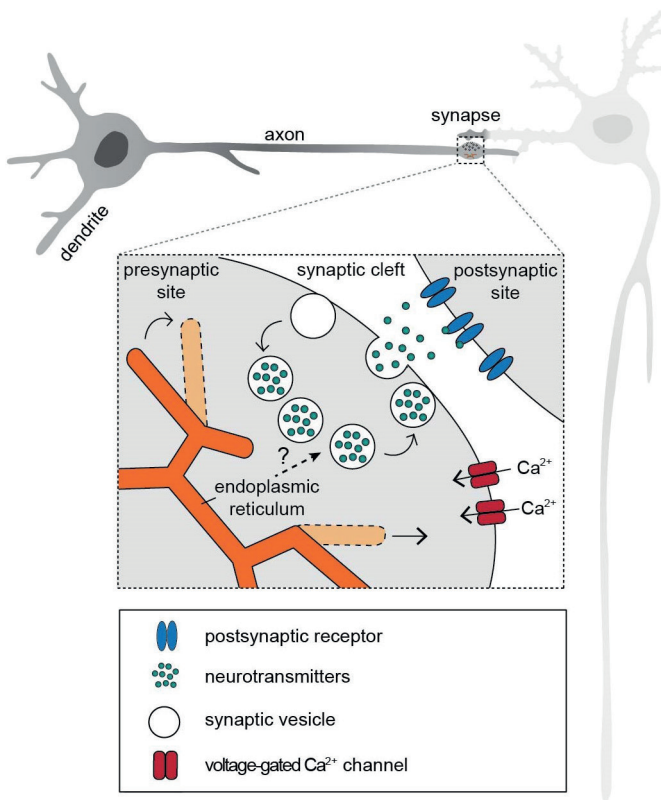


Figure 2.

The synaptic vesicle cycle

A schematic illustration of a synaptic contact formed between the axon and a dendrite of different neurons. The zoom represents a detailed overview of a synapse composed of a presynaptic site present at the axon, a postsynaptic site present at a dendrite, and a synaptic cleft in between. The presynaptic site is populated by synaptic vesicles containing neurotransmitters as well as specialized structures, such as the presynaptic endoplasmic reticulum (ER) network. When an action potential is present at a presynaptic site, voltage-gated Ca^{2+} channels will open. This results in a Ca^{2+} influx that drives the endocytosis of neurotransmitter-containing synaptic vesicles at the presynaptic membrane. The neurotransmitters are released in the synaptic cleft and bind to the postsynaptic receptors. Meanwhile, the synaptic vesicle membrane is recycled from the presynaptic membrane and refilled with neurotransmitters to replenish the local pool of neurotransmitter-containing synaptic vesicles. The role of the dynamic presynaptic ER structure during this highly coordinated process of synaptic vesicle recycling remains elusive.

and carefully selected model systems. The work in this thesis provides new insights in cytoskeletal-mediated mechanisms that underlie axon formation in human neurons, which marks one of the first steps in establishing neuronal polarity. By focusing on the functioning

of mature axons, this thesis uncovers new roles for the ER in modulating presynaptic function.

1

In *Chapter 2*, the dynamic transition of early neurodevelopmental stages in human iPSC-derived neurons are quantitatively and qualitatively profiled at a molecular and cellular level. This also includes a detailed characterization of axonal and dendritic microtubule remodeling processes in developing human neurons. By investigating the sequential processes during axon formation in human neurons, we demonstrate that initial axon formation follows a global distal-to-proximal reorganization in growing axons. *Chapter 3* provides new insights in the role of centrosomes during the onset of axon formation in human neurons. Centrosomes display MTOC functions during this initial axon developmental process, and this is particularly important for dynamic microtubule remodeling in growing axons and subsequent axon functioning. In *Chapter 4*, we explore the implication of ER structure and dynamics in presynaptic function. We report a specific interaction between ER receptor VAP and the newly identified VAP-associated protein SCR1. The VAP-SCR1 interactions are indispensable for ER integrity and remodeling as well as Ca²⁺-induced synaptic vesicle recycling. Finally, *Chapter 5* concludes this thesis by placing the key results in a broad perspective and by laying-out important research questions for future perspectives.

ACKNOWLEDGEMENTS

I would like to thank Sybren Portegies for co-producing the illustrations, and Harold MacGillavry, Robbelien Kooistra and Nicky Scheefhals for their constructive feedback on the text.

REFERENCES

- Al Jord, A., A. I. Lemaitre, N. Delgehyr, M. Faucourt, N. Spassky, and A. Meunier. 2014. 'Centriole amplification by mother and daughter centrioles differs in multiciliated cells', *Nature*, 516: 104-7.
- Anderson, R. G. 1972. 'The three-dimensional structure of the basal body from the rhesus monkey oviduct', *J Cell Biol*, 54: 246-65.
- Azevedo, F. A., L. R. Carvalho, L. T. Grinberg, J. M. Farfel, R. E. Ferretti, R. E. Leite, W. Jacob Filho, R. Lent, and S. Herculano-Houzel. 2009. 'Equal numbers of neuronal and nonneuronal cells make the human brain an isometrically scaled-up primate brain', *J Comp Neurol*, 513: 532-41.
- Baas, P. W., J. S. Deitch, M. M. Black, and G. A. Banker. 1988. 'Polarity orientation of microtubules in hippocampal neurons: uniformity in the axon and nonuniformity in the dendrite', *Proc Natl Acad Sci U S A*, 85: 8335-9.
- Baas, P. W., L. A. White, and S. R. Heidemann. 1987. 'Microtubule polarity reversal accompanies regrowth of amputated neurites', *Proc Natl Acad Sci U S A*, 84: 5272-6.
- Basto, R., K. Brunk, T. Vinadogrova, N. Peel, A. Franz, A. Khodjakov, and J. W. Raff. 2008. 'Centrosome amplification can initiate tumorigenesis in flies', *Cell*, 133: 1032-42.
- Basto, R., J. Lau, T. Vinogradova, A. Gardiol, C. G. Woods, A. Khodjakov, and J. W. Raff. 2006. 'Flies without centrioles', *Cell*, 125: 1375-86.
- Benavides-Piccione, R., I. Ballesteros-Yanez, J. DeFelipe, and R. Yuste. 2002. 'Cortical area and species differences in dendritic spine morphology', *J Neurocytol*, 31: 337-46.
- Bezprozvanny, I., and E. T. Kavalali. 2020. 'Presynaptic endoplasmic reticulum and neurotransmission', *Cell Calcium*, 85: 102133.
- Bobinnec, Y., A. Khodjakov, L. M. Mir, C. L. Rieder, B. Edde, and M. Bornens. 1998. 'Centriole disassembly *in vivo* and its effect on centrosome structure and function in vertebrate cells', *J Cell Biol*, 143: 1575-89.
- Bradke, F., and C. G. Dotti. 1999. 'The role of local actin instability in axon formation', *Science*, 283: 1931-4.
- Bystron, I., C. Blakemore, and P. Rakic. 2008. 'Development of the human cerebral cortex: Boulder Committee revisited', *Nat Rev Neurosci*, 9: 110-22.
- Castellanos, E., P. Dominguez, and C. Gonzalez. 2008. 'Centrosome dysfunction in *Drosophila* neural stem cells causes tumors that are not due to genome instability', *Curr Biol*, 18: 1209-14.
- Cavanagh, J. B. 1984. 'The problems of neurons with long axons', *Lancet*, 1: 1284-7.
- Conduit, P. T., A. Wainman, and J. W. Raff. 2015. 'Centrosome function and assembly in animal cells', *Nat Rev Mol Cell Biol*, 16: 611-24.
- Corbit, K. C., P. Aanstad, V. Singla, A. R. Norman, D. Y. Stainier, and J. F. Reiter. 2005. 'Vertebrate Smoothed functions at the primary cilium', *Nature*, 437: 1018-21.
- de Anda, F. C., G. Pollarolo, J. S. Da Silva, P. G. Camoletto, F. Feiguin, and C. G. Dotti. 2005. 'Centrosome localization determines neuronal polarity', *Nature*, 436: 704-8.
- De Gregorio, C., R. Delgado, A. Ibacache, J. Sierralta, and A. Couve. 2017. '*Drosophila* Atlastin in motor neurons is required for locomotion and presynaptic function', *J Cell Sci*, 130: 3507-16.
- de Juan-Sanz, J., G. T. Holt, E. R. Schreiter, F. de Juan, D. S. Kim, and T. A. Ryan. 2017. 'Axonal

- Endoplasmic Reticulum Ca⁽²⁺⁾ Content Controls Release Probability in CNS Nerve Terminals', *Neuron*, 93: 867-81.e6.
- De Juan Romero, C., and V. Borrell. 2015. 'Coevolution of radial glial cells and the cerebral cortex', *Glia*, 63: 1303-19.
- Defelipe, J. 2011. 'The evolution of the brain, the human nature of cortical circuits, and intellectual creativity', *Front Neuroanat*, 5: 29.
- Dehay, C., H. Kennedy, and K. S. Kosik. 2015. 'The outer subventricular zone and primate-specific cortical complexification', *Neuron*, 85: 683-94.
- Desai, A., and T. J. Mitchison. 1997. 'Microtubule polymerization dynamics', *Annu Rev Cell Dev Biol*, 13: 83-117.
- Dotti, C. G., C. A. Sullivan, and G. A. Banker. 1988. 'The establishment of polarity by hippocampal neurons in culture', *J Neurosci*, 8: 1454-68.
- Emery, N. J., and N. S. Clayton. 2005. 'Evolution of the avian brain and intelligence', *Curr Biol*, 15: R946-50.
- Espuny-Camacho, I., K. A. Michelsen, D. Gall, D. Linaro, A. Hasche, J. Bonnefont, C. Bali, D. Orduz, A. Bilheu, A. Herpoel, N. Lambert, N. Gaspard, S. Peron, S. N. Schiffmann, M. Giugliano, A. Gaillard, and P. Vanderhaeghen. 2013. 'Pyramidal neurons derived from human pluripotent stem cells integrate efficiently into mouse brain circuits *in vivo*', *Neuron*, 77: 440-56.
- Esteves, T., A. Durr, E. Mundwiller, J. L. Loureiro, M. Boutry, M. A. Gonzalez, J. Gauthier, K. H. El-Hachimi, C. Depienne, M. P. Muriel, R. F. Acosta Lebrigio, M. Gausson, A. Noreau, F. Speziani, A. Dionne-Laporte, J. F. Deleuze, P. Dion, P. Coutinho, G. A. Rouleau, S. Zuchner, A. Brice, G. Stevanin, and F. Darios. 2014. 'Loss of association of REEP2 with membranes leads to hereditary spastic paraplegia', *Am J Hum Genet*, 94: 268-77.
- Evsyukova, I., C. Plestant, and E. S. Anton. 2013. 'Integrative mechanisms of oriented neuronal migration in the developing brain', *Annu Rev Cell Dev Biol*, 29: 299-353.
- Farina, F., J. Gaillard, C. Guerin, Y. Coute, J. Sillibourne, L. Blanchoin, and M. Thery. 2016. 'The centrosome is an actin-organizing centre', *Nat Cell Biol*, 18: 65-75.
- Fietz, S. A., I. Kelava, J. Vogt, M. Wilsch-Brauninger, D. Stenzel, J. L. Fish, D. Corbeil, A. Riehn, W. Distler, R. Nitsch, and W. B. Huttner. 2010. 'OSVZ progenitors of human and ferret neocortex are epithelial-like and expand by integrin signaling', *Nat Neurosci*, 13: 690-9.
- Fish, J. L., C. Dehay, H. Kennedy, and W. B. Huttner. 2008. 'Making bigger brains-the evolution of neural-progenitor-cell division', *J Cell Sci*, 121: 2783-93.
- Freal, A., D. Rai, R. P. Tas, X. Pan, E. A. Katrukha, D. van de Willige, R. Stucchi, A. Aher, C. Yang, A. F. M. Altelaar, K. Vocking, J. A. Post, M. Harterink, L. C. Kapitein, A. Akhmanova, and C. C. Hoogenraad. 2019. 'Feedback-Driven Assembly of the Axon Initial Segment', *Neuron*, 104: 305-21.e8.
- Gaspard, N., T. Bouschet, R. Hourez, J. Dimidschstein, G. Naeije, J. van den Aemele, I. Espuny-Camacho, A. Herpoel, L. Passante, S. N. Schiffmann, A. Gaillard, and P. Vanderhaeghen. 2008. 'An intrinsic mechanism of corticogenesis from embryonic stem cells', *Nature*, 455: 351-7.
- Geraldo, S., U. K. Khanzada, M. Parsons, J. K. Chilton, and P. R. Gordon-Weeks. 2008. 'Targeting of the F-actin-binding protein drebrin by the microtubule plus-tip protein EB3 is required for neuritogenesis', *Nat Cell Biol*, 10: 1181-9.

- Goodwin, P. R., J. M. Sasaki, and P. Juo. 2012. 'Cyclin-dependent kinase 5 regulates the polarized trafficking of neuropeptide-containing dense-core vesicles in *Caenorhabditis elegans* motor neurons', *J Neurosci*, 32: 8158-72.
- Hansen, D. V., J. H. Lui, P. R. Parker, and A. R. Kriegstein. 2010. 'Neurogenic radial glia in the outer subventricular zone of human neocortex', *Nature*, 464: 554-61.
- Hazan, J., N. Fonknechten, D. Mavel, C. Paternotte, D. Samson, F. Artiguenave, C. S. Davoine, C. Cruaud, A. Durr, P. Wincker, P. Brottier, L. Cattolico, V. Barbe, J. M. Burgunder, J. F. Prud'homme, A. Brice, B. Fontaine, B. Heilig, and J. Weissenbach. 1999. 'Spastin, a new AAA protein, is altered in the most frequent form of autosomal dominant spastic paraplegia', *Nat Genet*, 23: 296-303.
- Huttenlocher, P. R. 1979. 'Synaptic density in human frontal cortex - developmental changes and effects of aging', *Brain Res*, 163: 195-205.
- Huttenlocher, P. R., C. de Courten, L. J. Garey, and H. Van der Loos. 1982. 'Synaptogenesis in human visual cortex--evidence for synapse elimination during normal development', *Neurosci Lett*, 33: 247-52.
- Ishikawa, H., and W. F. Marshall. 2011. 'Ciliogenesis: building the cell's antenna', *Nat Rev Mol Cell Biol*, 12: 222-34.
- Jan, Y. N., and L. Y. Jan. 1998. 'Asymmetric cell division', *Nature*, 392: 775-8.
- Karsenti, E., S. Kobayashi, T. Mitchison, and M. Kirschner. 1984. 'Role of the centrosome in organizing the interphase microtubule array: properties of cytoplasts containing or lacking centrosomes', *J Cell Biol*, 98: 1763-76.
- Kelava, I., and M. A. Lancaster. 2016. 'Stem Cell Models of Human Brain Development', *Cell Stem Cell*, 18: 736-48.
- Klos Dehring, D. A., E. K. Vldar, M. E. Werner, J. W. Mitchell, P. Hwang, and B. J. Mitchell. 2013. 'Deuterosome-mediated centriole biogenesis', *Dev Cell*, 27: 103-12.
- Knoblich, J. A. 2010. 'Asymmetric cell division: recent developments and their implications for tumour biology', *Nat Rev Mol Cell Biol*, 11: 849-60.
- Kole, M. H., S. U. Ilshner, B. M. Kampa, S. R. Williams, P. C. Ruben, and G. J. Stuart. 2008. 'Action potential generation requires a high sodium channel density in the axon initial segment', *Nat Neurosci*, 11: 178-86.
- Lancaster, M. A., M. Renner, C. A. Martin, D. Wenzel, L. S. Bicknell, M. E. Hurles, T. Homfray, J. M. Penninger, A. P. Jackson, and J. A. Knoblich. 2013. 'Cerebral organoids model human brain development and microcephaly', *Nature*, 501: 373-9.
- Leterrier, C. 2018. 'The Axon Initial Segment: An Updated Viewpoint', *J Neurosci*, 38: 2135-45.
- Linaro, D., B. Vermaercke, R. Iwata, A. Ramaswamy, B. Libe-Philippot, L. Boubakar, B. A. Davis, K. Wierda, K. Davie, S. Poovathingal, P. A. Penttila, A. Bilheu, L. De Bruyne, D. Gall, K. K. Conzelmann, V. Bonin, and P. Vanderhaeghen. 2019. 'Xenotransplanted Human Cortical Neurons Reveal Species-Specific Development and Functional Integration into Mouse Visual Circuits', *Neuron*, 104: 972-86.e6.
- Liu, X., K. Hashimoto-Torii, M. Torii, C. Ding, and P. Rakic. 2010. 'Gap junctions/hemichannels modulate interkinetic nuclear migration in the forebrain precursors', *J Neurosci*, 30: 4197-209.
- Liu, X., M. Somel, L. Tang, Z. Yan, X. Jiang, S. Guo, Y. Yuan, L. He, A. Oleksiak, Y. Zhang, N. Li, Y. Hu, W. Chen, Z. Qiu, S. Paabo, and P. Khaitovich. 2012. 'Extension of cortical synaptic

- development distinguishes humans from chimpanzees and macaques', *Genome Res*, 22: 611-22.
- Maniar, T. A., M. Kaplan, G. J. Wang, K. Shen, L. Wei, J. E. Shaw, S. P. Koushika, and C. I. Bargmann. 2011. 'UNC-33 (CRMP) and ankyrin organize microtubules and localize kinesin to polarize axon-dendrite sorting', *Nat Neurosci*, 15: 48-56.
- Maroof, A. M., S. Keros, J. A. Tyson, S. W. Ying, Y. M. Ganat, F. T. Merkle, B. Liu, A. Goulburn, E. G. Stanley, A. G. Elefanty, H. R. Widmer, K. Eggan, P. A. Goldstein, S. A. Anderson, and L. Studer. 2013. 'Directed differentiation and functional maturation of cortical interneurons from human embryonic stem cells', *Cell Stem Cell*, 12: 559-72.
- Meka, D. P., R. Scharrenberg, and F. Calderon de Anda. 2020. 'Emerging roles of the centrosome in neuronal development', *Cytoskeleton (Hoboken)*, 77: 84-96.
- Mennella, V., B. Keszthelyi, K. L. McDonald, B. Chhun, F. Kan, G. C. Rogers, B. Huang, and D. A. Agard. 2012. 'Subdiffraction-resolution fluorescence microscopy reveals a domain of the centrosome critical for pericentriolar material organization', *Nat Cell Biol*, 14: 1159-68.
- Mitchison, T. J. 1993. 'Localization of an exchangeable GTP binding site at the plus end of microtubules', *Science*, 261: 1044-7.
- Montenegro, G., A. P. Rebelo, J. Connell, R. Allison, C. Babalini, M. D'Aloia, P. Montieri, R. Schule, H. Ishiura, J. Price, A. Strickland, M. A. Gonzalez, L. Baumbach-Reardon, T. Deconinck, J. Huang, G. Bernardi, J. M. Vance, M. T. Rogers, S. Tsuji, P. De Jonghe, M. A. Pericak-Vance, L. Schols, A. Orlicchio, E. Reid, and S. Zuchner. 2012. 'Mutations in the ER-shaping protein reticulon 2 cause the axon-degenerative disorder hereditary spastic paraplegia type 12', *J Clin Invest*, 122: 538-44.
- Mora-Bermudez, F., F. Badsha, S. Kanton, J. G. Camp, B. Vernot, K. Kohler, B. Voigt, K. Okita, T. Maricic, Z. He, R. Lachmann, S. Paabo, B. Treutlein, and W. B. Huttner. 2016. 'Differences and similarities between human and chimpanzee neural progenitors during cerebral cortex development', *Elife*, 5.
- Moritz, M., M. B. Braunfeld, V. Guenebaut, J. Heuser, and D. A. Agard. 2000. 'Structure of the gamma-tubulin ring complex: a template for microtubule nucleation', *Nat Cell Biol*, 2: 365-70.
- Nano, M., and R. Basto. 2017. 'Consequences of Centrosome Dysfunction During Brain Development', *Adv Exp Med Biol*, 1002: 19-45.
- Neukirchen, D., and F. Bradke. 2011. 'Neuronal polarization and the cytoskeleton', *Semin Cell Dev Biol*, 22: 825-33.
- Nicholas, C. R., J. Chen, Y. Tang, D. G. Southwell, N. Chalmers, D. Vogt, C. M. Arnold, Y. J. Chen, E. G. Stanley, A. G. Elefanty, Y. Sasai, A. Alvarez-Buylla, J. L. Rubenstein, and A. R. Kriegstein. 2013. 'Functional maturation of hPSC-derived forebrain interneurons requires an extended timeline and mimics human neural development', *Cell Stem Cell*, 12: 573-86.
- Nigg, E. A., and J. W. Raff. 2009. 'Centrioles, centrosomes, and cilia in health and disease', *Cell*, 139: 663-78.
- Nishimura, A. L., M. Mitne-Neto, H. C. Silva, A. Richieri-Costa, S. Middleton, D. Cascio, F. Kok, J. R. Oliveira, T. Gillingwater, J. Webb, P. Skehel, and M. Zatz. 2004. 'A mutation in the vesicle-trafficking protein VAPB causes late-onset spinal muscular atrophy and amyotrophic lateral sclerosis', *Am J Hum Genet*, 75: 822-31.
- Noctor, S. C., V. Martinez-Cerdeno, L. Ivic, and A. R. Kriegstein. 2004. 'Cortical neurons arise in

- symmetric and asymmetric division zones and migrate through specific phases', *Nat Neurosci*, 7: 136-44.
- Otani, T., M. C. Marchetto, F. H. Gage, B. D. Simons, and F. J. Livesey. 2016. '2D and 3D Stem Cell Models of Primate Cortical Development Identify Species-Specific Differences in Progenitor Behavior Contributing to Brain Size', *Cell Stem Cell*, 18: 467-80.
- Ozturk, Z., C. J. O'Kane, and J. J. Perez-Moreno. 2020. 'Axonal Endoplasmic Reticulum Dynamics and Its Roles in Neurodegeneration', *Front Neurosci*, 14: 48.
- Petanjek, Z., M. Judas, G. Simic, M. R. Rasin, H. B. Uylings, P. Rakic, and I. Kostovic. 2011. 'Extraordinary neoteny of synaptic spines in the human prefrontal cortex', *Proc Natl Acad Sci U S A*, 108: 13281-6.
- Pollard, K. S., S. R. Salama, N. Lambert, M. A. Lambot, S. Coppens, J. S. Pedersen, S. Katzman, B. King, C. Onodera, A. Siepel, A. D. Kern, C. Dehay, H. Igel, M. Ares, Jr., P. Vanderhaeghen, and D. Haussler. 2006. 'An RNA gene expressed during cortical development evolved rapidly in humans', *Nature*, 443: 167-72.
- Poulton, J. S., J. C. Cuningham, and M. Peifer. 2017. 'Centrosome and spindle assembly checkpoint loss leads to neural apoptosis and reduced brain size', *J Cell Biol*, 216: 1255-65.
- Powell, S. K., R. J. Rivas, E. Rodriguez-Boulan, and M. E. Hatten. 1997. 'Development of polarity in cerebellar granule neurons', *J Neurobiol*, 32: 223-36.
- Pulvers, J. N., J. Bryk, J. L. Fish, M. Wilsch-Brauninger, Y. Arai, D. Schreier, R. Naumann, J. Helppi, B. Habermann, J. Vogt, R. Nitsch, A. Toth, W. Enard, S. Paabo, and W. B. Huttner. 2010. 'Mutations in mouse *Aspm* (abnormal spindle-like microcephaly associated) cause not only microcephaly but also major defects in the germline', *Proc Natl Acad Sci U S A*, 107: 16595-600.
- Reillo, I., C. de Juan Romero, M. A. Garcia-Cabezas, and V. Borrell. 2011. 'A role for intermediate radial glia in the tangential expansion of the mammalian cerebral cortex', *Cereb Cortex*, 21: 1674-94.
- Rhyu, M. S., L. Y. Jan, and Y. N. Jan. 1994. 'Asymmetric distribution of numb protein during division of the sensory organ precursor cell confers distinct fates to daughter cells', *Cell*, 76: 477-91.
- Rizzoli, S. O. 2014. 'Synaptic vesicle recycling: steps and principles', *Embo j*, 33: 788-822.
- Rohatgi, R., L. Milenkovic, and M. P. Scott. 2007. 'Patched1 regulates hedgehog signaling at the primary cilium', *Science*, 317: 372-6.
- Schelski, M., and F. Bradke. 2017. 'Neuronal polarization: From spatiotemporal signaling to cytoskeletal dynamics', *Mol Cell Neurosci*, 84: 11-28.
- Shi, Y., P. Kirwan, and F. J. Livesey. 2012. 'Directed differentiation of human pluripotent stem cells to cerebral cortex neurons and neural networks', *Nat Protoc*, 7: 1836-46.
- Shimogori, T., V. Banuchi, H. Y. Ng, J. B. Strauss, and E. A. Grove. 2004. 'Embryonic signaling centers expressing BMP, WNT and FGF proteins interact to pattern the cerebral cortex', *Development*, 131: 5639-47.
- Shitamukai, A., and F. Matsuzaki. 2012. 'Control of asymmetric cell division of mammalian neural progenitors', *Dev Growth Differ*, 54: 277-86.
- Simons, M., J. Gloy, A. Ganner, A. Bullerkotte, M. Bashkurov, C. Kronig, B. Schermer, T. Benzing, O. A. Cabello, A. Jenny, M. Mlodzik, B. Polok, W. Driever, T. Obara, and G. Walz. 2005.

- 'Inversin, the gene product mutated in nephronophthisis type II, functions as a molecular switch between Wnt signaling pathways', *Nat Genet*, 37: 537-43.
- Skehel, P. A., K. C. Martin, E. R. Kandel, and D. Bartsch. 1995. 'A VAMP-binding protein from *Aplysia* required for neurotransmitter release', *Science*, 269: 1580-3.
- Somel, M., H. Franz, Z. Yan, A. Lorenc, S. Guo, T. Giger, J. Kelso, B. Nickel, M. Dannemann, S. Bahn, M. J. Webster, C. S. Weickert, M. Lachmann, S. Paabo, and P. Khaitovich. 2009. 'Transcriptional neoteny in the human brain', *Proc Natl Acad Sci U S A*, 106: 5743-8.
- Sonnen, K. F., L. Schermelleh, H. Leonhardt, and E. A. Nigg. 2012. '3D-structured illumination microscopy provides novel insight into architecture of human centrosomes', *Biol Open*, 1: 965-76.
- Sousa, A. M. M., K. A. Meyer, G. Santpere, F. O. Gulden, and N. Sestan. 2017. 'Evolution of the Human Nervous System Function, Structure, and Development', *Cell*, 170: 226-47.
- Stepanova, T., J. Slemmer, C. C. Hoogenraad, G. Lansbergen, B. Dortland, C. I. De Zeeuw, F. Grosveld, G. van Cappellen, A. Akhmanova, and N. Galjart. 2003. 'Visualization of microtubule growth in cultured neurons via the use of EB3-GFP (end-binding protein 3-green fluorescent protein)', *J Neurosci*, 23: 2655-64.
- Stiess, M., and F. Bradke. 2011. 'Neuronal polarization: the cytoskeleton leads the way', *Dev Neurobiol*, 71: 430-44.
- Stiess, M., N. Maghelli, L. C. Kapitein, S. Gomis-Ruth, M. Wilsch-Brauninger, C. C. Hoogenraad, I. M. Tolic-Norrelykke, and F. Bradke. 2010. 'Axon extension occurs independently of centrosomal microtubule nucleation', *Science*, 327: 704-7.
- Stoeckli, E. T. 2018. 'Understanding axon guidance: are we nearly there yet?', *Development*, 145.
- Stone, M. C., F. Roegiers, and M. M. Rolls. 2008. 'Microtubules have opposite orientation in axons and dendrites of *Drosophila* neurons', *Mol Biol Cell*, 19: 4122-9.
- Sudhof, T. C. 2004. 'The synaptic vesicle cycle', *Annu Rev Neurosci*, 27: 509-47.
- Summerville, J. B., J. F. Faust, E. Fan, D. Pendin, A. Daga, J. Formella, M. Stern, and J. A. McNew. 2016. 'The effects of ER morphology on synaptic structure and function in *Drosophila melanogaster*', *J Cell Sci*, 129: 1635-48.
- Taverna, E., M. Gotz, and W. B. Huttner. 2014. 'The cell biology of neurogenesis: toward an understanding of the development and evolution of the neocortex', *Annu Rev Cell Dev Biol*, 30: 465-502.
- Terasaki, M. 2018. 'Axonal endoplasmic reticulum is very narrow', *J Cell Sci*, 131.
- Theveneau, E., and R. Mayor. 2012. 'Neural crest delamination and migration: from epithelium-to-mesenchyme transition to collective cell migration', *Dev Biol*, 366: 34-54.
- Tsai, L. H., and J. G. Gleeson. 2005. 'Nucleokinesis in neuronal migration', *Neuron*, 46: 383-8.
- van Beuningen, S. F., and C. C. Hoogenraad. 2016. 'Neuronal polarity: remodeling microtubule organization', *Curr Opin Neurobiol*, 39: 1-7.
- von Bartheld, C. S., J. Bahney, and S. Herculano-Houzel. 2016. 'The search for true numbers of neurons and glial cells in the human brain: A review of 150 years of cell counting', *J Comp Neurol*, 524: 3865-95.
- Vora, S. M., and B. T. Phillips. 2016. 'The benefits of local depletion: The centrosome as a scaffold for ubiquitin-proteasome-mediated degradation', *Cell Cycle*, 15: 2124-34.
- Wallingford, J. B., and B. Mitchell. 2011. 'Strange as it may seem: the many links between Wnt signaling, planar cell polarity, and cilia', *Genes Dev*, 25: 201-13.

-
- Witte, H., D. Neukirchen, and F. Bradke. 2008. 'Microtubule stabilization specifies initial neuronal polarization', *J Cell Biol*, 180: 619-32.
- Wu, Y., C. Whiteus, C. S. Xu, K. J. Hayworth, R. J. Weinberg, H. F. Hess, and P. De Camilli. 2017. 'Contacts between the endoplasmic reticulum and other membranes in neurons', *Proc Natl Acad Sci U S A*, 114: E4859-e67.
- Yalcin, B., L. Zhao, M. Stofanko, N. C. O'Sullivan, Z. H. Kang, A. Roost, M. R. Thomas, S. Zaessinger, O. Blard, A. L. Patto, A. Sohail, V. Baena, M. Terasaki, and C. J. O'Kane. 2017. 'Modeling of axonal endoplasmic reticulum network by spastic paraplegia proteins', *Elife*, 6.
- Yau, K. W., P. Schatzle, E. Tortosa, S. Pages, A. Holtmaat, L. C. Kapitein, and C. C. Hoogenraad. 2016. 'Dendrites *In vitro* and *In vivo* Contain Microtubules of Opposite Polarity and Axon Formation Correlates with Uniform Plus-End-Out Microtubule Orientation', *J Neurosci*, 36: 1071-85.
- Yu, W., and P. W. Baas. 1994. 'Changes in microtubule number and length during axon differentiation', *J Neurosci*, 14: 2818-29.
- Zhao, B., D. P. Meka, R. Scharrenberg, T. Konig, B. Schwanke, O. Kobler, S. Windhorst, M. R. Kreutz, M. Mikhaylova, and F. Calderon de Anda. 2017. 'Microtubules Modulate F-actin Dynamics during Neuronal Polarization', *Sci Rep*, 7: 9583.
- Zhao, X., D. Alvarado, S. Rainier, R. Lemons, P. Hedera, C. H. Weber, T. Tukul, M. Apak, T. Heiman-Patterson, L. Ming, M. Bui, and J. K. Fink. 2001. 'Mutations in a newly identified GTPase gene cause autosomal dominant hereditary spastic paraplegia', *Nat Genet*, 29: 326-31.
- Zmuda, J. F., and R. J. Rivas. 1998. 'The Golgi apparatus and the centrosome are localized to the sites of newly emerging axons in cerebellar granule neurons *in vitro*', *Cell Motil Cytoskeleton*, 41: 18-38.
- Zuchner, S., G. Wang, K. N. Tran-Viet, M. A. Nance, P. C. Gaskell, J. M. Vance, A. E. Ashley-Koch, and M. A. Pericak-Vance. 2006. 'Mutations in the novel mitochondrial protein REEP1 cause hereditary spastic paraplegia type 31', *Am J Hum Genet*, 79: 365-9.

2.



Quantitative mapping of transcriptome and proteome dynamics during polarization of human iPSC-derived neurons

Feline W. Lindhout^{1*}, Robbelien Kooistra^{1*}, Sybren Portegies^{1*}, Lotte J. Herstel¹, Riccardo Stucchi^{1,2}, Basten L. Snoek³, Maarten Altelaar², Harold D. MacGillavry¹, Corette J. Wierenga¹, Casper C. Hoogenraad^{1,4,5}

¹Cell Biology, Neurobiology and Biophysics, Department of Biology, Faculty of Science, Utrecht University, 3584 CH Utrecht, The Netherlands.

²Biomolecular Mass Spectrometry and Proteomics, Bijvoet Center for Biomolecular Research and Utrecht Institute for Pharmaceutical Sciences, Utrecht University, 3584 CH Utrecht, The Netherlands.

³Theoretical Biology and Bioinformatics, Utrecht University, 3584 CH Utrecht, The Netherlands.

⁴Department of Neuroscience, Genentech, Inc, South San Francisco, CA 94080, USA.

⁵Lead Contact

*authors contributed equally

Elife (2020), *in press*

Preprint available on BioRxiv; doi: 10.1101/2020.04.21.052498

ABSTRACT

The differentiation of neuronal stem cells into polarized neurons is a well-coordinated process which has mostly been studied in classical non-human model systems, but to what extent these findings are recapitulated in human neurons remains unclear. To study neuronal polarization in human neurons, we cultured hiPSC-derived neurons, characterized early developmental stages, measured electrophysiological responses, and systematically profiled transcriptomic and proteomic dynamics during these steps. The neuron transcriptome and proteome shows extensive remodeling, with differential expression profiles of ~1,100 transcripts and ~2,200 proteins during neuronal differentiation and polarization. We also identified a distinct axon developmental stage marked by the relocation of axon initial segment proteins and increased microtubule remodeling from the distal (stage 3a) to the proximal (stage 3b) axon. This developmental transition coincides with action potential maturation. Our comprehensive characterization and quantitative map of transcriptome and proteome dynamics provides a solid framework for studying polarization in human neurons.

INTRODUCTION

Neuronal development is a complex multistep process in which neurons undergo dramatic morphological changes, including migration, axon outgrowth, dendritogenesis, and synapse formation. Much of the fundamental knowledge about neuronal development is based on experimental studies in non-human model systems, such as *Drosophila*, *C. Elegans*, mice and rats (Zhao and Bhattacharyya 2018). However, to what extent the knowledge obtained in animal models can be extrapolated to human neuronal development remains largely unclear. Moreover, analysis of human-specific characteristics is hindered by the difficulty in obtaining human brain tissue. The generation of human induced pluripotent stem cells (iPSCs) has provided a critical step forward for studying the development and function of human neuronal cells.

In recent years, many labs have used human iPSC-derived neuronal cultures to study fundamental neurobiological questions. This has contributed to our understanding of processes such as neuronal polarity, spine development and synaptic plasticity in human cells. For example, human iPSC-derived model systems have been used to study dynamic changes in gene expression during early neurogenesis, and to study polarization of neuronal progenitors (Compagnucci et al. 2015; Grassi et al. 2020). In addition, human synaptic transmission and plasticity have been studied at single cell level in hiPSC-derived neurons, and human-specific protein functions have been shown to regulate excitatory synaptic transmission specifically in human neurons (Meijer et al. 2019; Marro et al. 2019). These examples illustrate how the use of human iPSC-derived neurons as a model system can lead to novel findings for human neurodevelopment.

One of the classic model systems to study neuronal development are dissociated rat hippocampal neurons, developed by Banker and collaborators (Dotti, Sullivan, and Banker

1988). These neurons undergo five well-defined developmental stages, transforming from round, spherical cells to fully mature, polarized neurons (Craig and Banker 1994). First, the symmetric young neuron forms small processes (stage 1) and multiple neurites (stage 2). Next the cells undergo polarization, where one neurite is specified as the axon (stage 3), while the remaining neurites will further develop into dendrites. The axon rapidly extends and further matures by the formation of the axon initial segment (AIS) (Leterrier 2018). The AIS is required for generating action potentials (APs) and maintaining neuronal polarity. In addition to the classic AIS component Ankyrin-G (AnkG), the microtubule binding protein Trim46 also localizes to the AIS and is critical for axon formation by forming parallel microtubule bundles in the proximal axon (van Beuningen et al. 2015; Gumy et al. 2017; Harterink et al. 2018). As the neuron matures, the developing axons and dendrites undergo significant morphological and molecular changes and form dendritic spines (stage 4-5), which allow for the formation of synaptic contacts and the establishment of functional neuron-to-neuron interactions (Harris and Kater 1994; Fletcher, De Camilli, and Banker 1994; Grabrucker et al. 2009). In depth proteomic analysis of primary rat neurons in culture have identified a number of specific pathways and unique protein profiles that contribute to various aspects of neurodevelopment processes (Frese et al. 2017). Proper characterization and quantitative profiling of transcriptome and proteome dynamics is essential to study the specific neurodevelopment events in human iPSC-derived neuronal cultures, including early developmental changes such as neuronal polarization and axon specification.

In this study, we performed extensive characterization of the early developmental stages of hiPSC-derived neurons by immunocytochemistry, electrophysiology, RNA sequencing, and stable isotope labeling combined with high-resolution liquid chromatography-tandem mass spectrometry (LC-MS/MS). We established transcriptomic and proteomic profiles of the early developmental stages (stage 1-3), comprising 14,551 transcripts and 7,512 protein identifications, of which we assessed 1,163 and 2,218 factors that showed differential expression, respectively. These transcriptomic and proteomic profiles point to the importance of microtubule cytoskeleton remodeling in the early stage of neuronal development. Combining this framework with additional methods such as genetic manipulation and live-cell imaging allowed us to investigate the cellular and molecular processes during neuronal polarization and axon outgrowth. Specifically, we identified a distinct, previously unrecognized developmental stage during early axon development, characterized by the reorganization of the axonal microtubule network and relocation of AIS proteins from the distal to proximal axon. The transition through these early axon developmental stages coincided with the time window in which maturation of action potentials occurred. Together, our study provides a quantitative description of transcriptomic and proteomic profiles of hiPSC-derived neuron cultures, which is a rich resource for further analyses of critical signaling pathways during early human neurodevelopment.

RESULTS

Characterization of developmental stages in human iPSC-derived neurons

2 We first systematically assessed if the human iPSC-derived neurons proceed through the initial neurodevelopmental stages, which have previously been described in dissociated rat neurons (Dotti, Sullivan, and Banker 1988). The hiPSC-derived neuron cultures were obtained by neuronal induction of neuronal stem cells (NSCs) and maintained up to ~15 days (Axol Bioscience, Protocol Version 5.0, Human iPSC-derived Neural Stem Cells). hiPSC-derived neurons were transduced with FUGW-GFP lentivirus to visualize cell morphologies, and immunostained at different timepoints (day 1, 5 and 14) for proliferation marker Ki67 and NSC marker Nestin to identify NSCs (stage 1), neuron specific markers β 3-Tubulin and MAP2 to identify differentiated neurons (stage 2), and AIS markers AnkG and Trim46 to identify polarized neurons (stage 3) (Fig 1A,B). The presence of these markers indicated a clear developmental transition over time: stage 1 NSCs (~day 1) differentiated into stage 2 neurons with a characteristic neuronal morphology (~day 5), and subsequently developed axons containing AIS structures (~day 14) (Fig 1C-E). Accordingly, axon width showed a developmental decrease over time, whereas dendrite width remained relatively stable (Fig S1A,B). These observations indicate that hiPSC-derived neurons have a relatively prolonged development compared to dissociated rat neurons, consistent with the protracted development of the human brain (Dotti, Sullivan, and Banker 1988; Petanjek et al. 2011). This further supports the emerging evidence showing species-dependent differences in developmental timing of human and non-human neurons *in vivo* and *in vitro* (Shi, Kirwan, and Livesey 2012; Espuny-Camacho et al. 2013; Nicholas et al. 2013; Otani et al. 2016; Linaro et al. 2019). We further analyzed the structural AIS organization in axons of hiPSC-derived neurons by quantifying the average fluorescence intensity profiles of Trim46 and AnkG (Fig 1F,G). Consistent with previous reports in dissociated rat neurons, we found that Trim46 and AnkG localization largely overlapped, with the peak of AnkG intensity located ~6 μ m more distally than the peak Trim46 intensity (Fig 1F,G) (van Beuningen et al. 2015). The AIS structure was also enriched for voltage-gated sodium channels (Nav), which strongly overlapped with AnkG structures (Fig S1C). In summary, these data demonstrate that human iPSC-derived neurons follow the characteristic sequence of developmental stages during neuronal polarization, which occurs at a relatively slower rate than non-human neurons.

Action potential firing of polarized human iPSC-derived neurons

To determine whether the polarized human iPSC-derived neurons are able to fire APs, we performed whole-cell patch clamp recordings of stage 3 neurons. We observed AP firing upon positive somatic current stimulation in nearly all cells (59/61). Neuronal excitability was quantified as the number of APs in response to increasing current stimuli (steps of 5 pA; 400 ms) in 54 neurons (Fig 1H,I). Of these, 22 neurons (41%) fired multiple times upon higher current stimulation, while 32 neurons (59%) fired only once independent of stimulus strength (Fig S1D). Neurons that fired one AP showed more immature intrinsic

cell properties, including depolarized resting membrane potential, lower input resistance, smaller maximum sodium currents and smaller after-hyperpolarization (Fig S1E-H). Spontaneous AP firing or incoming spontaneous synaptic responses were only observed in a few neurons (4/22). This is in line with previous studies reporting that synapse formation typically starts around two weeks after neuronal induction in human iPSC-derived neurons (Zhang et al. 2013). Together, the immunofluorescence and electrophysiology data indicate that human iPSC-derived neurons develop functional axons after neuronal polarization.

Transcriptomic profiling of developing human iPSC-derived neurons

To assess global changes in gene expression during differentiation and neuronal polarization, we next performed an unbiased, in-depth analysis of the transcript expression profiles during early neuronal development. To this end, we collected human iPSC-derived neurons at the previously described developmental stages and monitored mRNA expression changes using quantitative population-based transcriptome analysis. The synchronized differentiation and relatively slow development of these cultures enabled us to select time points at which particular stages manifested in the majority of the cells. The cells were sampled for RNA analysis at days 1, 3, and 7, corresponding to stage 1, the onset of stage 2, and the onset of stage 3, respectively. At the same days, we collected samples for in-depth proteome analysis, which is discussed below. In two biological replicates with each two technical replicates, we identified transcripts corresponding to 14,551 genes by RNA sequencing (Table 1, Fig S2A). Of these, 9,655 transcripts were successfully quantified at all time points and normalized to reads per million for further analysis (Table 2). As expected, most genes with significantly altered expression were found between day 1 and day 7: 614 genes were downregulated and 549 genes were upregulated at day 7 compared to day 1 (FDR <0.05 (Yoav Benjamini and Yosef Hochberg, 1995)) (Table 3, Fig 2A, Fig S2B). Gene ontology (GO) enrichment analysis of downregulated genes indicates that many of the top enriched GO terms relate to processes involved in cell proliferation, such as DNA replication, cell cycle, and cell division (Table 4, Fig 2B). Upregulated genes correspond to several cellular components and biological processes including nervous system development, neuron projection, and axonogenesis (Table 4, Fig 2C). Consistently, upregulation of many neurodevelopmental-related and axonogenesis-related genes was previously observed in differentiating mouse embryonic stem cells (ESCs) and iPSCs as well as human ESCs (Wu et al. 2010; Chen et al. 2013). Interestingly, upregulated genes also showed enrichment of several GO terms related to the microtubule cytoskeleton (Fig 2C). Among the highly downregulated genes were several proliferation factors, such as SOX2, NOTCH1, and OTX2 (Table 3). Furthermore, the chromokinesin motor proteins KIF4a and KIF22, involved in cell proliferation by regulating spindle microtubule dynamics during mitosis, were downregulated (Almeida and Maiato 2018; Bisht, Tomschik, and Gatlin 2019). Conversely, genes of several neuronal and axonal kinesins are upregulated, including KIF1a, KIF5c, and KIF21b (Table 3) (Hirokawa and Tanaka 2015). Additionally, the neuron-specific tubulin TUBB3 and the axonal microtubule associated protein MAPT are upregulated

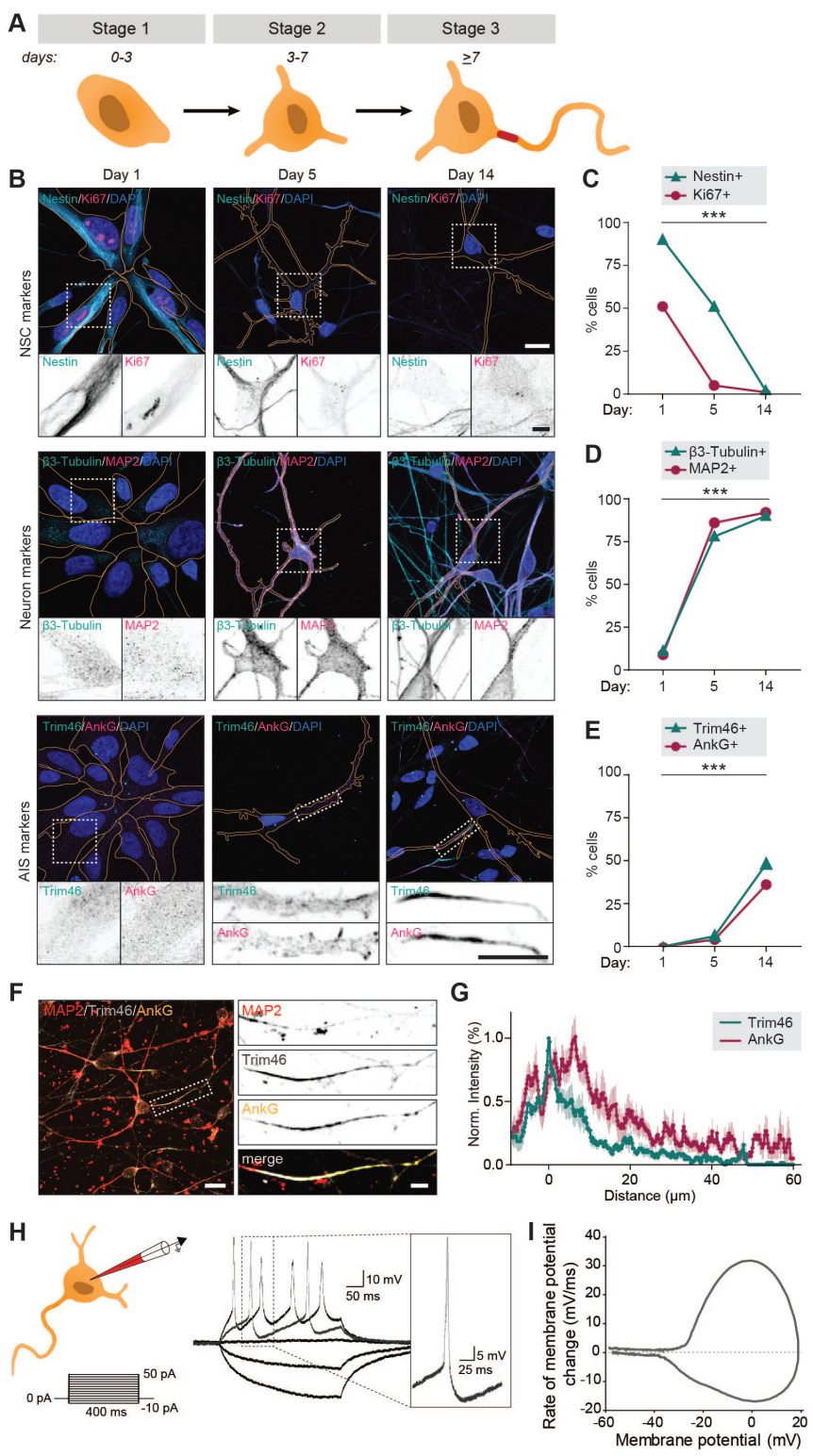


Figure 1.**Successful and protracted transition of early developmental stages in human iPSC-derived neurons**

A. Schematic illustration and timing of neurodevelopmental stages 1, 2 and 3 in human iPSC-derived NSCs/neurons.

B. Representative images of stage 1 (day 1), 2 (day 5) and 3 (day 14) hiPSC-derived NSCs/neurons. Cells were subjected to FUGW-GFP lentivirus and immunostained for NSC markers Nestin and Ki67, or neuron markers β 3-Tubulin and MAP2, or AIS markers AnkG and Trim46. Outline of cells was defined by the FUGW-GFP signal. Scale bar: 15 μ m in overview, 5 μ m in zooms.

C. Quantifications of percentage of human iPSC-derived NSCs positive for Ki67 or Nestin at 1, 5 or 14 days in culture. N=2, n=100-109 cells.

D. Quantifications of percentage of human iPSC-derived neurons positive for β 3-Tubulin or MAP2 at 1, 5 or 14 days in culture. N=2, n=100-109 cells.

E. Quantifications of percentage of human iPSC-derived neurons positive for AnkG or Trim46 at 1, 5 or 14 days in culture. N=2, n=100-109 cells.

F. Representative image of a polarized human iPSC-derived neuron immunostained for MAP2, Trim46 and AnkG. Zoom represents the AIS structure. Scale bar: 20 μ m in overview, 5 μ m in zoom.

G. Quantifications of average normalized fluorescent intensity profiles for Trim46 and AnkG at proximal axons (n=9) of human iPSC-derived neurons (day 15), distances are normalized to Trim46 peak intensities.

H. Left: Schematic illustration of the experimental electrophysiology setup. To determine AP frequency, somatic current injections from -10 pA to 50 pA (steps of 5 pA, 400 ms) were applied. Right: Representative example of evoked AP firing in a human iPSC-derived neuron, response to hyperpolarizing and two depolarizing current steps, recorded at day 14. Insert: first AP to minimal (rheobase) current injection.

I. Phase plot of a single AP of a human iPSC-derived neuron that fires multiple APs recorded at day 14.

NSC: neuronal stem cell, **AIS:** axon initial segment, **AP:** action potential. Used tests: Chi-square test (day 1 vs. day 14) (**C-E**); *** $p < 0.001$; error bars are \pm SEM.

(Table 3). The dynamic shift in the transcriptome reflects a population-wide transformation from proliferating cells to terminal differentiating cells with intrinsic neuronal properties, and highlights changes in the microtubule cytoskeleton expression profiles at the onset of stage 3.

Proteomic profiling of developing human iPSC-derived neurons

In addition to transcriptome analysis, we assessed gene expression on the translational level by performing mass spectrometry based quantitative proteomics. We collected samples for proteome analysis on the same days as described above for RNA sequencing. We identified 7,512 proteins in two replicates and quantified 5,620 proteins across all three time points (Table 5, Fig S2C). Of these, 2,218 proteins showed a changed expression profile during differentiation and neurodevelopment. We assessed the global proteome changes

by unsupervised clustering, and identified six clusters with distinct expression profiles (Fig 2D,E; Table 5). Proteins in clusters 1, 2, and 3 were upregulated, and proteins present in cluster 4, 5, and 6 were downregulated during early neuronal development. Moreover, many proteins within specific clusters showed overlap in functions (Fig 2D,E; Table 5). Cluster 1 contains proteins that show a slight increase from day 1 to day 7. GO enrichment analysis revealed enrichment of several terms related to neuronal differentiation and intracellular transport mechanisms, which reflects cell-autonomous remodeling of molecular processes (Fig 2D, Table5). One of the upregulated proteins in cluster 1 is KLC1, a subunit of the microtubule motor protein, which was found to be required for neuronal differentiation from human embryonic stem cells (Killian et al. 2012). The AIS protein Trim46, which is known to regulate neuron polarity and axon specification by controlling microtubule organization during development, was also found in this cluster (van Beuningen et al. 2015). Furthermore, this cluster contains Camsap1, Camsap2 and Camsap3, proteins which localize to the minus ends of microtubules to stabilize them, thereby regulating neuronal polarity (Jiang et al. 2014). Proteins in cluster 2 present a considerable increase in relative expression from day 3 to day 7, which coincides with the onset of axon formation and development (stage 3). Accordingly, enriched GO terms include proteins associated with neuronal development, axonogenesis, and other axon-related mechanisms (Fig 2D). Similarly, the GO terms neuronal development, axon, and synapse were also upregulated during differentiation of immortalized human neural progenitor cells (Song et al. 2019). Among the highly upregulated proteins in this cluster are several members of the Septin family: neuronal-specific Sept3, Sept5, and Sept6 (Table 5). Although mechanistic insights remain unclear, emerging evidence implicates Septins as potential factors for establishing neuronal polarity (Falk, Boubakar, and Castellani 2019). Septins interact with actin and microtubule networks and could affect neuronal polarity by regulating cytoskeleton dynamics (Spiliotis 2018; Falk, Boubakar, and Castellani 2019). Sept6 specifically is suggested to play a role in axonal filopodia formation as well as in dendritic branching, and its increased expression coincides with axonal outgrowth (Cho et al. 2011; Hu et al. 2012). Moreover, examples of proteins with the highest relative expression in this cluster are DCX, Tau, Ncam1, Basp1, Snap91, and Syt1, which are generally considered to be neuronal differentiation and polarization markers (Table 5). These data confirm the neuronal identity of the human iPSC-derived cells, and the presence of cellular machinery involved in axon development. Cluster 3 represents proteins with increased expression from day 1 to day 3, and minimal changes in expression from day 3 to day 7. This cluster comprises proteins enriched in GO terms that are associated with cell metabolism and (re)localization of intracellular and extracellular components, which correspond to substantial changes in the cellular proteome (Fig 2D). Proteins in this cluster that show differential expression from day 1 to day 3 include Sox4 and Sox11, both members of the SoxC transcription factor family (Table 5). These factors are involved in neurogenesis and their expression induces subsequent expression of neuron-specific genes (Kavyanifar, Turan, and Lie 2018). Also represented in this cluster are Arpc2 and Arpc4, subunits of the Arp2/3 complex. The Arp2/3 complex mediates actin polymerization and is required for

formation of lamellipodia and filopodia as well as axon guidance (Chou and Wang 2016). Clusters 4, 5, and 6 encompass proteins that are downregulated during the differentiation of NSCs into polarized neurons. GO analysis of these clusters reveals that they contain proteins involved in intracellular metabolism and homeostasis, genomic translation, the cell cycle, and biosynthesis of amino acids and peptides (Fig 2E). Downregulation of DNA replication and cell cycle-related proteins is also reported to coincide with terminal differentiation in neuroblastoma cells and with development of cultured rat neurons (Murillo et al. 2017; Frese et al. 2017). These results suggest that the overall proteome dynamics are indicative of cellular processes such as cell cycle exit and neuronal differentiation.

Comparison of transcriptomic and proteomic profiles of developing human iPSC-derived neurons

To compare the transcriptome and proteome dynamics, we performed correlative analysis of the relative RNA and protein expressions on day 7 compared to day 1 (Table 6). Based on their annotated gene names we were able to compare the expression dynamics of 7,021 factors. Of these, 4,536 followed the same trend for transcriptomic and proteomic expression changes, and overall, we found a significant correlation between the relative transcriptomic and proteomic expression profiles (Fig 2F). In agreement with the observed immunofluorescence, typical stem cell markers (NOTCH1, SOX2, MKI67, LIN28A, OTX2, and NES) showed a downregulation of both RNA and protein levels during neuronal differentiation. RNA levels as well as protein levels of typical neuron markers (DCX, ENO2, SYP, MAP2, STMN1, and TUBB3) and of axonal markers (TRIM46, MAPT, BASP1, ANK3, NCAM1, GAP43, and NFASC) displayed a marked increase during neuronal development (Fig 2G,H). Through quantitative analysis of transcriptomic and proteomic dynamics we were able to characterize human iPSC-derived neuronal differentiation and identify early neurodevelopmental processes in an unbiased manner. This quantitative map of neuronal transcriptome and proteome dynamics provides a rich resource for further analyses and may identify molecular mechanisms involved in neuronal polarity and axon specification.

Identification and characterization of intermediate stages during axon specification

Transcriptomic and proteomic profiling of developing neurons revealed that axonal components are upregulated after ~7 days, and assembled AIS structures were detected at proximal axons after ~14 days. Next, we studied the process of axon specification in human iPSC-derived neurons in more detail, and investigated the appearance of AIS proteins at different timepoints between day 5 and 11. In stage 2 neurons, in which neurites are unpolarized and have similar lengths, Trim46 and AnkG proteins appeared as punctate structures in one or more neurites in a subset of neurons (Fig 3A,B). Quantification of the relative abundance of stage 2 neurons lacking AIS proteins (referred to as stage 2a), or containing AIS proteins at one or more neurites (referred to as stage 2b), showed a developmental transition over time from stage 2a to stage 2b neurons (Fig 3A,B). Stage

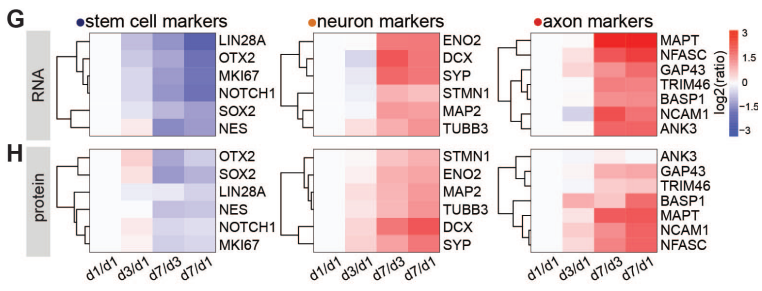
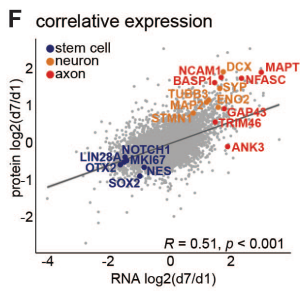
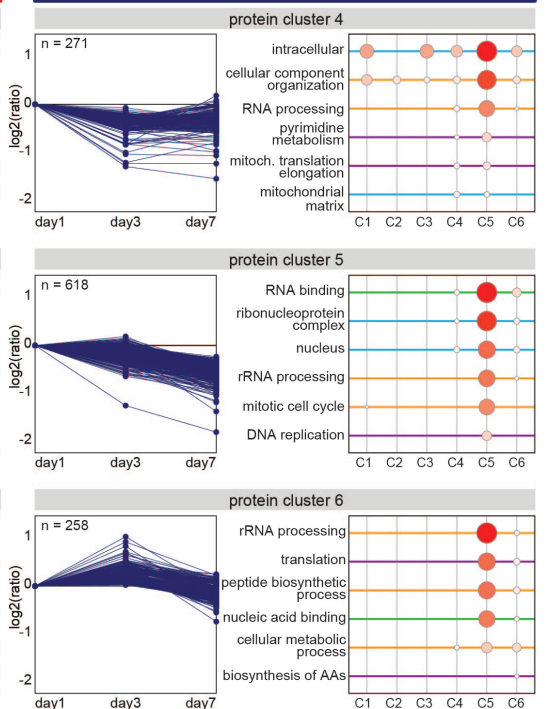
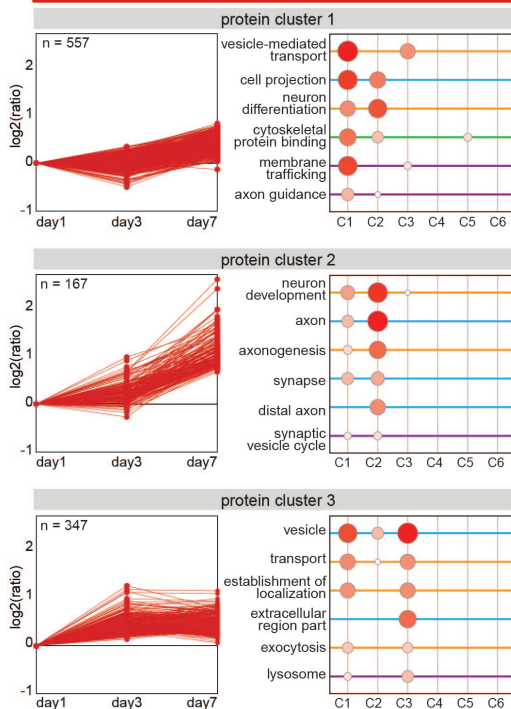
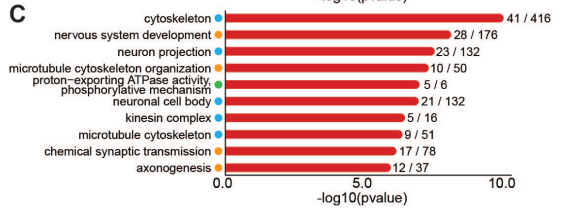
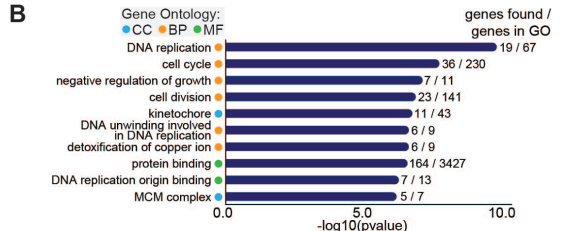
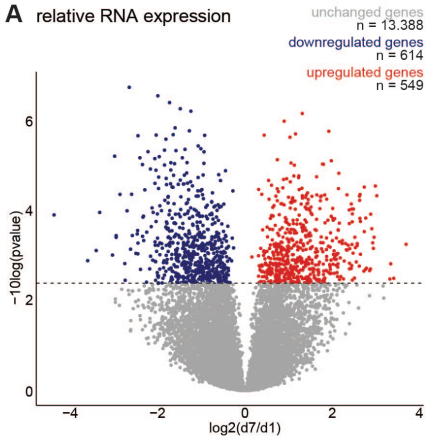


Figure 2.**Transcriptomic and proteomic profiling of early developmental stages in human iPSC-derived neurons**

A. Volcanoplots of differentially expressed transcripts between day 7 and day 1 (false discovery rate (FDR) $p < 0.05$, Benjamini & Hochberg corrected).

B,C. Top 10 most significantly enriched GO terms of downregulated (**B**) and upregulated (**C**) genes at day 7. Representative cellular components (CC, cyan), biological processes (BP, yellow), molecular function (MF, green), FDR $p < 0.05$, Benjamini & Hochberg corrected.

D,E. Six clusters with distinct protein expression profiles, divided in upregulated (**D**) and downregulated (**E**) protein expression, obtained by unsupervised clustering, and the GO enrichment analysis for each cluster. Representative cellular components (CC, cyan), biological processes (BP, yellow), molecular function (MF, green).

F. Correlative analysis of relative transcriptomic and proteomic expression levels (day7/day1) (Pearson's correlation, $R = 0.51$, $p < 0.0001$). Highlighted are some typical stem cell (blue), neuron (yellow), and axon (red) markers.

G,H. Heatmaps showing the relative expression of RNA (**G**) and protein (**H**) levels of typical stem cell, neuron, and axon markers at different timepoints.

3 neurons were morphologically defined by the appearance of a single elongated neurite, the future axon, which has grown at least twice as long as the other neurites. Interestingly, we found that AIS proteins in stage 3 neurons first appeared as noncontinuous structures consisting of multiple smaller puncta and stretches that cover distal parts of the axon (referred to as stage 3a), prior to their more conventional localization in the AIS at the proximal axon (referred to as stage 3b) (Fig 3A,B). Quantification of the abundance of these neurodevelopmental stages over time revealed a developmental decline of stage 2b neurons that was accompanied with an increase of stage 3a neurons, as well as an increase of stage 3b neurons with a relatively later onset (Fig 3C). We further characterized the distribution of AIS proteins by measuring their lengths and distances to the soma at each stage. Developmental changes in the length of AnkG and Trim46 structures were observed, as the total neurite length covered by Trim46 or AnkG signals was strongly increased by ~40% in stage 3a neurons, and significantly reduced by ~55% in stage 3b neurons (Fig 3D; Fig S3A).

Moreover, the axonal Trim46 and AnkG structures were localized more distally in stage 3a neurons, as the distance from the soma to both the start as well as the end of the Trim46 and AnkG appearance was significantly larger compared to stage 3b neurons (Fig 3E; Fig S3B-D). The axonal localization of NaV during development shows a similar dynamic profile as Trim46 and AnkG (Fig S3D). These data imply that axon specification (transition stage 2-3) in human iPSC-derived neurons can be subdivided in 4 steps (stage 2a, 2b, 3a and 3b) based on the subcellular localization of AIS proteins. Here, AIS proteins first

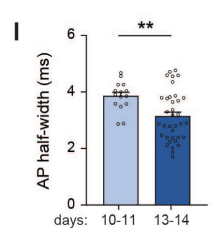
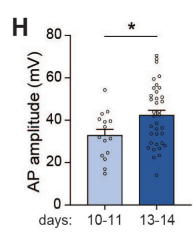
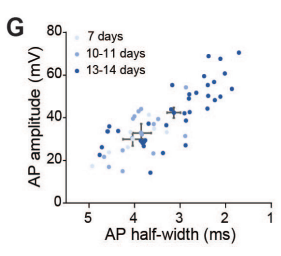
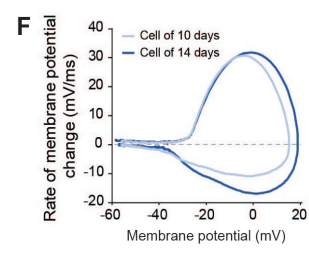
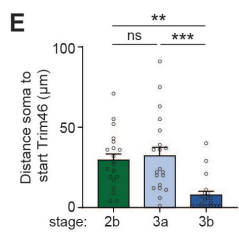
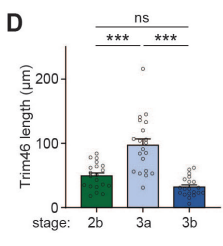
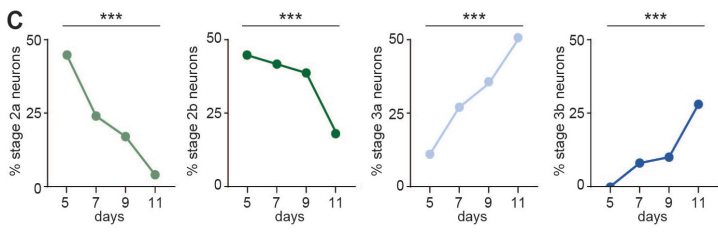
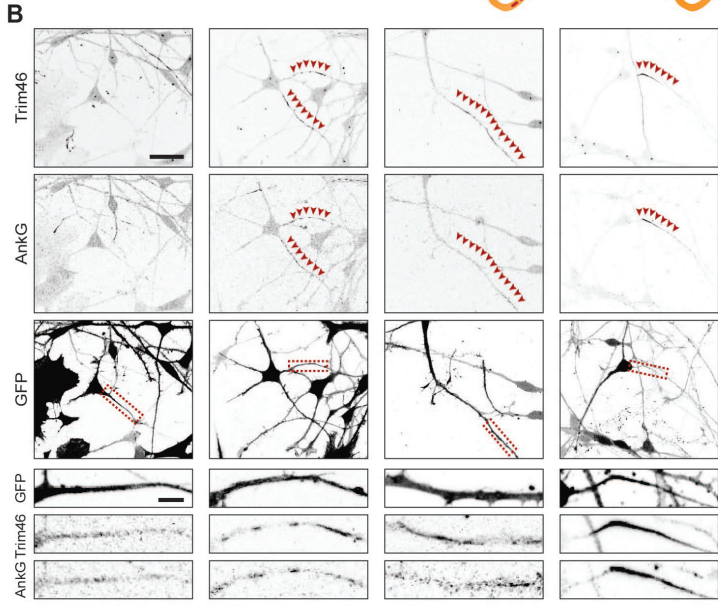
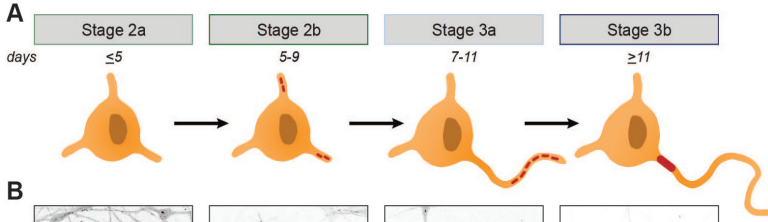


Figure 3.

Extra developmental stage and gradual action potential maturation during axon specification

A. Schematic illustration and timing of neurodevelopmental stages 2a, 2b, 3a and 3b in human iPSC-derived NSCs/neurons.

B. Representative images of stage 2a, 2b, 3a, and 3b hiPSC-derived neurons. Cells were subjected to FUGW-GFP lentivirus and immunostained for AnkG and Trim46. Arrowheads mark Trim46 and AnkG accumulations. Scale bar: 40 μm overview, 5 μm zooms.

C. Quantifications of percentage neurons in stage 2a, 2b, 3a or 3b. N=2, n=50-55 neurons.

D. Quantifications total Trim46 length in neurites of stage 2b, 3a and 3b human iPSC-derived neurons. N=2, n=20 cells.

E. Quantifications of distance soma to start of the Trim46 signal in neurites of stage 2b, 3a and 3b human iPSC-derived neurons. N=2, n=20 cells.

F. Phase plots of a representative AP recorded of a human iPSC-derived neuron at 10 days and 14 days.

G. Scatter plot of AP amplitude versus AP half-width grouped by days after plating (N=4; 7 days: n=7 cells, 10-11 days: n=15 cells, 13-14 days: n=36 cells).

H. AP amplitude recorded in human iPSC-derived neurons of 10-11 days (n=15 cells) and 13-14 days (n=36 cells).

I. AP half-width recorded in human iPSC-derived neurons of 10-11 days (n=15 cells) and 13-14 days (n=36 cells).

Used tests: Chi-square test with Bonferroni post-hoc correction (**C**), One-way ANOVA with Bonferroni post-hoc correction (**D**, **E**), Student's t-test (**H**), Mann-Whitney U test (**I**), *** $p < 0.001$, ** $p < 0.01$, * $p < 0.05$, ns $p \geq 0.05$; error bars are \pm SEM.

form relatively long, noncontinuous structures in the distal axon before accumulating at the proximal axon to form the AIS structure.

Action potential maturation coinciding with onset of axon development

We next investigated whether the different organization of AIS components in stage 3a and 3b neurons is accompanied by differences in electrical properties. Local clustering of voltage-gated ion channels at AIS structures, as observed in stage 3b neurons, are important to facilitate mature APs (Kole et al. 2008). Hence, we hypothesized that the noncontinuous appearance of NaV channels at distal axons in the newly identified stage 3a neurons affect AP firing. To address this, we performed electrophysiological experiments of neurons from day 7 to 14 to capture the developmental transition from stage 3a to stage 3b neurons. Our recordings showed progressive maturation of physiological properties during this developmental time window (Fig 3F,G). Neurons recorded on day 13-14 fired APs with a larger amplitude and shorter half-width compared to 10-11 days old neurons (Fig 3H,I). No differences in AP amplitude and half-width were found between neurons of 7 and 10-11

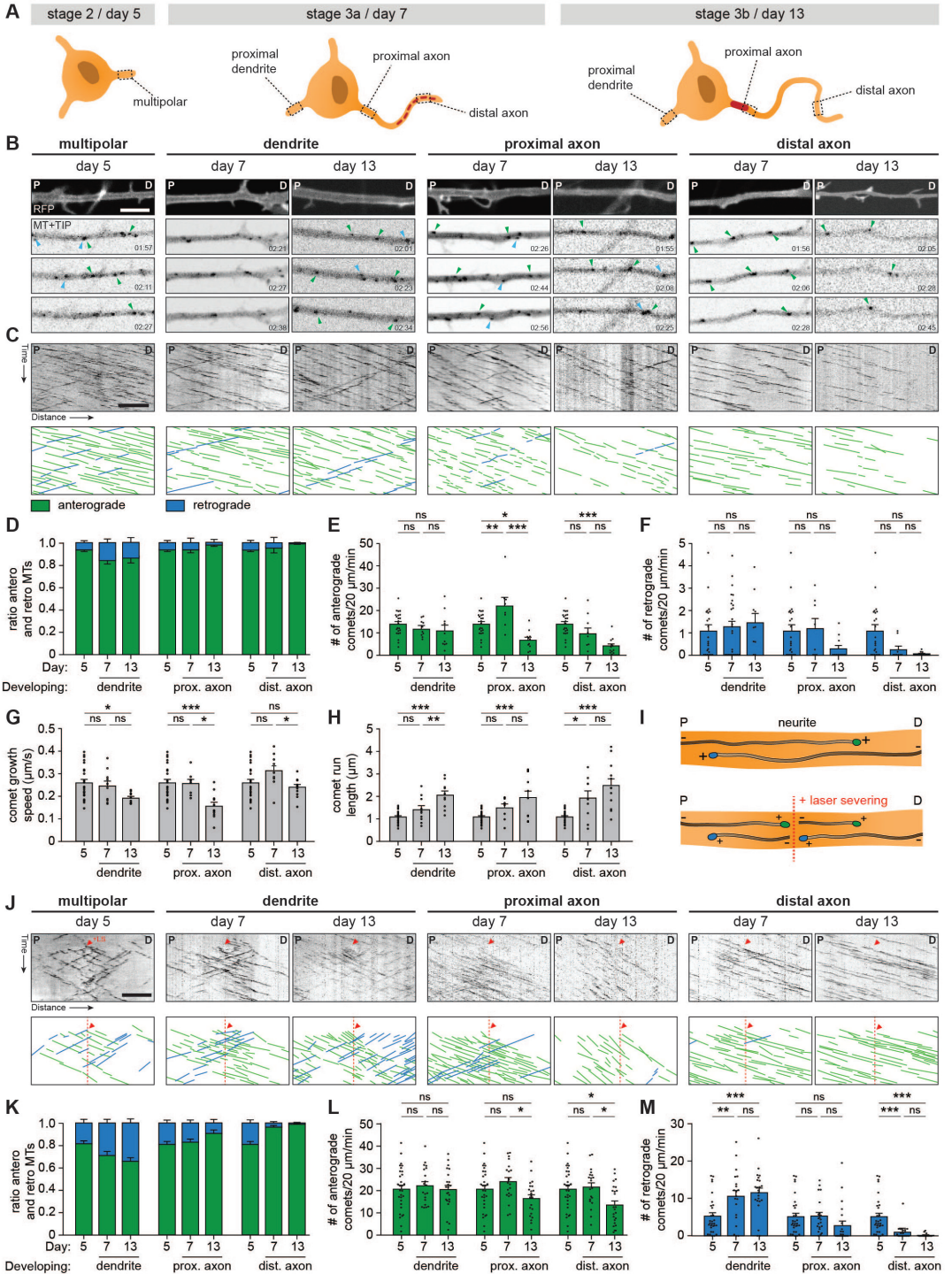


Figure 4.

Axonal microtubule cytoskeleton is reorganized in a distal-to-proximal fashion during human iPSC-derived neuronal development.

A. Schematic illustration of stage 2 (day 5), 3a (day 7) and 3b (day 14) human iPSC-derived neurons. Different locations of the neurons that are imaged have been outlined and annotated.

B. Stills from a spinning-disk time-lapse recording of specified neurites transfected with MARCKS-tagRFP_IRES_GFP-MACF18 at specific time points. The top panel is a still of a typical example neurite in MARCKS-tagRFP. The other panels show moving GFP-MT+TIP comets (GFP-MACF18) pointing in either an anterograde direction (green arrowheads) or retrograde direction (blue arrowheads). P indicates the proximal direction and D the distal direction of the neurite. Scale bars, 5 μ m.

C. Kymographs and schematic representations of time-lapse recordings shown in B. Scale bars: 5 μ m.

D. Quantifications of the ratios of comets pointing in anterograde (green) or retrograde (blue) direction. N=3, n=8-23 cells.

E. Quantifications of the number of comets per minute pointing in the anterograde direction. N=3, n=8-23 cells.

F. Quantifications of the number of comets per minute pointing in the retrograde direction. N=3, n=8-23 cells.

G. Quantifications of the growth speed of comets. N=3, n=9-4723 traces in 8-23 cells.

H. Quantifications of the distance of run length of comets. N=3, n=9-4723 traces in 8-23 cells.

I. Schematic representation of microtubule laser-severing (LS) experiments.

J. Kymographs and schematic representations of time-lapse recordings of LS experiments shown in S4B. Red arrowheads and dotted lines indicate when LS is performed. Scale bars: 5 μ m.

K. Quantifications of the ratios of comets pointing in anterograde (green) or retrograde (blue) direction, 10 μ m before and after the LS position. N=3, n=20-30 cells.

L. Quantifications of the number of comets per minute pointing in the anterograde direction, 10 μ m before and after the LS position. N=3, n=20-30 cells.

M. Quantifications of the number of comets per minute pointing in the retrograde direction, 10 μ m before and after the LS position. N=3, n=20-30 cells.

Used tests: One-way ANOVA including Tukey's post-hoc analysis (**E-H, L, M**); *** p<0.001, ** p<0.005, * p<0.05, ns p \geq 0.05; error bars are \pm SEM

days. However, on day 7, neurons fired APs with smaller after-hyperpolarization (data not shown), possibly reflecting a developmental increase in potassium channels (Song et al. 2013). Other intrinsic properties, like resting membrane potential, input resistance, AP firing threshold and maximum sodium current, remained stable during this developmental period. Together, these results indicate a developmental maturation of specific AP properties, which coincides with the timing of the developmental transition from stage 3a to stage 3b neurons.

Mapping microtubule reorganization in the newly identified developmental stages

The transcriptomic and proteomic profiles point to the importance of microtubule cytoskeleton remodeling during axon specification. Indeed, AIS dynamics are reported to be regulated by the underlying axonal microtubule cytoskeleton (Stepanova et al. 2003; Kleele et al. 2014; van Beuningen et al. 2015; Yau et al. 2016). Therefore, we assessed changes in the microtubule network in axons and dendrites of developing human iPSC-derived neurons by systematically analyzing plus-end dynamics and orientations of microtubules at different locations (Fig 4A). We performed two-color live-cell imaging to visualize neuronal morphology and microtubule plus-end tracking proteins (MT+TIPs), respectively (Fig 4B,C). Bidirectional MT+TIP movement, as shown by comets moving in both the anterograde and retrograde direction, was observed during stage 2 (day 5), with a preference for the anterograde direction (Fig 4D). Over time, this preference shifted towards more retrograde movement in developing dendrites, and towards unidirectional anterograde movement in developing axons (Fig 4D). These changes are consistent with differences in microtubule organization in axons and dendrites found in rodent neurons (Yau et al. 2016; Schatzle, Kapitein, and Hoogenraad 2016). In similar fashion to the distal to proximal reorganization of AIS proteins (Fig 3), the observed shift towards a unidirectional microtubule organization in axons occurred first in distal parts of the axon, followed by proximal reorganization. The observed developmental changes in anterograde and retrograde ratios are mostly explained by changes in retrograde comets, as the total number of retrograde comets was increased in dendrites and decreased in axons of (Fig 4E,F). The comet growth speed is slightly reduced during development, while comet run length increased markedly, suggesting a reduction in catastrophe events during axon and dendrite development (Fig 4G,H, S4A,B). Imaging of MT+TIPs provides information about the dynamic ends of microtubules, but the fraction of moving comets does not directly reflect the orientations of all microtubules (Yau et al. 2016). To analyze microtubule orientations of both dynamic and stable microtubules, we combined our previous live-cell imaging approach with laser-severing. Cutting microtubules with a short-pulsed laser generates new microtubule ends, which allows for analysis of newly formed MT+TIPs (Fig 4I,J, S4C,D). Following laser severing, a strong shift towards a balanced, bidirectional orientation in developing dendrites is observed (Fig 4K). The number of comets in both directions increased during development, with those moving in the retrograde direction increasing more (Fig 4L,M). This suggests the presence of a larger pool of stable, minus-end out microtubules in dendrites. In developing axons, the shift towards unidirectional, plus-end out microtubules was more notably observed following laser severing (Fig 4K). Laser severing led to a large increase in the number of anterogradely moving comets (Fig 4L), suggesting the presence of a stable pool of plus-end out microtubules. These results indicate that the microtubule remodeling in a distal to proximal fashion coincides with relocation of AIS proteins. Together, these data show that axon specification is characterized by the reorganization of the axonal microtubule network and relocation of the AIS from the distal to proximal axon (Fig S4E).

DISCUSSION

To better understand neuronal differentiation and polarization in human cells, we performed an in-depth characterization of human iPSC-derived neurons during these developmental processes. We systematically assessed the early stages of human neurodevelopment in culture, including axon specification (transition stage 2-3), and performed transcriptomic and proteomic profiling during these steps. We describe previously undescribed intermediate stages of axonal outgrowth (stage 2a, 2b, 3a and 3b), which is characterized by a distal to proximal reorganization of the axonal microtubule network and relocation of AIS proteins.

Development of polarized and functional human iPSC-derived neurons

In this study we showed that NSCs consistently gave rise to polarized and functional human neurons, which was demonstrated by the loss of cell proliferation and NSC markers, and the appearance of neuron-specific and AIS markers. These neurons form a single axon with a functional AIS, and exhibit AP firing. As expected, AP properties and cell intrinsic variables appeared immature compared to other studies performed at later developmental stages (Bardy et al. 2016; Gunhanlar et al. 2018). Passive physiological properties were comparable to neurons recorded from ex vivo fetal cortical brain tissue (Moore et al. 2009). We consistently observed neurons that fired a single AP and neurons that fired multiple APs at different developmental stages. The reason for this difference remains unknown, but may indicate variation in the maturation, cell morphology or other factors that could contribute to cellular heterogeneity of the culture. Non-human neurons develop at faster rates: for example, rat dissociated neurons reach stage 3 after approximately 1.5 days in culture, and cortical development in maturation in mammals ranging from mouse to primate is both faster and less complex than in humans (Dotti, Sullivan, and Banker 1988; Clowry, Molnar, and Rakic 2010; Molnar and Clowry 2012; Silbereis et al. 2016; Marchetto et al. 2019). We found that human iPSC-derived neurons transition to stage 3 in approximately 7 days, which is consistent with the described prolonged development of human neurons *in vivo* and *in vitro* (Grabrucker et al. 2009). The slow rate of development is also reflected in the lack of spontaneous AP firing or incoming synaptic responses as mature synapses have likely not formed yet. Co-culturing with astrocytes could benefit synaptogenesis, as this has been shown to promote synaptic connectivity (Tang et al. 2013). The prolonged development of human iPSC-derived neurons allows studying neurobiological processes, such as AP maturation and AIS assembly, with higher temporal resolution.

Quantitative profiles of transcriptomic and proteomic of early human neurodevelopment

Quantitative transcriptome analysis identified 549 upregulated genes and 614 downregulated genes during early stages of neurodevelopment. As expected, and in agreement with changes observed in other differentiating cell types, GO term enrichment analysis showed strong downregulation of genes related to cell proliferation during terminal differentiation (An et al. 2014; Gao, Yourick, and Sprando 2014; Tripathi et al. 2014). Simultaneously, genes related to neurodevelopmental processes such as neurite formation and axonogenesis are

upregulated, which is in line with changes previously observed in mouse iPSCs and human ESCs (Wu et al. 2010; Chen et al. 2013). To determine if regulatory changes of transcripts are reflected in protein expression, we performed quantitative proteome analysis. We identified 2,218 proteins with more than two-fold expression changes during the first stages of neurodevelopment, indicating that significant remodeling of the proteome takes place during early stages. We identified six clusters of expression profiles and conducted GO enrichment analysis, which revealed a coordinated proteomic rearrangement during neurodevelopment. Proteins related to neuronal differentiation are upregulated and proteins related to cell proliferation are downregulated. Similar changes are observed in dissociated rodent neurons, differentiating neural crest and immortalized human neural progenitor cells, confirming the neuronal identity adopted by our human iPSC-derived cells (Kobayashi et al. 2009; Frese et al. 2017; Song et al. 2019). Similar to changes in protein expression levels, RNA expression also showed a strong increase of factors involved in neuronal differentiation and polarization, such as TUBB3 and TRIM46. Indeed, RNA and protein dynamics were generally correlated, indicating a coordinated cellular reprogramming into neurons. Furthermore, reorganization of the microtubule cytoskeleton is reflected in both transcriptome and proteome profiles during early neurodevelopment. However, differences between transcriptome and proteome dynamics during early neurodevelopment are also observed. This may reflect a temporal shift in regulation of transcription and translation. In addition, possible regulatory mechanisms on the protein level might be at play. Together, these data provide a rich resource for both the transcriptome and proteome dynamics in developing human neurons, which can be used in future studies to advance our understanding of the molecular mechanisms involved in neuronal differentiation and polarity.

Distal to proximal relocation of AIS proteins during axon development

A critical event in early neurodevelopment is the polarization of a symmetric cell into a neuron, which is initiated by the formation of a single axon (Dotti, Sullivan, and Banker 1988; Craig and Banker 1994). Here, we studied the onset of polarity in human iPSC-derived neurons in detail, and found that axon specification proceeds through a multistage process with multiple intermediate steps. We observed that AIS proteins Trim46, AnkG and NaV first appear as long noncontinuous structures in distal regions of the axons at the onset of stage 3 (stage 3a), and later relocate and cluster at proximal regions to form the stable AIS structures (stage 3b). In conjunction, we also found a distal-to-proximal reorganization of the microtubule cytoskeleton network in axons. This is marked by a developmental shift towards the characteristic uniform, plus-end out orientation in growing axons. Although the precise relation between AIS formation and microtubule remodeling in early axon development is unclear, various studies have shown the cooperative interaction between AIS components and microtubule structures during axon development (Leterrier et al. 2011; Freal et al. 2016). Recently Fréal et al., described a feedback-based mechanism that drives AIS assembly, in which membrane, scaffolding, and microtubule(-associated)

proteins, including AnkG and Trim46, cooperate to form a stable AIS-microtubule structure in the proximal axon (Freal et al. 2019). It has been shown that AnkG can act as a scaffold to recruit Trim46-positive microtubules and subsequently direct AIS protein trafficking to the proximal axon (Freal et al. 2019). The possible function of AIS proteins in the distal axon remains elusive. Similar to their function in stabilizing microtubules in the proximal axon following proper AIS formation, redistribution of AIS proteins in the distal axon may help to locally stabilize microtubules and drive axon outgrowth. AnkG in distal axons may provide additional support to the formation of Trim46-positive parallel microtubules during outgrowth. Then, as Trim46 moves proximally, the axonal microtubule network close to the cell body is remodeled to the characteristic uniform plus-end out orientation. This idea is consistent with the observed shift of the unidirectional parallel microtubule organization in the distal parts of the axon first, followed by proximal reorganization. Finally, AnkG and Trim46 together may drive AIS assembly at the proximal axon, as previously described in dissociated rodent neurons (Freal et al. 2019). It remains unknown if the observed intermediate step of distal AIS protein accumulation is unique to human neurons. Axons in humans grow significantly longer compared to rodents, thus additional regulatory mechanisms enhancing axon outgrowth might be at play in humans. Alternatively, it is possible that these changes have not been observed in rodent neurons because of their relatively faster development. We also observed differences in microtubule dynamics, as MT+TIP growth speeds are higher than those found in rodent neurons *in vitro* and *in vivo*, hinting at species-specific regulation of microtubule dynamics in human neurons (Stepanova et al. 2003; Kleele et al. 2014; Yau et al. 2016). Future studies are required to examine the potential human-specific attributes of neuronal polarity and axon outgrowth.

In summary, our quantitative map of neuronal transcriptome and proteome dynamics provides a rich resource for future analysis of early neurodevelopmental processes in human iPSC-derived neurons. We investigated early development in human neurons and uncovered an intermediate axon developmental step, thereby illustrating the potential of this model system to study neurobiological processes in human cells in stage 3 neurons. This study also provides a framework and excellent starting point for further studies that aim to complement our understanding of neuronal polarization in human cells.

ACKNOWLEDGEMENTS

We thank Dr. Didier Trono for the lentiviral vector, and Nicky Scheefhals for critically reading the manuscript. This work was supported by the Netherlands Organization for Scientific Research (NWO-ALW-VICI, 865.10.010, CCH), the Netherlands Organization for Health Research and Development (ZonMW-TOP, 912.16.058, CCH), the European Research Council (ERC) (ERC-consolidator, 617050, CCH), and the research program of the Foundation for Fundamental Research on Matter (FOM, #16NEPH05, CJW).

AUTHOR CONTRIBUTIONS

FWL, RK and SP designed the research, conducted experiments, and wrote the article together with LJH. RS conducted and analyzed the mass spectrometry experiments supervised by MA, LJH performed and interpreted the electrophysiology data supervised by CJW, RK and BLS provided and interpreted the RNA sequencing analysis. HDM edited the article. CCH designed the experimental plan, supervised the research and wrote the article.

DECLARATION OF INTERESTS

Casper Hoogenraad is an employee of Genentech, Inc., a member of the Roche group. The authors declare that they have no additional conflict of interest.

MATERIAL AND METHODS

hiPSC-derived neuronal cell culture

Human iPSC-derived cortical neuronal progenitor cells (NPCs; ax0016, Axol Bioscience) from a female newborn donor were obtained, expanded and differentiated following Axol Bioscience protocols (Human iPSC-derived Neural Stem Cells, Protocol version 5.0). For expansion of hiPSC-derived NPCs, cells were thawed and quenched with Neuronal Expansion-XF Medium (ax0030, Axol Bioscience), centrifuged (200 g, 5 min), resuspended in Neuronal Plating-XF medium (ax0033, Axol Bioscience), and plated (~500k per well) on six-wells plates pre-coated with freshly-thawed SureBond (ON, 37°C; ax0041, Axol Bioscience) in PBS at 37°C with 5% CO₂. Medium was replaced on the next day by Neuronal Expansion-XF Medium supplemented with EGF (20 ng/ml; AF-100-15, Peprotech) and FGF (20 ng/ml; 100-18B, Peprotech). Medium was refreshed every two days, and cells were passaged when cultures reached a 70-80% confluency. For passaging, cells were washed once with PBS, incubated with Unlock (5 min, 37°C; ax0044, Axol Bioscience), quenched with Neuronal Expansion-XF Medium, and centrifuged (200 g, 5 min). Cell pellets were resuspended in Neuronal Plating-XF medium and plated in a 1:3 ratio on six-wells plates pre-coated with freshly-thawed SureBond (see above). After three passaging rounds, cells were frozen in KnockOut Serum Replacement (10828028, Life Technologies) with 10% DMSO and stored in liquid nitrogen. For neuronal differentiation of hiPSC-derived NPCs, cells were thawed and quenched with Neuronal Expansion-XF Medium, centrifuged (200 g, 5 min), resuspended in Neuronal Plating-XF medium, and plated on 12 mm (~100k per well) or 18 mm (~200k per well) pre-coated glass coverslips in respectively a 24-wells or 12-wells plate at 37°C with 5% CO₂. Coating of coverslips was performed directly before plating: coverslips were first incubated with ReadySet (45 min, 37°C; ax0041+, Axol Bioscience), washed four times with sterilized water, and incubated with freshly-thawed 1x SureBond (1h, 37°C; ax0041+, Axol Bioscience) in PBS. After 24 hours (day 1), the medium was fully replaced by Neuronal Maintenance-XF Medium (ax0032, Axol Bioscience), and after another 24 hours (day 2) by Neuronal Differentiation-XF Medium (ax0034, Axol Bioscience). Three days later (day 5), half of the medium was replaced by Differentiation-XF Medium. Next day (day 6), half of the medium was replaced by Neuronal Maintenance-XF Medium, again one day later (day 7),

and every three days during further maintenance. Cells were kept in culture for maximum ~15 days to ensure high quality of the cultures.

Lentivirus and lentiviral infection

The constructs used for lentiviral transduction are FUGW-GFP (Addgene #14883, (Lois et al. 2002)) and Marcks-tagRFP-T-plres-GCN4-MacF18. Marcks-tagRFP-T-pIRES-GCN4-MacF18 cloning is previously described (Yau et al. 2016). The construct was subcloned into the pSIN-TRE-mSEAP-hPGK-rtTA2sM2 lentiviral vector (kindly provided by Dr. Didier Trono, Ecole Polytechnique Fédérale de Lausanne, Switzerland) wherein the neuron-specific synapsin promoter has substituted the PGK promoter. Generation of lentiviral particles was performed as previously described (Yau et al. 2014). Lentiviral transduction of cells was performed two hours after plating. The tetracycline-dependent expression was induced by adding 500 ng/ml doxycycline to the medium two days before imaging.

Antibodies

Primary antibodies used in this study: mouse-IgG1 anti-Nestin (1:200; MAB5326, Millipore), rabbit anti-Ki67 (1:500; ab92742, Abcam), mouse-IgG2b anti- β -Tubulin (1:400; 082M4845, Sigma), chicken anti-MAP2 (1:2000; ab5392, Abcam), rabbit anti-Trim46 (1:500; homemade (van Beuningen et al. 2015)), mouse-IgG1 anti-AnkG (1:200; 33-8800, Life Technologies), mouse-IgG1 anti-PanNav (1:200; S8809, Sigma). Secondary antibodies used in this study: anti-rabbit Alexa 405 (A31556, Life Technologies), anti-mouse-IgG1 Alexa 488 (A21121, Life Technologies), anti-rabbit Alexa 568 (A11036, Life Technologies), anti-mouse Alexa 568 (A11031, Life Technologies), anti-mouse-IgG2b Alexa 594 (A21145, Life Technologies), anti-rabbit Alexa 647 (A21245, Life Technologies), anti-mouse Alexa 647 (A21236, Life Technologies), anti-mouse-IgG2a Alexa 647 (A21241, Life Technologies), anti-chicken Alexa 647 (A21449, Life Technologies).

Immunofluorescence

Cells were fixed for 5-10 min in PBS with 4% paraformaldehyde/4% sucrose at room temperature, and washed three times with PBS. For immunofluorescence stainings, fixed cells were sequentially incubated with primary and secondary antibodies dissolved in gelate dilution buffer (GDB; 0.2% BSA, 0.8 M NaCl, 0.5% Triton X-100, 30 mM phosphate buffer, pH 7.4), and washed three times with PBS after every antibody incubation step. Coverslips were mounted on glass slides using Vectashield mounting medium (Vector laboratories) with or without DAPI.

Microscopy

Fixed cells were imaged using a LSM700 confocal laser-scanning microscope (Zeiss) with a Plan-Apochromat 63x NA 1.4 oil DIC; EC Plan-Neofluar 40x, NA 1.3 Oil DIC; and a Plan-Apochromat 20x, NA 0.8 objective. Live-cell acquisition was performed using spinning-disk confocal microscopy on an inverted research microscope Nikon Eclipse Ti-E,

equipped with a perfect focus system (Nikon) and a spinning disk-based confocal scanner unit (CSU-X1-A1, Yokogawa). The system was also equipped with an ASI motorized stage with the piezo plate MS-2000-XYZ (ASI), Photometric Evolve Delta 512 EMCCD camera (Photometric) controlled by the MetaMorph 7.8 software (Molecular Devices), or Photometric PRIME BSI sCMOS camera (version USB 3) as upgrade of EMCCD and controlled by the MetaMorph 7.10 software (Molecular Devices). The system was equipped with Plan Apo VC 60x NA 1.4 oil-immersion objective (Nikon) and S Fluor 100x NA 0.5-1.3 oil-immersion objective (Nikon) for photoablation experiments. A 491 nm 100 mW Calypso (Cobolt) and a 561 nm 100 mW Jive (Cobolt) laser were used as the light sources. We used an ET-GFP filter set (49002, Chroma) for imaging of proteins tagged with GFP and an ET-mCherry filter set (49008, Chroma) for imaging of proteins tagged with tag-RFP. For the photoablation experiments we used an ILas system (Roper Scientific France/ PICT-IBiSA, Institut Curie, currently Gataca Systems) mounted on a Nikon Eclipse microscope described above. A 355 nm passively Q-switched pulsed laser (Teem Photonics) was used for the photoablation together with a S Fluor 100x 0.5-1.3 NA oil objective (Nikon).

Image quantification and analysis

Quantifying neuronal differentiation and polarization: To measure neuronal differentiation and polarization over time, cells were identified using DAPI staining and scored to be positive or negative for the indicated NSC, neuron differentiation and axon markers.

Quantification of stage 2a, 2b, 3a and 3b neurons: To determine the transition of neurodevelopmental stages over time, neurons were identified using DAPI and MAP2-positive immunofluorescence, and scored for neurodevelopmental stage 2a, 2b, 3a and 3b. Stage 2a and stage 2b neurons contained unipolar neurites of similar lengths. In stage 2a neurons, all neurites were negative for Trim46. In stage 2b neurons, one or more neurites were positive for Trim46. Stage 3a and stage 3b neurons were identified by the presence of a single elongated neurite, the future axon, that was at least twice as long as the other neurites. In stage 3a neurons, Trim46 appeared as distal non-continuous stretches at distal axons. In stage 3b neurons, Trim46 showed a dense accumulation at proximal axons.

Live-cell imaging

For all live-cell imaging of microtubule dynamics without laser severing, time-lapse acquisition was performed using the 491 nm 100 mW Calypso (200ms exposure) and 561 nm 100 mW Jive (200ms exposure) with 1 frame per second (fps) for 5 minutes. Sixteen-bit images were projected onto the EMCCD chip with intermediate lens 2.0X (Edmund Optics) at a magnification of 0.111 $\mu\text{m}/\text{pixel}$ at 60x, or onto the sCMOS chip with no intermediate lens at a magnification of 0.150 $\mu\text{m}/\text{pixel}$ at 60x. For all live-cell imaging of microtubule dynamics with laser severing, time-lapse acquisition was performed using the 491 nm 100 mW Calypso (50-200 ms exposure, depending on the expression level) and 561nm 100mW Jive (50-200ms exposure, depending on the expression level) with 1 fps for 3 minutes, and photoablation was induced after 30s. Sixteen-bit images were projected onto

the sCMOS chip with no intermediate lens at a magnification of 0.063 $\mu\text{m}/\text{pixel}$ at 100x. All imaging was performed in full conditioned differentiation (day 5) or maintenance (day 7 or 13) medium for hiPSC-derived neuron cultures (Axol Bioscience), and cells were kept at 37°C with 5% CO₂ using a stage top incubator (model INUBG2E-ZILCS, Tokai Hit). For analysis, kymographs were generated using the FIJI plugin KymoResliceWide v.0.4 (<https://github.com/ekatruxha/KymoResliceWide>), and parameters of microtubule plus-end dynamics were determined by manually tracing microtubule growth events.

Electrophysiology

A 12 mm coverslip containing hiPSC-derived neurons (7–14 days after plating) was transferred to the microscope recording chamber before the start of each experiment. Coverslips were continuously perfused with carbonated (95% O₂, 5% CO₂) artificial cerebrospinal fluid (ACSF, in mM: 126 NaCl, 3 KCl, 2.5 CaCl₂, 1.3 MgCl₂, 26 NaHCO₃, 1.25 NaH₂PO₄, 20 glucose; with an osmolarity of \sim 310 mOsm/L) at a rate of approximately 1 ml/min. As an acute change in extracellular osmolarity has previously been reported to affect the excitability properties of neurons, an extra medium refreshment was done the day before recording (Pasantes-Morales 1996). Bath temperature was monitored and maintained at 30–32 °C throughout the experiment. Recording pipettes (resistance of 4–7 M Ω) were pulled from thick-walled borosilicate glass capillaries (World Precision Instruments) and filled with internal solution (in mM: 140 K-gluconate, 4 KCl, 0.5 EGTA, 10 HEPES, 4 MgATP, 0.4 NaGTP, 4 Na₂-Phosphocreatine; with pH 7.3 and osmolarity 295 mOsm/L), containing 30 μM Alexa 568 (Thermo Fisher Scientific) to facilitate visualization of cells. For post hoc cellular identification, biocytin was included in the internal solution. On an upright microscope, hiPSC-derived neurons were visually identified with a 60x water immersion objective (Nikon NIR Aplanachromat; NA 1.0) and selected for whole-cell somatic patch clamp recordings. Cells were kept at a baseline holding potential of -60 mV in both voltage and current clamp throughout the recording. Data was analyzed with pCLAMP software and custom-written MATLAB scripts.

Sample preparation RNA sequencing

\sim 100,000 hiPSC-derived NPCs were plated per well for bulk RNA sequencing samples. Prior to sample preparation, all equipment and surfaces were cleaned with RNaseZap (Sigma-Aldrich). Replicates of hiPSC-derived neurons were harvested at three different timepoints of differentiation (days 1, 3, and 7) with 200 μl Trizol (Invitrogen) per sample and stored at -80 °C until sequencing. RNA extraction, cDNA library preparation (CEL-Seq2 protocol), quality control for aRNA and cDNA, and sequencing on a NextSeq500 High output 1x75 bp paired end run with 2% sequencing depth were performed by Single Cell Discoveries (Utrecht, The Netherlands).

Bioinformatic analysis RNA sequencing

Mapping to reference transcriptome Hg19 was performed by Single Cell Discoveries

(Utrecht, The Netherlands). The following investigations were done in R statistical software (R Core Team, 2019) with the use of packages ggplot2 (Wickham, 2009) and pheatmap (Kolde, 2019). The raw read counts were normalized to reads per million for each gene. Genes observed in less than 5 samples were excluded from further analysis. To determine differential expression a linear regression ANOVA model was used where gene expression is explained by timepoint + biological replicate and technical replicate (nested in the biological replicate). To obtain the differences (in both p-value and effect between the timepoints) a Tukey-test was performed for each gene using the same model. We corrected for multiple-testing by pairwise comparison using the `p.adjust()` function in R with the 'BH' setting (R Core Team, 2020). Genes with an adjusted p-value < 0.05 were used for further investigation. GO enrichment was done using the hypergeometric test `phyper()` in R (R Core Team, 2020), the set of GO terms was obtained from Ensembl Biomart for Human genes version GRCh38.p13. Comparison between transcriptomics and proteomics was done by selecting genes present in both datasets based on their public name.

Sample preparation for mass spectrometry (TMT labeling)

Replicates of hiPSC-derived neurons were harvested with lysis buffer (8 M Urea, 50 mM ammonium bicarbonate (Sigma), EDTA-free protease inhibitor Cocktail (Roche)) at three distinct differential time points (days 1, 3, and 7). Lysates were sonicated on ice with a Bioruptor (Diagenode) and cleared by centrifugation at 2500 g for 10 min. The protein concentration of the samples was determined by Bradford assay. Per sample 100 µg of proteins were reduced (5 mM DTT, 55°C, 1 hour), alkylated (10 mM Iodoacetamide, 30 min in the dark) and sequentially digested by LysC (Protein-enzyme ratio 1:50, 37°C, 4 h) and trypsin (Protein-enzyme ratio 1:50, 37°C, overnight). After digestion (overnight), formic acid (final concentration 3%) was used to acidify the samples and resulting peptides were afterwards desalted with Sep-Pak C18 columns (Waters). Samples were labeled with stable isotope TMT-6plex labeling, according to manufacturer's instruction (Thermo Fisher Scientific). In short, peptides were resuspended in 80 µl of 50 mM HEPES buffer, 12.5% ACN (pH 8.5), while TMT reagents were dissolved in 50 µl anhydrous ACN. We added 25 µl of each dissolved TMT reagent to a correspondent sample according to the following scheme:

day 1 (replicate A) = TMT-126 / day 1 (replicate B) = TMT-129

day 3 (replicate A) = TMT-127 / day 3 (replicate B) = TMT-130

day 7 (replicate A) = TMT-128 / day 7 (replicate B) = TMT-131

Following incubation (room temperature) for 1 hour, the reaction was quenched with 5% hydroxylamine. Differentially TMT-labeled peptides were mixed in equal ratios and dried in a vacuum concentrator.

Peptide fractionation

Mixed TMT-labeled peptides were solubilized in 10mM ammonium hydroxide, pH 10.0 and subsequently fractionated using basic pH reverse phase HPLC. Peptides were

loaded on a Gemini 3 μ m C18 110A 100 x 1.0 mm column (Phenomenex) using an Agilent 1100 pump equipped with a degasser and a photodiode array (PDA) detector. Peptides were concentrated on the column at 100 μ l/min using 100% buffer A (10mM ammonium hydroxide, pH 10) after which the fractionation gradient was applied as follow: 5% solvent B (10mM ammonium hydroxide in 90% ACN, pH 10) to 30% B in 53 mins, 70% B in 7 min and increased to 100% B in 3 min at a flow rate of 100 μ l/min. In total 60 fractions of 1 min were collected using an Agilent 1260 infinity fraction collector and then concatenated into 12 final fractions. Collected fractions were vacuum-dried, reconstituted in 5% formic acid/5% DMSO and stored at -80°C prior to mass spectrometry analysis.

Mass spectrometry analysis

We analyzed the samples on an Orbitrap Q-Exactive HF mass spectrometer (Thermo Fisher Scientific) coupled online to an Agilent UPLC 1290 system (Agilent Technologies). Peptides were loaded onto a trap column (Reprosil C18, 3 μ m, 2 cm x 100 μ m; Dr. Maisch) and separated on an analytical column (Poroshell 120 EC-C18, 2.7 μ m, 50cm x 75 μ m; Agilent Technologies). Peptides were trapped for 10 min at 5 μ l/min in solvent A (0.1M acetic acid in H₂O) and then separated at a flow rate of approximately 300 nl/min (split flow from 0.2ml/min) by applying a 120 min linear gradient as follows: 13% up to 40% solvent B (0.1M acetic acid in 80% ACN) in 95 min, 40-100% in 3 min and finally 100% for 1 min. The mass spectrometer was operated in data-dependent acquisition mode. Full MS spectra from m/z 375-1600 were acquired at a resolution of 60.000 with an automatic gain control (AGC) target value of 3e6 and maximum injection time (IT) of 20 ms. The 15 most intense precursor ions were selected for HCD fragmentation. HCD fragmentation was performed at a normalized collision energy (NCE) of 32%. MS/MS spectra were obtained at a 30.000 resolution with an AGC target of 1e5 and maximum injection time (IT) of 50 ms. Isolation window was set at 1.0 m/z and dynamic exclusion to 16.0s.

Data processing proteomics

Raw MS files were processed for data analysis with Proteome Discoverer 1.4 (Thermo Fisher Scientific). A database search was performed using the Swissprot homo sapiens database and Mascot (version 2.5.1, Matrix Science, UK) as search engine. Carbamidomethylation of cysteines was set as a fixed modification, and oxidation of methionine, acetylation at the N-termini, TMT-6plex of lysine residues and TMT-6plex at the peptide N-termini were set as variable modifications. Trypsin was set as cleavage specificity, allowing a maximum of two missed cleavages. Data filtering was performed using percolator, resulting in 1% false discovery rate (FDR). Additional filters were search engine rank 1 and mascot ion score > 20. Only unique peptides were included for quantification and the obtained TMT ratios were normalized to the median. Common contaminant proteins (such as keratins and albumin) were removed from the list.

Bioinformatic analysis proteomics

All mass spectrometry data were analyzed using R statistical software (R Core Team, 2017). To infer protein dynamics upon differentiation, TMT reporter intensity values of hiPSC neurons at time point day 3 and day 7 were normalized to their correspondent day 1 or alternatively day 7 was normalized to day 3. TMT generated ratios (previously normalized to the median) were then log₂-transformed. A log₂-transformed mean of the TMT-ratios of the individual replicates was calculated. Proteins with less than 3 peptides used for TMT quantification or with a reporter ion variability > 100% in at least one TMT-ratio (high reporter ions variability) or with a median log₂ fold-change > 0.4 between the replicates in at least one TMT-ratio (high replicate variability) were excluded from the analyses. Good correlation of replicates was assessed by comparing TMT ratios of all quantified proteins at different time points using Pearson correlation. Proteins with an absolute log₂ fold-change > 0.3 between day 3 and day 1 or between day 7 and day 3 or between day 7 and day 1 were considered significantly regulated. Only significant regulated proteins were subjected to cluster analysis by using K-means clustering in R. Functional enrichment analysis within different clusters of expression profiles was performed using gProfilerR package in R (Raudvere et al., 2019). Network analyses were performed using the GeneMania plugin (Montejo et al., 2010) within Cytoscape (Shannon et al., 2003). Heatmaps in the Figures were prepared applying hierarchical clustering using Euclidean distance.

Statistical Analysis

Data processing and statistical analyses were performed using Prism GraphPad (version 8.0) software. All statistical tests are described in the corresponding Figure legends. Differences were considered significant when $P < 0.05$, and P-values are represented as: * $P < 0.05$, ** $P < 0.01$, and *** $P < 0.001$.

REFERENCES

- Almeida, A. C., and H. Maiato. 2018. 'Chromokinesins', *Curr Biol*, 28: R1131-r35.
- An, X., V. P. Schulz, J. Li, K. Wu, J. Liu, F. Xue, J. Hu, N. Mohandas, and P. G. Gallagher. 2014. 'Global transcriptome analyses of human and murine terminal erythroid differentiation', *Blood*, 123: 3466-77.
- Bardy, C., M. van den Hurk, B. Kakaradov, J. A. Erwin, B. N. Jaeger, R. V. Hernandez, T. Eames, A. A. Paucar, M. Gorris, C. Marchand, R. Jappelli, J. Barron, A. K. Bryant, M. Kellogg, R. S. Lasken, B. P. Rutten, H. W. Steinbusch, G. W. Yeo, and F. H. Gage. 2016. 'Predicting the functional states of human iPSC-derived neurons with single-cell RNA-seq and electrophysiology', *Mol Psychiatry*, 21: 1573-88.
- Benjamini Y., Hochberg Y. 1995. 'Controlling the False Discovery Rate: A Practical and Powerful Approach to Multiple Testing', *J of the Royal Statistical Society: Series B (Methodological)*, 57: 289-300.
- Bisht, J. S., M. Tomschik, and J. C. Gatlin. 2019. 'Induction of a Spindle-Assembly-Competent M Phase in *Xenopus* Egg Extracts', *Curr Biol*, 29: 1273-85.e5.
- Chen, X., Q. Gu, X. Wang, Q. Ma, H. Tang, X. Yan, X. Guo, H. Yan, J. Hao, and F. Zeng. 2013. 'Directed neuronal differentiation of mouse embryonic and induced pluripotent stem cells and their gene expression profiles', *Int J Mol Med*, 32: 25-34.
- Cho, S. J., H. Lee, S. Dutta, J. Song, R. Walikonis, and I. S. Moon. 2011. 'Septin 6 regulates the cytoarchitecture of neurons through localization at dendritic branch points and bases of protrusions', *Mol Cells*, 32: 89-98.
- Chou, F. S., and P. S. Wang. 2016. 'The Arp2/3 complex is essential at multiple stages of neural development', *Neurogenesis (Austin)*, 3: e1261653.
- Clowry, G., Z. Molnar, and P. Rakic. 2010. 'Renewed focus on the developing human neocortex', *J Anat*, 217: 276-88.
- Compagnucci, C., S. Petrini, N. Higurashi, M. Trivisano, N. Specchio, S. Hirose, E. Bertini, and A. Terracciano. 2015. 'Characterizing PCDH19 in human induced pluripotent stem cells (iPSCs) and iPSC-derived developing neurons: emerging role of a protein involved in controlling polarity during neurogenesis', *Oncotarget*, 6: 26804-13.
- Craig, A. M., and G. Banker. 1994. 'Neuronal polarity', *Annu Rev Neurosci*, 17: 267-310.
- Dotti, C. G., C. A. Sullivan, and G. A. Banker. 1988. 'The establishment of polarity by hippocampal neurons in culture', *J Neurosci*, 8: 1454-68.
- Espuny-Camacho, I., K. A. Michelsen, D. Gall, D. Linaro, A. Hasche, J. Bonnefont, C. Bali, D. Orduz, A. Bilheu, A. Herpoel, N. Lambert, N. Gaspard, S. Peron, S. N. Schiffmann, M. Giugliano, A. Gaillard, and P. Vanderhaeghen. 2013. 'Pyramidal neurons derived from human pluripotent stem cells integrate efficiently into mouse brain circuits in vivo', *Neuron*, 77: 440-56.
- Falk, J., L. Boubakar, and V. Castellani. 2019. 'Septin functions during neuro-development, a yeast perspective', *Curr Opin Neurobiol*, 57: 102-09.
- Fletcher, T. L., P. De Camilli, and G. Banker. 1994. 'Synaptogenesis in hippocampal cultures: evidence indicating that axons and dendrites become competent to form synapses at different stages of neuronal development', *J Neurosci*, 14: 6695-706.
- Freal, A., C. Fassier, B. Le Bras, E. Bullier, S. De Gois, J. Hazan, C. C. Hoogenraad, and F. Couraud. 2016. 'Cooperative Interactions between 480 kDa Ankyrin-G and EB Proteins

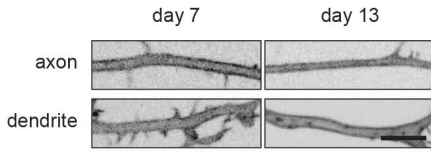
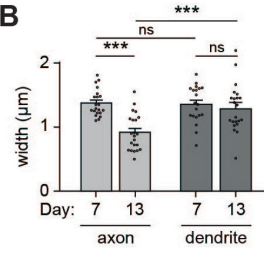
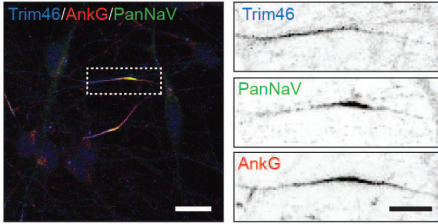
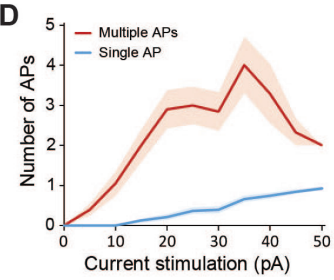
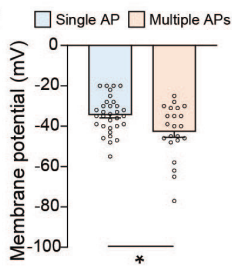
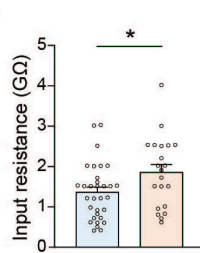
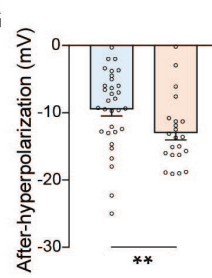
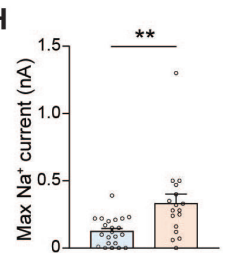
- Assemble the Axon Initial Segment', *J Neurosci*, 36: 4421-33.
- Freal, A., D. Rai, R. P. Tas, X. Pan, E. A. Katrukha, D. van de Willige, R. Stucchi, A. Aher, C. Yang, A. F. M. Altelaar, K. Vocking, J. A. Post, M. Harterink, L. C. Kapitein, A. Akhmanova, and C. C. Hoogenraad. 2019. 'Feedback-Driven Assembly of the Axon Initial Segment', *Neuron*, 104: 305-21.e8.
- Frese, C. K., M. Mikhaylova, R. Stucchi, V. Gautier, Q. Liu, S. Mohammed, A. J. R. Heck, A. F. M. Altelaar, and C. C. Hoogenraad. 2017. 'Quantitative Map of Proteome Dynamics during Neuronal Differentiation', *Cell Rep*, 18: 1527-42.
- Gao, X., J. J. Yourick, and R. L. Sprando. 2014. 'Transcriptomic characterization of C57BL/6 mouse embryonic stem cell differentiation and its modulation by developmental toxicants', *PLoS One*, 9: e108510.
- Grabrucker, A., B. Vaida, J. Bockmann, and T. M. Boeckers. 2009. 'Synaptogenesis of hippocampal neurons in primary cell culture', *Cell Tissue Res*, 338: 333-41.
- Grassi, D. A., P. L. Brattas, M. E. Jonsson, D. Atacho, O. Karlsson, S. Nolbrant, M. Parmar, and J. Jakobsson. 2020. 'Profiling of lincRNAs in human pluripotent stem cell derived forebrain neural progenitor cells', *Heliyon*, 6: e03067.
- Gumy, L. F., E. A. Katrukha, I. Grigoriev, D. Jaarsma, L. C. Kapitein, A. Akhmanova, and C. C. Hoogenraad. 2017. 'MAP2 Defines a Pre-axonal Filtering Zone to Regulate KIF1- versus KIF5-Dependent Cargo Transport in Sensory Neurons', *Neuron*, 94: 347-62.e7.
- Gunhanlar, N., G. Shpak, M. van der Kroeg, L. A. Gouty-Colomer, S. T. Munshi, B. Lendemeijer, M. Ghazvini, C. Dupont, W. J. G. Hoogendijk, J. Gribnau, F. M. S. de Vrij, and S. A. Kushner. 2018. 'A simplified protocol for differentiation of electrophysiologically mature neuronal networks from human induced pluripotent stem cells', *Mol Psychiatry*, 23: 1336-44.
- Harris, K. M., and S. B. Kater. 1994. 'Dendritic spines: cellular specializations imparting both stability and flexibility to synaptic function', *Annu Rev Neurosci*, 17: 341-71.
- Harterink, M., S. L. Edwards, B. de Haan, K. W. Yau, S. van den Heuvel, L. C. Kapitein, K. G. Miller, and C. C. Hoogenraad. 2018. 'Local microtubule organization promotes cargo transport in *C. Elegans* dendrites', *J Cell Sci*, 131.
- Hirokawa, N., and Y. Tanaka. 2015. 'Kinesin superfamily proteins (KIFs): Various functions and their relevance for important phenomena in life and diseases', *Exp Cell Res*, 334: 16-25.
- Hu, J., X. Bai, J. R. Bowen, L. Dolat, F. Korobova, W. Yu, P. W. Baas, T. Svitkina, G. Gallo, and E. T. Spiliotis. 2012. 'Septin-driven coordination of actin and microtubule remodeling regulates the collateral branching of axons', *Curr Biol*, 22: 1109-15.
- Jiang, K., S. Hua, R. Mohan, I. Grigoriev, K. W. Yau, Q. Liu, E. A. Katrukha, A. F. Altelaar, A. J. Heck, C. C. Hoogenraad, and A. Akhmanova. 2014. 'Microtubule minus-end stabilization by polymerization-driven CAMSAP deposition', *Dev Cell*, 28: 295-309.
- Kavyanifar, A., S. Turan, and D. C. Lie. 2018. 'SoxC transcription factors: multifunctional regulators of neurodevelopment', *Cell Tissue Res*, 371: 91-103.
- Killian, R. L., J. D. Flippin, C. M. Herrera, A. Almenar-Queralt, and L. S. Goldstein. 2012. 'Kinesin light chain 1 suppression impairs human embryonic stem cell neural differentiation and amyloid precursor protein metabolism', *PLoS One*, 7: e29755.
- Kleele, T., P. Marinkovic, P. R. Williams, S. Stern, E. E. Weigand, P. Engerer, R. Naumann, J. Hartmann, R. M. Karl, F. Bradke, D. Bishop, J. Herms, A. Konnerth, M. Kerschensteiner, L. Godinho, and T. Misgeld. 2014. 'An assay to image neuronal microtubule dynamics in

mice', *Nat Commun*, 5: 4827.

- Kobayashi, D., J. Kumagai, T. Morikawa, M. Wilson-Morifuji, A. Wilson, A. Irie, and N. Araki. 2009. 'An integrated approach of differential mass spectrometry and gene ontology analysis identified novel proteins regulating neuronal differentiation and survival', *Mol Cell Proteomics*, 8: 2350-67.
- Kolde R. 2019. pheatmap: Pretty Heatmaps. R package version 1.0.12.
- Kole, M. H., S. U. IIschner, B. M. Kampa, S. R. Williams, P. C. Ruben, and G. J. Stuart. 2008. 'Action potential generation requires a high sodium channel density in the axon initial segment', *Nat Neurosci*, 11: 178-86.
- Leterrier, C. 2018. 'The Axon Initial Segment: An Updated Viewpoint', *J Neurosci*, 38: 2135-45.
- Leterrier, C., H. Vacher, M. P. Fache, S. A. d'Ortoli, F. Castets, A. Autillo-Touati, and B. Dargent. 2011. 'End-binding proteins EB3 and EB1 link microtubules to ankyrin G in the axon initial segment', *Proc Natl Acad Sci U S A*, 108: 8826-31.
- Linaro, D., B. Vermaercke, R. Iwata, A. Ramaswamy, B. Libe-Philippot, L. Boubakar, B. A. Davis, K. Wierda, K. Davie, S. Poovathingal, P. A. Penttila, A. Bilheu, L. De Bruyne, D. Gall, K. K. Conzelmann, V. Bonin, and P. Vanderhaeghen. 2019. 'Xenotransplanted Human Cortical Neurons Reveal Species-Specific Development and Functional Integration into Mouse Visual Circuits', *Neuron*, 104: 972-86.e6.
- Lois, C., E. J. Hong, S. Pease, E. J. Brown, and D. Baltimore. 2002. 'Germline transmission and tissue-specific expression of transgenes delivered by lentiviral vectors', *Science*, 295: 868-72.
- Marchetto, M. C., B. Hrvov-Mihic, B. E. Kerman, D. X. Yu, K. C. Vadodaria, S. B. Linker, I. Narvaiza, R. Santos, A. M. Denli, A. P. Mendes, R. Oefner, J. Cook, L. McHenry, J. M. Grasmick, K. Heard, C. Fredlender, L. Randolph-Moore, R. Kshirsagar, R. Xenitopoulos, G. Chou, N. Hah, A. R. Muotri, K. Padmanabhan, K. Semendeferi, and F. H. Gage. 2019. 'Species-specific maturation profiles of human, chimpanzee and bonobo neural cells', *Elife*, 8.
- Marro, S. G., S. Chanda, N. Yang, J. A. Janas, G. Valperga, J. Trotter, B. Zhou, S. Merrill, I. Yousif, H. Shelby, H. Vogel, M. Y. S. Kalani, T. C. Sudhof, and M. Wernig. 2019. 'Neuroigin-4 Regulates Excitatory Synaptic Transmission in Human Neurons', *Neuron*, 103: 617-26.e6.
- Meijer, M., K. Rehbach, J. W. Brunner, J. A. Classen, H. C. A. Lammertse, L. A. van Linge, D. Schut, T. Krutenko, M. Hebisch, L. N. Cornelisse, P. F. Sullivan, M. Peitz, R. F. Toonen, O. Brustle, and M. Verhage. 2019. 'A Single-Cell Model for Synaptic Transmission and Plasticity in Human iPSC-Derived Neurons', *Cell Rep*, 27: 2199-211.e6.
- Molnar, Z., and G. Clowry. 2012. 'Cerebral cortical development in rodents and primates', *Prog Brain Res*, 195: 45-70.
- Moore, A. R., R. Filipovic, Z. Mo, M. N. Rasband, N. Zecevic, and S. D. Antic. 2009. 'Electrical excitability of early neurons in the human cerebral cortex during the second trimester of gestation', *Cereb Cortex*, 19: 1795-805.
- Murillo, J. R., L. Goto-Silva, A. Sanchez, F. C. S. Nogueira, G. B. Domont, and M. Junqueira. 2017. 'Quantitative proteomic analysis identifies proteins and pathways related to neuronal development in differentiated SH-SY5Y neuroblastoma cells', *EuPA Open Proteom*, 16: 1-11.
- Nicholas, C. R., J. Chen, Y. Tang, D. G. Southwell, N. Chalmers, D. Vogt, C. M. Arnold, Y. J. Chen,

- E. G. Stanley, A. G. Elefanty, Y. Sasai, A. Alvarez-Buylla, J. L. Rubenstein, and A. R. Kriegstein. 2013. 'Functional maturation of hPSC-derived forebrain interneurons requires an extended timeline and mimics human neural development', *Cell Stem Cell*, 12: 573-86.
- Otani, T., M. C. Marchetto, F. H. Gage, B. D. Simons, and F. J. Livesey. 2016. '2D and 3D Stem Cell Models of Primate Cortical Development Identify Species-Specific Differences in Progenitor Behavior Contributing to Brain Size', *Cell Stem Cell*, 18: 467-80.
- Pasantés-Morales, H. 1996. 'Volume regulation in brain cells: cellular and molecular mechanisms', *Metab Brain Dis*, 11: 187-204.
- Petanjek, Z., M. Judas, G. Simic, M. R. Rasin, H. B. Uylings, P. Rakic, and I. Kostovic. 2011. 'Extraordinary neoteny of synaptic spines in the human prefrontal cortex', *Proc Natl Acad Sci U S A*, 108: 13281-6.
- R Core Team (2020). R: A language and environment for statistical computing. R Foundation for Statistical Computing, Vienna, Austria. URL <http://www.R-project.org/>
- Schatzle, P., L. C. Kapitein, and C. C. Hoogenraad. 2016. 'Live imaging of microtubule dynamics in organotypic hippocampal slice cultures', *Methods Cell Biol*, 131: 107-26.
- Shi, Y., P. Kirwan, and F. J. Livesey. 2012. 'Directed differentiation of human pluripotent stem cells to cerebral cortex neurons and neural networks', *Nat Protoc*, 7: 1836-46.
- Silbereis, J. C., S. Pochareddy, Y. Zhu, M. Li, and N. Sestan. 2016. 'The Cellular and Molecular Landscapes of the Developing Human Central Nervous System', *Neuron*, 89: 248-68.
- Song, M., O. Mohamad, D. Chen, and S. P. Yu. 2013. 'Coordinated development of voltage-gated Na⁺ and K⁺ currents regulates functional maturation of forebrain neurons derived from human induced pluripotent stem cells', *Stem Cells Dev*, 22: 1551-63.
- Song, Y., K. Subramanian, M. J. Berberich, S. Rodriguez, I. J. Latorre, C. M. Luria, R. Everley, M. W. Albers, T. J. Mitchison, and P. K. Sorger. 2019. 'A dynamic view of the proteomic landscape during differentiation of ReNcell VM cells, an immortalized human neural progenitor line', *Sci Data*, 6: 190016.
- Spiliotis, E. T. 2018. 'Spatial effects - site-specific regulation of actin and microtubule organization by septin GTPases', *J Cell Sci*, 131.
- Stepanova, T., J. Slemmer, C. C. Hoogenraad, G. Lansbergen, B. Dortland, C. I. De Zeeuw, F. Grosveld, G. van Cappellen, A. Akhmanova, and N. Galjart. 2003. 'Visualization of microtubule growth in cultured neurons via the use of EB3-GFP (end-binding protein 3-green fluorescent protein)', *J Neurosci*, 23: 2655-64.
- Tang, X., L. Zhou, A. M. Wagner, M. C. Marchetto, A. R. Muotri, F. H. Gage, and G. Chen. 2013. 'Astroglial cells regulate the developmental timeline of human neurons differentiated from induced pluripotent stem cells', *Stem Cell Res*, 11: 743-57.
- Tripathi, A. K., A. K. Patel, R. K. Shah, A. B. Patel, T. M. Shah, V. D. Bhatt, and C. G. Joshi. 2014. 'Transcriptomic dissection of myogenic differentiation signature in caprine by RNA-Seq', *Mech Dev*, 132: 79-92.
- van Beuningen, S. F. B., L. Will, M. Harterink, A. Chazeau, E. Y. van Battum, C. P. Frias, M. A. M. Franker, E. A. Katrukha, R. Stucchi, K. Vocking, A. T. Antunes, L. Slenders, S. Doulkeridou, P. Sillevius Smitt, A. F. M. Altelaar, J. A. Post, A. Akhmanova, R. J. Pasterkamp, L. C. Kapitein, E. de Graaff, and C. C. Hoogenraad. 2015. 'TRIM46 Controls Neuronal Polarity and Axon Specification by Driving the Formation of Parallel Microtubule Arrays', *Neuron*, 88: 1208-26.

-
- Wu, J. Q., L. Habegger, P. Noisa, A. Szekely, C. Qiu, S. Hutchison, D. Raha, M. Egholm, H. Lin, S. Weissman, W. Cui, M. Gerstein, and M. Snyder. 2010. 'Dynamic transcriptomes during neural differentiation of human embryonic stem cells revealed by short, long, and paired-end sequencing', *Proc Natl Acad Sci U S A*, 107: 5254-9.
- Wickham H. 2016. 'ggplot 2: elegant graphics for data analysis'. Second edition.
- Yau, K. W., P. Schatzle, E. Tortosa, S. Pages, A. Holtmaat, L. C. Kapitein, and C. C. Hoogenraad. 2016. 'Dendrites In vitro and In vivo Contain Microtubules of Opposite Polarity and Axon Formation Correlates with Uniform Plus-End-Out Microtubule Orientation', *J Neurosci*, 36: 1071-85.
- Yau, K. W., S. F. van Beuningen, I. Cunha-Ferreira, B. M. Cloin, E. Y. van Battum, L. Will, P. Schatzle, R. P. Tas, J. van Krugten, E. A. Katrukha, K. Jiang, P. S. Wulf, M. Mikhaylova, M. Harterink, R. J. Pasterkamp, A. Akhmanova, L. C. Kapitein, and C. C. Hoogenraad. 2014. 'Microtubule minus-end binding protein CAMSAP2 controls axon specification and dendrite development', *Neuron*, 82: 1058-73.
- Zhang, Y., C. Pak, Y. Han, H. Ahlenius, Z. Zhang, S. Chanda, S. Marro, C. Patzke, C. Acuna, J. Covy, W. Xu, N. Yang, T. Danko, L. Chen, M. Wernig, and T. C. Sudhof. 2013. 'Rapid single-step induction of functional neurons from human pluripotent stem cells', *Neuron*, 78: 785-98.
- Zhao, X., and A. Bhattacharyya. 2018. 'Human Models Are Needed for Studying Human Neurodevelopmental Disorders', *Am J Hum Genet*, 103: 829-57.

A**B****C****D****E****F****G****H**

Supplementary Figure 1.

Successful and protracted transition of developmental stages in human iPSC-derived neurons

A. Representative images of neurite morphology at different locations (axon, dendrite) at day 7 and 13. Scale bar: 5 μm .

B. Quantifications of neurite width at different locations (axon, dendrite) at day 7 and 13. N=3, n=20-23.

C. Representative image of a polarized human iPSC-derived neuron (day 13) immunostained for Trim46, PanNaV and AnkG. Zoom represents the AIS structure. Scale bars: 10 μm in overview, 5 μm in zooms.

D. Number of APs versus input current injection of hiPSC-derived neurons (day 7-14) that fire multiple APs (red, n=20 cells) or fire only one AP (blue, n=32 cells). We excluded two cells in the multiple firing group, due to variation in baseline. Shown is the mean \pm SEM.

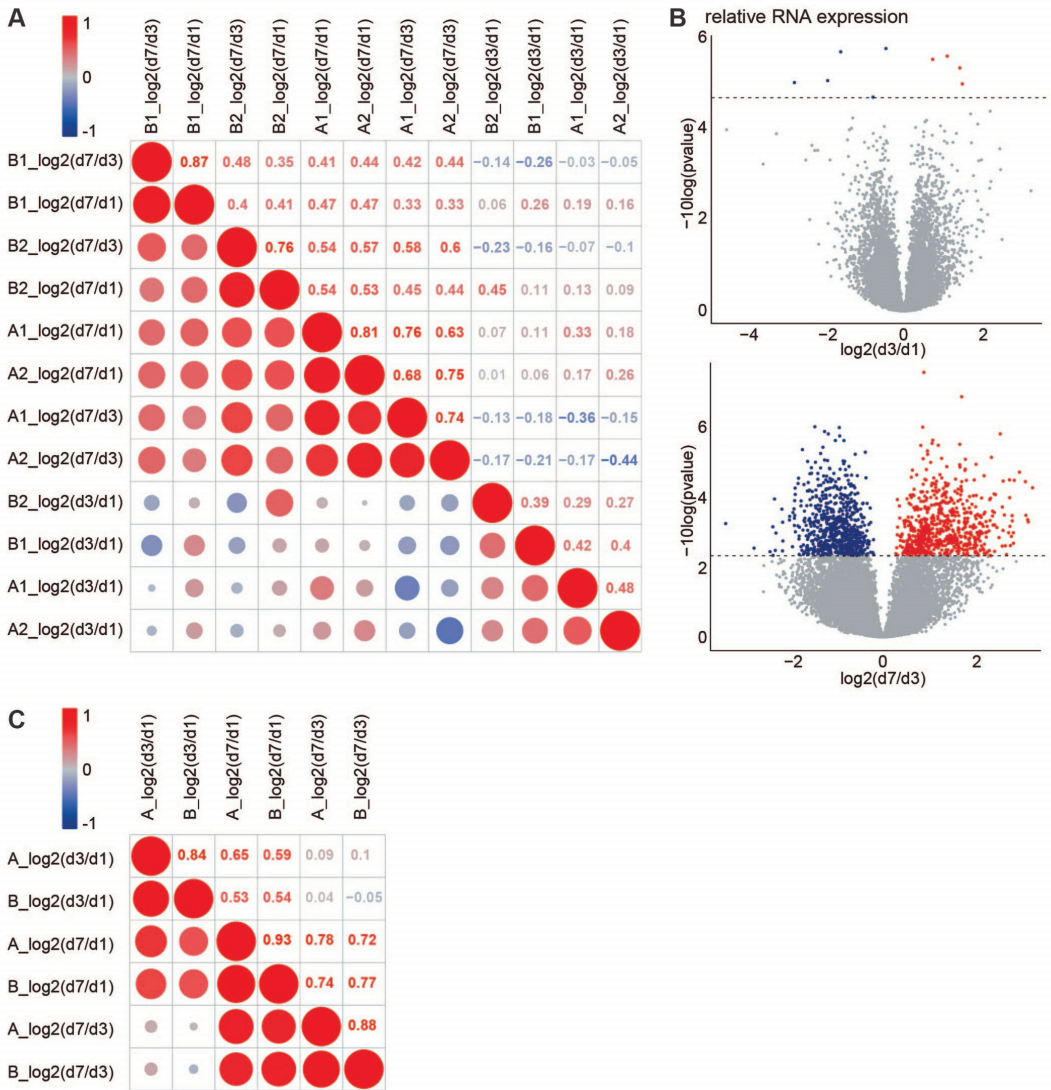
E. Resting membrane potential of human iPSC-derived neurons that fire a single AP (n=32 cells) or multiple APs (n = 22 cells).

F. Input resistance of human iPSC-derived neurons that fire a single AP (n=32 cells) or multiple APs (n=21 cells).

G. AP after-hyperpolarization of human iPSC-derived neurons that fire a single AP (n=32 cells) or multiple APs (n=22 cells).

H. Maximum sodium current of human iPSC-derived neurons that fire a single AP (n=22 cells) or multiple APs (n=17 cells).

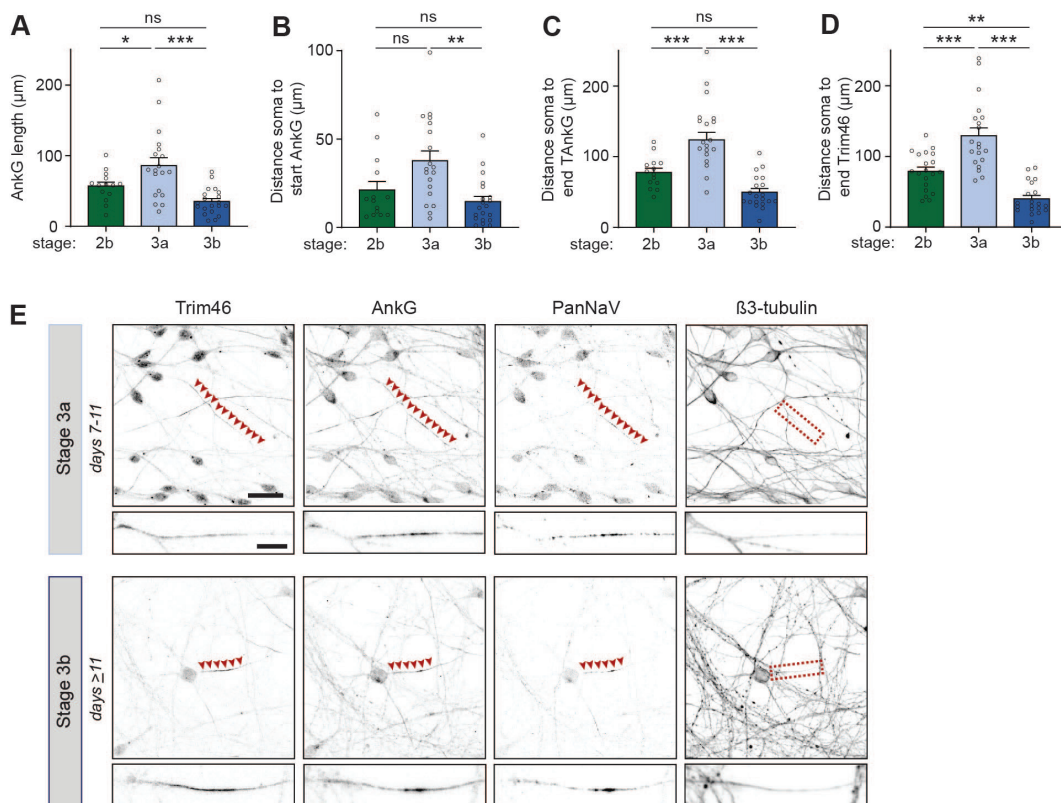
Used tests: One-way ANOVA with Tukey's post-hoc analysis (**B**), Mann-Whitney U test (**E-H**); *** p<0.001, ** p<0.01, * p<0.05, ns p \geq 0.05; error bars are \pm SEM.



Supplementary Figure 2.

Transcriptomic and proteomic profiling of early developmental stages in human iPSC-derived neurons

- A.** Correlation matrix of biological and technical replicates used for transcriptome analysis.
- B.** Volcanoplot of differentially expressed transcripts day3/day1 and day7/day3 (false discovery rate (FDR) cutoff $p < 0.05$, Benjamini & Hochberg corrected).
- C.** Correlation matrix of technical replicates used for proteome analysis.



Supplementary Figure 3.

Extra developmental stage and gradual action potential maturation during axon specification

A. Quantifications of distance soma to distal end of Trim46 signal in neurites of stage 2b, 3a and 3b human iPSC-derived neurons. N=2, n=20 cells.

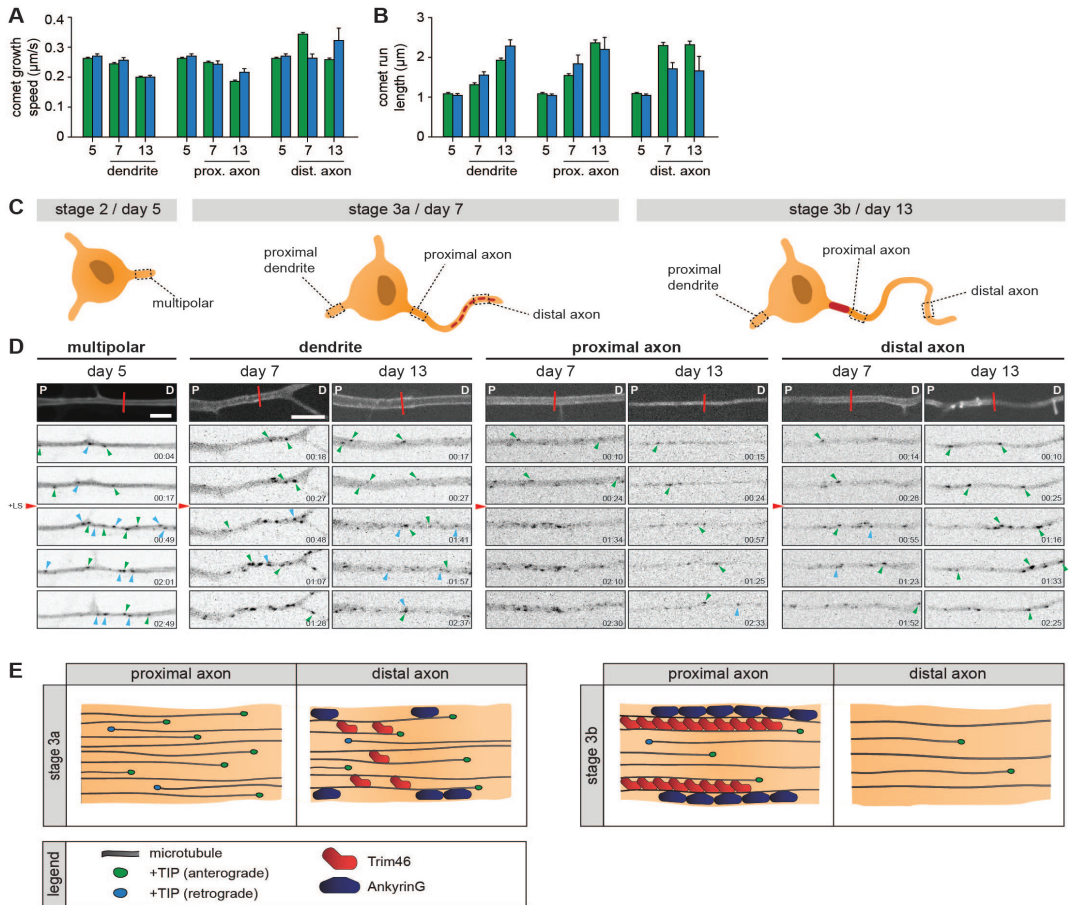
B. Quantifications of total Ankg length in neurites of stage 2b, 3a and 3b human iPSC-derived neurons. N=2, n=14-20 cells.

C. Quantifications of distance soma to start of the Ankg signal in neurites of stage 2b, 3a and 3b human iPSC-derived neurons. N=2, n=14-20 cells.

D. Quantifications of distance soma to distal end of Ankg signal in neurites of stage 2b, 3a and 3b human iPSC-derived neurons. N=2, n=14-20 cells.

E. Representative images of localization of voltage-gated sodium channels in stage 3a and 3b human iPSC-derived neurons. Cells were immunostained for Trim46, Ankg, PanNav and β3-tubulin. Arrowheads mark PanNav localizations. Scale bar: 20 μm in overview, 5 μm in zoom.

Used tests: One-way ANOVA including post-hoc analysis with Bonferroni correction (**A-D**); *** p<0.001, ** p<0.01, * p<0.05, ns p≥0.05; error bars are ± SEM.



Supplementary Figure 4.

Microtubule organization during human iPSC-derived neuronal development

A. Quantifications of the growth speed of comets pointing in the anterograde (green) or retrograde (blue) direction. $N=3$, $n=9-4723$ traces in 8-23 cells.

B. Quantifications of the distance of run length of comets pointing in the anterograde (green) or retrograde (blue) direction. $N=3$, $n=9-4723$ traces in 8-23 cells.

C. Schematic illustration of stage 2 (day 5), 3a (day 7) and 3b (day 14) hiPSC-derived neurons. Different locations of the neurons that are imaged have been outlined and annotated.

D. Stills from a spinning-disk time-lapse recording of specified neurites transfected with MARCKS-tagRFP_IRES_GFP-MACF18 at specific time points. The top panel is a still of a typical example neurite in MARCKS-tagRFP. The other panels show moving GFP-MT+TIP comets (GFP-MACF18) pointing in either an anterograde direction (green arrowheads) or retrograde direction (blue arrowheads). Red line indicates location of laser severing, and red arrowhead indicates time of laser severing. P indicates the proximal direction and D the distal direction of the neurite. Scale bars: 5 μm .

E. Schematic illustration of the proposed distal to proximal reorganization of the axon during stage 3a and stage 3b.

Table 1 - 6 are available online as source data at BioRxiv (doi: 10.1101/2020.04.21.052498).

3.



Centrosome-mediated microtubule remodeling during axon formation in human iPSC-derived neurons

Feline W. Lindhout¹, Sybren Portegies¹, Robbelien Kooistra¹, Riccardo Stucchi^{1,2}, Lotte J. Herstel¹, Nicky Scheefhals¹, Maarten Altelaar², Harold D. MacGillavry¹, Corette J. Wierenga¹, Casper C. Hoogenraad^{1,3,4}

¹Cell Biology, Neurobiology and Biophysics, Department of Biology, Faculty of Science, Utrecht University, 3584 CH Utrecht, The Netherlands.

²Biomolecular Mass Spectrometry and Proteomics, Bijvoet Center for Biomolecular Research and Utrecht Institute for Pharmaceutical Sciences, Utrecht University, 3584 CH Utrecht, the Netherlands.

³Department of Neuroscience, Genentech, Inc, South San Francisco, CA 94080, USA.

⁴Lead Contact

Submitted, *under review*

ABSTRACT

Axon formation critically relies on local microtubule remodeling, and marks the first step in establishing neuronal polarity. However, the function of the microtubule-organizing centrosomes during the onset of axon formation is still under debate. Here, we demonstrate that centrosomes play an essential role in controlling axon formation in human induced pluripotent stem cell (iPSC)-derived neurons. Depleting centrioles, the core components of centrosomes, in unpolarized human neuronal stem cells results in various axon developmental defects at later stages, including immature action potential firing, mislocalization of axonal microtubule-associated Trim46 proteins, suppressed expression of growth cone proteins and affected growth cone morphologies. Live-cell imaging of microtubules reveals that centriole loss prevents axonal microtubule reorganization towards the unique parallel plus-end out microtubule bundles during early development. We propose that centrosomes mediate microtubule remodeling during early axon development in human iPSC-derived neurons, thereby laying the foundation for further axon development and function.

INTRODUCTION

Neuronal polarity is established by a series of highly coordinated processes starting with the formation of the future axon. During axon specification, the first step of axon formation, one of the multiple unpolarized neurites of a neuron displays extensive growth. Axonal outgrowth critically relies on local cytoskeleton reorganization and growth cone dynamics (Dotti, Sullivan, and Banker 1988; Witte, Neukirchen, and Bradke 2008). Next, the newly developed axon undergoes significant reorganization as it matures, thereby adopting axon-specific hallmarks required for its function. An essential component of mature axons is the axon initial segment (AIS), a specialized compartment at the base of the axon where specific proteins (e.g. AnkG scaffolds, microtubule-organizing protein Trim46, and voltage-gated sodium and potassium channels) assemble in a highly organized manner (Leterrier 2018; Freal et al. 2019). The AIS is crucial for maintaining neuronal polarity and generating action potentials (APs). The characteristic shaping and subsequent propagation of APs is facilitated by the local clustering of voltage-gated channels at the AIS (Kole et al. 2008). Another particularly important aspect of mature axons is their unique microtubule organization. In growing axons, the microtubule network undergoes extensive remodeling, as it shifts from a mixed microtubule polarity to a uniform plus-end out microtubule organization (Yau et al. 2016). Trim46 proteins targeted to the AIS act as regulators of these axonal microtubule rearrangements, by forming parallel microtubule bundles in proximal axons (van Beuningen et al. 2015). In contrast, dendrites contain a microtubule organization of mixed polarities, and gain additional minus-end out microtubules during development. This prominent difference in microtubule organization between axons and dendrites is essential for neuronal development and function, as it contributes to polarized cargo transport and the characteristic neuronal morphology (Baas et al. 1988; Yau et al. 2016). However, while microtubule remodeling in growing axons is important for axon specification and development, the mechanisms driving these microtubule cytoskeletal rearrangements remain largely unresolved.

Centrosomes, the main microtubule organizing center (MTOC) in most animal cells, are essential for organizing the microtubule network in unpolarized neurons (Tsai and Gleeson 2005; Stiess et al. 2010; Meka, Scharrenberg, and Calderon de Anda 2020). These small, membrane-less and centrally-localized organelles are composed of two centrioles surrounded by the pericentriolar material (PCM) (Moritz et al. 2000). The majority of the microtubules are typically nucleated from γ -Tubulin Ring Complexes (γ TuRCs) embedded in the PCM (Moritz et al. 2000). During neuronal development, centrosomes gradually lose their function as MTOC as they transform into cilia, major signalling hubs in polarized cells (Stiess et al. 2010; Ishikawa and Marshall 2011). In dissociated rodent neurons, this process was reported to occur during axon development, but the exact temporal relation between axon specification and the declining MTOC function of centrosomes is unclear (Stiess et al. 2010). The importance of centrosome function in early neurodevelopment is illustrated by the increasing number of identified mutations in centrosomal proteins causing microcephaly and other neurodevelopmental disorders (Nano and Basto 2017). However, the precise function of centrosomes as MTOC for different processes of early axon development is still under debate.

Progress in understanding the role of centrosomes during axon specification has been hindered due to a number of technical challenges. In particular, centrosomes are found to display different functions in neurodevelopment in different species, resulting in conflicting findings. This is mostly illustrated by the poor recapitulation of human neurodevelopmental disorders caused by centrosome dysfunction in *Drosophila* and mice, whereas ferrets robustly model these diseases (Basto et al. 2006; Castellanos, Dominguez, and Gonzalez 2008; Pulvers, Bryk, Fish, Wilsch-Brauninger, et al. 2010; Pulvers, Bryk, Fish, Wilsch-Brauninger, et al. 2010; Johnson et al. 2018). Axon outgrowth can also be differently affected by centrosomes, as this process is perturbed with centrosome dysfunction in mice and peripheral axons of zebrafish, but not in dissociated rodent neurons and central axons of zebrafish (Stiess et al. 2010; de Anda et al. 2010; Andersen and Halloran 2012). The molecular mechanisms that underlie the observed species-specific differences remain largely unknown. Another technical challenge is presented by dissociated rodent neurons in culture, which are classically used to study axon developmental processes, as they likely undergo repolarization after being polarized *in vivo* rather than *de novo* polarization (Barnes and Polleux 2009). Together, this highlights the importance of studying the role of centrosomes in *de novo* polarization using human neurons. The development of human induced pluripotent stem cells (iPSCs) now enables studying the molecular mechanisms that drive the transition of an unpolarized human neuronal stem cell to a polarized human neuron (Lancaster et al. 2013). An additional important feature of human neurons is their significant protracted development, which allows for a more detailed investigation of the temporal processes underlying neuronal polarity (Otani et al. 2016; Linaro et al. 2019). To illustrate this, neurogenesis occurs after ~1 week in rodents, whereas this takes about ~3 months in humans, both *in vivo* and *in vitro* (Shi, Kirwan, and Livesey 2012; Espuny-

Camacho et al. 2013; Otani et al. 2016; Sousa et al. 2017). Thus, the profound slower development of human iPSC-derived neurons increases the temporal resolution to study axonal processes (Espuny-Camacho et al. 2013; Otani et al. 2016 Linaro, 2019 #9). Altogether, this emphasizes the relevance of studying centrosome functions during axon development in human iPSC-derived neurons as a model system.

In this study, we used a multidisciplinary approach, by combining human iPSC-derived neuron cultures with live-cell imaging, electrophysiology and mass spectrometry analysis, to examine the role of centrosomes during early axon development. We found that centrosomes display microtubule organizing functions during axon specification, and this function is gradually lost during further axon development. Moreover, Trim46 localization shifts from a pericentriolar region to the AIS during neuron development, coinciding with the developmental decline of centrosomal microtubule organizing functions. Differentiation of centriole-depleted neuronal stem cells (NSCs) results in various axonal developmental defects, including immature action potential firing, mislocalization of Trim46 proteins, growth cone perturbations, and impaired axonal microtubule remodeling. Together, these data imply that centrosomes mediate microtubule remodeling during axon specification in human iPSC-derived neurons, which is necessary for correct axon formation during further development.

RESULTS

Centrosomes display microtubule organizing functions during axon specification

We first examined whether centrosomes display microtubule organizing functions during axon specification in human neurons, by testing their potential to nucleate microtubules. To address this, we determined the endogenous levels of centrosomal γ -Tubulin, an essential microtubule nucleating protein, at different developmental stages of hiPSC-derived neurons. The neurodevelopmental stages were defined as follows: stage 1 (day 0) as Ki67-positive NSCs; stage 2 (day 7) as differentiated unpolarized MAP2-positive neurons with Trim46-negative processes; stage 3 (day 12) as differentiated polarized MAP2-positive neurons with Trim46-positive axons (Fig 1A,B). We identified centrosomes with centriole marker Centrin, and quantified the intensity levels of γ -Tubulin co-localizing with Centrin (Fig 1A,B). We found that the γ -Tubulin levels at centrosomes were consistently high in stage 1 and stage 2 neurons, and markedly reduced by ~50% in stage 3 neurons, consistent with previous findings in dissociated rat neurons (Fig 1A-C) (Stiess et al. 2010). These results suggest that centrosomes display microtubule organizing functions during the early developmental stages of human iPSC-derived neurons, i.e. during axon specification, but not during later stages.

Centrosome-associated localization of AIS protein Trim46 in early-stage human neurons

An important hallmark of axon development is the assembly of the AIS in the proximal axon, which occurs after the developmental decline of the microtubule organizing function of centrosomes in dissociated rat hippocampal neurons (Stiess et al. 2010). Surprisingly, we observed that the AIS protein Trim46 was localized at centrosomes prior to AIS assembly (stage 1-2), as shown by co-localization of Trim46 with the centrosome markers Centrin and γ -Tubulin (Fig 1D). Similarly, centrosome-associated localization of Trim46 was observed in human HeLa cells, but not in dissociated rat hippocampal neurons or mouse IMCD3 cells (Fig S1A). Previous studies showed that Trim46 is a microtubule binding protein, however, a possible association with centrosomal proteins or structures has not been investigated (van Beuningen et al. 2015). Thus, we sought to identify which centrosome substructure coincided with Trim46. Localization experiments by confocal microscopy showed that Trim46 appeared as an oval structure which only partially overlapped with the centriolar and pericentriolar structures marked by Centrin and γ -Tubulin, respectively (Fig 1D). To gain more in-depth structural insights, we aimed to resolve centrosomal nanostructures by STED microscopy and observed that Trim46 appeared as a cloud of punctae surrounding but not overlapping with γ -Tubulin structures (Fig 1E). The γ -Tubulin structures mark the outer layer of the pericentriolar material as well as the minus-end nucleation sites of microtubules, suggesting that Trim46 associates with the starting points of centrosomal microtubules (Mennella et al. 2012). Examples of other cells also showed a consistent alignment of Trim46 puncta surrounding γ -Tubulin, which in turn surrounded Centrin puncta representing the centriolar core. Together, these data suggest that specifically in human cells, Trim46 localizes to centrosome-associated structures.

Trim46 localization shifts from centrosomes to axonal microtubules during development

Next, we studied the localization of Trim46 over time in developing human iPSC-derived neurons. We observed a clear decline of Trim46 staining at the pericentriolar region while the intensity of axonal Trim46 levels increased during development. More specifically, the pericentriolar Trim46 levels remained high in stage 2 neurons and were markedly decreased in stage 3 neurons, following the same trend as γ -Tubulin (Fig 1F). Consistently, we observed a similar shift of Trim46 staining from centrosomes to dense peripheral microtubules arrays in maturing human iPSC-derived glia cells, which are present at low abundance in the human iPSC-derived neuron cultures (Fig S1B). Together, the neuronal data suggest that Trim46 localization shifts from the pericentriolar region to peripheral axonal microtubule arrays.

Centrinone-B treatment depletes centrioles in neuronal stem cells

To study the effect of centrosome dysfunction on axon specification, we next aimed to remove centrioles in human iPSC-derived NSCs by using Centrinone-B treatment. The

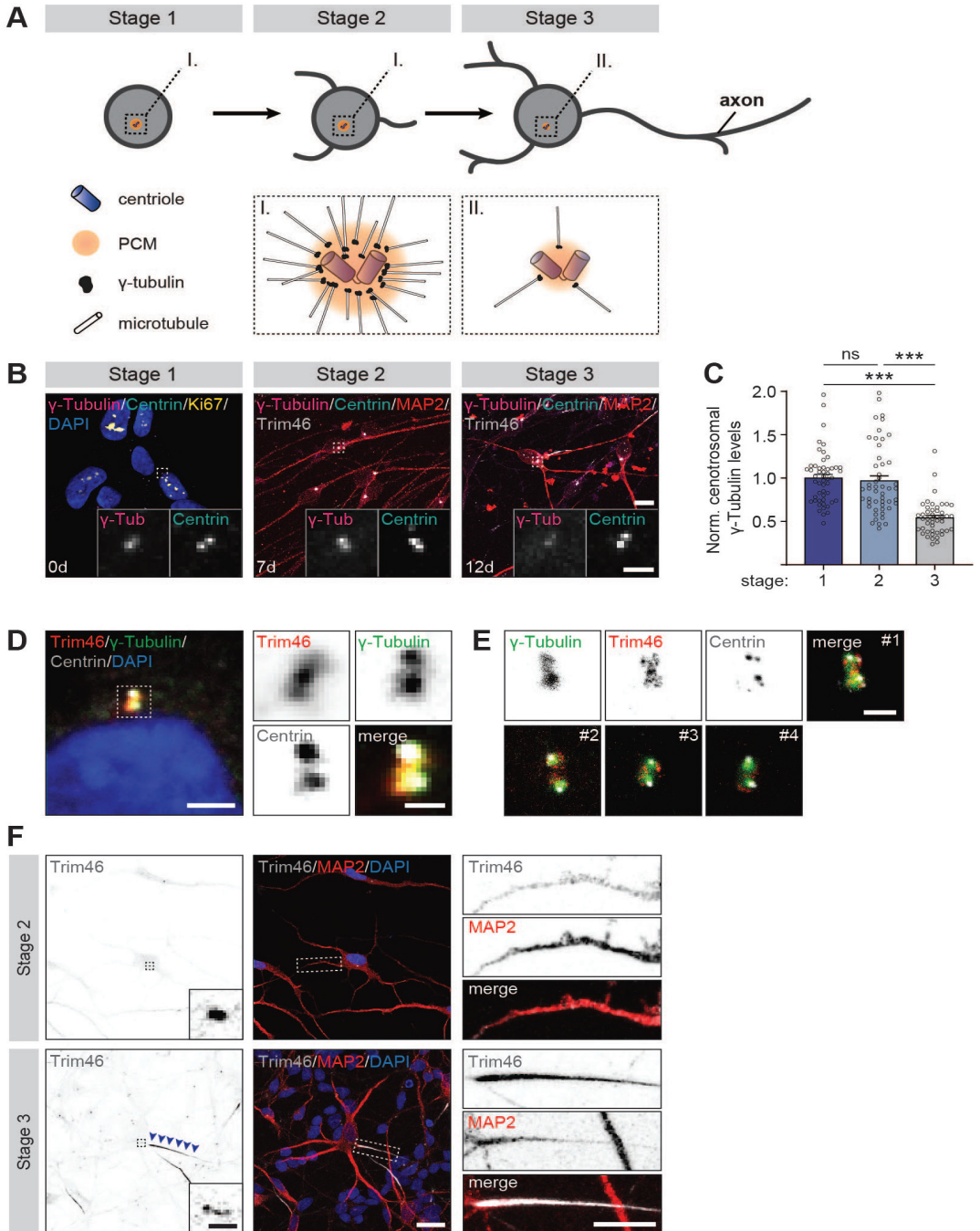


Figure 1.

Centrosomes display MTOC function and Trim46 appearance during axon specification

A. Schematic illustration of centrosomal MTOC function in neurodevelopmental stages 1, 2 and 3 in human iPSC-derived NSCs/neurons.

B. Typical examples of stage 1 (day 0), stage 2 (day 7) and stage 3 (day 12) human iPSC-derived NSCs/neurons immunostained for γ -Tubulin and Centrin. Cells were co-immunostained with Ki67 (day 0) or Trim46 and MAP2 (day 7 and 12) to define their neuronal stages. Scale bars: 10 μ m in overview, 2 μ m in zooms.

C. Quantifications of normalized γ -Tubulin fluorescent intensities at centrosomes in stage 1, 2 and 3 human iPSC-derived neurons. N=2, n=46-51 cells.

D. Human iPSC-derived NSCs (day 0) immunostained for Trim46, γ -Tubulin and Centrin. Zoom represents centrosome structure. Scale bars: 5 μ m in overview, 2 μ m in zooms.

E. Centrosomes of human iPSC-derived NSCs (day 0) with STED imaging of Trim46 and Centrin immunostaining, and confocal imaging of γ -Tubulin immunostaining. Merged images show different examples of centrosome structures. Scale bar: 1 μ m.

F. Typical examples of stage 2 and stage 3 human iPSC-derived neurons immunostained for Trim46 and MAP2. Inserts represent centrosomes. Zooms on the right represent a non-polarized neurite or a developing axon in stage 2 or stage 3 neurons, respectively. Scale bars: 20 μ m in overview, 1 μ m in insert, 10 μ m in zoom.

Data information: Data represent mean \pm SEM. One-way ANOVA including post-hoc analysis with Bonferroni correction (**B, C**). *** $p < 0.001$, ns $p > 0.05$

efficient and robust centriole loss by Centrinone-B treatment has previously been validated in various other cell types (Wong et al. 2015). Centrinone-B is a PLK4-inhibitor that blocks centriole duplication during cell division in proliferating cells, thereby generating a mixed population of cells containing 0, 1 or 2 centrioles. We treated human iPSC-derived NSCs for 0, 2 or 5 days with Centrinone-B prior to neuronal induction and quantified the number of centrioles per cell. Centrioles were defined as puncta with overlapping staining of Pericentrin and Centrin (Fig 2A). We observed successful removal of either 1 or 2 centrioles in ~50% of the NSCs after 2 days of Centrinone-B treatment, which was not significantly enhanced after a prolonged 5 day treatment (Fig 2B). Additionally, Centrinone-B treatment increased the number of cells with a characteristic neuron-like morphology, even before inducing neuronal differentiation. This premature neuronal differentiation phenotype is a well-described hallmark of centrosome dysfunction in various *in vivo* or 3D *in vitro* systems, as it underlies microcephaly and other neurodevelopmental disorders (Lancaster et al. 2013). We found significantly more neurons upon 2 days of Centrinone-B treatment, measured as the relative number of cells that were positive for neuron differentiation markers MAP2 or γ -Tubulin, or proliferation marker Ki67 (Fig S2A-E). Together, these data show that Centrinone-B treatment results in successful depletion of centrioles in human iPSC-derived neuronal cells, and that it recapitulates neuronal developmental phenotypes that are broadly associated with centrosome defects.

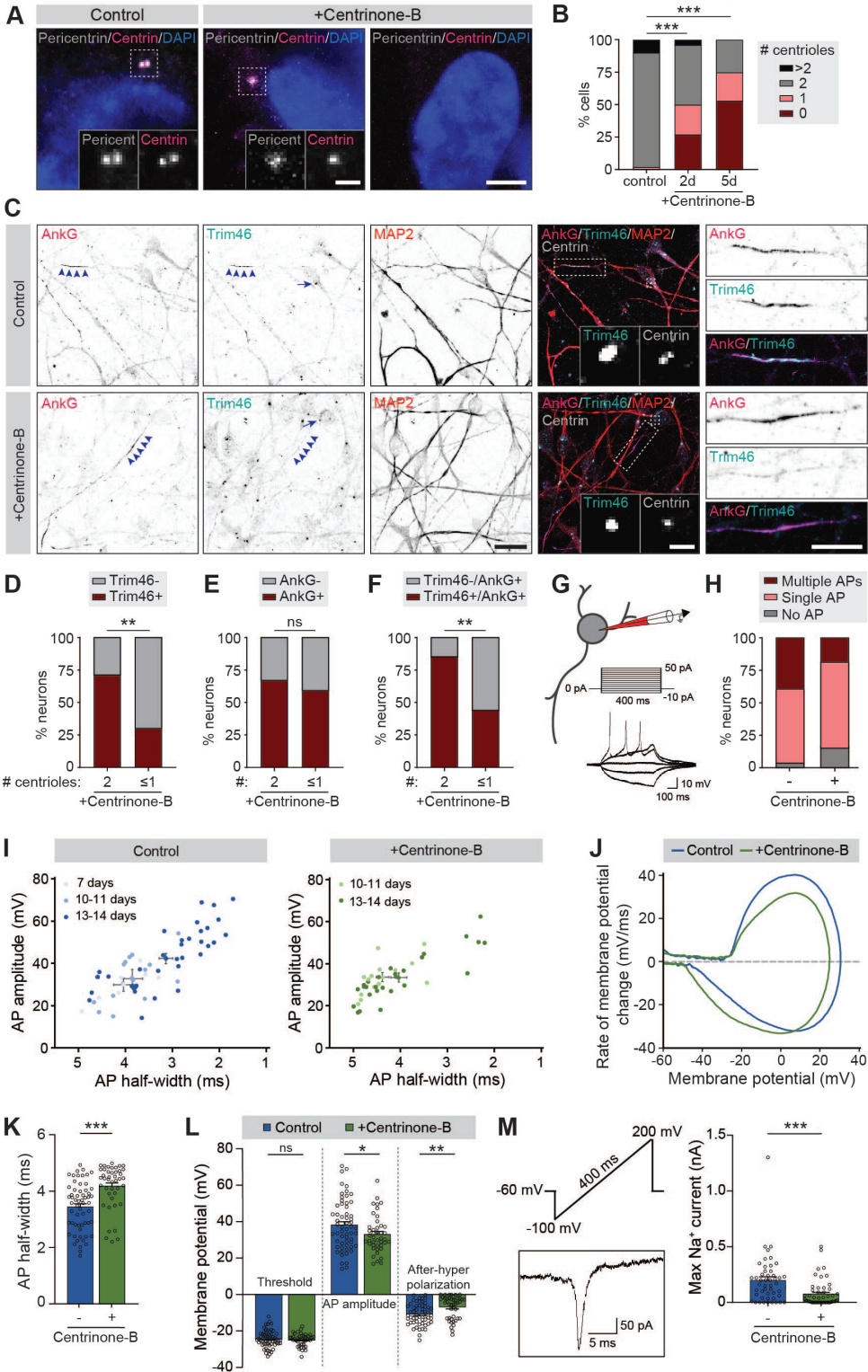


Figure 2.

Centriole loss in NSCs perturbs subsequent axonal Trim46 targeting and action potential maturation

A. Typical examples of Centrinone-B treated or control human iPSC-derived NSCs immunostained for Pericentrin and Centrin. Inserts represent centriole(s). Scale bar: 5 μm in overview, 2 μm in inserts.

B. Quantifications of the percentage of cells with 0, 1 or 2 centrioles per cell after 0 (control), 2 or 5 days Centrinone-B treatment. N=2, n=48-51 cells.

C. Typical examples of Centrinone-B treated or control human iPSC-derived neurons (12-15 days) immunostained for AnkG, Trim46, MAP2 and Centrin. Inserts represent centrosomes, zooms on the right represent AIS structures. Scale bars: 20 μm in overview, 2 μm in insert, 10 μm in zooms.

D. Quantifications of percentage of human iPSC-derived neurons (12-15 days) treated with Centrinone-B containing a Trim46-positive or Trim46-negative process. Neurons are subdivided in populations containing 2 centrioles, or less than 2 centrioles, based on Centrin immunostaining. N=3, n=31-53 cells.

E. Quantifications of percentage of human iPSC-derived neurons (12-15 days) treated with Centrinone-B containing an AnkG-positive or AnkG-negative process. Neurons are subdivided in populations containing 2 centrioles, or less than 2 centrioles, based on Centrin immunostaining. N=2, n=27-32 cells.

F. Quantifications of percentage human iPSC-derived neurons (12-15 days) treated with Centrinone-B containing AnkG-positive processes that are Trim46-positive or Trim46-negative. Neurons are subdivided in populations containing 2 centrioles, or less than 2 centrioles, based on Centrin immunostaining. N=2, n=27 cells.

G. Top: Schematic illustration of the experimental electrophysiology setup. To determine action potential (AP) frequency, somatic current injections from -10 pA to 50 pA (steps of 5 pA, 400 ms) were applied. Bottom: Representative example of evoked AP firing in a Centrinone-B treated human iPSC-derived neuron, response to hyperpolarizing and first two depolarizing current steps, recorded at day 13.

H. Neuronal excitability was recorded in 54/61 control cells and 53/54 Centrinone-B treated cells. Percentage of cells firing zero, one or multiple APs in control (N=4; no AP: n=2, single AP: n=32, multiple APs: n=22) versus Centrinone-B treated cultures (N=3; no AP: n=9, single AP: n=34, multiple APs: n=10).

I. Scatter plots of AP amplitude versus AP half-width grouped by days after plating for Centrinone-B treated (10-11 days: n=14 cells, 13-14 days: n=28 cells) and control (7 days: n=7 cells, 10-11 days: n=15 cells, 13-14 days: n=36 cells) human iPSC-derived neurons.

J. Phase plots of a representative AP of a human iPSC-derived neuron treated with Centrinone-B and a control neuron of 13 and 14 days, respectively.

K. AP half-width recorded in Centrinone-B treated (n=43 cells) and control human iPSC-derived neurons (n=59 cells).

L. AP threshold, amplitude and after-hyperpolarization recorded in Centrinone-B treated (n=43 cells) and control human iPSC-derived neuron cultures (n=59 cells).

M. Left top: Schematic representation of the voltage ramp protocol used to determine maximum sodium current; membrane potential was changed from -100 mV to 200 mV in 400 ms. Left bottom: Representative example of maximum sodium peak recorded of a control neuron at day 13. Right: Maximum sodium peak in Centrinone-B treated (n=52 cells) and control human iPSC-derived neurons (n=48 cells).

Data information: Data represents mean \pm SEM. Chi-square-test including post-hoc analysis with Bonferroni correction (**B**, **D**, **E**, **F**); Mann Whitney test (**K**, **L**: after-hyperpolarization, **M**), Student's t test (**L**: AP amplitude). *** $p < 0.001$, ** $p < 0.01$, * $p < 0.05$, ns $p > 0.05$

Centriole loss perturbs axonal targeting of Trim46

We next asked whether these prematurely differentiated neurons upon Centrinone-B treatment follow normal developmental timing and grow functional axons. To investigate the role of centrosomes during axon specification, we assessed if the development of early-stage axons was affected by centriole loss. An important aspect of early-stage axon development is the specific sorting of axonal proteins, including AIS proteins such as Trim46 and AnkG. Thus, we tested if the axon-specific localization of Trim46 and AnkG was affected by Centrinone-B induced centriole removal. We divided the neurons treated with Centrinone-B into subpopulations containing 2 or <1 centriole(s), as defined by Centrin immunostaining (Fig 2C). Cells were co-immunostained with Trim46 and AnkG to quantify the number of cells containing a Trim46-positive and/or AnkG-positive process (Fig 2C). We observed a marked ~50% reduction of cells with a Trim46-positive process in the subpopulation containing <1 centriole(s) compared to cells still containing 2 centrioles, whereas no changes were observed for AnkG (Fig 2D,E). Consistently, cells containing <1 centriole(s) showed reduced Trim46 co-localization at AnkG-positive axonal structures (Fig 2F). Together, these data imply that centrosomes are required for the targeting of Trim46, but not AnkG, to axons during early stages of neuronal development.

Centriole loss leads to immature action potential firing

The axonal targeting of Trim46 and AnkG is required to assemble the AIS, the highly specialized structure essential for mature and efficient AP firing. Thus, we assessed if the observed differential effects on axon protein targeting upon centriole depletion correlate with changes in AP properties. We performed whole-cell patch clamp recordings of control or Centrinone-B treated neurons of 7-14 days, which coincides with early axon development. To measure neuronal excitability, we determined the number of APs fired with increasing somatic current injection (steps of 5 pA; 400 ms) (Fig 2G, Fig S2F). In Centrinone-B treated cultures, ~17% of neurons did not fire APs, whereas this was only ~3% in control cultures (Fig 2H). Of the firing neurons, there were less Centrinone-B treated neurons that fired multiple APs compared to control. Neurons that did not fire APs did generate small peaks upon current stimulation, indicating the opening of sodium channels, but no positive feedback to rapidly increase the membrane potential as is characteristic of APs. In addition, neurons treated with Centrinone-B did not display a progressive maturation of AP properties from day 10 to day 14, as was observed in control neurons (Fig 2I). APs fired by Centrinone-B treated neurons appeared more immature, as they were wider, had smaller amplitudes and smaller after-hyperpolarizations (Fig 2J-L, S2G,H). In Centrinone-B treated neurons the input resistance was also higher, but membrane potential did not differ from control (Fig S2I,J). Although AP threshold was not affected by Centrinone-B treatment (Fig 2L), maximum sodium currents were significantly smaller in Centrinone-B treated neurons (Fig 2M). Together, the electrophysiology recordings from Centrinone-B treated neurons show more immature AP firing and reduced sodium currents, thereby highlighting the functional relevance of centrosome-mediated control mechanisms during early stages of neuronal development.

Centriole depletion results in reduced expression of growth cone proteins

The centriole-depleted NSCs develop into neurons with structural and functional perturbations in axon development. Next, we aimed to quantify effects of centriole depletion during axon specification with unbiased profiling. Therefore, we performed mass spectrometry based quantitative proteomics analysis on days 1, 3, and 7, which roughly corresponds with developmental stage 1, onset of stage 2, and onset of stage 3, respectively. We compared the proteome dynamics during early neurodevelopment of replicates of Centrinone-B treated and control neurons (Fig S3A, Table 1). Centrinone-B treatment did not markedly alter the relative protein expression over time (Fig 3A). The protein expression profile of control neurons showed a developmental shift, which corresponds to the transitions from stage 1 to stage 2, and from stage 2 to stage 3 (Fig S3B). Protein expression of centriole-depleted neurons largely follows the same trend (Fig S3C). In both populations, proteins considered specific for NSCs are downregulated at days 3 and 7 (e.g. Ki67, Nestin, Otx, Notch1), whereas neuronal proteins are upregulated (e.g. Stathmin1, Map2, Doublecortin, Tub β 3) (Fig S3D). The onset of stage 3 marks axon specification and indeed we observed strong upregulation of the axonal proteins Trim46 and Tau at day 7, which was not affected by Centrinone-B treatment (Fig 3B). Expression of the growth cone proteins Basp1, Gap43, and Marcks was increased at day 3 in controls as well as Centrinone-B treated neurons. This upregulation was even stronger at day 7 in control neurons, but was markedly suppressed in the centriole-depleted neurons (Fig 3C, Fig S3D). Together, the quantitative proteome analysis shows that treatment with Centrinone-B does not dramatically alter the protein expression profile during early stages of neurodevelopment. However, these results indicate a specific effect on growth cone proteins upon loss of centrioles.

Centriole loss affects neurite growth cone morphology

Next, we examined if the reduced expression of growth cone proteins resulted in defects of axonal growth cone morphology. We found that in control neurons the size of growth cones is relatively large early in development and decreases over time (Fig 3D,E). Growth cones of centriole-depleted neurons remained smaller at day 5, and their size decreased even further later in development. As microtubules are essential components to shape growth cones, we investigated whether manipulation of the microtubule cytoskeleton mimicked the effect of centriole depletion on growth cone size (Dent, Gupton, and Gertler 2011). Indeed, treatment with Nocodazole, a microtubule destabilizer, also resulted in smaller growth cones already at day 5 (Fig 3D,E). Interestingly, Nocodazole treatment did not show an additional effect on growth cone size in centriole depleted neurons, which suggests similar underlying mechanisms. To study the effect of centriole depletion on growth cones more specifically, we categorized three subtypes: fan-like, torpedo-like, and bulb-like (Fig 3F) (van der Vaart et al. 2013). We found a majority of fan-like growth cones at day 5, which shifted to more torpedo-like and bulb-like growth cones as axons matured (Fig 3G). Neither Centrinone-B nor Nocodazole treatment altered the relative abundance of these types

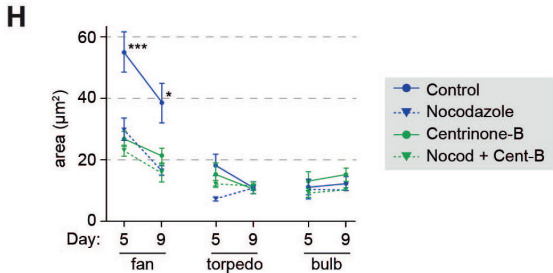
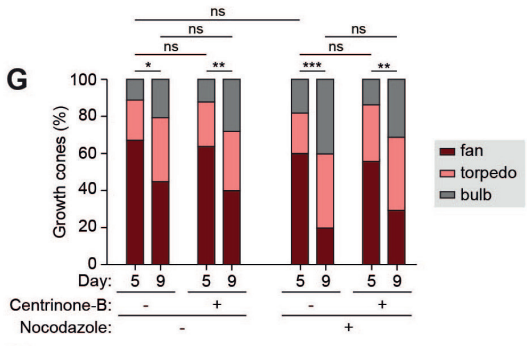
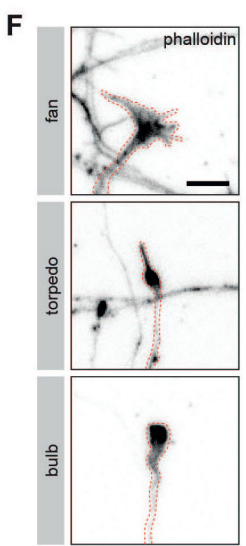
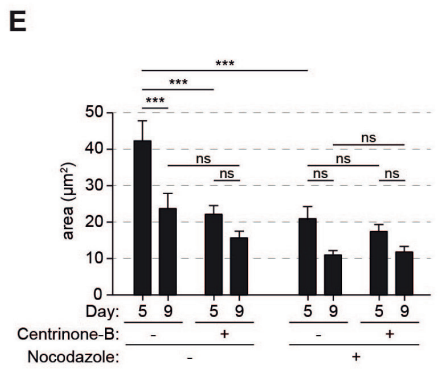
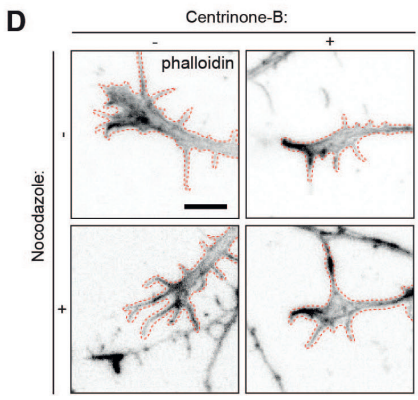
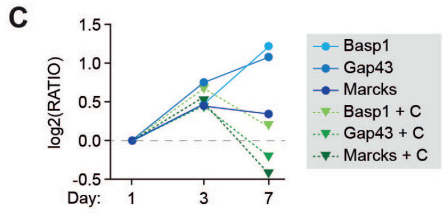
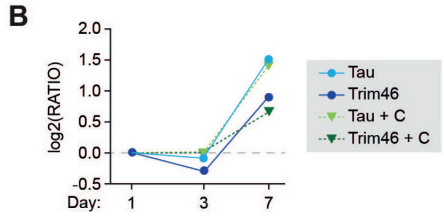
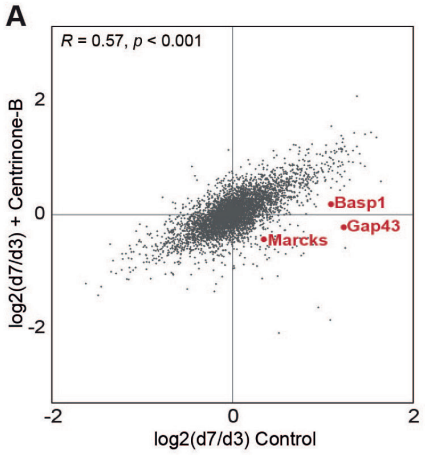


Figure 3.

Centriole loss in NSCs is accompanied with changes in neurite growth cone morphology

A. Correlative plot of changes in protein abundance between control neurons and neurons treated with Centrinone-B (day7/day3). Pearson correlation $R=0.5716$, $p<0.001$. Specific, significantly changing growth cone proteins highlighted in red.

B. Protein abundance profile over time for axon-related proteins Trim46 and Tau in control neurons and neurons treated with Centrinone-B (+C).

C. Protein abundance profile over time for growth cone-related proteins Basp1, Gap43 and Marcks in control neurons and neurons treated with Centrinone-B (+C).

D. Representative images of fan-like growth cones at day 5 of control and Centrinone-B treated neurons in untreated, or nocodazole-treated conditions. Growth cone visualized by immunostaining for phalloidin. Scale bar = 5 μ m.

E. Quantifications of the average area (μm^2) of growth cones of control and Centrinone-B treated neurons in untreated, or nocodazole-treated conditions at different time points. $N=3$, $n=25-83$.

F. Representative images of different growth cone morphological categories: fan-like, torpedo-like and bulb-like. Scale bar = 5 μ m.

G. Quantifications of the ratios of different subtypes (fan-like, torpedo-like, bulb-like) of growth cones of control and Centrinone-B treated neurons in untreated, or nocodazole-treated conditions at different time points.

H. Quantifications of the average area (μm^2) of different subtypes (fan-like, torpedo-like, bulb-like) of growth cones of control and Centrinone-B treated neurons in untreated, or nocodazole-treated conditions at different time points. $N=3$, $n=5-55$.

Data information: Data represent mean \pm SEM. One-way ANOVA including Tukey's post-hoc analysis (**E**), Chi-square-test including post-hoc analysis with Bonferroni correction (**G**), One-way ANOVA including Sidak's post-hoc analysis (**H**). *** $p<0.001$, ** $p<0.005$, ns $p\geq 0.05$

of growth cones. However, Centrinone-B as well as Nocodazole treatment did result in significantly smaller fan-like growth cones at day 5, which in control neurons are considerably larger than torpedo- and bulb-like growth cones (Fig 3H). This effect was distinct for fan-like growth cones, as the sizes of torpedo-like and bulb-like growth cones were unaffected, which suggests that the observed decrease of growth cone size is specifically due to affected fan-like growth cones (Fig 3E,H). The actin cytoskeleton is another important cytoskeletal component at growth cones, and was previously found to be controlled by microtubules as well as centrosome activity in dissociated rodent neurons (Zhao et al. 2017; Meka et al. 2019). Here, we observed no changes in local levels of F-actin at growth cones, suggesting that the reduced size of fan-like growth cones is not caused by changes in F-actin levels in growth cones (Fig S3E). Together, these results indicate that centriole depletion causes growth cone morphology defects during axon outgrowth, presumably by perturbing the underlying microtubule network.

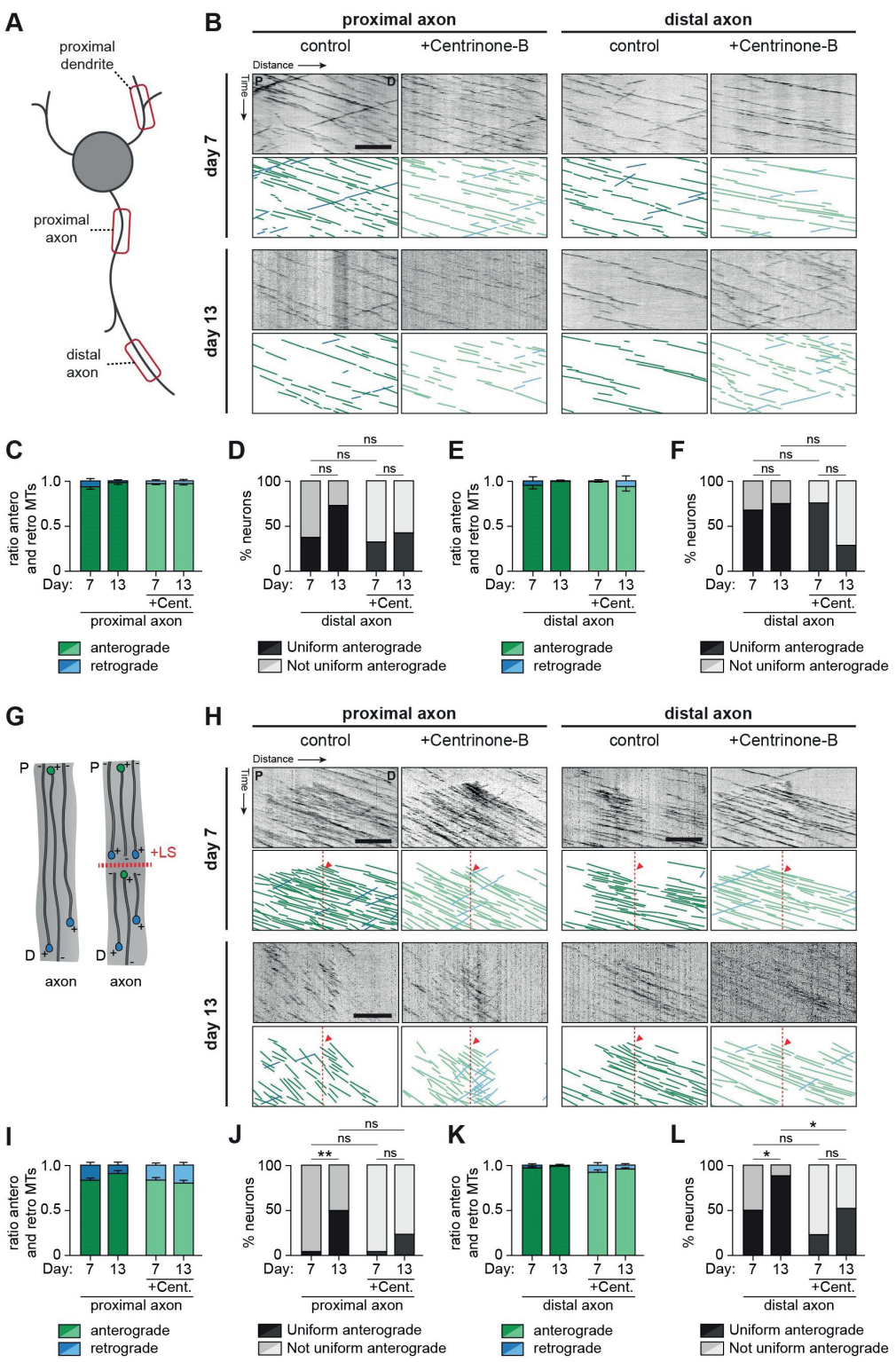


Figure 4.

Centriole loss restrains microtubule remodeling during early axon development

A. Schematic illustration of stage 3 human iPSC-derived neurons. Different locations of the neurons that are imaged have been outlined and annotated.

B. Kymographs and schematic representations of time-lapse recordings as shown in **S4B**, for different positions (proximal axon; distal axon), time points (day 7; day 13) and conditions (control; Centrinone-B). Scale bar: 5 μ m.

C. Quantifications of the ratios of comets pointing in anterograde (green) or retrograde (blue) direction in the proximal axon. N= 3, n= 7-11 cells.

D. Quantifications of the percentage of neurons exhibiting uniform, or not uniform comet orientations in the anterograde direction in the proximal axon. N= 3, n= 7-11 cells.

E. Quantifications of the ratios of comets pointing in anterograde (green) or retrograde (blue) direction in the distal axon. N= 3, n= 8-12 cells.

F. Quantifications of the percentage of neurons exhibiting uniform, or not uniform comet orientations in the anterograde direction in the distal axon. N= 3, n= 8-12 cells.

G. Schematic representation of microtubule laser-severing (LS) experiments.

H. Kymographs and schematic representations of time-lapse recordings as shown in **S4Q** following LS, for different positions (proximal axon; distal axon), time points (day 7; day 13) and conditions (control; Centrinone-B). Red line and red arrowhead denote location and time of LS. Scale bars: 5 μ m.

I. Quantifications of the ratios of comets pointing in anterograde (green) or retrograde (blue) direction in the proximal axon following LS. N=3, n=19-30 cells.

J. Quantifications of the percentage of neurons exhibiting uniform, or not uniform comet orientations in the anterograde direction in the proximal axon following LS. N= 3, n= 19-30 cells.

K. Quantifications of the ratios of comets pointing in anterograde (green) or retrograde (blue) direction in the distal axon following LS. N=3, n=19-30 cells.

L. Quantifications of the percentage of neurons exhibiting uniform, or not uniform orientations in the anterograde direction in the distal axon following LS. N= 3, n= 19-30 cells.

Data information: Data represent mean \pm SEM. Chi-square-test including post-hoc analysis with Bonferroni correction (**D,F,J,L**); *** $p < 0.001$, ** $p < 0.005$, * $p < 0.05$, ns $p \geq 0.05$

Centriole loss perturbs microtubule reorganization in developing axons

To gain more insight into the potential role of centrosomes on the organization of the axonal microtubule cytoskeleton, we studied the effect of centriole loss on the microtubule remodeling processes during development. We systematically analyzed plus-end dynamics and orientations of microtubules at different cellular compartments on day 7 and 13, which coincide with the onset of stage 3 and late stage 3, respectively, in control and Centrinone-B treated neurons (Fig 4A). We used two-color live-cell imaging to visualize neurite morphology and microtubule plus-end tracking proteins (MT+TIPs) (Fig 4B, S4B, Movie S1). In control neurons, we observed the characteristic adoption of a unidirectional,

plus-end out organization of microtubules in axons over time, in a distal-to-proximal fashion (Fig 4C-F). This shift towards a uniform orientation between day 7 and 13 corresponded to a decrease of retrogradely moving comets in most control neurons (Fig S4C-F). This developmental shift is less prevalent upon centriole loss, as shown by a decrease in neurons with uniform anterogradely moving comets (Fig 4D-F). Moreover, this was accompanied by a less distinct decrease in the number of retrograde comets over time compared to control (Fig S4C-F). The reorganization of microtubules corresponded with trends towards a decrease in the comet growth speed in control but not in Centrinone-B treated neurons, whereas comet run length was not changed over time in both conditions (Fig S4J-O, Table2,3). Imaging of MT+TIPs only provides information about the dynamic ends of microtubules, but does not account for stabilized microtubules. Thus, we next aimed to analyze the microtubule orientations of the total axonal microtubule network, including both sTable and dynamic microtubules. This was addressed by combining our approach with laser-severing to generate new microtubule ends by cutting microtubules with a short-pulsed laser, which triggers newly formed MT+TIPs (Fig 4G,H, S4Q, Movie S2) (Yau et al. 2016). Following laser severing of microtubules in axons, we observed an increase in the total number of mostly retrograde comets, which reflects the sTable pool of minus-end out microtubules (Fig S4D,F,S,U). In line with previous results, we found that the impaired shift towards uniform anterogradely moving comets in Centrinone-B treated neurons was more profound following laser-severing (Fig 4I-J, S4R-U). This is most strikingly observed at distal axon regions of day 13 neurons, the most mature axonal stage, as ~90% of the axons of control neurons showed a uniform plus-end out microtubule whereas this is ~50% in Centrinone-B treated neurons (Fig 4L). In dendrites, a shift towards a mixed microtubule network is observed in both control and Centrinone-B treated neurons (Fig S4A,G-I,P,V-X). Together, these data suggest that centriole loss is important for the unique axon-specific reorganization towards uniform plus-end out microtubules.

DISCUSSION

Multiple studies attempted to address the possible role of centrosomes during axon development. Early reports suggested that microtubule nucleation is important for axon formation and outgrowth in dissociated rodent neurons, and proposed that centrosomes could play an important role in axon development (Ahmad et al. 1994). Indeed, in *Drosophila* neurons, centrosome dysfunction affected axon formation and outgrowth (de Anda et al. 2005). In dissociated rodent neuron cultures, centrosome positioning was found to correlate with sites of newly emerging axons (Zmuda and Rivas 1998; de Anda et al. 2005). However, centrosome removal in polarized neurons did not affect further axon outgrowth in dissociated rodent neurons (Stiess et al. 2010). Nevertheless, the role of centrosomes in axon specification remained largely unexplored. This is mostly due to technical challenges that prevent investigation of the very early molecular processes that drive axon specification. Here, we used human iPSC-derived neurons to investigate centrosome function during axon specification. We uncovered that centrosomes are important for microtubule remodeling

during early axon development, thereby setting-up the foundation for subsequent axon maturation and functioning.

Trim46 localizes at the centrosome and AIS at different stages of neuronal development

Trim46 was identified as a microtubule-associated protein localizing to the proximal part of the AIS, where it locally binds and stabilizes parallel microtubule bundles (van Beuningen et al. 2015). In this study we report the uncharacteristic localization of Trim46 near centrosomes in unpolarized neurons, which is shifted towards axons during neuronal polarization. Interestingly, a similar developmental shift was previously reported for NDEL1, a dynein regulating protein (Kuijpers et al. 2016). It remains unknown if there are additional microtubule associated proteins showing the developmental translocation from centrosomes to axons. Remarkably, the axonal accumulation of Trim46 was perturbed upon centriole removal, likely signifying a differentially organized axonal microtubule network. Consistent with this idea, we observed less parallel plus-end out microtubules in axons upon centriole loss. Previous *in vitro* reconstitution assays revealed that Trim46 binding favors bundles of parallel oriented microtubules (Freal et al. 2019). High resolution imaging showed that Trim46 appeared as small punctae surrounding the outer layer of the pericentriolar material and did not coincide with previously resolved structures of centrosomal proteins (Mennella et al. 2012). Considering that Trim46 is a microtubule-associated protein favoring parallel microtubule bundles, we speculate that Trim46 localizes to the starting points of centrosomal microtubule arrays nucleated from γ TuRCs at the PCM (Freal et al. 2019). Hence, centrosomes are likely to represent the site with the highest occurrence of parallel oriented microtubules in cells with a radial microtubule network. The function of centrosome-associated Trim46 remains elusive, although it is tempting to speculate that it plays a role in stabilizing the parallel oriented microtubules, consistent with its previous reported function in axons (van Beuningen et al. 2015).

Dissecting the mechanistic role of centrosomes in axon development

Our data indicates that the centrosome is a critical regulator of axonal microtubule organization during early neuronal development. First, we show that centrosomes display microtubule organizing functions during the process of axon specification, and not in polarized neurons. This illustrates the potential of centrosomes, as main MTOCs, to contribute to microtubule remodeling during onset of axon development. Second, centriole loss had distinct effects on AIS assembly and function, as illustrated by the absence of microtubule binding Trim46 proteins, and more immature AP firing and reduced sodium currents. It is likely that the perturbed centrosome-mediated microtubule remodeling underlies the observed functional defects. Third, at earlier developmental stages, centriole loss affected growth cone formation, which was mimicked by drug treatments that cause microtubule destabilization. Fourth, we found that centriole loss results in a marked delay in the axon-specific uniform plus-end out microtubule reorganization. The precise mechanism

of how centrioles mediate axonal microtubule rearrangements in human iPSC-derived neurons remains largely unclear. Developmental decline of centrosomal microtubule nucleation is a controlled process occurring after axon specification (Stiess et al. 2010). Perturbing this controlled timing by removing centrioles prior to axon specification may result in a differentially organized microtubule network in young neurons. Interestingly, a relative increase in acentrosomal microtubules was found in epithelial cells subjected to Centrinone-B induced centriole loss (Martin et al. 2018). We speculate that premature centriole loss may promote acentrosomal microtubule nucleation in axons and thereby increase minus-end out microtubules. Alternatively, centrosomes were also found to play a role in non-microtubule functions that are relevant for neurodevelopment, such as intracellular signaling, protein homeostasis and organizing the actin cytoskeleton (Conduit, Wainman, and Raff 2015; Farina et al. 2016; Vora and Phillips 2016; Meka, Scharrenberg, and Calderon de Anda 2020). However, it remains unknown to what extent these functions contribute to axon formation. Altogether, our data show that centrosomes are critical for setting-up the correct microtubule organization during axon specification, which is important for subsequent microtubule remodeling in growing axons.

Centrosome dysfunction results in premature differentiation and repressed axon development

Neurodevelopment is orchestrated by a highly temporal controlled sequence of events. Centrosome dysfunction significantly perturbs this coordinated timing, resulting in microcephaly disorders (Nano and Basto 2017). These reduced brain sizes are mostly attributed to a reduction of the NSC pool, due to premature differentiation and cell death (Nano and Basto 2017). Here we show that NSCs prematurely differentiate into neurons when centrosome function is impaired, consistent with previous reports in human iPSC-derived cerebral organoids (Lancaster et al. 2013). However, previous studies did not reveal whether these prematurely differentiated neurons subsequently follow normal developmental timing and are able to grow functional axons. Here we found reversed timing effects on axon development in prematurely differentiated neurons, as centriole loss perturbed microtubule remodeling during axon formation. The structural axon developmental defects were also accompanied by compromised axon function, as demonstrated by impaired AP firing and reduced sodium currents with centrosome dysfunction. Presumably, the observed functional axon defects are the result of a perturbed organization of the axonal microtubule network in centriole-depleted neurons. Setting-up the distinct microtubule organization in axons and dendrites is an important aspect of neuron polarity, and altering this process might have severe consequences for polarized cargo transport and further neurodevelopment (van Beuningen and Hoogenraad 2016). In the brain, correct timing of axonal outgrowth during neurodevelopment is key, as axon pathfinding is steered by gradients of chemical attractants or repellents that are highly spatiotemporally controlled (Stoeckli 2018). We therefore speculate that centrosome-mediated alterations in axon development may significantly affect axon targeting and neuronal innervation *in vivo*. To this end, it would be

interesting to direct future research in addressing the long-term functional consequences of an altered axonal microtubule network due to centrosome dysfunction.

ACKNOWLEDGEMENTS

We thank Dr. Didier Trono for kindly providing the lentiviral vector. This work was supported by the Netherlands Organization for Scientific Research (NWO-ALW-VICI, 865.10.010, CCH), the Netherlands Organization for Health Research and Development (ZonMW-TOP, 912.16.058, CCH), the European Research Council (ERC) (ERC-consolidator, 617050, CCH), and the research program of the Foundation for Fundamental Research on Matter (FOM, #16NEPH05, CJW).

AUTHOR CONTRIBUTIONS

FWL initiated the study, designed and performed experiments, and wrote the article together with SP, RK and LJH. SP designed and performed experiments for the growth cone analysis, RK provided the microtubule live-imaging data, RS conducted the mass spectrometry experiments supervised by MA, LJH performed and interpreted the electrophysiology experiments supervised by CJW, and NS provided the STED microscopy data supported by HDM. HDM edited the article. CCH designed the experimental plan, supervised the research and edited the article.

DECLARATION OF INTERESTS

Casper Hoogenraad is an employee of Genentech, Inc., a member of the Roche group. The authors declare that they have no additional conflict of interest.

MATERIAL AND METHODS

Human iPSC-derived neuron culture

Human iPSC-derived neuronal stem cells (ax0016, Axol Bioscience) were purchased, expanded and subjected to neuronal differentiation and maintenance as previously prescribed (Lindhout et al. 2020). In brief, for expansion of human iPSC-derived NSCs, cells were plated on SureBond-coated plastic wells of a six-wells plate, and kept in Neuronal Plating-XF medium (ax0033, Axol Bioscience) at 37°C with 5% CO₂. On the next day, medium was replaced by Neuronal Expansion-XF Medium supplemented with EGF (20 ng/ml; AF-100-15, Peprotech) and FGF (20 ng/ml; 100-18B, Peprotech), which was refreshed every two days. For cell passaging, cells were washed once with PBS, dissociated with Unlock (ax0044, Axol Bioscience), and plated and maintained on pre-coated wells as described above. For neuronal differentiation, human iPSC-derived NSCs were plated on ReadySet/SureBond-coated glass coverslips and kept in Neuronal Plating-XF medium (ax0033, Axol Bioscience) at 37°C with 5% CO₂. Cells were plated at a density of ~40k cells per well for control and ~60k cells per well or Centrinone-B-treated conditions, to compensate for the decreased proliferating rates caused by dysfunctional centrosomes. Neuronal induction was induced two days after plating by gradually replacing the medium

to Neuron Differentiation-XF Medium (ax0032, Axol Bioscience), and differentiated neurons were next maintained in Neuronal Maintenance-XF Medium (ax0034, Axol Bioscience).

Primary rat hippocampal neuron, HeLa and IMCD3 cell culture

Dissociated rat hippocampal neuron cultures were prepared as previously described (Lindhout et al. 2019). In brief, neurons were obtained from embryonic day 18 rat pups, plated on poly-L-lysine/laminin-coated coverslips (100k/well), and kept in Neurobasal medium (NB) supplemented with 2% B27, 0.5 mM glutamine, 16.6 μ M glutamate, and 1% penicillin/streptomycin at 37°C with 5% CO₂. HeLa or IMCD3 cells were plated on plastic for expansion and 18 mm coverslips for experiments, and kept in DMEM/Ham's F10 (50%/50%) medium supplemented with 10% FCS and 1% penicillin/streptomycin at 37°C with 5% CO₂.

Pharmacological treatments

For centriole loss experiments, cells were treated with Centrinone-B (500 nM; HY-18683, MedChemExpress) 1 hour after plating and treatment was continued with every following medium change to prevent unintentional wash-out. For growth cone experiments, if indicated, cells were treated for 24h with 20 nM Nocodazole (Sigma-Aldrich, M1404) prior to fixation.

Lentiviral infection

Constructs expressed by lentiviral infections in this study are FUGW-GFP (Addgene #14883, (Lois et al. 2002)) and Marcks-tagRFP-T-plres-GCN4-MacF18. Cloning of Marcks-tagRFP-T-pIRES-GCN4-MacF18 is described previously (Yau et al. 2014). In short, the construct was subcloned into the lentiviral vector pSIN-TRE-mSEAP-hPGK-rtTA2sM2 (kind gift from Dr. Didier Trono, Ecole Polytechnique Fédérale de Lausanne, Lausanne, Switzerland) in which the PGK promotor was substituted by the neuron-specific synapsin promotor. Lentiviral particles were generated as described previously (Yau et al. 2014). Cells were transduced with lentivirus 2 hours after plating. The tetracycline-dependent expression was induced two days before imaging by supplementing the medium with 500 ng/ml doxycycline.

Antibodies

The following primary antibodies were used in this study: mouse-IgG1 anti- γ -Tubulin (1:500; T6557, Life Technologies), mouse-IgG2a anti-Centrin (1:300; 20H5, Millipore), rabbit anti-Ki67 (1:500; ab92742, Abcam), chicken anti-MAP2 (1:2000; ab5392, Abcam), rabbit anti-Trim46 (1:500; homemade, (van Beuningen et al. 2015)), mouse-IgG1 anti-Nestin (1:200; MAB5326, Millipore), mouse-IgG1 anti- α -Tubulin (1:1000; T-5168, Sigma), rabbit anti-pericentrin (1:500; 923701, BioLegend), mouse-IgG1 anti-AnkG (1:200; 33-8800, Life Technologies), mouse-IgG2b anti- β 3-Tubulin (1:400; T8660, Sigma). The following secondary antibodies were used in this study: anti-chicken Alexa 405 (ab175675, Abcam), anti-rabbit Alexa 488 (A11034, Life Technologies), anti-chicken Alexa 488 (A11039, Life

Technologies), anti-mouse Alexa 488 (A11029, Life Technologies), anti-mouse-IgG1 Alexa 488 (A21121, Life Technologies), anti-rabbit Alexa 568 (A11036, Life Technologies), anti-mouse Alexa 568 (A11031, Life Technologies), anti-mouse-IgG1 Alexa 594 (A21125, Life Technologies), anti-mouse-IgG2a Alexa 594 (A21135, Life Technologies), anti-chicken Alexa 647 (A21449, Life Technologies), anti-rabbit Alexa 647 (A21245, Life Technologies) anti-mouse Alexa 647 (A21236, Life Technologies), anti-mouse-IgG2a Alexa 647 (A21241, Life Technologies), phalloidin Alexa 647 (A22287, Life Technologies).

Immunofluorescence

For centrosomal stainings, cells were fixed for 10 min in methanol at -20°C. For all other experiments, cells were fixed for 10 min in PBS with 4% formaldehyde/4% sucrose (for neurons) or 10 min in PBS with 4% formaldehyde (for non-neuronal cells) at room temperature. After fixation, cells were washed three times with PBS. Next, fixed cells were sequentially incubated with primary and secondary antibodies diluted in gelate dilution buffer (GDB; 0.2% BSA, 0.8 M NaCl, 0.5% Triton X-100, 30 mM phosphate buffer, pH 7.4). Cells were washed three times with PBS after every antibody incubation, and coverslips were mounted using Vectashield mounting medium (Vector laboratories) with or without DAPI.

Microscopy

Confocal microscopy of fixed cells was performed on a LSM700 confocal laser-scanning microscope (Zeiss) equipped with the following objectives: 1) a Plan-Apochromat 63x NA 1.4 oil DIC; 2) a EC Plan-Neofluar 40x NA 1.3 Oil DIC; and 3) a Plan-Apochromat 20x NA 0.8 objective. Dual-color gated STED (gSTED) imaging was performed on a Leica TCS SP8 STED 3X microscope using a HC PL APO 100x/ N.A. 1.4 oil immersion STED WHITE objective. The 488, 590 and 647 nm wavelengths of pulsed white laser (80MHz) were used to excite Alexa 488-labeled γ -Tubulin, Alexa 594-labeled Centrin and Alexa647-labeled Trim46, respectively. Alexa 594 and Alexa 647 were depleted with the 775 nm pulsed depletion laser and an internal Leica HyD hybrid detector (100% gain) with a time gate of $0.3 \leq t_g \leq 6$ ns was used. Spinning-disk confocal microscopy for live-cell imaging was performed on an inverted microscope Nikon Eclipse Ti-E, which was equipped with a spinning disk-based confocal scanner unit (CSU-X1-A1, Yokogawa), an ASI motorized stage with the piezo plate MS-2000-XYZ (ASI), and the perfect focus system (Nikon). We used the following cameras: 1) a Photometric Evolve Delta 512 EMCCD camera controlled by the MetaMorph 7.8 software (Molecular Devices), or 2) a Photometric PRIME BSI sCMOS camera (version USB 3), controlled by the MetaMorph 7.10 software (Molecular Devices). We used the 491 nm 100mW Calypso (Cobolt) and 561 nm 100mW Jive (Cobolt) lasers as light sources. For imaging of GFP-tagged proteins we used an ET-GFP filter set (49002, Chroma), for imaging of proteins with tag-RFP we used an ET-mCherry filter set (49008, Chroma). For live-cell imaging with photoablation, we used an ILas system (Roper Scientific France/PICT-IBiSA, Institut Curie, currently Gataca Systems) mounted on the

Nikon Eclipse microscope described above. We used a 355 nm passively Q-switched pulsed laser (Teem Photonics) for the photoablation, together with the S Fluor 100x 0.5-1.3 NA oil objective (Nikon). To cut several microtubules simultaneously, we moved the same laser beam along the line positioned perpendicular to several microtubules. All live-cell imaging experiments were performed in full conditioned differentiation (day 5) or maintenance (days 7 and 13) medium for human iPSC-derived neuron cultures (Axol). To keep cells at 37°C with 5% CO₂ we used a stage top incubator (model INUBG2E-ZILCS, Tokai Hit).

Image quantification and analysis

Determining centrosomal γ -Tubulin levels: Centrosomal γ -Tubulin levels were quantified in stage 1 (day 0; Ki67-positive), stage 2 (day 7; MAP2-positive and axonal Trim46-negative) and stage 3 neurons (day 12; MAP2-positive and axonal Trim46-positive). Centrosomes were identified by co-localization of γ -Tubulin and Centrin. A region of interest was manually drawn around centrosomes defined by the Centrin signal, and the average γ -Tubulin immunofluorescence intensity within this region was measured and corrected for background intensities. The mean intensities of each neurodevelopmental stage were normalized to the mean intensity of stage 1 neurons.

Measuring development of neuronal differentiation: To determine the effect of Centrinone-B treatment on neuronal differentiation over time, cells were identified using DAPI staining and scored to be positive or negative for Ki67, MAP2 or β 3-Tubulin.

Quantifying growth cone morphologies: Growth cone size was measured by manually drawing a region of interest based on phalloidin signal and measuring the area in μm^2 . Growth cones were categorized as fan-like, torpedo-like or bulb-like based on shape.

Live-cell imaging

For microtubule dynamics experiments without laser severing, time-lapse acquisition was performed using the 491 nm 100 mW Calypse (200 ms exposure) and 561 nm 100 mW Jive (200 ms exposure) with 1 frame per second (fps) for 5 minutes, with a Plan Apo VC 60x NA 1.4 oil immersion objective (Nikon). 16-bit images were projected onto the EMCCD chip with intermediate lens 2.0X (Edmund Optics) at a magnification of 0.111 $\mu\text{m}/\text{pixel}$ at 60x, or onto the sCMOS chip with no intermediate lens at a magnification of 0.150 $\mu\text{m}/\text{pixel}$ at 60x. For microtubule dynamics experiments with laser severing, Time-lapse acquisition was performed using the 491 nm 100 mW Calypse (50-200 ms exposure) and 561 nm 100 mW Jive (50-200 ms exposure) with 1 fps for 3 minutes. Selected regions were subjected to photoablation between frame 30 and 31. 16-bit images were projected onto the sCMOS chip with no intermediate lens at a magnification of 0.063 $\mu\text{m}/\text{pixel}$ at 100x. For analysis of microtubule plus-end dynamics, kymographs were generated with the FIJI plugin KymoResliceWide v.0.4 (<https://github.com/ekatruxha/KymoResliceWide>), and tracing microtubule growth events were manually traced.

Electrophysiology

Before the start of each experiment, a 12 mm coverslip with Centrione-B treated or control human iPSC-derived neurons (paired cultures of 7–14 days after plating) was placed under the microscope. In the recording chamber, carbogenated (95% O₂, 5% CO₂) artificial cerebrospinal fluid (ACSF, in mM: 126 NaCl, 3 KCl, 2.5 CaCl₂, 1.3 MgCl₂, 26 NaHCO₃, 1.25 NaH₂PO₄, 20 glucose; with an osmolarity of ~310 mOsm/L) was continuously perfused at a rate of approximately 1 ml/min. An extra medium refreshment was conducted one day before recording, to prevent changes in excitability due to acute differences in extracellular osmolarity (Pasantés-Morales 1996). ACSF was warmed before entering the bath and the temperature was maintained at 30–32 °C. Recording pipettes pulled from thick-walled borosilicate glass capillaries (World Precision Instruments) had a resistance of 4–7 MΩ and were filled with internal solution (in mM: 140 K-gluconate, 4 KCl, 0.5 EGTA, 10 HEPES, 4 MgATP, 0.4 NaGTP, 4 Na₂-Phosphocreatine; with pH 7.3 and osmolarity 295 mOsm/L). To facilitate visualization of cells during the experiment and post hoc, the internal solution was supplemented with 30 μM Alexa 568 (Thermo Fisher Scientific) and biocytin, respectively. We selected individual neurons with a 60x water immersion objective (Nikon NIR Apochromat; NA 1.0) and performed whole-cell somatic patch clamp recordings. During the recordings in both voltage and current clamp, cells were kept at a holding potential of -60 mV. Recordings were acquired with an Axopatch 200B amplifier (Molecular Devices) using pClamp 10 software. Data was analyzed with Clampfit 10.7 software and custom-written MATLAB scripts.

Mass spectrometry

To obtain sample preparations for mass spectrometry (TMT labeling), biological replicates of control and Centrione-B treated human iPSC-derived neurons were harvested at three different time points (days 1, 3, and 7) of differentiation with lysis buffer (8 M urea, 50 mM ammonium bicarbonate (Sigma), EDTA-free protease inhibitor cocktail (Roche)). Lysates were sonicated on ice using Bioruptor (Diagenode) and cleared by centrifugation at 2500g for 10 minutes. Protein concentration was determined using Bradford assay. From each condition 100 μg of proteins were reduced (5 mM DTT, 55 °C, 1 hour), alkylated (10 mM Iodoacetamide, 30 minutes in the dark) and sequentially digested by LysC (Protein-enzyme ratio 1:50, 37 °C, 4 h) and trypsin (Protein-enzyme ratio 1:50, 37 °C, overnight). After overnight digestion, samples were acidified with formic acid (final concentration 3%) and resulting peptides were then desalted using Sep-Pak C18 columns (Waters). Samples were subjected to stable isotope TMT-6plex labeling according to manufacturer's instruction (Thermo Fisher Scientific). In brief, peptides were resuspended in 80 μl of 50 mM HEPES buffer, 12.5% ACN with pH 8.5 while TMT reagents were dissolved in 50 μl anhydrous ACN. For labeling, 25 μl of each dissolved TMT reagent were added to the correspondent sample according to the following scheme:

Control human iPSC sample, day 1 = TMT-126 / Centrione-B human iPSC sample, day 1 = TMT-129

Control human iPSC sample, day 3 = TMT-127 / Centrione-B human iPSC sample, day 3 = TMT-130

Control human iPSC sample, day 7 = TMT-128 / Centrinone-B human iPSC sample, day 7 = TMT-131
Following incubation at room temperature for 1 hour, the reaction was quenched using 5% hydroxylamine. Differentially TMT-labeled peptides were mixed in equal ratios and dried in a vacuum concentrator. Peptide fractionation, MS analysis, data processing, and bioinformatic analysis of the samples were performed as described before (Lindhout et al. 2020). The mass spectrometry proteomics data have been deposited to the ProteomeXchange Consortium via the PRIDE partner repository with the dataset identifier PXD020227 (Perez-Riverol et al. 2019).

Statistical analysis

All statistical analyses were performed using Prism GraphPad (version 8.0) software. Statistical tests are described in the corresponding Figure legends. P-values are annotated as follows: * $p < 0.05$, ** $p < 0.01$, *** $p < 0.001$, and ns $p \geq 0.05$.

3

REFERENCES

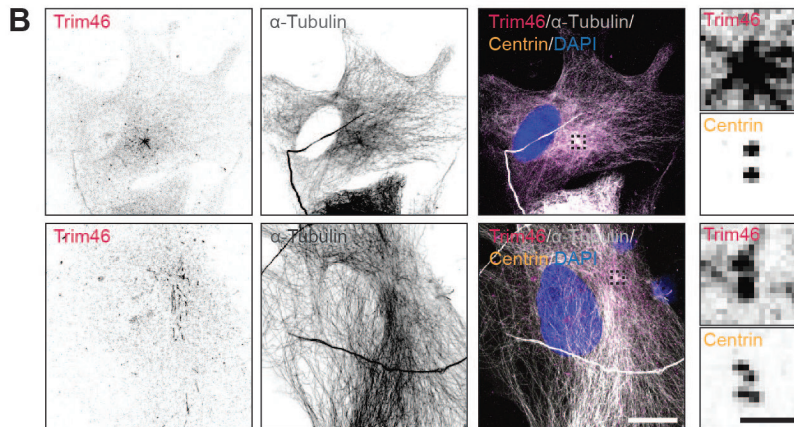
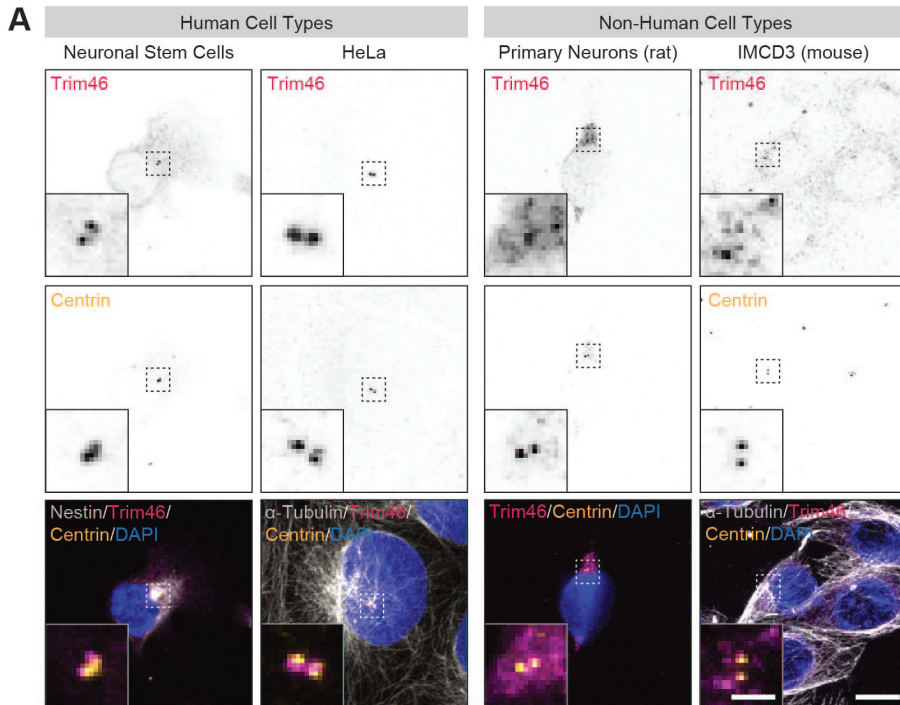
- Ahmad, F. J., H. C. Joshi, V. E. Centonze, and P. W. Baas. 1994. 'Inhibition of microtubule nucleation at the neuronal centrosome compromises axon growth', *Neuron*, 12: 271-80.
- Andersen, E. F., and M. C. Halloran. 2012. 'Centrosome movements in vivo correlate with specific neurite formation downstream of LIM homeodomain transcription factor activity', *Development*, 139: 3590-9.
- Baas, P. W., J. S. Deitch, M. M. Black, and G. A. Banker. 1988. 'Polarity orientation of microtubules in hippocampal neurons: uniformity in the axon and nonuniformity in the dendrite', *Proc Natl Acad Sci U S A*, 85: 8335-9.
- Barnes, A. P., and F. Polleux. 2009. 'Establishment of axon-dendrite polarity in developing neurons', *Annu Rev Neurosci*, 32: 347-81.
- Basto, R., J. Lau, T. Vinogradova, A. Gardiol, C. G. Woods, A. Khodjakov, and J. W. Raff. 2006. 'Flies without centrioles', *Cell*, 125: 1375-86.
- Castellanos, E., P. Dominguez, and C. Gonzalez. 2008. 'Centrosome dysfunction in *Drosophila* neural stem cells causes tumors that are not due to genome instability', *Curr Biol*, 18: 1209-14.
- Conduit, P. T., A. Wainman, and J. W. Raff. 2015. 'Centrosome function and assembly in animal cells', *Nat Rev Mol Cell Biol*, 16: 611-24.
- de Anda, F. C., K. Meletis, X. Ge, D. Rei, and L. H. Tsai. 2010. 'Centrosome motility is essential for initial axon formation in the neocortex', *J Neurosci*, 30: 10391-406.
- de Anda, F. C., G. Pollarolo, J. S. Da Silva, P. G. Camoletto, F. Feiguin, and C. G. Dotti. 2005. 'Centrosome localization determines neuronal polarity', *Nature*, 436: 704-8.
- Dent, E. W., S. L. Gupton, and F. B. Gertler. 2011. 'The growth cone cytoskeleton in axon outgrowth and guidance', *Cold Spring Harb Perspect Biol*, 3.
- Dotti, C. G., C. A. Sullivan, and G. A. Banker. 1988. 'The establishment of polarity by hippocampal neurons in culture', *J Neurosci*, 8: 1454-68.
- Espuny-Camacho, I., K. A. Michelsen, D. Gall, D. Linaro, A. Hasche, J. Bonnefont, C. Bali, D. Orduz, A. Bilheu, A. Herpoel, N. Lambert, N. Gaspard, S. Peron, S. N. Schiffmann, M. Giugliano, A. Gaillard, and P. Vanderhaeghen. 2013. 'Pyramidal neurons derived from human pluripotent stem cells integrate efficiently into mouse brain circuits in vivo', *Neuron*, 77: 440-56.
- Farina, F., J. Gaillard, C. Guerin, Y. Coute, J. Sillibourne, L. Blanchoin, and M. They. 2016. 'The centrosome is an actin-organizing centre', *Nat Cell Biol*, 18: 65-75.
- Freal, A., D. Rai, R. P. Tas, X. Pan, E. A. Katrukha, D. van de Willige, R. Stucchi, A. Aher, C. Yang, A. F. M. Altelaar, K. Vocking, J. A. Post, M. Harterink, L. C. Kapitein, A. Akhmanova, and C. C. Hoogenraad. 2019. 'Feedback-Driven Assembly of the Axon Initial Segment', *Neuron*, 104: 305-21.e8.
- Ishikawa, H., and W. F. Marshall. 2011. 'Ciliogenesis: building the cell's antenna', *Nat Rev Mol Cell Biol*, 12: 222-34.
- Johnson, M. B., X. Sun, A. Kodani, R. Borges-Monroy, K. M. Girsakis, S. C. Ryu, P. P. Wang, K. Patel, D. M. Gonzalez, Y. M. Woo, Z. Yan, B. Liang, R. S. Smith, M. Chatterjee, D. Coman, X. Papademetris, L. H. Staib, F. Hyder, J. B. Mandeville, P. E. Grant, K. Im, H. Kwak, J. F. Engelhardt, C. A. Walsh, and B. I. Bae. 2018. 'Aspm knockout ferret reveals an evolutionary mechanism governing cerebral cortical size', *Nature*, 556: 370-75.

- Kole, M. H., S. U. Ilschner, B. M. Kampa, S. R. Williams, P. C. Ruben, and G. J. Stuart. 2008. 'Action potential generation requires a high sodium channel density in the axon initial segment', *Nat Neurosci*, 11: 178-86.
- Kuijpers, M., D. van de Willige, A. Freal, A. Chazeau, M. A. Franker, J. Hofenk, R. J. Rodrigues, L. C. Kapitein, A. Akhmanova, D. Jaarsma, and C. C. Hoogenraad. 2016. 'Dynein Regulator NDEL1 Controls Polarized Cargo Transport at the Axon Initial Segment', *Neuron*, 89: 461-71.
- Lancaster, M. A., M. Renner, C. A. Martin, D. Wenzel, L. S. Bicknell, M. E. Hurles, T. Homfray, J. M. Penninger, A. P. Jackson, and J. A. Knoblich. 2013. 'Cerebral organoids model human brain development and microcephaly', *Nature*, 501: 373-9.
- Leterrier, C. 2018. 'The Axon Initial Segment: An Updated Viewpoint', *J Neurosci*, 38: 2135-45.
- Linaro, D., B. Vermaercke, R. Iwata, A. Ramaswamy, B. Libe-Philippot, L. Boubakar, B. A. Davis, K. Wierda, K. Davie, S. Poovathingal, P. A. Penttila, A. Bilheu, L. De Bruyne, D. Gall, K. K. Conzelmann, V. Bonin, and P. Vanderhaeghen. 2019. 'Xenotransplanted Human Cortical Neurons Reveal Species-Specific Development and Functional Integration into Mouse Visual Circuits', *Neuron*, 104: 972-86.e6.
- Lindhout, F. W., Y. Cao, J. T. Kevenaar, A. Bodzeta, R. Stucchi, M. M. Boumpoutsari, E. A. Katrukha, M. Altelaar, H. D. MacGillavry, and C. C. Hoogenraad. 2019. 'VAP-SCRN1 interaction regulates dynamic endoplasmic reticulum remodeling and presynaptic function', *Embo j*, 38: e101345.
- Lindhout, F.W., R. Kooistra, S. Portegies, L.J. Herstel, R. Stucchi, B.L. Snoek, M. Altelaar, H.D. MacGillavry, C.J. Wierenga, C.C. Hoogenraad. 2020. 'Quantitative mapping of transcriptome and proteome dynamics during polarization of human iPSC-derived neurons', *BioRxiv* doi: <https://doi.org/10.1101/2020.04.21.052498>
- Lois, C., E. J. Hong, S. Pease, E. J. Brown, and D. Baltimore. 2002. 'Germline transmission and tissue-specific expression of transgenes delivered by lentiviral vectors', *Science*, 295: 868-72.
- Martin, M., A. Veloso, J. Wu, E. A. Katrukha, and A. Akhmanova. 2018. 'Control of endothelial cell polarity and sprouting angiogenesis by non-centrosomal microtubules', *Elife*, 7.
- Meka, D. P., R. Scharrenberg, and F. Calderon de Anda. 2020. 'Emerging roles of the centrosome in neuronal development', *Cytoskeleton (Hoboken)*.
- Meka, D. P., R. Scharrenberg, B. Zhao, O. Kobler, T. König, I. Schaefer, B. Schwanke, S. Klykov, M. Richter, D. Eggert, S. Windhorst, C. G. Dotti, M. R. Kreutz, M. Mikhaylova, and F. Calderon de Anda. 2019. 'Radial somatic F-actin organization affects growth cone dynamics during early neuronal development', *EMBO Rep*, 20: e47743.
- Mennella, V., B. Keszthelyi, K. L. McDonald, B. Chhun, F. Kan, G. C. Rogers, B. Huang, and D. A. Agard. 2012. 'Subdiffraction-resolution fluorescence microscopy reveals a domain of the centrosome critical for pericentriolar material organization', *Nat Cell Biol*, 14: 1159-68.
- Moritz, M., M. B. Braunfeld, V. Guenebaut, J. Heuser, and D. A. Agard. 2000. 'Structure of the gamma-tubulin ring complex: a template for microtubule nucleation', *Nat Cell Biol*, 2: 365-70.
- Nano, M., and R. Basto. 2017. 'Consequences of Centrosome Dysfunction During Brain Development', *Adv Exp Med Biol*, 1002: 19-45.
- Otani, T., M. C. Marchetto, F. H. Gage, B. D. Simons, and F. J. Livesey. 2016. '2D and 3D Stem Cell

Models of Primate Cortical Development Identify Species-Specific Differences in Progenitor Behavior Contributing to Brain Size', *Cell Stem Cell*, 18: 467-80.

- Pasantés-Morales, H. 1996. 'Volume regulation in brain cells: cellular and molecular mechanisms', *Metab Brain Dis*, 11: 187-204.
- Perez-Riverol, Y., A. Csordas, J. Bai, M. Bernal-Llinares, S. Hewapathirana, D. J. Kundu, A. Inuganti, J. Griss, G. Mayer, M. Eisenacher, E. Pérez, J. Uszkoreit, J. Pfeuffer, T. Sachsenberg, S. Yilmaz, S. Tiwary, J. Cox, E. Audain, M. Walzer, A. F. Jarnuczak, T. Ternent, A. Brazma, and J. A. Vizcaíno. 2019. 'The PRIDE database and related tools and resources in 2019: improving support for quantification data', *Nucleic Acids Res*, 47: D442-d50.
- Pulvers, J. N., J. Bryk, J. L. Fish, M. Wilsch-Brauninger, Y. Arai, D. Schreier, R. Naumann, J. Helppi, B. Habermann, J. Vogt, R. Nitsch, A. Toth, W. Enard, S. Paabo, and W. B. Huttner. 2010. 'Mutations in mouse *Aspm* (abnormal spindle-like microcephaly associated) cause not only microcephaly but also major defects in the germline', *Proc Natl Acad Sci U S A*, 107: 16595-600.
- Pulvers, J. N., J. Bryk, J. L. Fish, M. Wilsch-Bräuninger, Y. Arai, D. Schreier, R. Naumann, J. Helppi, B. Habermann, J. Vogt, R. Nitsch, A. Tóth, W. Enard, S. Pääbo, and W. B. Huttner. 2010. 'Mutations in mouse *Aspm* (abnormal spindle-like microcephaly associated) cause not only microcephaly but also major defects in the germline', *Proc Natl Acad Sci U S A*, 107: 16595-600.
- Shi, Y., P. Kirwan, and F. J. Livesey. 2012. 'Directed differentiation of human pluripotent stem cells to cerebral cortex neurons and neural networks', *Nat Protoc*, 7: 1836-46.
- Sousa, A. M. M., K. A. Meyer, G. Santpere, F. O. Gulden, and N. Sestan. 2017. 'Evolution of the Human Nervous System Function, Structure, and Development', *Cell*, 170: 226-47.
- Stiess, M., N. Maghelli, L. C. Kapitein, S. Gomis-Ruth, M. Wilsch-Brauninger, C. C. Hoogenraad, I. M. Tollic-Norrelykke, and F. Bradke. 2010. 'Axon extension occurs independently of centrosomal microtubule nucleation', *Science*, 327: 704-7.
- Stoeckli, E. T. 2018. 'Understanding axon guidance: are we nearly there yet?', *Development*, 145.
- Tsai, L. H., and J. G. Gleeson. 2005. 'Nucleokinesis in neuronal migration', *Neuron*, 46: 383-8.
- van Beuningen, S. F. B., L. Will, M. Harterink, A. Chazeau, E. Y. van Battum, C. P. Frias, M. A. M. Franker, E. A. Katrukha, R. Stucchi, K. Vocking, A. T. Antunes, L. Slenders, S. Doukeridou, P. Sillevius Smitt, A. F. M. Altelaar, J. A. Post, A. Akhmanova, R. J. Pasterkamp, L. C. Kapitein, E. de Graaff, and C. C. Hoogenraad. 2015. 'TRIM46 Controls Neuronal Polarity and Axon Specification by Driving the Formation of Parallel Microtubule Arrays', *Neuron*, 88: 1208-26.
- van Beuningen, S. F., and C. C. Hoogenraad. 2016. 'Neuronal polarity: remodeling microtubule organization', *Curr Opin Neurobiol*, 39: 1-7.
- van der Vaart, B., W. E. van Riel, H. Doodhi, J. T. Kevenaer, E. A. Katrukha, L. Gumy, B. P. Bouchet, I. Grigoriev, S. A. Spangler, K. L. Yu, P. S. Wulf, J. Wu, G. Lansbergen, E. Y. van Battum, R. J. Pasterkamp, Y. Mimori-Kiyosue, J. Demmers, N. Olieric, I. V. Maly, C. C. Hoogenraad, and A. Akhmanova. 2013. 'CFEOM1-associated kinesin KIF21A is a cortical microtubule growth inhibitor', *Dev Cell*, 27: 145-60.
- Vora, S. M., and B. T. Phillips. 2016. 'The benefits of local depletion: The centrosome as a scaffold for ubiquitin-proteasome-mediated degradation', *Cell Cycle*, 15: 2124-34.

- Witte, H., D. Neukirchen, and F. Bradke. 2008. 'Microtubule stabilization specifies initial neuronal polarization', *J Cell Biol*, 180: 619-32.
- Wong, Y. L., J. V. Anzola, R. L. Davis, M. Yoon, A. Motamedi, A. Kroll, C. P. Seo, J. E. Hsia, S. K. Kim, J. W. Mitchell, B. J. Mitchell, A. Desai, T. C. Gahman, A. K. Shiau, and K. Oegema. 2015. 'Cell biology. Reversible centriole depletion with an inhibitor of Polo-like kinase 4', *Science*, 348: 1155-60.
- Yau, K. W., P. Schatzle, E. Tortosa, S. Pages, A. Holtmaat, L. C. Kapitein, and C. C. Hoogenraad. 2016. 'Dendrites In vitro and In vivo Contain Microtubules of Opposite Polarity and Axon Formation Correlates with Uniform Plus-End-Out Microtubule Orientation', *J Neurosci*, 36: 1071-85.
- Yau, K. W., S. F. van Beuningen, I. Cunha-Ferreira, B. M. Cloin, E. Y. van Battum, L. Will, P. Schatzle, R. P. Tas, J. van Krugten, E. A. Katrukha, K. Jiang, P. S. Wulf, M. Mikhaylova, M. Harterink, R. J. Pasterkamp, A. Akhmanova, L. C. Kapitein, and C. C. Hoogenraad. 2014. 'Microtubule minus-end binding protein CAMSAP2 controls axon specification and dendrite development', *Neuron*, 82: 1058-73.
- Zhao, B., D. P. Meka, R. Scharrenberg, T. König, B. Schwanke, O. Kobler, S. Windhorst, M. R. Kreutz, M. Mikhaylova, and F. Calderon de Anda. 2017. 'Microtubules Modulate F-actin Dynamics during Neuronal Polarization', *Sci Rep*, 7: 9583.
- Zmuda, J. F., and R. J. Rivas. 1998. 'The Golgi apparatus and the centrosome are localized to the sites of newly emerging axons in cerebellar granule neurons in vitro', *Cell Motil Cytoskeleton*, 41: 18-38.

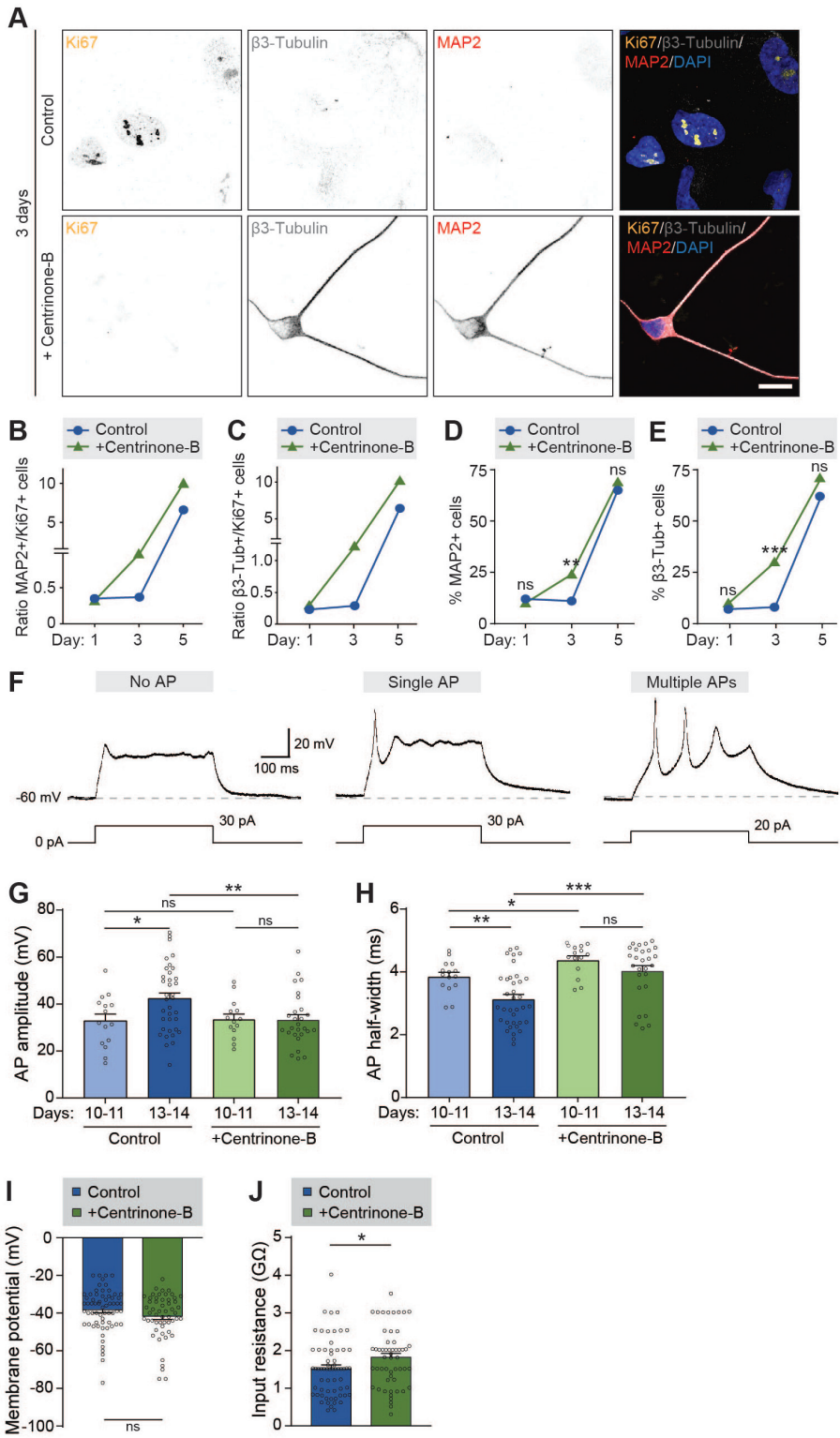


Supplementary Figure 1.

Centrosomes display MTOC function and local Trim46 appearance during axon specification

A. Typical examples of human iPSC-derived NSCs (day 0), HeLa cells, primary dissociated rat neurons (day 0) and mouse IMCD3 cells immunostained for Trim46 and Centrin, and co-immunostained with Nestin or α -Tubulin if indicated. Inserts represent centrosomes. Scale bars: 10 μ m in overview, 2 μ m in inserts.

B. Typical examples of mature human iPSC-derived glia cells (day 17) immunostained for Trim46, Centrin and α -Tubulin. Zooms represent centrosomes. Scale bars: 20 μ m in overview, 1 μ m in zooms

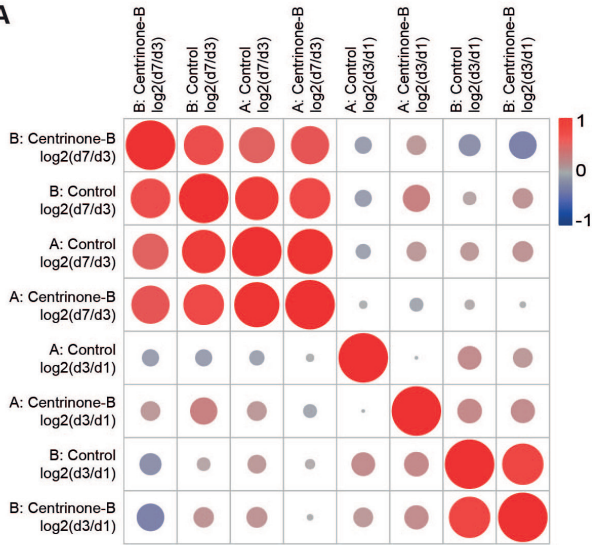


Supplementary Figure 2.

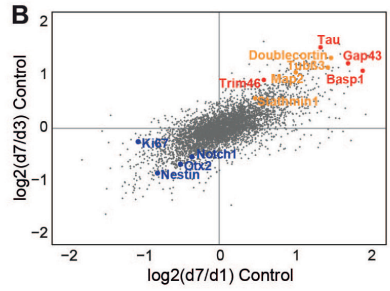
Centriole loss perturbs axonal Trim46 targeting and action potential maturation

- A.** Typical examples of human iPSC-derived NSCs/neurons (day 3) with 0 (control) or 3 days Centrinone-B treatment, and immunostained for Ki67, β 3-Tubulin and MAP2. Scale bar: 15 μ m in overview.
- B.** Quantifications of the ratio MAP2-positive/Ki67-positive Centrinone-B treated or control human iPSC-derived NSCs/neurons at day 1, 3 and 5. N=2, n=54-110 cells.
- C.** Quantifications of the ratio β 3-Tubulin-positive/Ki67-positive Centrinone-B treated or control human iPSC-derived NSCs/neurons at day 1, 3 and 5. N=2, n=49-104 cells.
- D.** Quantifications of the percentage of MAP2-positive Centrinone-B treated or control human iPSC-derived neurons at day 1, 3 and 5. N=2, n=121-165 cells.
- E.** Quantifications of the percentage β 3-Tubulin-positive Centrinone-B treated or control human iPSC-derived neurons at day 1, 3 and 5. N=2, n=121-165 cells.
- F.** Representative examples of evoked AP firing in Centrinone-B treated human iPSC-derived neurons recorded at day 11. Shown is the response to a single depolarizing current step of a neuron that fires no APs, a neuron that fires a single AP and a neuron that fires multiple APs. The offset current (I_{hold}) was adjusted to keep the baseline membrane potential at approximately -60 mV (dashed lines).
- G.** AP amplitude recorded in Centrinone-B treated and control human iPSC-derived neurons of 10-11 days (control: n=15 cells, +Centrinone-B: n=14 cells) and 13-14 days (control: n=36 cells, +Centrinone-B: n=27 cells).
- H.** AP half-width recorded in Centrinone-B treated and control human iPSC-derived neurons of 10-11 days (control: n=15 cells, +Centrinone-B: n=14 cells) and 13-14 days (control: n=36 cells, +Centrinone-B: n=27 cells).
- I.** Resting membrane potential of Centrinone-B treated (n=54 cells) and control (n=64 cells) human iPSC-derived neurons.
- J.** Input resistant of Centrinone-B treated (n=54 cells) and control (n=63 cells) human iPSC-derived neurons.
- Data information: Data represent mean \pm SEM. Chi-square-test including post-hoc analysis with Bonferroni correction (**D**, **E**); Student's t test (**F**, **G**: control 10-11 vs 13-14 days); Mann Whitney test (**G**: control vs Centrinone-B, **I**). *** $p < 0.001$, ** $p < 0.01$, * $p < 0.05$, ns $p > 0.05$

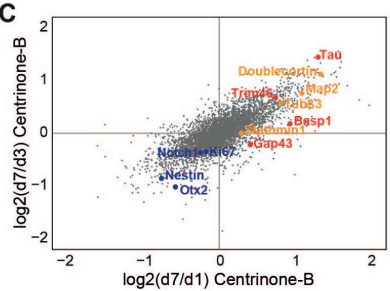
A



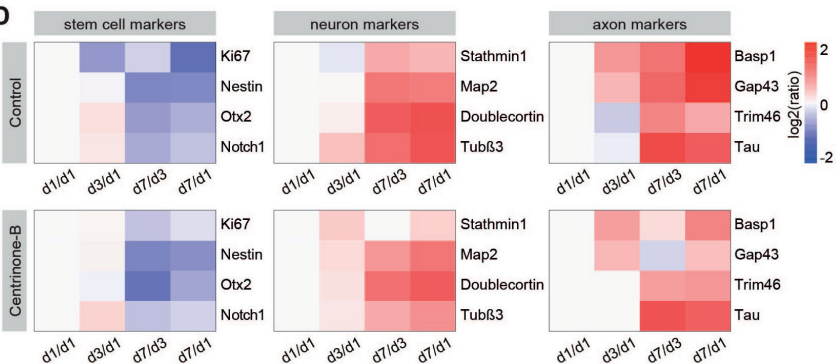
B



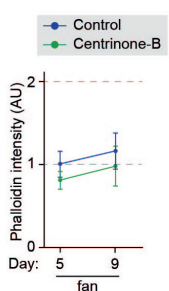
C



D



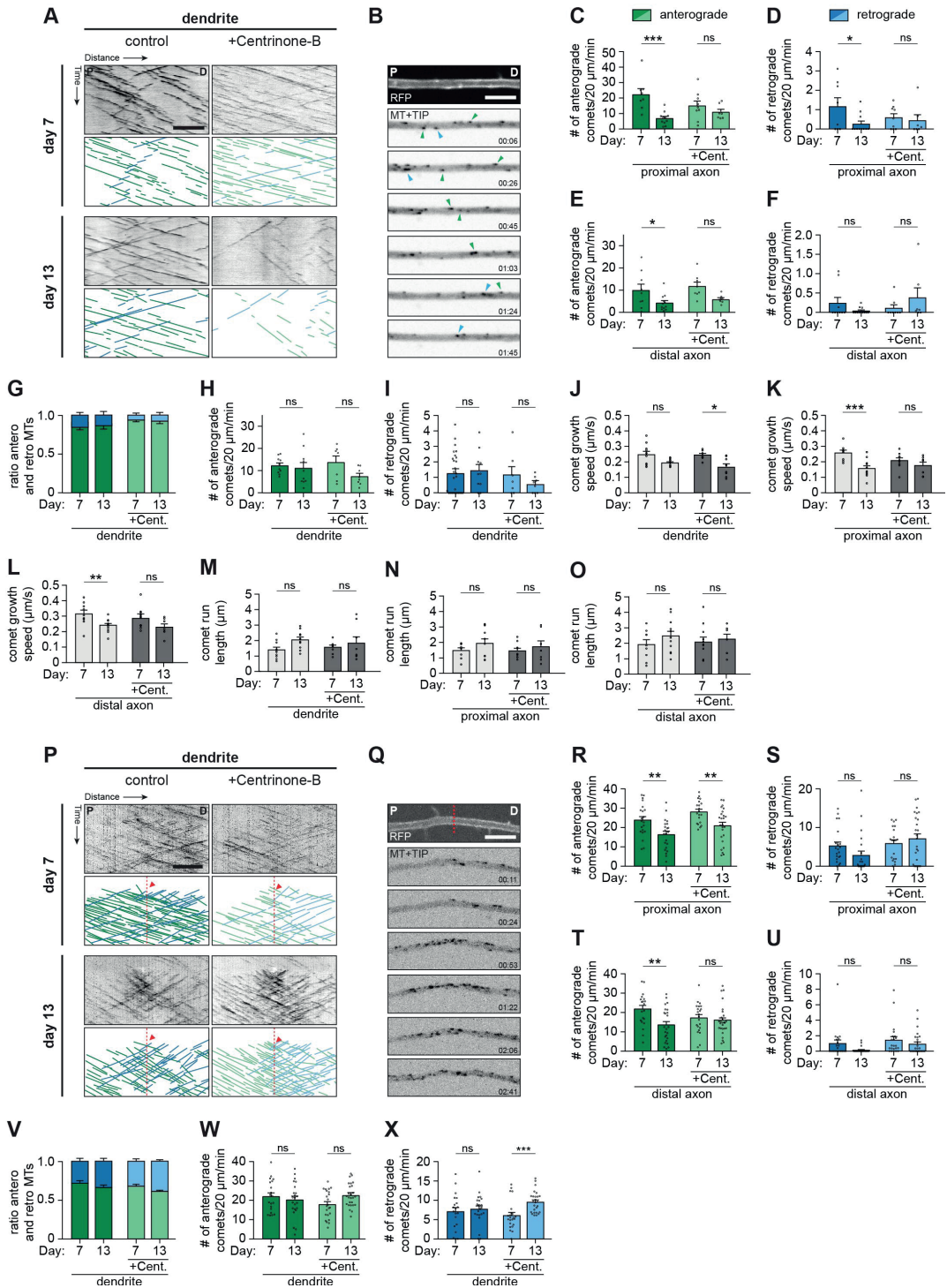
E



Supplementary Figure 3.

Developmental proteome dynamics upon centriole loss

- A.** Correlative matrix of biological replicas of control neurons or Centrinone-B (Cent-B) treated neurons used for proteome analysis.
 - B.** Correlative analysis of relative protein expression in control neurons at day 7 to day 3 and day 1. Specific stem cell markers (blue), neuron markers (yellow), and axon markers (red) are highlighted.
 - C.** Correlative analysis of relative protein expression in Centrinone-B treated neurons at day 7 to day 3 and day 1. Specific stem cell markers (blue), neuron markers (yellow), and axon markers (red) are highlighted.
 - D.** Relative protein expression over time for stem cell proteins, neuron proteins, and axon proteins.
 - E.** Quantification of the total phalloidin intensity in a fan-like growth cone at day 5 and day 9.
- Data information: Data represent mean \pm SEM.



Supplementary Figure 4.

Centriole loss restrains microtubule remodeling during early axon development

A. Kymographs and schematic representations of time-lapse recordings of dendrites, for different time points (day 7; day 13) and conditions (control; Centrinone-B). Scale bars, 5 μ m.

B. Example stills from a spinning-disk time-lapse recording of a neurite transfected with mRFP and GFP-MT+TIP. The top panel is a still of a neurite in mRFP, showing neurite morphology. The other panels show moving GFP-MT+TIP comets pointing in either an anterograde direction (green arrowheads) or retrograde direction (blue arrowheads). P indicates the proximal direction and D the distal direction of the neurite. Timestamp in minutes:seconds given on bottom right. Scale bars, 5 μ m.

C. Quantifications of the number of comets per minute pointing in the anterograde direction in the proximal axon. N= 3, n= 7-11 cells.

D. Quantifications of the number of comets per minute pointing in the retrograde direction in the proximal axon. N= 3, n= 7-11 cells.

E. Quantifications of the number of comets per minute pointing in the anterograde direction in the distal axon. N= 3, n= 8-12 cells.

F. Quantifications of the number of comets per minute pointing in the retrograde direction in the distal axon. N= 3, n= 8-12 cells.

G. Quantifications of the ratios of comets pointing in anterograde (green) or retrograde (blue) direction in the dendrite. N=3, n=7-10 cells.

H. Quantifications of the number of comets per minute pointing in the anterograde direction in the dendrite. N=3, n=7-10 cells.

I. Quantifications of the number of comets per minute pointing in the retrograde direction in the dendrite. N=3, n=7-10 cells.

J-L. Quantifications of the growth speed of comets in the dendrite (**J**), proximal axon (**K**), and distal axon (**L**). N=3 , n=9-2406 traces in 7-10 cells.

M-O. Quantifications of the distance of run length of comets in the dendrite (**M**), proximal axon (**N**), and distal axon (**O**). N=3 , n=n=9-2406 traces in 7-10 cells.

P. Kymographs and schematic representations of time-lapse recordings of laser severing (LS) experiments of dendrites, for different time points (day 7; day 13) and conditions (control; centrinone-B). Red line and red arrowhead denote location and time of LS. Scale bars, 5 μ m.

Q. Example stills from a spinning-disk time-lapse recording of a neurite transfected with mRFP and GFP-MT+TIP. Red line denotes the location of LS. Scale bars, 5 μ m.

R. Quantifications of the number of comets per minute pointing in the anterograde direction in the proximal axon following LS. N=3 , n=19-30 cells.

S. Quantifications of the number of comets per minute pointing in the retrograde direction in the proximal axon following LS. N=3 , n=19-30 cells.

T. Quantifications of the number of comets per minute pointing in the anterograde direction in the distal axon. N=3 , n=19-30 cells.

U. Quantifications of the number of comets per minute pointing in the retrograde direction in the distal axon. N=3 , n=19-30 cells.

V. Quantifications of the ratios of comets pointing in anterograde (green) or retrograde (blue) direction in the dendrite following LS. N=3, n=19-30 cells.

W. Quantifications of the number of comets per minute pointing in the anterograde direction in the dendrite following LS. N=3, n=19-30 cells.

X. Quantifications of the number of comets per minute pointing in the retrograde direction in the dendrite following LS. N=3, n=19-30 cells.

Data information: Data represent mean \pm SEM. One-way ANOVA including Sidak's post-hoc analysis (**C-F,H-O,R-U,W,X**), *** $p < 0.001$, ** $p < 0.005$, * $p < 0.05$, ns $p \geq 0.05$

4.



VAP–SCRN1 interaction regulates dynamic endoplasmic reticulum remodeling and presynaptic function

Feline W. Lindhout¹, Yujie Cao^{1*}, Josta T Kevenaar^{1*}, Anna Bodzezata^{1*}, Riccardo Stucchi^{1,2}, Maria M Boumpoutsari¹, Eugene A Katrukha¹, Maarten Altelaar², Harold D MacGillavry¹ & Casper C Hoogenraad^{1,2,3}

¹Cell Biology, Neurobiology and Biophysics, Department of Biology, Faculty of Science, Utrecht University, 3584 CH Utrecht, The Netherlands.

²Biomolecular Mass Spectrometry and Proteomics, Bijvoet Center for Biomolecular Research and Utrecht Institute for Pharmaceutical Sciences, Utrecht University, 3584 CH Utrecht, The Netherlands.

³Department of Neuroscience, Genentech, Inc, South San Francisco, CA 94080, USA.

⁴Lead Contact

*authors contributed equally

ABSTRACT

In neurons, the continuous and dynamic endoplasmic reticulum (ER) network extends throughout the axon, and its dysfunction causes various axonopathies. However, it remains largely unknown how ER integrity and remodeling modulate presynaptic function in mammalian neurons. Here, we demonstrated that ER membrane receptors VAPA and VAPB are involved in modulating the synaptic vesicle (SV) cycle. VAP interacts with secernin-1 (SCRN1) at the ER membrane via a single FFAT-like motif. Similar to VAP, loss of SCRN1 or SCRN1-AP interactions resulted in impaired SV cycling. Consistently, SCRN1 or VAP depletion was accompanied by decreased action potential-evoked Ca^{2+} responses. Additionally, we found that VAP-SCRN1 interactions play an important role in maintaining ER continuity and dynamics, as well as presynaptic Ca^{2+} homeostasis. Based on these findings, we propose a model where the ER-ocalized VAP-SCRN1 interactions provide a novel control mechanism to tune ER remodeling and thereby modulate Ca^{2+} dynamics and SV cycling at presynaptic sites. These data provide new insights into the molecular mechanisms controlling ER structure and dynamics, and highlight the relevance of ER function for SV cycling.

INTRODUCTION

The continuous and dynamic ER network is one of the most abundant organelles in cells. In neurons, somatodendritic domains contain both rough and smooth ER, whereas axons exclusively exhibit smooth ER. The smooth ER lacks ribosomes and is not involved in translation; instead, it is important for Ca^{2+} homeostasis, lipid synthesis and delivery, and signaling. The relevance of axonal ER in particular is highlighted by various human axonopathies caused by mutations in different generic ER proteins. More specifically, dysfunction of ER-shaping proteins such as atlastin-1, reticulon-2, receptor expression-enhancing protein 1 (REEP1), and receptor expression-enhancing protein 2 (REEP2) leads to hereditary spastic paraplegia (HSP), whereas mutations in ER receptor VAMP-associated protein B (VAPB) cause amyotrophic lateral sclerosis (ALS; Hazan et al, 1999; Zhao et al, 2001; Nishimura et al, 2004; Zuchner et al, 2006; Montenegro et al, 2012; Esteves et al, 2014; Yalcin et al, 2017). Together, these pathologies hint for an increased sensitivity for proper ER structure and function in axons.

Recent ultrastructural three-dimensional analysis revealed that the ER in axons is comprised of a conserved and unique organization (Wu et al, 2017; Yalcin et al, 2017; Terasaki, 2018). The axonal ER structure consists of narrow ER tubules, which occasionally form cisternae at tubular branch points with comparably small lumen (Wu et al, 2017; Yalcin et al, 2017; Terasaki, 2018). This distinctive ER network extends throughout all axon branches with a relative constant density of only 1–2 narrow tubules per diameter, while remaining continuous with the rest of the ER network (Wu et al, 2017; Yalcin et al, 2017; Terasaki, 2018). At presynaptic terminals, the ER forms a local tubular network opposing the active zone. This presynaptic ER structure often wraps around mitochondria and is in close proximity to the

plasma membrane, and it regularly forms tight membrane contact sites with these structures (Wu et al, 2017; Yalcin et al, 2017). Moreover, fast dynamics of axonal ER was observed in *Drosophila* neurons using fluorescent recovery after photo-bleaching (FRAP) analysis, suggesting that the neuronal ER network likely undergoes dynamic remodeling (Wang et al, 2016; Yalcin et al, 2017). However, the precise role of the dynamic ER network in axons and at presynaptic sites remains poorly understood.

Emerging evidence implies that the presynaptic ER is engaged in modulating the tightly controlled Ca^{2+} -induced SV cycle (Summerville et al, 2016; De Gregorio et al, 2017; de Juan-Sanz et al, 2017). In *Drosophila* neurons, it was reported that homologues of the HSP-associated ER-shaping proteins atlastin-1 and reticulon-1 are implicated in controlling neurotransmitter release at neuromuscular junctions, as loss of these proteins resulted in a marked decrease in SV cycling (Summerville et al, 2016; De Gregorio et al, 2017). In mammalian neurons, recent reports showed that presynaptic Ca^{2+} levels in the ER are locally elevated during evoked neuronal transmission, suggesting that the presynaptic ER buffers Ca^{2+} to modulate SV cycling (de Juan-Sanz et al, 2017).

Moreover, the ER transmembrane protein VAP was originally identified as regulator of synaptic transmission in *Aplysia californica*, where it was specifically expressed in neuronal tissue (Skehel et al, 1995). Conversely, mammalian VAPA and VAPB are ubiquitously expressed in different cell types and its intracellular localization is restricted to ER membranes. VAPs act as key players in facilitating tight membrane contact sites between the ER and other intracellular membranes, which represent functional interactions through which Ca^{2+} exchange and lipid transfer occur (Muallem et al, 2017; Wu et al, 2018). VAP contains a C-terminal transmembrane domain which is inserted into the ER membrane, and a cytoplasmic N-terminal tail with a coiled-coil domain and a major sperm protein (MSP) domain. The MSP domain exhibits a FFAT(-like) binding site, which is unique for VAP proteins. Many VAP-associated proteins (> 100) with such a FFAT(-like) motif have been described (Murphy & Levine, 2016). This includes the cytoplasmic protein SCRN1, which contains a N-terminal C69 domain and a C-terminal coiled-coil domain and was predicted to have FFAT(-like) motifs (Murphy & Levi-e, 2016). The large number of FFAT-containing proteins typically localize to distinct subcellular structures, which has led to the general idea that VAP may act as a key ER receptor.

In this study, we demonstrated that ER membrane protein VAP and cytoplasmic VAP-associated protein SCRN1 are important for Ca^{2+} -driven SV cycling. We found that VAP interacts with SCRN1 at the ER membrane through a single FFAT-like motif. Decreasing these ER-localized VAP-SCRN1 interactions was accompanied by a number of phenotypes, including discontinuous ER tubules, impaired ER dynamics, elevated basal presynaptic Ca^{2+} levels, and decreased SV cycling. Together, these data point toward a model where ER remodeling, mediated by VAP-SCRN1 interactions is engaged in modulating Ca^{2+} dynamics and SV cycling at presynaptic sites.

RESULTS

ER proteins VAPA and VAPB are involved in regulating SV cycling

To determine whether the ER proteins VAPA and VAPB could be involved in modulating presynaptic function, we first mapped their subcellular localization in primary rat hippocampal neurons. Similar as reported previously in *Drosophila* neurons, we found that endogenous VAPA and VAPB appeared as punctae present along ER structures in axons which often co-localized with presynaptic marker synaptotagmin (Syt; Pennetta et al, 2002). At somatodendritic regions, endogenous VAPA and VAPB revealed a more diffuse patchy staining pattern that co-localized with expressed ER membrane protein Sec61 β (Fig 1A).

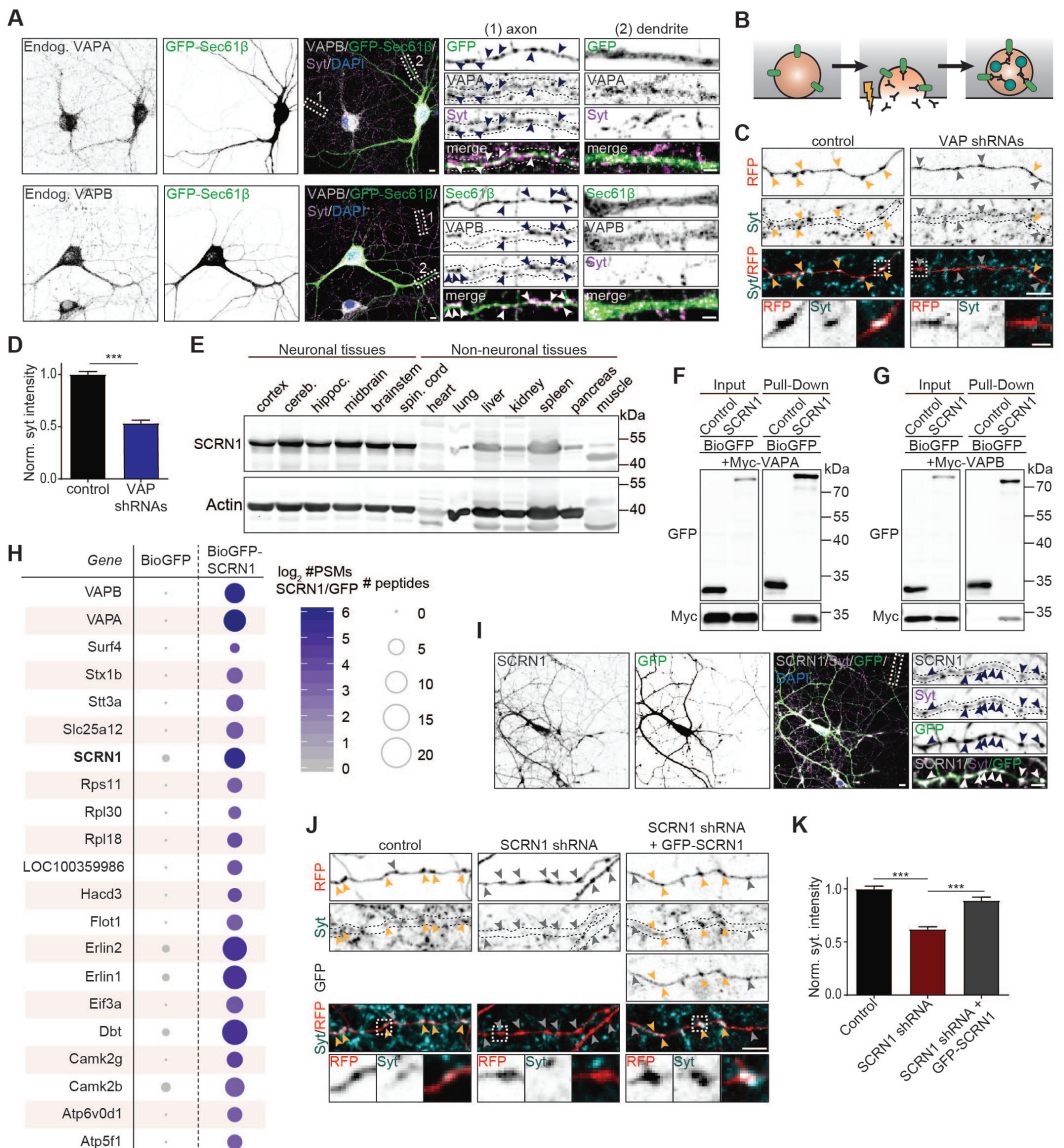


Figure 1.

VAP and VAP-associated protein SCRN1 modulate SV cycling

A. Endogenous localization of VAPA or VAPB and Syt in hippocampal neurons (DIV16) expressing GFP-Sec61 β . Zooms represent (1) an axonal structure with presynaptic boutons (arrowheads), and (2) a dendritic structure. Scale bars: 10 μ m (full size) and 5 μ m (zoom).

B. Schematic illustration of the Syt antibody uptake assay: live neurons were stimulated with bicuculline and incubated with primary Syt antibodies, and next neurons were fixed and stained with secondary antibodies.

C. Representative image of Syt antibody uptake at axons of hippocampal neurons (DIV18) co-expressing RFP and pSuper empty vector or VAPA/B shRNAs. Yellow and gray arrowheads mark presynaptic boutons with and without internalized Syt, respectively. Zooms represent typical boutons. Scale bars: 5 μ m (full size) and 2 μ m (zoom).

D. Quantifications of fluorescence intensity of internalized endogenous Syt at single presynaptic boutons of hippocampal neurons (DIV18) co-expressing RFP and pSuper empty vector or VAPA/B shRNAs. N = 2, n = 288–541 boutons.

E. Western blot of endogenous SCRN1 expression in indicated adult rat neuronal and non-neuronal tissues. Cereb., cerebellum. Hippoc., hippocampus. Spin., spinal.

F. Pull-down assay of HEK293T cells co-expressing Myc-VAPA with BioGFP or BioGFP-SCRN1.

G. Pull-down assay of HEK293T cells co-expressing Myc-VAPB with BioGFP or BioGFP-SCRN1.

H. Scaled representation of SCRN1-associated proteins identified with pull-down assay followed by mass spectrometry analysis of purified BioGFP or BioGFP-SCRN1 from HEK293T cell lysates with adult rat brain extracts. All candidates showed > 10 enrichment of PSM compared to control.

I. Endogenous localization of SCRN1 and Syt in cortical neurons (DIV18) expressing GFP. Zoom represents an axon structure with presynaptic boutons (arrowheads). Scale bars: 10 μ m (full size) and 5 μ m (zoom).

J. Representative image of Syt antibody uptake at axons of hippocampal neurons (DIV18) co-expressing RFP and pSuper empty vector, SCRN1 shRNA, or SCRN1 shRNA with GFP-SCRN1. Yellow and gray arrowheads mark presynaptic boutons with and without internalized Syt, respectively. Zooms represent typical boutons. Scale bars: 5 μ m (full size) and 2 μ m (zoom).

K. Quantifications of fluorescence intensity of internalized endogenous Syt at single presynaptic boutons of hippocampal neurons (DIV18) co-expressing RFP and pSuper empty vector, SCRN1 shRNA alone, or SCRN1 shRNA with GFP-SCRN1. N = 2, n = 201–300 boutons.

Data information: Data represent mean \pm SEM; ***P < 0.001, by Mann–Whitney U-test. Source data are available online for this Figure.

Exogenous HA-VAPA and HA-VAPB were observed at ER structures throughout neurons and also partially co-localized with presynaptic boutons (Fig S1A). Thus, VAP is abundantly present at ER structures throughout the cell including at presynaptic sites. To test whether VAP could be engaged in regulating synaptic functions, we next investigated whether VAPA and VAPB are engaged in modulating the SV cycle. This was addressed using the Syt antibody uptake assay, which provides a quantifiable read-out of exo- and endocytosis

recognizing the luminal side of SV membrane protein Syt, while neurons were briefly stimulated by bicuculline. Subsequently, neurons were fixed and the fluorescence intensity of internalized Syt at individual presynaptic boutons was measured. VAP was depleted from neurons by expressing shRNAs targeting VAPA and VAPB, which we have validated in the previous studies (Teuling et al, 2007; Kuijpers et al, 2013). Co-depletion of VAPA and VAPB showed a marked decrease (~ 50%) in Syt internalization compared to control cells (Fig 1C,D). In addition, VAPA and VAPB knockdown resulted in a slight decrease in bouton size and bouton density (Fig 1C, S1B,C). In summary, we observed that loss of function of ER proteins VAPA and VAPB was accompanied by decreased SV cycling and defects in bouton maintenance.

VAPA and VAPB associate with brain-enriched SCRIN1 proteins

VAPs function as ER receptors for a large number of VAP-associated proteins containing a FFAT or FFAT-like motif (Murphy & Levine, 2016). To gain more insight into the underlying mechanism of VAP at presynaptic sites, we sought to identify the VAP interactor(s) that could be involved in controlling this function. In a recent study, many new VAP-associated proteins were identified by pull-down and mass spectrometry analysis, including the cytoplasmic protein SCRIN1 (Murphy & Levine, 2016). Western blot analysis of lysates from different rat tissues using two different antibodies revealed that SCRIN1 is abundantly enriched in brain tissues (Fig 1E, S1D). This is consistent with the reported enriched expression of SCRIN1 in the brain as described in various online expression databases (Protein Atlas, Expression Atlas, Alan Brain Atlas). We confirmed the association between VAP and SCRIN1 with various biochemical assays. First, we conducted a pull-down experiment on lysates of HEK293T cells co-expressing biotinylated GFP (BioGFP) or GFP-SCRIN1 (BioGFP-SCRIN1) and Myc-VAPA or Myc-VAPB. Both Myc-VAPA and Myc-VAPB efficiently co-precipitated with BioGFP-SCRIN1 (Fig 1F, G). Next, we examined the SCRIN1 interactome using a more unbiased approach and performed BioGFP-SCRIN1 pull-downs followed by mass spectrometry analysis using HEK293T cell lysates and adult rat brain extracts. The associations between SCRIN1 and the VAPs were identified in both HEK293T lysates and brain extracts (Fig 1H, S1E). Of all potential SCRIN1-interacting proteins, both VAPA and VAPB showed the highest peptide-spectrum match (PSM) values in both datasets. Together, these biochemical data indicated that VAPs are associated with SCRIN1.

VAP-associated protein SCRIN1 is involved in modulating SV cycling

We next tested whether SCRIN1 was present at presynaptic sites and if this protein could be engaged in modulating SV cycling. Similar to VAP, immunostaining for endogenous SCRIN1 revealed a punctate pattern throughout the neuron and regularly co-localized with presynaptic marker Syt (Fig 1I). Exogenous GFP-SCRIN1 showed a diffuse cytoplasmic signal, which also co-localized with presynaptic boutons (Fig S1F). To conduct loss-of-function experiments, we next generated and validated three shRNA targeting SCRIN1 and continued our depletion experiments with a single shRNA (Fig S1G–J). We tested the role of

SCRN1 in SV cycling by conducting the Syt uptake assay in neurons depleted from SCRN1. SCRN1 knockdown also showed a marked decrease (~40%) in relative Syt internalization compared to control cells, thereby phenocopying the effect of VAP knockdown (Fig 1J,K). The presynaptic phenotype in SCRN1 knockdown neurons was rescued by expressing wild-type GFP-SCRN1 (Fig 1J, K). Together, these results illustrate that SCRN1 depletion, similarly to VAP depletion, results in impaired SV cycling.

SCRN1 does not exhibit autolytic protease activity

To better understand the molecular function of VAP-associated protein SCRN1, we next tested whether its conserved proteolytic domain could be involved. Like all SCRN family members, SCRN1 contains a C69 protease domain and therefore belongs to the N-terminal nucleophile (Ntn) aminohydrolases superfamily (Pei & Grishin, 2003). Proteolytic activity in this superfamily relies on autolytic cleavage of the auto-inhibitory N-terminal of the precursor protein by the mature protein (Fig S2A). This cleavage occurs right before the catalytic site of the protein, which is a cysteine residue in the SCRN family. Sequence alignment of the SCRN proteins revealed that the position of the predicted catalytic cysteine including the flanking residues is shared in SCRN2 and SCRN3, but not in SCRN1 (Fig S2B). We analyzed N-terminal SCRN cleavage by conducting Western blotting of lysates from HEK293T cells expressing wild-type GFP-SCRN1, GFP-SCRN2, or GFP-SCRN3 (Fig S2C). In lysates of GFP-SCRN2 and GFP-SCRN3 expressing cells, we identified a low molecular weight band corresponding to the predicted size of GFP fused to the N-terminal cleavage product. Conversely, this cleavage product was not observed in lysates of GFP-SCRN1 expressing cells. Moreover, mutant SCRN1, SCRN2, and SCRN3 constructs in which the predicted catalytic cysteine was replaced by a non-catalytic alanine residue also did not show a cleavage product (Fig S2C). These data suggest that SCRN1, unlike its family members SCRN2 and SCRN3, does not exhibit autolytic protease activity.

SCRN1 is recruited to VAP at the ER membrane

To further examine the function of VAP-associated protein SCRN1, we next assessed whether the subcellular localization of SCRN1 could be controlled by VAP. This was addressed by conducting co-expression experiments of GFP-SCRN1 and HA-VAPA or HA-VAPB in cultured neurons and COS7 cells. In COS7 cells, the ER structures are relatively less compact and easier to visualize than in neurons. GFP-SCRN1 expression alone in neurons or COS7 cells showed a diffuse cytoplasmic distribution, which only partly coincided with ER structures (Fig 2A and B). In neurons, co-expression of GFP-SCRN1 with either HA-VAPA or HA-VAPB resulted in the formation of dense VAP/SCRN1-positive clusters at neurites (Fig 2C). COS7 cells co-expressing GFP-SCRN1 and HA-VAPA or HA-VAPB showed marked differences in SCRN1 localization, as it induced abundant SCRN1 recruitment to VAP at the ER membrane (Fig 2D) This observation suggests that enhancing the number of VAPs at the ER membrane allows for increased SCRN1 binding, presumably because it decreases the competition with other FFAT(-

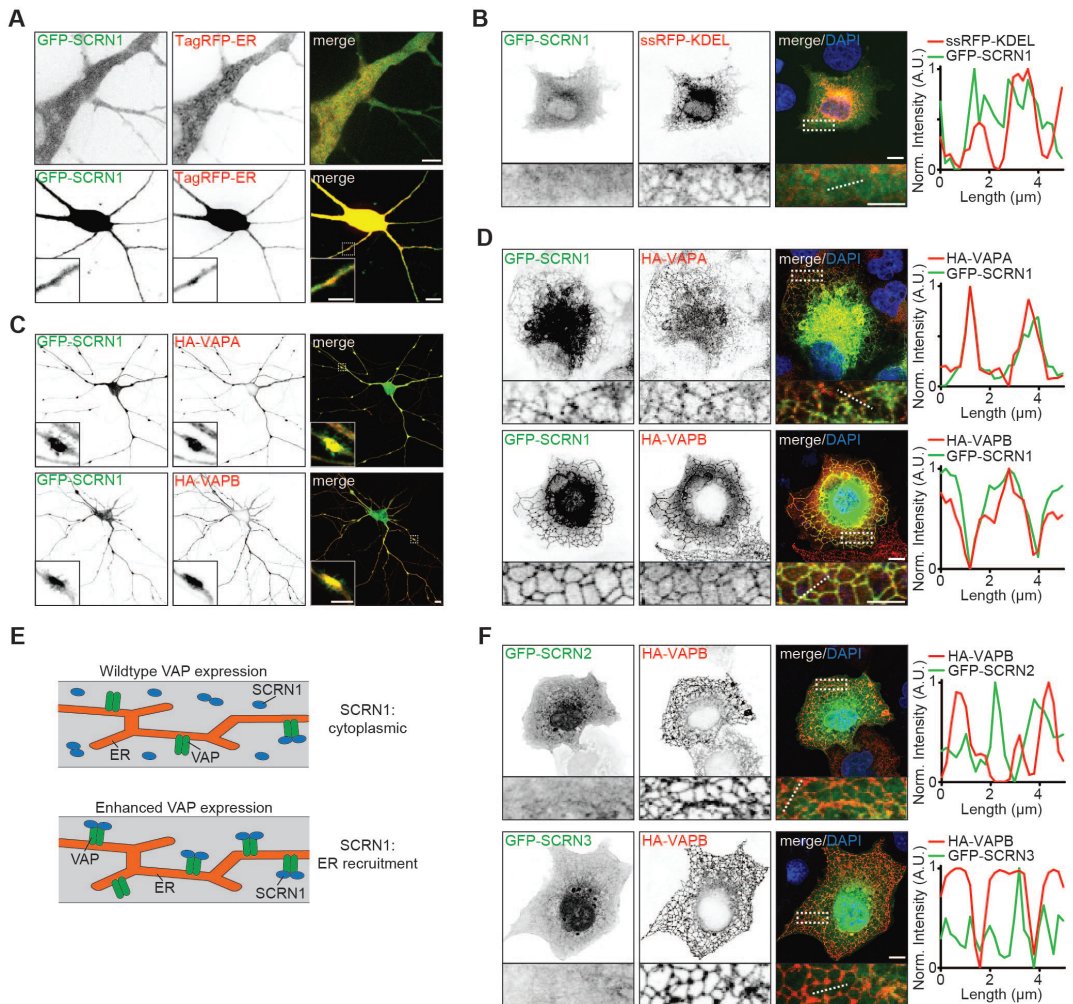


Figure 2.
SCR1 is recruited to VAP at the ER membrane

A. Localization of GFP-SCR1 and TagRFP-ER in hippocampal neurons (DIV16–18). Scale bars: 10 μm (bottom panel, full size) and 5 μm (top panel; bottom panel, zoom).

B. Localization of GFP-SCR1 and ssRFP-KDEL in COS7 cells with normalized intensity plot of indicated line (dotted). Scale bars: 10 μm (full size) and 5 μm (zoom).

C. Hippocampal neurons (DIV16) co-expressing GFP-SCR1 with HA-VAPA or HA-VAPB. Scale bars: 10 μm (full size) and 5 μm (zoom).

D. COS7 cells co-expressing GFP-SCR1 with HA-VAPA or HA-VAPB with normalized intensity plot of indicated line (dotted). Scale bars: 10 μm (full size) and 5 μm (zoom).

E. Schematic illustration of SCR1 recruitment to ER membranes upon increasing VAP levels.

F. COS7 cells co-expressing HA-VAPB with GFP-SCR2 or GFP-SCR3 with normalized intensity plot of indicated line (dotted). Scale bars: 10 μm (full size) and 5 μm (zoom).

like)-containing proteins for the VAP-binding pockets (Fig 2E). Next, we assessed whether the observed recruitment to VAP at ER structures is shared within the SCRIN family. Contrarily, we observed no change in GFP-SCRIN2 or GFP-SCRIN3 localization when co-expressed with HA-VAPB in COS7 cells (Fig 2F). Together, these data indicate that SCRIN1, and not SCRIN2 and SCRIN3, is recruited to VAP at the ER membrane.

SCRIN1 interacts with VAP through a single FFAT-like motif

Next, we sought to determine the specific domains responsible for the interaction between VAP and SCRIN1. We found that the C-terminal coiled-coil region of SCRIN1 and the N-terminal major sperm protein (MSP) domain of VAPB are the minimal binding domains required for this interaction, as shown by co-expression experiments in COS7 cells and pull-down analysis of HEK293T lysates (Fig S2D–I, 3A,E, S3B). The MSP domain of VAP contains a FFAT(-like) motif binding site, and FFAT(-like) motifs are found in the majority of the VAP-interacting proteins (Loewen et al, 2003; Murphy & Levine, 2016). Indeed, we found that the FFAT binding motif in VAP is responsible for the interaction with SCRIN1. The VAP mutant VAP-K87D/M89D, in which FFAT binding is disrupted, was no longer able to recruit GFP-SCRIN1 (Fig 3A,B,E) (Kaiser et al, 2005). Next, we searched for FFAT(-like) motifs in SCRIN1 using a previously reported algorithm and identified four potential FFAT-like motifs (Fig S3A) (Murphy & Levine, 2016). We generated SCRIN1 constructs with single-point mutations for each single FFAT-like motif (Fig 3A). VAP association was disrupted when mutating the most C-terminal FFAT-like motif in SCRIN1 (GFP-SCRIN1-F402A), but not the other motifs, as shown by pull-down assays and co-expression experiments (Fig 3C–F, S3B–D). Sequence alignment of the SCRIN family members revealed that this newly identified FFAT-like motif in SCRIN1 is not shared with the other two SCRIN family members, which is consistent with our observation that exogenous VAP is unable to recruit GFP-SCRIN2 and GFP-SCRIN3 (Fig 2F, 3G). Together, these data show that the MSP domains of VAPA and VAPB interact with a single FFAT-like motif in the C-terminal region of SCRIN1.

SCRIN1 and VAP are required for proper ER morphology

Previously, it was shown that VAP interactions with FFAT-containing proteins are engaged in maintaining ER morphology (Kaiser et al, 2005). Next, we aimed to investigate whether its interaction with SCRIN1 at the ER membrane could be important for this function. Similar to previously reported results, we found that COS7 cells expressing VAP-K87D/M89D, VAP mutant lacking proper FFAT binding, showed a robust phenotype that was characterized by non-reticular VAP structures throughout the cytosol (Fig 3B, 4A, S4A) (Kaiser et al, 2005). Likewise, similar aberrant VAP-positive structures were found in COS7 cells expressing wild-type HA-VAP and GFP-SCRIN1-F402A or GFP-SCRIN1-N, both lacking a functional FFAT-like motif (Fig 3C, S3C, 4A, S4A,B). These observed phenotypes were also detected with ER luminal marker TagRFP-ER, indicating that the non-reticular VAP signals represent affected underlying ER structures (Fig S4C,D). Similarly, both in VAP and

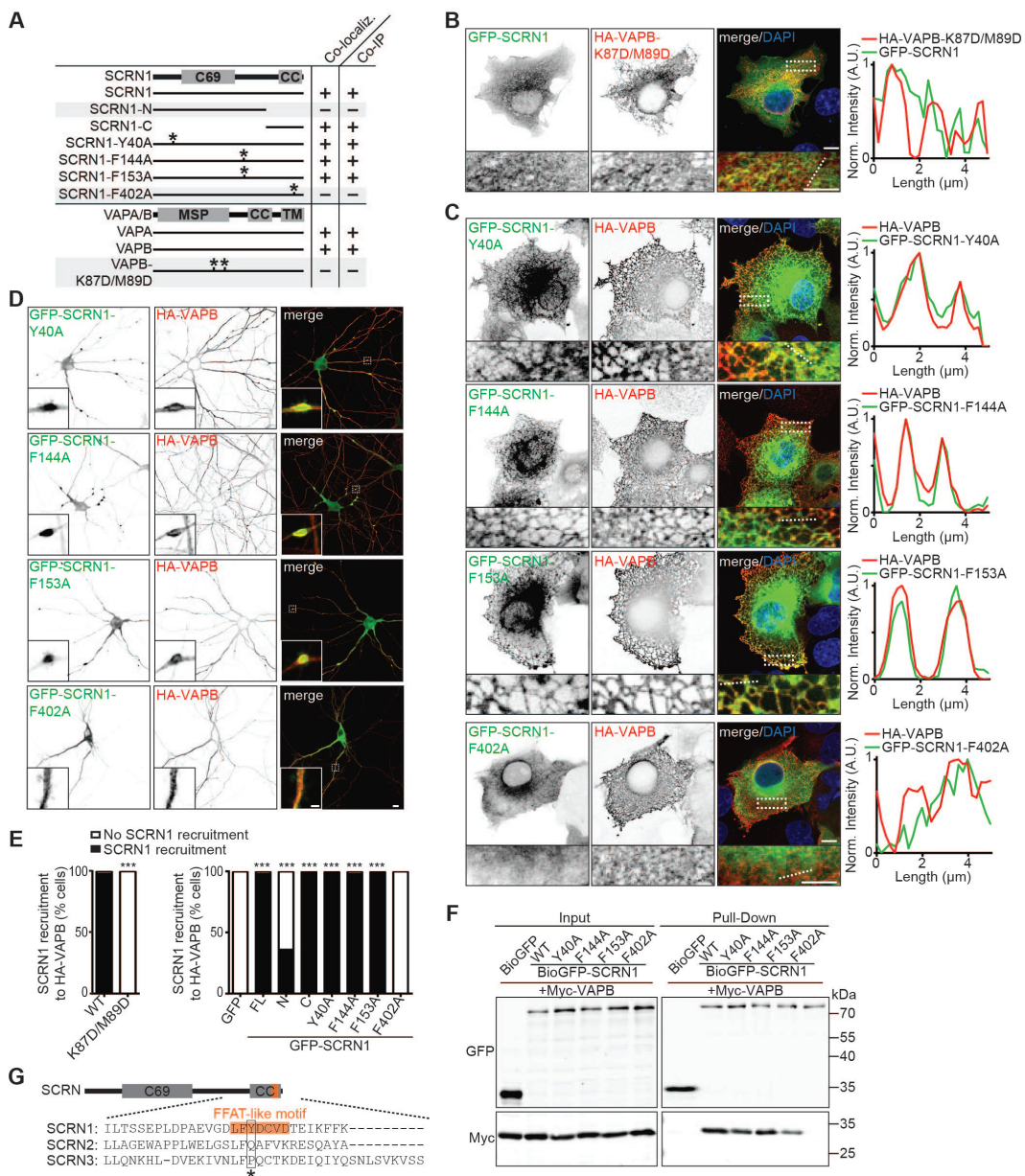


Figure 3.

VAP-SCRN1 interaction at the ER is mediated by a single FFAT-like motif

A. Schematic overview of SCRN1 and VAP constructs (asterisks represent mutations). Indicated is if expressed VAP/SCRN1 proteins co-localize in both hippocampal neurons and COS cells, and co-precipitate in pull-down assays.

B. COS7 cells co-expressing GFP-SCRN1 with HA-VAPB-K87D/M89D. Normalized intensity plot represents indicated line (dotted). Scale bars: 10 μ m (full size) and 5 μ m (zoom).

C. COS7 cells co-expressing HA-VAPB with GFP-SCRN1-Y40A, GFP-SCRN1-F144A, GFP-SCRN1-

F153A, or GFP-SCRN1-F402A. Normalized intensity plot represents indicated line (dotted). Scale bars: 10 μm (full size) and 5 μm (zoom).

D. Hippocampal neurons (DIV16) co-expressing HA-VAPB with GFP-SCRN1-Y40A, GFP-SCRN1-F144A, GFP-SCRN1-F153A, or GFP-SCRN1-F402A. Scale bars: 10 μm (full size) and 5 μm (zoom).

E. Quantifications of SCRN1 recruitment to VAPB-positive structures in COS7 cells (%). Left graph: co-expression of GFP-SCRN1 with HA-VAPB or HA-VAPB-K87D/M89D (N = 2–3, n = 44–46). Right graph: co-expression of HA-VAPB with GFP or GFP-SCRN1-FL, GFP-SCRN1-N, GFP-SCRN1-C, GFP-SCRN1-Y40A, GFP-SCRN1-F144A, GFP-SCRN1-F153A, or GFP-SCRN1-F402A (N = 2–3, n = 41–64).

F. Pull-down assay of HEK293T cells co-expressing Myc-VAPB with GFP, GFP-SCRN1-WT, GFP-SCRN1-Y40A, GFP-SCRN1-F144A, GFP-SCRN1-F153A, or GFP-SCRN1-F402A.

G. Sequence alignment of the C-terminal human SCRN1, SCRN2, and SCRN3. Amino acid position 3 (asterisk) in FFAT-like motif (orange) of SCRN1 is not shared in SCRN2 and SCRN3.

Data information: ***P < 0.001, by chi-square test with post hoc analysis including Bonferroni correction. Source data are available online for this Figure.

in SCRN1 knockdown neurons, as well as in neurons expressing GFP-SCRN1-F402A, ER morphology was severely disrupted (Fig 4B). Notably, in these neurons we observed dense ER patches surrounded by less dense or absent ER structures. On the other hand, neurons overexpressing wild-type SCRN1 also showed dense ER patches; however, these did seem properly connected to the rest of the ER structure. Thus, structural disruptions in ER morphology were consistently observed when the VAP-SCRN1 interactions were abrogated (Fig 4A). As such, expression of SCRN1-F402A showed the same phenotype on ER morphology as SCRN1 depletion, suggesting that SCRN1-F402A may act as a dominant-negative. As SCRN1-F402A is cytoplasmic, it could recruit and capture endogenous SCRN1 to the cytoplasmic pool, thereby preventing it from binding to VAP and execute its function at the ER. Indeed, oligomerization is a common feature of the Ntn aminohydrolases superfamily, and pull-down assays showed that both SCRN1 and SCRN1-F402A were associated with other SCRN1 proteins (Fig S4E,F). These results confirm that SCRN1 undergoes oligomerization and that SCRN1-F402A could act as a dominant-negative. Together, these data indicate that both SCRN1 and VAP are required for proper ER morphology, which is mediated by VAP-SCRN1 interactions at the ER membrane.

SCRN1 and VAP are engaged in maintaining ER continuity and dynamics

The ER structure undergoes constant remodeling while remaining continuous for proper functioning. Thus, next we sought to determine the effect of VAP and SCRN1 on both ER continuity and dynamics. We used live-cell imaging to map ER dynamics in cells expressing luminal ER marker TagRFP-ER. We observed fast remodeling of ER structures in both neurons and COS7 cells, ranging from ER tubule growth events and structural ER “wiggling” events (Fig 4C,D, S4G). The dense ER patches observed when expressing wild-

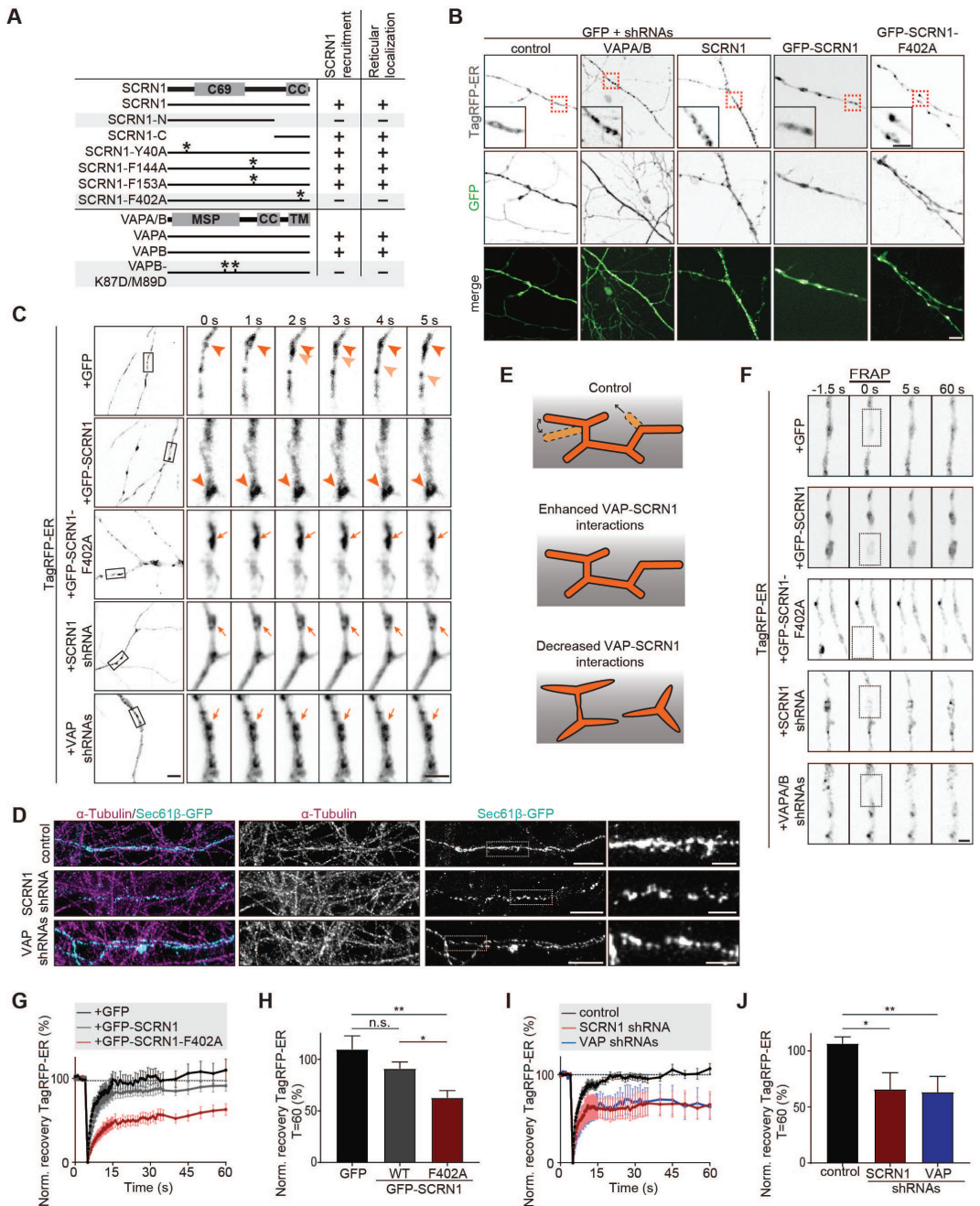


Figure 4.

VAP and SCRN1 control ER continuity and remodeling

A. Summary of observed phenotypes on SCRN1 recruitment and ER morphology in cells co-expressing indicated SCRN1 and VAP constructs (asterisks represent mutations).

B. Live hippocampal neurons (DIV17–18) co-expressing TagRFP-ER with GFP, GFP-SCRN1, GFP-

- SCRN1-F402A, SCRN1 shRNA, or VAPA/B shRNAs. Scale bars: 5 μm (full size) and 2 μm (zoom).
- C.** Time-lapse of TagRFP-ER dynamics in hippocampal neurons (DIV16–18) co-expressing GFP, GFP-SCRN1, GFP-SCRN1-F402A, SCRN1 shRNA, or VAPA/B shRNAs. Intact and sTable ER structures (dark arrowheads), intact and dynamic ER structures (light arrowheads), and impaired non-dynamic ER structures (arrows) are indicated. Scale bars: 5 μm (full size) and 2 μm (zoom).
- D.** Schematic illustration of the effect of VAP-SCRN1 interactions on ER structure and dynamics.
- E.** ER nanostructures visualized with GFP-Sec61 β in axons of hippocampal neurons (DIV18) immunostained for α -tubulin and co-expressed with pSuper empty vector, SCRN1 shRNA, or VAPA/B shRNAs, and subjected to expansion microscopy. Scale bars: 2 μm (full size) and 500 nm (zoom).
- F.** FRAP experiment of TagRFP-ER in hippocampal neurons (DIV17–18) co-expressing GFP, GFP-SCRN1, and GFP-SCRN1-F402A. Scale bar: 2 μm .
- G.** Average normalized fluorescent TagRFP-ER recovery after photo-bleaching in hippocampal neurons (DIV17–18) co-expressing GFP, GFP-SCRN1, and GFP-SCRN1-F402A. N = 2, n = 9 neurons.
- H.** Normalized fluorescent TagRFP-ER recovery after photo-bleaching at T = 60 s in hippocampal neurons (DIV17–18) co-expressing GFP, GFP-SCRN1, and GFP-SCRN1-F402A. N = 2, n = 9 neurons.
- I.** Average normalized fluorescent TagRFP-ER recovery after photo-bleaching in hippocampal neurons (DIV18) co-expressing pSuper empty vector, SCRN1 shRNA, and VAPA/B shRNAs. N = 4, n = 6–12 neurons.
- J.** Normalized fluorescent TagRFP-ER recovery after photo-bleaching at T = 60 s in hippocampal neurons (DIV18) co-expressing pSuper empty vector, SCRN1 shRNA, and VAPA/B shRNAs. N = 4, n = 6–12 neurons.
- Data information: Data represent mean \pm SEM; n.s.: not significant; *P < 0.05; **P < 0.01, by Mann–Whitney U-test.
-

type SCRN1 represented stabilized ER structures (Fig 4C,D, S4G). On the other hand, decreasing SCRN1 or VAP levels, or expressing dominant-negative SCRN1-F402A mutant, resulted in overall impaired dynamics of the dense ER patches that seemed partially discontinuous with the remaining ER structures (Fig 4C,D, S4G). To gain more detailed insights into the role of VAP-SCRN1 interactions on ER morphology, we next sought to visualize ER nanostructures in neurons using the recently developed expansion microscopy (ExM) technique (Tillberg et al, 2016). This ExM approach allows for a ~4.5-fold physical sample magnification by isotropic chemical expansion and has been validated to preserve the nanoscale organization within different biological specimens (reviewed in Wassie et al, 2019). Here, we successfully resolved the dense neuronal ER structures, which enabled us to distinguish individual ER tubules and sheets in neurons expressing ER membrane marker GFP-Sec61 β (Fig 4E, S4H,I). Consistent with reported EM studies, we observed that the axonal ER network was comprised of 1 or 2 ER tubules per diameter and regularly formed tubular structures (Fig 4D; Terasaki, 2018; Wu et al, 2017; Yalcin et al, 2017). VAP or SCRN1 knockdown neurons showed marked differences on ER nanostructures.

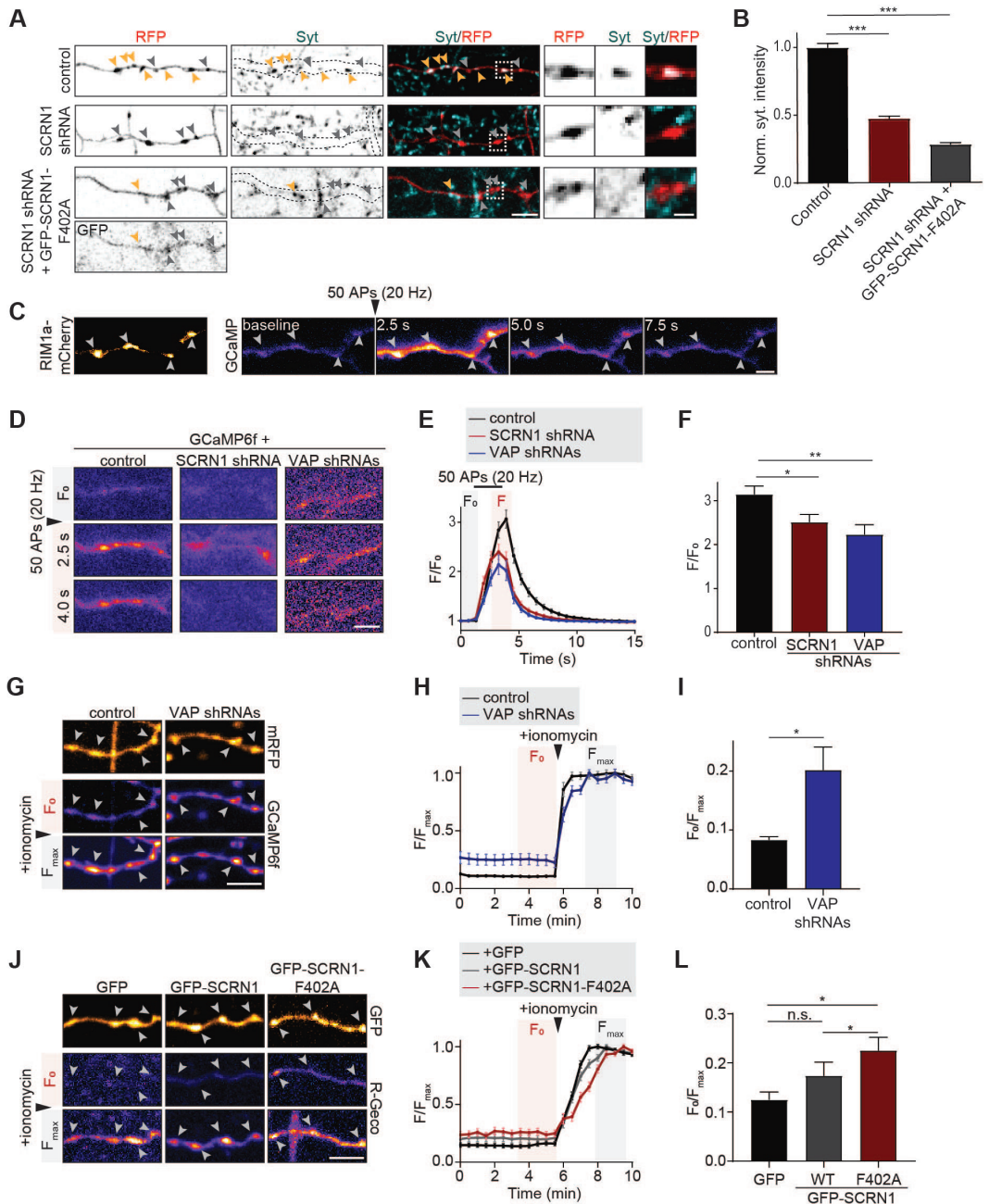


Figure 5.

VAP and SCRIN1 control Ca²⁺ homeostasis and presynaptic release

A. Representative image of Syt antibody uptake at axons of hippocampal neurons (DIV18) co-expressing RFP and pSuper empty vector, SCRIN1 shRNA, or SCRIN1 shRNA with GFP-SCRIN1-F402A. Yellow and gray arrowheads mark presynaptic boutons with and without internalized Syt,

respectively. Zooms represent typical boutons. Scale bars: 5 μm (full size) and 2 μm (zoom).

B. Quantifications of fluorescence intensity of internalized endogenous Syt at individual presynaptic boutons of hippocampal neurons (DIV18) co-expressing RFP and pSuper empty vector, SCRN1 shRNA, or SCRN1 shRNA with GFP-SCRN1-F402A. $N = 2$, $n = 201\text{--}300$ boutons.

C. Representative time-lapse of cytosolic GCaMP6f upon electric field stimulation (50 APs, 20 Hz) in axons of hippocampal neurons (DIV21) co-expressed with RIM1a-mCherry to visualize presynaptic sites (arrowheads). Scale bar: 5 μm .

D. Time-lapses of cytosolic GCaMP6f upon electric field stimulation (50 APs, 20 Hz) in axons of hippocampal neurons (DIV21) co-expressing pSuper control, SCRN1 shRNA, or VAPA/B shRNAs. Scale bar: 5 μm .

E. Average normalized response of GCaMP6f fluorescent intensity at presynaptic boutons upon stimulation (50 APs, 20 Hz) in hippocampal neurons (DIV21) co-expressing pSuper empty vector, SCRN1 shRNA, or VAPA/B shRNAs. $N = 5\text{--}6$, $n = 15\text{--}27$.

F. Average normalized peak response of GCaMP6f at presynaptic boutons upon stimulation (50 APs, 20 Hz) in hippocampal neurons (DIV21) co-expressing pSuper empty vector, SCRN1 shRNA, or VAPA/B shRNAs. $N = 5\text{--}6$, $n = 15\text{--}27$.

G. Representative time-lapse of cytosolic GCaMP6f before (F_0) and after (F_0) ionomycin treatment at axons of hippocampal neurons (DIV18) co-expressed with mRFP and pSuper empty vector or VAPA/B shRNAs. Arrowheads mark presynaptic boutons. Scale bar: 5 μm .

H. Basal GCaMP6f fluorescence (F) normalized to the maximum GCaMP6f fluorescence (F_{max}) after ionomycin treatment at presynaptic boutons of hippocampal neurons (DIV18) co-expressing mRFP with pSuper empty vector or VAPA/B shRNAs. $N = 2$, $n = 47\text{--}50$.

I. Average basal GCaMP6f fluorescence (F_0) normalized to the max GCaMP6f fluorescence intensity (F_{max}) after ionomycin treatment at presynaptic boutons of hippocampal neurons (DIV18) co-expressing mRFP with pSuper empty vector or VAPA/B shRNAs. $N = 2$, $n = 47\text{--}50$.

J. Representative time-lapse of cytosolic R-GECO1 before (F_0) and after (F_{max}) ionomycin treatment at axons of hippocampal neurons (DIV18) co-expressing GFP, GFP-SCRN1, or GFP-SCRN1-F402A. Arrowheads mark presynaptic boutons. Scale bar: 5 μm .

K. Basal R-GECO1 fluorescence (F) normalized to the maximum R-GECO1 fluorescence (F_{max}) after ionomycin treatment at presynaptic boutons of hippocampal neurons (DIV18) co-expressing GFP, GFP-SCRN1, or GFP-SCRN1-F402A. $N = 3$, $n = 70\text{--}89$.

L. Average basal R-GECO1 fluorescence (F_0) normalized to the maximum R-GECO1 fluorescence intensity (F_{max}) after ionomycin treatment at presynaptic boutons of hippocampal neurons (DIV18) co-expressing GFP, GFP-SCRN1, or GFP-SCRN1-F402A. $N = 3$, $n = 70\text{--}89$.

Data information: Data represent mean \pm SEM; n.s.: not significant; * $P < 0.05$; ** $P < 0.01$; *** $P < 0.001$, by Mann-Whitney U-test.

More specifically, these neurons showed severe discontinuity of ER tubules in axons, and overall less dense and irregular ER structures in axons, dendrites, and soma (Fig 4E, S4H,I). To quantitatively validate the role of VAP-SCRN1 interactions on ER continuity and dynamics, we conducted FRAP experiments on the previously observed characteristic dense ER patches in TagRFP-ER expressing neurons. Consistent with previous indications,

photo-bleached TagRFP-ER co-expressed with either GFP or GFP-SCRN1 showed full recovery within 60 s of the ER patches (Fig 4F–H). This suggests rapid and complete redistribution of luminal ER content consistent with an intact ER structure. In contrast, the recovery of TagRFP-ER at ER patches was markedly reduced by ~45% in neurons expressing either GFP-SCRN-F402A, SCRN1 shRNA, or VAPA/B shRNAs, which implies incomplete redistribution of the luminal ER marker due to discontinuity (Fig 4F,I,J). Together, these data indicate that loss of VAP and SCRN1 results in discontinuous ER structures and impaired ER dynamics in neurons, which is mediated by VAP-SCRN1 interactions.

SCRN1-VAP interaction controls SV cycling

Next, we aimed to test whether the VAP-SCRN1 interactions at the ER membrane may be engaged in regulating the SV cycle, as we previously observed that VAP or SCRN1 depletion resulted in decreased SV cycling (Fig 1B–D,J,K). To test this, we conducted the Syt uptake assay in neurons depleted from SCRN1 and expressing SCRN1-F402A, thereby abolishing VAP-SCRN1 interactions. Unlike wild-type SCRN1 expression, exogenous mutant SCRN1-F402A was unable to rescue the effect of SCRN1 knockdown on SV cycling (Fig 5A,B). These data imply that the VAP-SCRN1 interactions, which we identified as regulators of ER remodeling, are engaged in modulating SV cycling at presynaptic sites.

VAP and SCRN1 are engaged in regulating evoked presynaptic Ca²⁺ responses

Neurotransmitter release is induced by a local cytoplasmic Ca²⁺ influx upon neuronal stimulation. Thus, to further investigate the phenotype of VAP and SCRN1 on SV cycling, we next assessed whether they are engaged in regulating evoked Ca²⁺ influx. To test this, we measured Ca²⁺ dynamics at single boutons with the genetically encoded Ca²⁺ indicator GCaMP6f and triggered trains of action potentials (50 APs, 20 Hz) using electric field stimulation (Fig 5C). Presynaptic boutons were identified as GCaMP6f-positive swellings along axons, which were shown to co-localize with the presynaptic active zone marker RIM1a-mCherry (Fig 5C). Loss of VAP or SCRN1 both resulted in a marked ~ 25% decreased peak amplitude of evoked Ca²⁺ transients (Fig 5D–F). These results indicate that both the ER receptor VAP and the VAP-interacting protein SCRN1 are involved in modulating presynaptic Ca²⁺ influx and thereby could affect SV cycling.

VAP-SCRN1 interactions modulate Ca²⁺ homeostasis at presynaptic sites

To better understand the effects of VAP and SCRN1 on evoked Ca²⁺ influx, we next sought to determine whether these proteins could interfere with ER-mediated Ca²⁺ homeostasis. Maintaining basal Ca²⁺ levels is one of the key functions of smooth ER, which is the only type of ER that is present in axons. Thus, we hypothesized that the observed structural ER defects with abolished VAP-SCRN1 interactions could perturb ER-mediated Ca²⁺ homeostasis and thereby affect Ca²⁺-mediated SV cycling. We compared relative basal Ca²⁺ levels at presynaptic sites in neurons expressing Ca²⁺ indicators GCaMP6f or R-GECO1, as well as mRFP or GFP to identify transfected cells and presynaptic boutons. Relative

basal Ca^{2+} levels were obtained by determining the ratio (F_0/F_{max}) of fluorescent GCaMP6f or R-GECO1 signals before (F_0) and after (F_{max}) ionomycin treatment. Ionomycin is an ionophore which induces Ca^{2+} permeability at membranes, thereby enables effectively saturating Ca^{2+} indicators to determine F_{max} . In VAP knockdown neurons, relative basal Ca^{2+} levels at single boutons were markedly elevated (~2.5-fold) compared to control (Fig 5G–I). This is in line with the observed decreased evoked Ca^{2+} influx, as higher basal Ca^{2+} levels will result in a lower extracellular-cytoplasmic Ca^{2+} concentration gradient. Consistently, presynaptic Ca^{2+} levels were significantly increased (~2-fold) with dominant-negative SCRN1-F402A expression, but not with SCRN1 wild-type expression, indicating that the observed effect is mediated by VAP-SCRN1 interactions (Fig 5J–L). Together, these data imply that ER-localized VAP-SCRN1 interactions are engaged in modulating basal Ca^{2+} levels at presynaptic sites.

DISCUSSION

The dynamic and continuous ER network extends throughout the axon, and evidence for its role in controlling presynaptic neurotransmitter release begins to emerge (Summerville et al, 2016; De Gregorio et al, 2017; de Juan-Sanz et al, 2017). In this study, we identified novel control mechanisms for ER remodeling, presynaptic Ca^{2+} homeostasis, and Ca^{2+} -induced SV cycling, which are mediated by ER receptor VAP together with VAP-interacting protein SCRN1. Together, these data point toward a model where VAP-SCRN1 interactions tune ER integrity and dynamics, and thereby could modulate basal Ca^{2+} levels and subsequently SV cycling at presynaptic sites.

SCRN1 is a VAP-interacting protein

Here, we demonstrated that loss of ER membrane receptor VAP results in discontinuous ER structures, impaired ER dynamics, and decreased SV cycling. This is in line with previous studies which already hinted for a role of VAP in maintaining ER morphology and regulating synaptic function (Skehel et al, 1995; Kaiser et al, 2005; Gomez-Suaga et al, 2019). To gain further mechanistic insights into the VAP-mediated phenotypes, we sought to identify a VAP-associated protein involved in this function. Hence, we selected SCRN1 as a potential candidate for several reasons. First, SCRN1 was abundantly expressed in brain tissue, as indicated by various expression databases (Protein Atlas, Expression Atlas, Alan Brain Atlas) and confirmed by our Western blot analysis of different rat tissues. Second, in non-neuronal cells, SCRN1 was found to play a role in regulating Ca^{2+} -controlled exocytosis, which is also a key process of the SV cycle (Way et al, 2002; Lin et al, 2015). We confirmed the interaction between VAP and SCRN1, and identified a single FFAT-like motif responsible for the interaction. Consistent with our hypothesis, we found that either SCRN1 depletion or dominant-negative SCRN1-F402A expression phenocopied the effect of VAP depletion on both ER remodeling and SV cycling. The dominant-negative effect was consistently more potent than the shRNA knockdown effect, similar to what is often observed when comparing dominant-negative and shRNA silencing expression constructs

of proteins. Here, the difference could be explained by incomplete depletion of endogenous SCRN1 during the SCRN1 shRNA silencing period, whereas on the other hand dominant-negative SCRN1-F402A actively recruits and captures endogenous SCRN1 proteins and thereby impairs its function. Nevertheless, we cannot exclude that additional functions of SCRN1-F402A might be at play. Together, our data indicate that SCRN1-VAP interactions are engaged in controlling the VAP-associated phenotypes, and further investigations are required to examine whether additional VAP-interacting proteins could also be involved in modulating SV cycling.

VAP-SCRN1 interactions control ER continuity and dynamics

The ER network is composed of a well-maintained interconnected structure that undergoes continuous remodeling for proper functioning. Here, we identified the VAP-SCRN1 interactions as critical regulators for maintaining ER structure and dynamics. Considering that VAPs are best known to act as major ER receptors by facilitating tight membrane contact sites between the ER and other organelles, it is tempting to speculate that these membrane contact sites might be engaged in controlling VAP-mediated functions on ER integrity and dynamics (Muallem et al, 2017; Wu et al, 2018). One plausible mechanism could be that these membrane contact sites may act as “anchor points” which locally stabilize the ER network. These VAP-facilitated membrane contact sites are abundantly present throughout the cell and can thus stabilize local spots within the large interconnected and highly dynamic ER network. As such, this hypothesis follows the assumption that proper ER integrity relies on a defined balance between ER dynamics and stability. In line with this, it was previously shown that depleting either ER-forming protein atlastin or ER-stabilizing protein reticulon resulted in ER tubule fragmentation, which could remarkably be rescued by depleting both proteins simultaneously (Wang et al, 2016). Alternatively, VAP-mediated membrane contact sites could control ER remodeling by enabling fast lipid delivery. We showed that ER remodeling in neurons is a fast process and that ER tubule growth events can occur in a few seconds. This fast ER remodeling requires the continuous and rapid rearrangement of lipids. This may be accomplished via fast lipid transfer at membrane contact sites between ER and other organelles, rather than via the relatively slower lipid synthesis and redistribution at the ER membrane. Note worthily, considering that VAPs are implicated in a wide range of functions, various other possible direct or indirect VAP-mediated mechanisms to control ER remodeling might be at play.

Maintaining axonal ER structures is important to preserve presynaptic function

In recent EM studies, it was reported that ER structures in axons show specific adaptations, characterized by small ER lumen and low density of 1–2 tubules per axon diameter. These adaptations likely allow the axonal ER to extend throughout all axon branches while remaining continuous with the remaining ER network, which is typically more dense and branched. In this study, we found that VAP and SCRN1 depletion affected ER structures throughout the cell, though axonal ER structures seemed most severely disrupted. Interestingly, mutations

in generic structural ER proteins such as atlastin-1, reticulon-2, REEP1, and REEP2 are causative for the axonopathy HSP (Hazan et al, 1999; Zhao et al, 2001; Nishimura et al, 2004; Zuchner et al, 2006; Montenegro et al, 2012; Esteves et al, 2014; Yalcin et al, 2017). Together, these findings indicate that the delicate ER network in axons is more sensitive to maintenance defects. Therefore, ubiquitous ER disruptions may result in more profound phenotypes on particularly axonal functions. Here, we demonstrated that the observed ER abrogations with decreased VAP-SCRN1 interactions were accompanied with impaired SV cycling at presynaptic sites. Consistent with this, recent studies in *Drosophila* neurons showed that loss of ER-shaping protein atlastin or reticulon also resulted in impaired ER structures as well as decreased neurotransmitter release (Summerville et al, 2016; De Gregorio et al, 2017). Together, these findings imply that ER structure and function are engaged in modulating SV cycling. Notably, investigating the direct relation between these phenotypes is challenging, as it is not feasible to specifically isolate the local function of ER at presynaptic sites since all ER membranes and lumen in the cell are continuous. Nevertheless, considering that the neuronal ER network remains fully continuous despite its complex cellular morphology may actually highlight the functional relevance of this continuity for its role at presynaptic sites. Toward this end, it would be interesting to direct future work on investigating whether the continuity of the neuronal ER network is important for the reported ER-mediated functions at presynaptic sites.

4

VAP-SCRN1 interactions modulate presynaptic Ca²⁺ dynamics and SV cycling

In this study, we reported that the ER defects observed with VAP or SCRN1 depletion are accompanied with reduced presynaptic Ca²⁺ influx and SV cycling. Considering that axonal ER structures are exclusively comprised of smooth ER, we hypothesized that defects in maintaining Ca²⁺ homeostasis, which is a key function of smooth ER, could provide a mechanistic link between the observed phenotypes on ER integrity and SV cycling. Previous reports already hinted for a correlation between ER-mediated Ca²⁺ homeostasis and neurotransmitter release. In a recent study, a feedback loop between ER Ca²⁺ concentration, presynaptic Ca²⁺ influx, and SV exocytosis was identified in dissociated rodent neurons (de Juan-Sanz et al, 2017). Additionally, in *Drosophila* HSP models, both impaired ER integrity and affected SV cycling were rescued upon Ca²⁺ bath application (Summerville et al, 2016). In this report, we found that loss of VAP-SCRN1 interactions in neurons results in elevated basal Ca²⁺ levels at presynaptic sites. This implies that the cytoplasmic-extracellular Ca²⁺ concentration gradient is reduced, which could explain the reduction in evoked Ca²⁺ response and subsequent decreased SV cycling. Consistently, previous reports in non-neuronal cells showed that VAP-mediated membrane contact sites regulate Ca²⁺ homeostasis and that SCRN1 controls Ca²⁺-dependent processes (Way et al, 2002; Lin et al, 2015; Paillusson et al, 2017). It remains poorly understood how prolonged increase in basal Ca²⁺ levels leads to reduced SV cycling. We speculate that chronic elevation of basal Ca²⁺ levels could result in compensatory responses that may lead to downscaled synaptic strength. This could be accomplished at different levels, e.g.,

by decreasing bouton size, lower number of synapses and SVs, and downregulation of proteins involved in the SV cycle machinery. Consistent with this idea, we observed less and smaller boutons in VAP knockdown neurons. In addition to the Ca^{2+} -mediated effects, the smooth ER in axons could also modulate SV cycling by controlling lipid homeostasis. The presynaptic membrane is comprised of a unique presynaptic lipid composition that is required for proper overall presynaptic function (Lauwers et al, 2016). Possibly, this presynaptic lipid composition could be facilitated and maintained by enabling lipid delivery at VAP-mediated membrane contact sites. Taken together, it would be interesting to direct future research in exploring the possible roles of VAP-SCRN1 interactions in controlling Ca^{2+} homeostasis and presynaptic lipid composition, and on how this could modulate the tightly spatiotemporal controlled SV cycle.

Molecular function of VAP-interacting protein SCRIN1

It remains unclear how the SCRIN1 interaction with VAP at the ER membrane may control the observed phenotypes on ER integrity. The C69 protease domain of SCRIN1 did not show proteolytic activity, whereas this was observed for family members SCRIN2 and SCRIN3. Thus, it is unlikely that the observed VAP-mediated functions involve enzymatic activity of SCRIN1. However, we did observe oligomerization of SCRIN1, which may hint for a scaffolding function of SCRIN1. Possibly, as scaffolding protein, SCRIN1 could promote stabilization of VAP interactions at membrane contact sites. Consistent with this, we observed increased stabilization of ER structures upon wild-type SCRIN1 expression. This highlights the importance of controlling the endogenous levels of SCRIN1 at the ER membrane in order to balance between ER dynamics and stability. This is supported by the observation that endogenous SCRIN1 proteins were not robustly localized at ER structures, whereas SCRIN1 proteins were fully recruited to VAP at the ER membrane upon elevating VAP and SCRIN1 levels. Similarly, it was previously shown that many other proteins containing a FFAT(-like) motif also did not fully coincide with ER structures (Murphy & Levine, 2016). Together, these findings imply that SCRIN1, as well as many other FFAT(-like) proteins, undergoes continuous cycles of competitive binding and unbinding to the limited available VAP-binding pockets. As such, we propose that controlling endogenous intracellular SCRIN1 levels, and thus competition with other VAP interactors, could be a novel mechanism to tune ER dynamics and subsequently presynaptic function. Moreover, unlike the ubiquitously expressed VAPs, SCRIN1 expression is highly enriched in brain tissue. Therefore, SCRIN1 may be engaged in controlling VAP-mediated functions in brain tissue specifically.

In summary, we propose that VAP-SCRIN1 interactions act as a novel control mechanism for dynamic ER remodeling, and consequently Ca^{2+} homeostasis and SV cycling. Future work is required to better understand the molecular function of VAP-SCRIN1 interactions in mediating ER integrity and Ca^{2+} -driven SV cycling. Finally, investigating additional ER-mediated control mechanisms that are engaged in modulating presynaptic function is required to obtain more insights into the precise function of the dynamic and continuous neuronal ER network in controlling SV cycling.

ACKNOWLEDGEMENTS

We thank Dr. Mike Boxem for providing the human cDNA library; Rian Stoffelen for her contributions to Fig 1E and F; and Ginny C. Farias Galdames and Arthur P.H. de Jong for critically reading the article. This work was supported by the Netherlands Organization for Scientific Research (NWO-ALW-VICI, CCH; NWO-VIDI, MA), the Netherlands Organization for Health Research and Development (ZonMW-TOP, CCH), the European Research Council (ERC; ERC-consolidator, CCH; ERC-StG, HDM), and the Proteins@Work program of the National Roadmap Large-scale Research Facilities of the Netherlands (MA).

AUTHOR CONTRIBUTIONS

FWL designed, conducted, and interpreted experiments, and wrote the article. YC performed biochemical experiments and cloned constructs. JTK initiated the study, cloned constructs, and performed initial experiments together with MMB. AB conducted the electric field stimulation experiments, RS performed the mass spectrometry experiments and was supported by MA, and EAK provided the expansion microscopy data. HDM gave advice throughout the project and edited the article. CCH supervised the research, coordinated the study, and edited the article.

CONFLICT OF INTEREST

CCH is an employee of Genentech, Inc., a member of the Roche group. The authors declare that they have no additional conflict of interest.

MATERIAL AND METHODS

Animals

All animal experiments were approved by the Animal Ethical Review Committee (DEC) of Utrecht University and performed in accordance with the guidelines for the welfare of experimental animals issued by the Dutch law and following European regulations (Guideline 86/609/EEC).

Primary rat neuron culture and transfection

Dissociated hippocampal and cortical neuron cultures were prepared from embryonic day 18 rat pups of mixed gender. Cells were plated on 18-mm glass coverslips coated with poly-L-lysine (37.5 mg/ml) and laminin (1.25 mg/ml) in a 12-well plate at a density of 100k/well for hippocampal neurons and 50k/well for cortical neurons. Cultures were maintained in Neurobasal medium (NB) supplemented with 2% B27, 0.5 mM glutamine, 16.6 μ M glutamate, and 1% penicillin/streptomycin at 37°C in 5% CO₂.

Neuron cultures were transfected using a mixture of 3.3 μ l lipofectamine 2000 (Invitrogen), 1.5–3.0 μ g DNA, and 200 μ l NB per coverslip. For knockdown experiments, a total of 1.5 μ g DNA of shRNA construct(s) was used per coverslip. The transfection mixture was added to the coverslips, which were placed in fresh NB supplemented with 0.5 mM glutamine, and incubated for 45–90 min. Next, coverslips were washed once in prewarmed NB and

transferred back to their original medium. Cells were maintained for 4 days (for knockdown experiments) or 24–48 h (for other experiments) prior to fixation or live-cell imaging.

Cell line culture and transfection

COS7 and HEK293T cells were cultured on plastic at 37°C in 5% CO₂ in DMEM/Ham's F10 (50%/50%) medium supplemented with 10% FCS and 1% penicillin/streptomycin. COS7 and HEK293T cells were plated on, respectively, 18-mm glass coverslips or plastic 1 day prior to transfection with MaxPEI (Polysciences). In brief, MaxPEI/DNA (3:1 ratio) was mixed in fresh serum-free DMEM or Ham's F10 medium, incubated for 20 min, and added to the cell culture. After 24 h, cells were either processed for biochemistry, fixed, or used for live-cell imaging.

DNA plasmids

The following plasmids are described previously: Myc-VAPA, Myc-VAPB, HA-VAPA (with E178G mutation), HA-VAPB, HA-VAPB-K87D/M89D, GFP-VAPB-TM, GFP-VAPB-MSP-CC, and VAPB-MSP-GFP (with E6I single nucleotide polymorphism and K139R mutation; Teuling et al, 2007); pGFPC1-Sec61 β (Hradsky et al, 2011); HA-BirA (de Boer et al, 2003); BioGFP (Jaworski et al, 2009); GW1-RFP and pGW1-GFP (Hoogenraad et al, 2005); pSuper vector (Brummelkamp et al, 2002); ssRFP-KDEL (Addgene plasmid #62236, gift from Dr. Erik Snapp; Snapp et al, 2006), TagRFP-ER (Schatzle et al, 2018), HA-Erlin1, and HA-Erlin2 (gift from Dr. Richard J.H. Wojcikiewicz; Pearce et al, 2007, 2009); GCaMP6f (Addgene plasmid #58514, gift from Prof. Adam E. Cohen; Venkatachalam & Cohen, 2014); and R-GECO1 (Addgene plasmid #45494, gift from Prof. Robert E. Campbell; Wu et al, 2013).

The cDNAs of SCR_N1a (AAH_40492.1), SCR_N2 (AAH_10408.2), and SCR_N3 (AAI_19685.1) were obtained from a human cDNA library kindly provided by Dr. Mike Boxem. All wild-type SCR_N1, SCR_N1-N (1–293), SCR_N1-C (293–414), SCR_N2, and SCR_N3 constructs were generated using PCR-based cloning strategies and inserted into β -actin (for HA-SCR_N1) or GW1 (for all other constructs) vectors. Constructs with single-point mutations were generated using site-directed mutagenesis. SCR_N1 FFAT-like mutant constructs were obtained for each predicted FFAT-like motif identified by a previously reported algorithm (Murphy & Levine, 2016). More specifically, SCR_N1-Y40A, SCR_N1-F144A, SCR_N1-F153A, and SCR_N1-F402A were generated by replacing the conserved hydrophobic phenylalanine or tyrosine residue for an alanine residue. Proteolytic dead mutant constructs SCR_N1-C9A, SCR_N2-C12A, and SCR_N3-C6A were generated by replacing the predicted proteolytic cysteine residue, as identified by the online MEROPS database, by a non-catalytic alanine residue. The RIM1a-mCherry construct was obtained by exchanging the HA-tag of the previously reported pAJ14063-pFUGW-RIM1aWT-HA construct (de Jong et al, 2018). The following shRNAs inserted in pSuper vectors were used in this study: VAPA shRNA #1 (5'-GCATGCAGAGTGCTGTTTC-3'; Teuling et al, 2007),

VAPA shRNA #2 (5'-GGAACTGATGGAAGAGTG-3'; Teuling et al, 2007), and VAPB shRNA #1 (5'-GGTGATGGAAGAGTGC-3'; Teuling et al, 2007); and SCRN1 shRNA #1 (5'-GATCCTTCCAGGTCCATAT-3'), SCRN1 shRNA#2 (5'-GCACTTACATCTCAATTGA-3'), and SCRN1 shRNA #3 (5'-CAGGCTTGGTTAGAACGA-3').

Antibodies

The following primary antibodies were used for this study: rabbit anti-VAPA (homemade #1006-04; Teuling et al, 2007) and anti-VAPB (homemade #1006-00; Teuling et al, 2007); mouse anti-synaptotagmin (SySy, 105311, clone 604.2); rabbit anti-SCRN1 (SySy, 289003; used in Fig 1E), rabbit anti-SCRN1 (Abcam, ab105355; used in Fig S1D), and rabbit anti-SCRN1 (Sigma, HPA024517, RRID:AB_2184811; used for all other experiments; validation SCRN1 antibodies in Fig S1G–J); guinea pig anti-vGlut (Millipore, ab5095); rat anti-HA (Roche, 1867423; used for immunostainings); mouse anti-HA (BioLegend, mms-101p, clone 16B12; used for immunoblots); mouse anti-actin (Chemicon, MAB1501R, clone C4); rabbit anti-GFP (Abcam, ab290); mouse anti-Myc (Santa Cruz, SC40, clone 9E10); and mouse α -Tubulin (Sigma, T5168, clone B-5-1-2, RRID:AB_477579). The following secondary antibodies were used for this study: anti-rabbit Alexa 488 (Life Technologies, A11034), anti-rabbit Alexa 568 (Life Technologies, A11036), anti-rat Alexa 568 (Life Technologies, A11077), anti-guinea pig Alexa 568 (Life Technologies, A11075), anti-mouse Alexa 647 (Life Technologies, A21236), anti-mouse anti-HRP (Dako, P0260), anti-rabbit anti-HRP (Dako, P0399), anti-mouse IRDye 680LT (Li-Cor, 926-68020), and anti-rabbit IRDye 800CW (Li-Cor, 926-32211).

Tissue extracts, cell extracts, and immunoblotting

To generate tissue extracts for Western blot and mass spectrometry analysis, different brain regions (cerebellum, cortex, hippocampus, midbrain, brainstem, and spinal cord) or whole brains were dissected from adult female rats. Samples were homogenized in ice-cold homogenization buffer (150 mM NaCl, 50 mM Tris, 0.1% SDS, 0.2% NP-40, pH 7.8) supplemented with 1 \times complete protease inhibitor cocktail (Roche), sonicated, and centrifuged (15 min, 900 g, 4°C). Protein concentrations of supernatant were measured using a BCA protein assay (Pierce). Next, 20 μ g protein per sample was resuspended in SDS sample buffer and boiled for 5 min at 95°C. To generate cell extracts for Western blot analysis, transfected HEK293T cells were washed and harvested in ice-cold PBS. Cells were centrifuged (5 min, 300 g, 4°C), and the pellet was resuspended in ice-cold lysis buffer (100 mM Tris, 150 mM NaCl, 1% Triton, pH 7.5) supplemented with 1 \times complete protease inhibitor cocktail (Roche). Cell lysates were centrifuged (5 min, 20,000 g, 4°C), and supernatant was resuspended in SDS sample buffer and boiled for 10 min at 100°C. Samples were resolved on SDS–page gels and transferred to nitrocellulose membranes (Bio-Rad) or polyvinylidene difluoride membranes (Millipore). Membranes were blocked for 30 min with PBS-T (PBS with 0.05% Tween) with 2% BSA. Next, membranes were sequentially incubated with primary and secondary antibodies diluted in PBS-T with 2%

BSA, and washed three times with PBS-T after each antibody incubation step. Proteins resolved on the membranes were visualized using Odyssey Infrared Imaging (Li-Cor Biosciences) or enhanced chemiluminescence.

Pull-down assays and mass spectrometry analysis

For biotin–streptavidin pull-down assays, HEK293T cells were co-transfected with BirA, BioGFP(-fusion) plasmids (used as bait), and an additional plasmid (used as prey). After ~ 24 h, cells were washed once with ice-cold PBS, harvested in ice-cold PBS supplemented with 0.5× complete protease inhibitor cocktail (Roche), and centrifuged (5 min, 300 g, 4°C). Cell pellets were resuspended in ice-cold lysis buffer (100 mM Tris, 150 mM NaCl, 1% Triton, pH 7.5) supplemented with 1× complete protease inhibitor cocktail, incubated for 10 min on ice, and centrifuged (5 min, 20,000 g, 4°C). Supernatant was used for the binding assay and for generating input samples by boiling for 5 min at 100°C in SDS sample buffer. Beads were pretreated before the binding assay. For regular pull-down assays with cell culture extracts, magnetic Dynabeads M-280 Streptavidin (Thermo Fisher Scientific) were prewashed once with normal washing buffer (20 mM Tris HCl, 150 mM KCl, 0.5% Triton, pH 7.5), incubated for 30 min at room temperature with blocking buffer (20 mM Tris, 150 mM KCl, 0.2 µg/µl CEA, pH 7.5), and washed twice with normal washing buffer. Binding of HEK293T cell lysates and beads was performed for 1 h at 4°C. Beads were subsequently washed five times using normal washing buffer and boiled for 5 min at 100°C in lysis buffer with SDS sample buffer to elute proteins and generate pull-down samples. Alternatively, for pull-down assays with whole brain extracts for mass spectrometry analysis, beads were prewashed twice with low salt buffer (100 mM KCl, 0.1% Triton X-100, 20 mM Tris, pH 7.6), twice with high salt buffer (500 mM KCl, 0.1% Triton X-100, 20 mM Tris, pH 7.6), and twice again in low salt buffer. Binding of HEK293T cell lysates and beads was performed for 1 h at 4°C in presence of whole rat brain extract (prepared as described above), and beads were subsequently washed five times using normal washing buffer. Mass spectrometry analysis of samples was conducted as described before (Cunha-Ferreira et al, 2018). All the mass spectrometry proteomics data have been deposited to the Pride database (<http://www.ebi.ac.uk/pride>) with the dataset identifier PXD014534.

Immunofluorescence staining

Cells were fixed for 10 min in 4% formaldehyde and 4% sucrose (neurons) or in 4% formaldehyde (COS7 cells) at room temperature and washed three times with PBS. Fixed neurons were sequentially incubated with primary and secondary antibodies diluted in GDB (0.2% BSA, 0.8 M NaCl, 0.5% Triton X-100, 30 mM phosphate buffer, pH 7.4). Fixed COS7 cells were first permeabilized for 10 min in PBS with 0.1% Triton-X, blocked for 30 min in PBS with 2% BSA, and sequentially incubated with primary and secondary antibodies diluted in PBS with 2% BSA. Cells were washed three times with PBS after each antibody incubation step.

Expansion microscopy sample preparation

Expansion microscopy was performed according to proExM protocol (Tillberg et al, 2016). Briefly, immunostained cells on 18-mm glass coverslips were incubated overnight in PBS with 0.1 mg/ml Acryloyl-X (Thermo Fisher, A20770) and 0.002% of 0.1 μm yellow-green Fluorospheres (Thermo Fisher, F8803). These bright fluorescent microspheres adhered to cell surfaces, thereby this cell boundary marker simplified the localization of cells in the expanded samples. Cells were washed three times with PBS and transferred to a gelation chamber (13 mm diameter, 120 μl volume) made of silicone molds (Sigma-Aldrich, GBL664107) on a parafilm-covered glass slide. The chamber was prefilled with monomer solution (PBS, 2 M NaCl, 8.625% (w/w) sodium acrylate, 2.5% (w/w) acrylamide, and 0.15% (w/w) N,N'-methylenebisacrylamide) supplemented with 0.4% (w/w) tetramethylethylenediamine (TEMED) accelerator and 0.2% (w/w) ammonium persulfate (APS) initiator. The gelation proceeded for 1 h at 37°C in a humidified incubator. Gels were further immersed into 2 ml of 8 units/ml proteinase-K in digestion buffer (pH 8.0, 50 mM Tris, 1 mM EDTA, 0.5% Triton X-100, 0.08 M guanidine HCl) solution for 4 h at 37°C for digestion. Gels were transferred to 50 ml deionized water for overnight expansion, and water was refreshed once to ensure the expansion reached plateau. Plasma-cleaned #1.5 coverslips for gel imaging were incubated in 0.1% poly-l-lysine to reduce gel's drift during acquisition. Gels were mounted using custom-printed imaging chambers (<https://www.tinkercad.com/things/7qqYCYgcbNU>). Expansion factor was calculated as a ratio of a gel's diameter to the diameter of gelation chamber and was in the range of 4.0–4.1.

Confocal microscopy

Confocal microscopy of fixed samples on glass coverslips was performed with a LSM 700 confocal laser-scanning microscope (Zeiss) equipped with a Plan-Apochromat 63x NA 1.40 oil DIC, EC Plan-Neofluar 40x NA1.30 Oil DIC, and a Plan-Apochromat 20x NA 0.8 objective. Each confocal image represents a maximum intensity projection of a z-series covering the region of interest. For fluorescence intensity measurements, settings were kept the same for all conditions. Confocal microscopy of fixed samples on expanded gels was performed with a Leica TCS SP8 STED 3X microscope using a HC PL APO 63x/1.20 W CORR CS2 water immersion objective. Images were acquired with lateral pixel size in the range of 70–80 nm and axial of 180 nm using internal HyD detector. If necessary, a drift correction of Z-stack was performed in Huygens Professional version 17.04 (Scientific Volume Imaging, The Netherlands) using cross-correlation between adjacent slices. All images were deconvolved in the same program, using the CMLE algorithm, with SNR:7 and 20 iterations. Movies of 3D reconstructions of z-stacks were performed in Blender version 2.79b (Blender Institute, Amsterdam).

Syt uptake assay

Hippocampal neurons were pretreated with 50 μM bicuculline (Sigma, 14340) in their original NB medium for 10 min at 37°C in 5% CO₂. Next, neurons were directly incubated

for 10 min with Syt antibodies targeting the luminal side of the synaptic vesicle protein, which were diluted (1:200) in the same original NB medium supplemented with 50 μ M bicuculline at 37°C in 5% CO₂. Next, cells were fixed, stained with secondary antibodies, and subjected to image quantifications and analysis.

Image quantification and analysis

Quantifications of fluorescent Syt intensity at presynaptic boutons: Presynaptic boutons were identified by swellings along the axon using expressed RFP as fill, similar as described previously (Bamji et al, 2003; Leal-Ortiz et al, 2008; Spangler et al, 2013). Fluorescent intensity of internalized Syt at each bouton was measured using a circular region of interest with a fixed size of \varnothing 1.39 μ m/ \varnothing 7 pix.

SCRN1 knockdown quantifications: SCRN1 knockdown efficiency was analyzed in cortical neurons (DIV4) co-transfected with RFP and a single SCRN1 shRNA. The average fluorescence intensity was measured of the somatic region without nucleus.

Quantifications of SCRN1 recruitment and ER morphology: For analyzing SCRN1 recruitment to ER in COS7 cells, the number of cells showing obvious enriched SCRN1 localization at ER structures was scored. For analyzing reticular ER structures in COS7 cells, the number of cells containing less than \sim 30% detectable ER tubules in cytoplasm was scored as “non-reticular ER localization”.

Live-cell imaging

Live-cell imaging (other than electric field stimulation experiments) was conducted on an inverted microscope Nikon Eclipse Ti-E (Nikon), equipped with a Plan Apo VC 100x NA 1.40 oil objective (Nikon), Plan Apo VC 60x N.A. 1.40 oil objective (Nikon), a Plan Apo VC 40x NA 1.40 oil objective (Nikon), a Yokogawa CSU-X1-A1 spinning disk confocal unit (Roper Scientific), a Photometrics Evolve 512 EMCCD camera (Roper Scientific), and an incubation chamber (Tokai Hit) mounted on a motorized XYZ stage (Applied Scientific Instrumentation), all controlled by MetaMorph (Molecular Devices) software. Cells were imaged in their original medium. During acquisition, the objective was kept at 37°C and the imaging chamber was kept at 37°C in 5% CO₂.

Relative basal Ca²⁺ levels' measurements

Hippocampal neurons were transfected with Ca²⁺ indicators GCaMP6f or R-GECO1, and mRFP or GFP to identify transfected neurons and presynaptic boutons. Field of views with axonal structures for all conditions were selected based on similar expression levels, while remaining blind for the expression levels of Ca²⁺ indicators. Duo-color time-lapses were acquired of 21 frames with 30-s time interval, with a Z-stack of three planes with 0.5- μ m interval for each frame, and cells were treated with 1–10 μ M ionomycin (Santa Cruz, SC3592) prior to frame 13. Fluorescent intensities of GCaMP6f or R-GECO1 at single boutons were measured for the maximum intensity projections of each frame using a fixed ROI. Fluorescent values were corrected for background fluorescence and normalized to the maximum fluorescent intensity within seven frames after ionomycin treatment (F/F

max). Relative basal Ca^{2+} levels were determined by the F_0/F_{max} ratio, where baseline values (F_0) were obtained by averaging the fluorescent intensities of the five frames prior to ionomycin treatment.

Fluorescent recovery after photo-bleaching

Fluorescent recovery after photo-bleaching experiments were conducted on the characteristic dense ER clusters in TagRFP-ER expressing hippocampal neurons showing this phenotype, or in regular dense ER structures for control conditions, using the ILas system (Roper Scientific; Fig 4E). Fluorescence recovery of TagRFP-ER in bleached regions can be interpreted as the result from two processes: (i) diffusion of TagRFP-ER within existing ER tubules (Yalcin et al, 2017) and (ii) local ER remodeling within the photo-bleached region. The FRAP area size and imaging settings were kept the same for all conditions. For analysis, fluorescence intensity of the bleached region was corrected for background noise and for overall bleaching occurring during acquisition. Next, the post-bleaching fluorescent recovery values were normalized to the baseline fluorescence, which was defined by the average fluorescent intensity of five initial frames prior to onset of photo-bleaching.

Electric field stimulation and real-time Ca^{2+} dynamics

All experiments were carried out in modified Tyrode's solution (pH 7.4, 25 mM HEPES, 119 mM NaCl, 2.4 mM KCl, 2 mM CaCl_2 , 2 mM MgCl_2 , 30 mM glucose). Objective was prewarmed to 37°C with objective heater (Tokai Hit). Hippocampal neurons were placed in a stimulation chamber (World Precision Instruments) and stimulated (50 Aps, 20 Hz) by electric field stimulation (platinum electrodes, 10 mm spacing, 1 ms pulses of 50 mA, alternating polarity) applied by constant current stimulus isolator (WPIA 385, World Precision Instruments) in the presence of 10 μM 6-cyano-7 nitroquinoxaline-2,3-dione and 50 μM D,L-2-amino-5-phosphonovaleric acid (CNQX/AP5; Tocris Bioscience). Imaging was performed on an inverted Nikon Eclipse TE2000 microscope equipped with mercury lamp (Nikon). Fluorescence emission was detected using a 40 \times oil-immersion objective [Nikon Apo, numerical aperture (NA) 1.3] and ET-GFP filter (GCaMP) or ET-mCherry (mCherry), together with a EMCCD camera (Evolve 512, Photometrics) controlled by MetaMorph 7.7 software (Molecular Devices). Images were acquired every 650 ms with exposure times between 50 and 100 ms in 1 \times 1 binning mode. Quantitative analyses of GCaMP experiments were performed with custom macros in Igor Pro (WaveMetrics) using an automated detection algorithm as described previously (Wienisch & Klingauf, 2006).

Statistical analysis

Statistical details are included in corresponding Figure legends. P-values are annotated as follows: *P < 0.05, **P < 0.01, and ***P < 0.001. Data processing and statistical analysis were conducted in Prism GraphPad (version 7.0) software.

REFERENCES

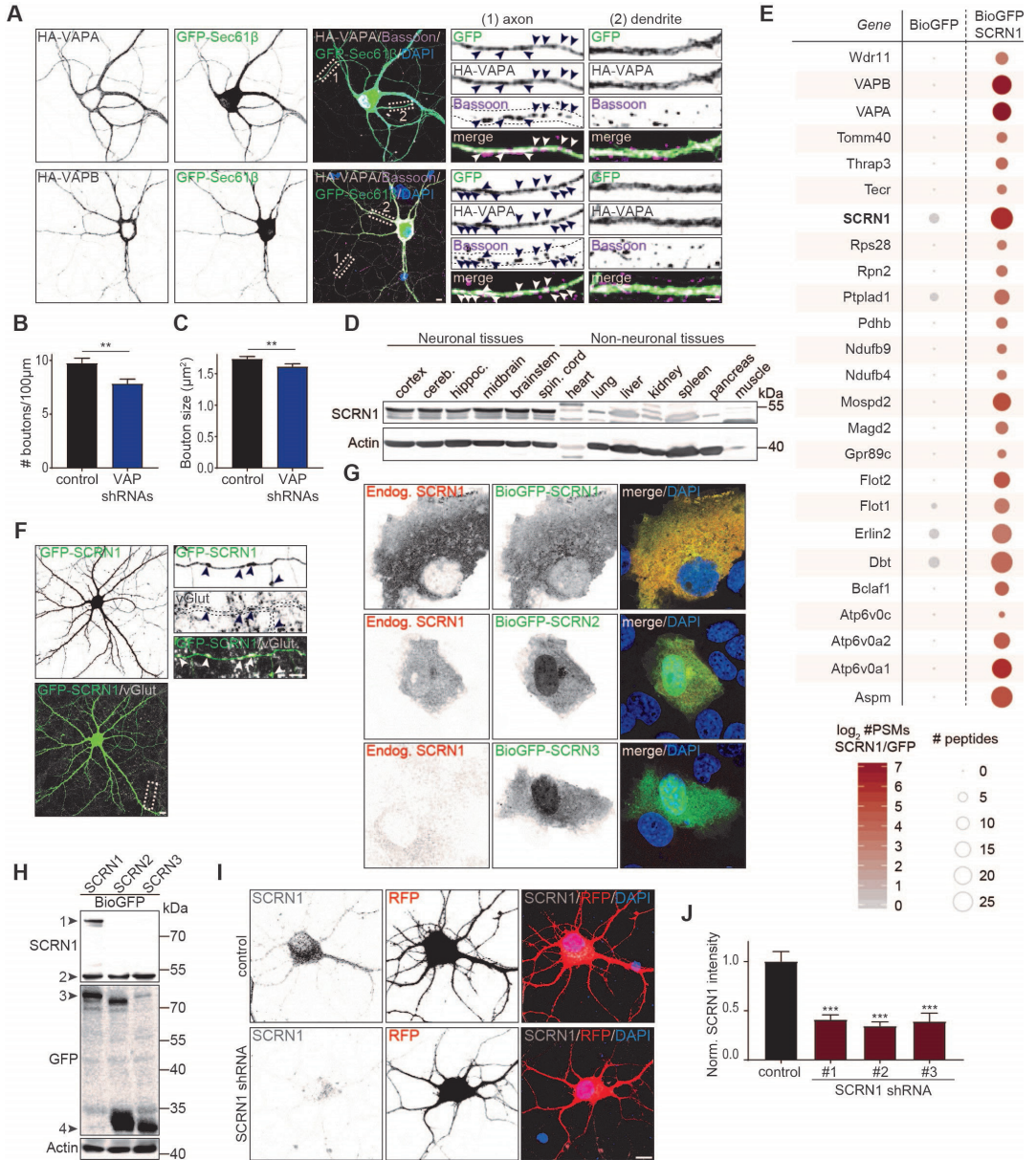
- Bamji, S. X., K. Shimazu, N. Kimes, J. Huelsken, W. Birchmeier, B. Lu, and L. F. Reichardt. 2003. 'Role of beta-catenin in synaptic vesicle localization and presynaptic assembly', *Neuron*, 40: 719-31.
- Brummelkamp, T. R., R. Bernards, and R. Agami. 2002. 'A system for stable expression of short interfering RNAs in mammalian cells', *Science*, 296: 550-3.
- Cunha-Ferreira, I., A. Chazeau, R. R. Buijs, R. Stucchi, L. Will, X. Pan, Y. Adolfs, C. van der Meer, J. C. Wolthuis, O. I. Kahn, P. Schatzle, M. Altelaar, R. J. Pasterkamp, L. C. Kapitein, and C. C. Hoogenraad. 2018. 'The HAUS Complex Is a Key Regulator of Non-centrosomal Microtubule Organization during Neuronal Development', *Cell Rep*, 24: 791-800.
- de Boer, E., P. Rodriguez, E. Bonte, J. Krijgsveld, E. Katsantoni, A. Heck, F. Grosveld, and J. Strouboulis. 2003. 'Efficient biotinylation and single-step purification of tagged transcription factors in mammalian cells and transgenic mice', *Proc Natl Acad Sci U S A*, 100: 7480-5.
- De Gregorio, C., R. Delgado, A. Ibacache, J. Sierralta, and A. Couve. 2017. '*Drosophila* Atlastin in motor neurons is required for locomotion and presynaptic function', *J Cell Sci*, 130: 3507-16.
- de Jong, A. P. H., C. M. Roggero, M. R. Ho, M. Y. Wong, C. A. Brautigam, J. Rizo, and P. S. Kaeser. 2018. 'RIM C2B Domains Target Presynaptic Active Zone Functions to PIP2-Containing Membranes', *Neuron*, 98: 335-49.e7.
- de Juan-Sanz, J., G. T. Holt, E. R. Schreiter, F. de Juan, D. S. Kim, and T. A. Ryan. 2017. 'Axonal Endoplasmic Reticulum Ca(2+) Content Controls Release Probability in CNS Nerve Terminals', *Neuron*, 93: 867-81.e6.
- Esteves, T., A. Durr, E. Mundwiler, J. L. Loureiro, M. Boutry, M. A. Gonzalez, J. Gauthier, K. H. El-Hachimi, C. Depienne, M. P. Muriel, R. F. Acosta Lebrigio, M. Gaussen, A. Noreau, F. Speziani, A. Dionne-Laporte, J. F. Deleuze, P. Dion, P. Coutinho, G. A. Rouleau, S. Zuchner, A. Brice, G. Stevanin, and F. Darios. 2014. 'Loss of association of REEP2 with membranes leads to hereditary spastic paraplegia', *Am J Hum Genet*, 94: 268-77.
- Hazan, J., N. Fonknechten, D. Mavel, C. Paternotte, D. Samson, F. Artiguenave, C. S. Davoine, C. Cruaud, A. Durr, P. Wincker, P. Brottier, L. Cattolico, V. Barbe, J. M. Burgunder, J. F. Prud'homme, A. Brice, B. Fontaine, B. Heilig, and J. Weissenbach. 1999. 'Spastin, a new AAA protein, is altered in the most frequent form of autosomal dominant spastic paraplegia', *Nat Genet*, 23: 296-303.
- Hoogenraad, C. C., A. D. Milstein, I. M. Ethell, M. Henkemeyer, and M. Sheng. 2005. 'GRIP1 controls dendrite morphogenesis by regulating EphB receptor trafficking', *Nat Neurosci*, 8: 906-15.
- Hradsky, J., V. Raghuram, P. P. Reddy, G. Navarro, M. Hupe, V. Casado, P. J. McCormick, Y. Sharma, M. R. Kreutz, and M. Mikhaylova. 2011. 'Post-translational membrane insertion of tail-anchored transmembrane EF-hand Ca²⁺ sensor calneurons requires the TRC40/Asna1 protein chaperone', *J Biol Chem*, 286: 36762-76.
- Jaworski, J., L. C. Kapitein, S. M. Gouveia, B. R. Dortland, P. S. Wulf, I. Grigoriev, P. Camera, S. A. Spangler, P. Di Stefano, J. Demmers, H. Krugers, P. Defilippi, A.

- Akhmanova, and C. C. Hoogenraad. 2009. 'Dynamic microtubules regulate dendritic spine morphology and synaptic plasticity', *Neuron*, 61: 85-100.
- Kaiser, S. E., J. H. Brickner, A. R. Reilein, T. D. Fenn, P. Walter, and A. T. Brunger. 2005. 'Structural basis of FFAT motif-mediated ER targeting', *Structure*, 13: 1035-45.
- Kuijpers, M., V. van Dis, E. D. Haasdijk, M. Harterink, K. Vocking, J. A. Post, W. Scheper, C. C. Hoogenraad, and D. Jaarsma. 2013. 'Amyotrophic lateral sclerosis (ALS)-associated VAPB-P56S inclusions represent an ER quality control compartment', *Acta Neuropathol Commun*, 1: 24.
- Lauwers, E., R. Goodchild, and P. Verstreken. 2016. 'Membrane Lipids in Presynaptic Function and Disease', *Neuron*, 90: 11-25.
- Leal-Ortiz, S., C. L. Waites, R. Terry-Lorenzo, P. Zamorano, E. D. Gundelfinger, and C. C. Garner. 2008. 'Piccolo modulation of Synapsin1a dynamics regulates synaptic vesicle exocytosis', *J Cell Biol*, 181: 831-46.
- Lin, S., T. Jiang, Y. Yu, H. Tang, S. Lu, Z. Peng, and J. Fan. 2015. 'Secernin-1 contributes to colon cancer progression through enhancing matrix metalloproteinase-2/9 exocytosis', *Dis Markers*, 2015: 230703.
- Loewen, C. J., A. Roy, and T. P. Levine. 2003. 'A conserved ER targeting motif in three families of lipid binding proteins and in Opi1p binds VAP', *Embo j*, 22: 2025-35.
- Montenegro, G., A. P. Rebelo, J. Connell, R. Allison, C. Babalini, M. D'Aloia, P. Montieri, R. Schule, H. Ishiura, J. Price, A. Strickland, M. A. Gonzalez, L. Baumbach-Reardon, T. Deconinck, J. Huang, G. Bernardi, J. M. Vance, M. T. Rogers, S. Tsuji, P. De Jonghe, M. A. Pericak-Vance, L. Schols, A. Orlandi, E. Reid, and S. Zuchner. 2012. 'Mutations in the ER-shaping protein reticulon 2 cause the axon-degenerative disorder hereditary spastic paraplegia type 12', *J Clin Invest*, 122: 538-44.
- Muallem, S., W. Y. Chung, A. Jha, and M. Ahuja. 2017. 'Lipids at membrane contact sites: cell signaling and ion transport', *EMBO Rep*, 18: 1893-904.
- Murphy, S. E., and T. P. Levine. 2016. 'VAP, a Versatile Access Point for the Endoplasmic Reticulum: Review and analysis of FFAT-like motifs in the VAPome', *Biochim Biophys Acta*, 1861: 952-61.
- Nishimura, A. L., M. Mitne-Neto, H. C. Silva, A. Richieri-Costa, S. Middleton, D. Cascio, F. Kok, J. R. Oliveira, T. Gillingwater, J. Webb, P. Skehel, and M. Zatz. 2004. 'A mutation in the vesicle-trafficking protein VAPB causes late-onset spinal muscular atrophy and amyotrophic lateral sclerosis', *Am J Hum Genet*, 75: 822-31.
- Paillasson, S., P. Gomez-Suaga, R. Stoica, D. Little, P. Gissen, M. J. Devine, W. Noble, D. P. Hanger, and C. C. J. Miller. 2017. 'alpha-Synuclein binds to the ER-mitochondria tethering protein VAPB to disrupt Ca(2+) homeostasis and mitochondrial ATP production', *Acta Neuropathol*, 134: 129-49.
- Pearce, M. M., Y. Wang, G. G. Kelley, and R. J. Wojcikiewicz. 2007. 'SPFH2 mediates the endoplasmic reticulum-associated degradation of inositol 1,4,5-trisphosphate receptors and other substrates in mammalian cells', *J Biol Chem*, 282: 20104-15.
- Pearce, M. M., D. B. Wormer, S. Wilkens, and R. J. Wojcikiewicz. 2009. 'An endoplasmic reticulum (ER) membrane complex composed of SPFH1 and SPFH2 mediates the ER-associated degradation of inositol 1,4,5-trisphosphate

receptors', *J Biol Chem*, 284: 10433-45.

- Pei, J., and N. V. Grishin. 2003. 'Peptidase family U34 belongs to the superfamily of N-terminal nucleophile hydrolases', *Protein Sci*, 12: 1131-5.
- Schatzle, P., M. Esteves da Silva, R. P. Tas, E. A. Katrukha, H. Y. Hu, C. J. Wierenga, L. C. Kapitein, and C. C. Hoogenraad. 2018. 'Activity-Dependent Actin Remodeling at the Base of Dendritic Spines Promotes Microtubule Entry', *Curr Biol*, 28: 2081-93.e6.
- Skehel, P. A., K. C. Martin, E. R. Kandel, and D. Bartsch. 1995. 'A VAMP-binding protein from *Aplysia* required for neurotransmitter release', *Science*, 269: 1580-3.
- Snapp, E. L., A. Sharma, J. Lippincott-Schwartz, and R. S. Hegde. 2006. 'Monitoring chaperone engagement of substrates in the endoplasmic reticulum of live cells', *Proc Natl Acad Sci U S A*, 103: 6536-41.
- Spangler, S. A., S. K. Schmitz, J. T. Kevenaar, E. de Graaff, H. de Wit, J. Demmers, R. F. Toonen, and C. C. Hoogenraad. 2013. 'Liprin-alpha2 promotes the presynaptic recruitment and turnover of RIM1/CASK to facilitate synaptic transmission', *J Cell Biol*, 201: 915-28.
- Summerville, J. B., J. F. Faust, E. Fan, D. Pendin, A. Daga, J. Formella, M. Stern, and J. A. McNew. 2016. 'The effects of ER morphology on synaptic structure and function in *Drosophila melanogaster*', *J Cell Sci*, 129: 1635-48.
- Terasaki, M. 2018. 'Axonal endoplasmic reticulum is very narrow', *J Cell Sci*, 131.
- Teuling, E., S. Ahmed, E. Haasdijk, J. Demmers, M. O. Steinmetz, A. Akhmanova, D. Jaarsma, and C. C. Hoogenraad. 2007. 'Motor neuron disease-associated mutant vesicle-associated membrane protein-associated protein (VAP) B recruits wild-type VAPs into endoplasmic reticulum-derived tubular aggregates', *J Neurosci*, 27: 9801-15.
- Venkatachalam, V., and A. E. Cohen. 2014. 'Imaging GFP-based reporters in neurons with multiwavelength optogenetic control', *Biophys J*, 107: 1554-63.
- Wang, S., H. Tukachinsky, F. B. Romano, and T. A. Rapoport. 2016. 'Cooperation of the ER-shaping proteins atlastin, lunapark, and reticulons to generate a tubular membrane network', *Elife*, 5.
- Way, G., N. Morrice, C. Smythe, and A. J. O'Sullivan. 2002. 'Purification and identification of secernin, a novel cytosolic protein that regulates exocytosis in mast cells', *Mol Biol Cell*, 13: 3344-54.
- Wienisch, M., and J. Klingauf. 2006. 'Vesicular proteins exocytosed and subsequently retrieved by compensatory endocytosis are nonidentical', *Nat Neurosci*, 9: 1019-24.
- Wu, H., P. Carvalho, and G. K. Voeltz. 2018. 'Here, there, and everywhere: The importance of ER membrane contact sites', *Science*, 361.
- Wu, Y., C. Whiteus, C. S. Xu, K. J. Hayworth, R. J. Weinberg, H. F. Hess, and P. De Camilli. 2017. 'Contacts between the endoplasmic reticulum and other membranes in neurons', *Proc Natl Acad Sci U S A*, 114: E4859-e67.
- Yalcin, B., L. Zhao, M. Stofanko, N. C. O'Sullivan, Z. H. Kang, A. Roost, M. R. Thomas, S. Zaessinger, O. Blard, A. L. Patto, A. Sohail, V. Baena, M. Terasaki, and C. J. O'Kane. 2017. 'Modeling of axonal endoplasmic reticulum network by spastic paraplegia proteins', *Elife*, 6.

- Zhao, X., D. Alvarado, S. Rainier, R. Lemons, P. Hedera, C. H. Weber, T. Tükel, M. Apak, T. Heiman-Patterson, L. Ming, M. Bui, and J. K. Fink. 2001. 'Mutations in a newly identified GTPase gene cause autosomal dominant hereditary spastic paraplegia', *Nat Genet*, 29: 326-31.
- Zuchner, S., G. Wang, K. N. Tran-Viet, M. A. Nance, P. C. Gaskell, J. M. Vance, A. E. Ashley-Koch, and M. A. Pericak-Vance. 2006. 'Mutations in the novel mitochondrial protein REEP1 cause hereditary spastic paraplegia type 31', *Am J Hum Genet*, 79: 365-9.

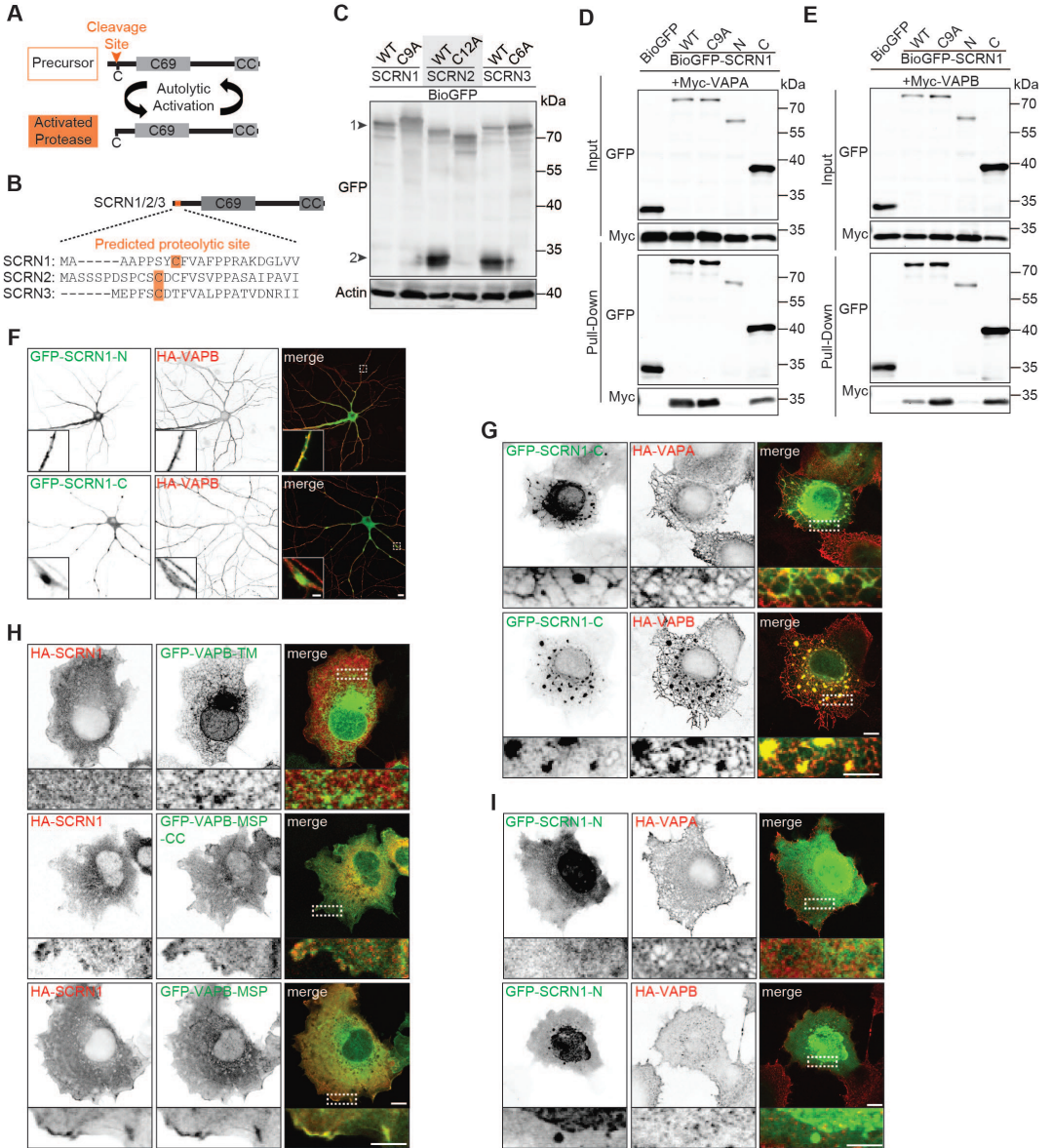


Supplementary Figure 1.

VAPs modulate bouton maintenance and are associated with brain-enriched SCRN1 proteins

- A.** Localization of exogenous HA-VAPA or HA-VAPB in neurons (DIV18) co-expressing GFP-Sec61 β and immunostained for bassoon. Zooms represent (1) an axonal structure with bassoon-positive presynaptic boutons (arrowheads), and (2) a dendritic structure. Scale bars: 10 μ m (full size) and 5 μ m (zoom).
- B.** Quantifications of bouton density in hippocampal neurons (DIV18) co-expressing RFP and pSuper empty vector or VAPA/B shRNAs. N = 2, n = 80 boutons.
- C.** Quantifications of bouton size in hippocampal neurons (DIV18) co-expressing RFP and pSuper empty vector or VAPA/B shRNAs. N = 2, n = 380–400 boutons.
- D.** Western blot of endogenous SCRN1 expression in indicated adult rat neuronal and non-neuronal tissues. Cereb., cerebellum. Hippoc., hippocampus. Spin., spinal.
- E.** Scaled representation of SCRN1-associated proteins identified with pull-down assay followed by mass spectrometry analysis of purified BioGFP or BioGFP-SCRN1 from HEK293T cell lysates. Selected candidates all showed > 10 enrichment of PSM compared to control.
- F.** Localization of exogenous GFP-SCRN1 in hippocampal neurons (DIV18) immunostained for vGlut. Zoom represents an axon structure with presynaptic sites (arrowheads). Scale bars: 10 μ m (full size) and 5 μ m (zoom).
- G.** COS7 cells expressing BioGFP-SCRN1, BioGFP-SCRN2, or BioGFP-SCRN3 and immunostained for SCRN1. Scale bar: 10 μ m.
- H.** Western blot of lysates from HEK293T cells expressing BioGFP-SCRN1, BioGFP-SCRN2, or BioGFP-SCRN3 and immunostained for indicated antibodies. Arrowheads represent (1) BioGFP-SCRN1 expression, (2) endogenous SCRN1 expression, (3) full-length BioGFP-SCRN proteins, and (4) N-terminal cleaved BioGFP-SCRN2 and BioGFP-SCRN3. Actin was used as loading control.
- I.** Cortical neurons (DIV4) co-expressing RFP with pSuper empty vector (control) or SCRN1 shRNA #1. Scale bar: 10 μ m.
- J.** Quantifications of fluorescence intensity of endogenous SCRN1 in cortical neurons (DIV4) co-expressing RFP with pSuper empty vector (control) or SCRN1 shRNA #1, #2, or #3. N = 2, n = 13–14 cells.

Data information: Data represent mean \pm SEM; **P < 0.01; ***P < 0.001, by Mann–Whitney U-test. Source data are available online for this Figure.



4

Supplementary Figure 2.

SCRN1 does not exhibit proteolytic activity and its C-terminal is recruited to VAP MSP domain

A. Schematic illustration of autolytic protease activation of C69 family members.

B. Sequence alignment of predicted proteolytic sites of SCRN family members according to the MEROPS database.

C. Western blot of lysates from HEK293T cells expressing BioGFP-SCRN1-WT, BioGFP-SCRN1-C9A, BioGFP-SCRN2-WT, BioGFP-SCRN2-C12A, BioGFP-SCRN3-WT, or BioGFP-SCRN3-C6A. Arrowheads represent (1) full-length BioGFP-SCRN proteins and (2) N-terminal cleaved BioGFP-SCRN2 and BioGFP-SCRN3.

D. Pull-down assay of HEK293T cells co-expressing Myc-VAPA with BioGFP, BioGFP-SCRN1-WT, BioGFP-SCRN1-C9A, BioGFP-SCRN1-N, or BioGFP-SCRN1-C.

E. Pull-down assay of HEK293T cells co-expressing Myc-VAPB with BioGFP, BioGFP-SCRN1-WT, BioGFP-SCRN1-C9A, BioGFP-SCRN1-N, or BioGFP-SCRN1-C.

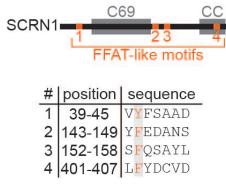
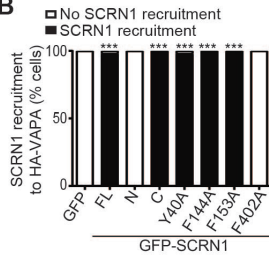
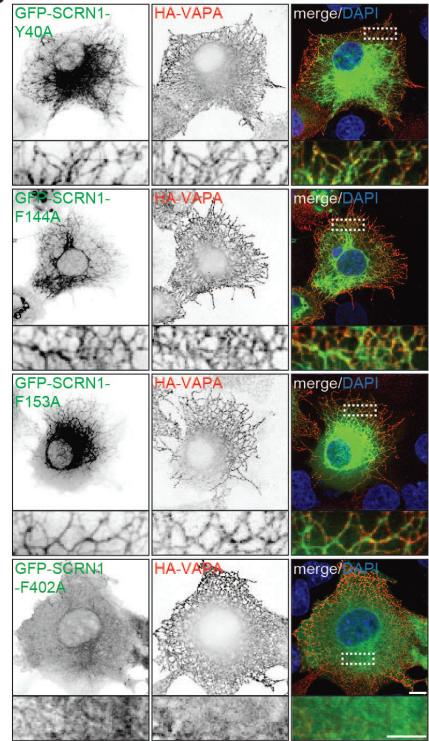
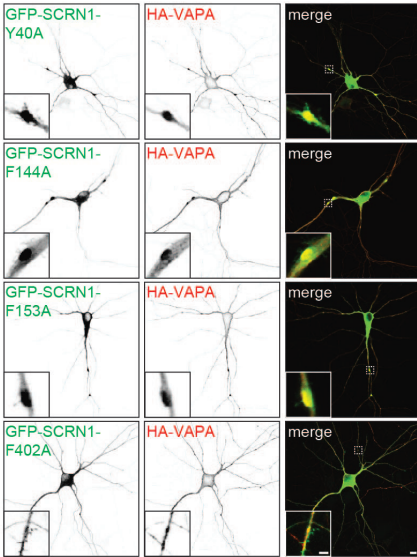
F. Hippocampal neurons (DIV16) co-expressing HA-VAPB with GFP-SCRN1-N or GFP-SCRN1-C. Scale bars: 10 μm (full size) and 2 μm (zoom).

G. COS7 cells co-expressing GFP-SCRN1-C with HA-VAPA or HA-VAPB. Scale bars: 10 μm (full size) and 5 μm (zoom).

H. COS7 cells co-expressing HA-SCRN1 with GFP-VAPB-TM, GFP-VAPB-MSP-CC, or GFP-VAPB-MSP. Scale bars: 10 μm (full size) and 5 μm (zoom).

I. COS7 cells co-expressing GFP-SCRN1-N with HA-VAPA or HA-VAPB. Scale bars: 10 μm (full size) and 5 μm (zoom).

Source data are available online for this Figure.

A**B****C****D**

4

Supplementary Figure 3.

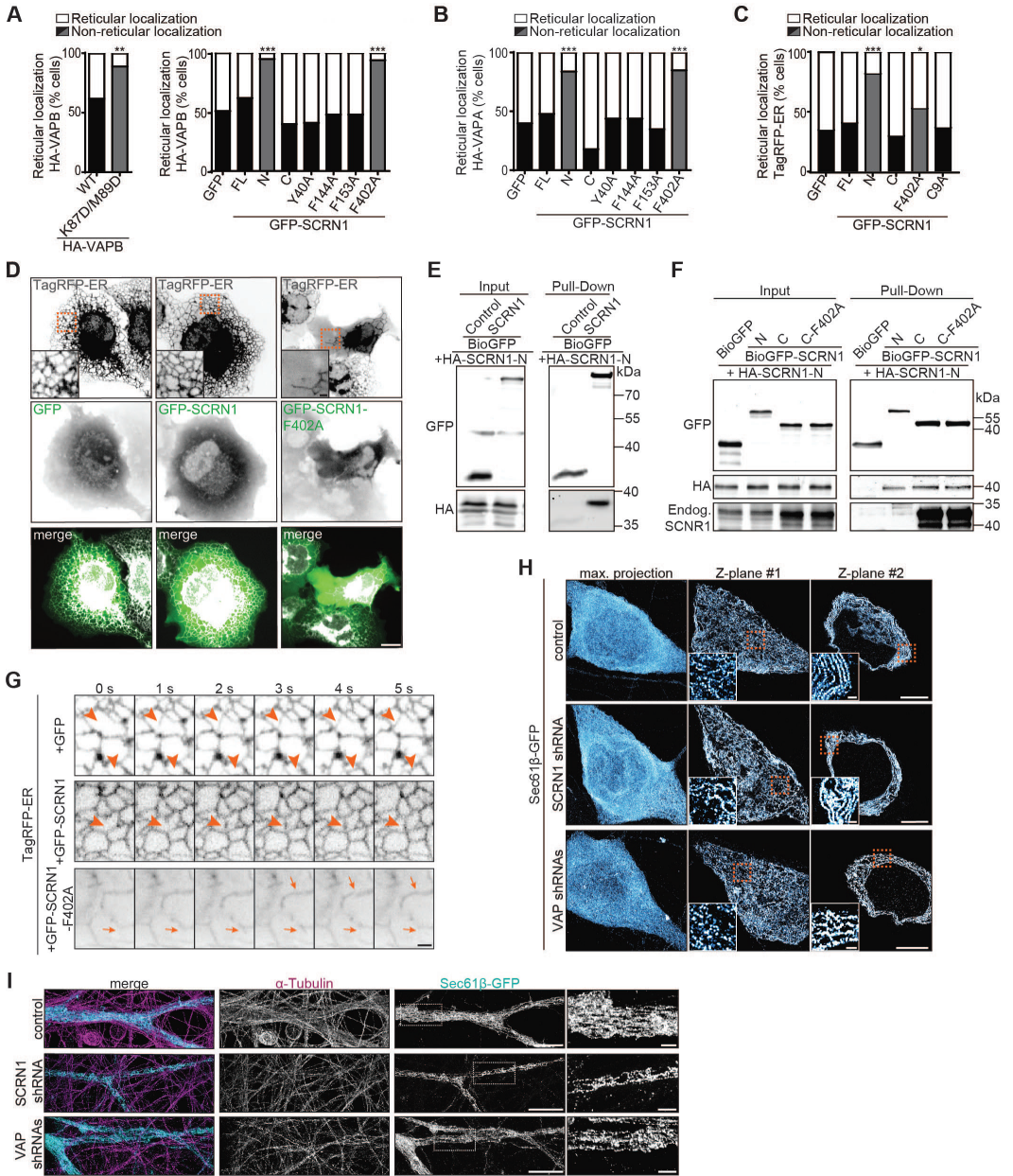
VAP-SCRN1 interaction at the ER is mediated by a single FFAT-like motif

A. Schematic representation of the four potential FFAT-like motifs in SCRN1. Amino acid position number 2 (orange) of the FFAT-like motifs was mutated to alanine residues.

B. Quantifications of SCRN1 recruitment to VAPA-positive structures in COS7 cells (%) co-expressing HA-VAPA with GFP or GFP-SCRN1, GFP-SCRN1-N, GFP-SCRN1-C, GFP-SCRN1-Y40A, GFP-SCRN1-F144A, GFP-SCRN1-F153A, or GFP-SCRN1-F402A. N = 2–3, n = 39–59.

C. COS7 cells co-expressing HA-VAPA with GFP-SCRN1-Y40A, GFP-SCRN1-F144A, GFP-SCRN1-F153A, or GFP-SCRN1-F402A. Scale bars: 10 μm (full size) and 5 μm (zoom).

D. Hippocampal neurons (DIV16) co-expressing HA-VAPA with GFP-SCRN1-Y40A, GFP-SCRN1-F144A, GFP-SCRN1-F153A, or GFP-SCRN1-F402A. Scale bars: 10 μm (full size) and 5 μm (zoom). Data information: ***P < 0.001, by chi-square test with post hoc analysis including Bonferroni correction.



4

Supplementary Figure 4.

SCRN1 oligomerizes and regulates ER remodeling together with VAP

A. Quantifications of reticular localization of expressed VAPB in COS7 cells (%). Cells with non-reticular ER structures contained < 30% detectable ER tubules in cytoplasm. Gray bars represent non-reticular localization accompanied with impaired VAP-SCRN1 interaction. Left: co-expression GFP-SCRN1 with HA-VAPB or HA-VAPB-K87D/M89D (N = 2–3, n = 44–46). Right: co-expression of HA-VAPB with GFP or GFP-SCRN1, GFP-SCRN1-N, GFP-SCRN1-C, GFP-SCRN1-Y40A, GFP-SCRN1-F144A, GFP-SCRN1-F153A, or GFP-SCRN1-F402A (N = 2–3, n = 41–64).

B. Quantifications of reticular localization in COS7 cells (%) co-expressing HA-VAPA with GFP or GFP-SCRN1, GFP-SCRN1-N, GFP-SCRN1-C, GFP-SCRN1-Y40A, GFP-SCRN1-F144A, GFP-SCRN1-F153A, or GFP-SCRN1-F402A. Cells with non-reticular ER structures contained < 30% detectable ER tubules in cytoplasm. Gray bars represent non-reticular localization accompanied with impaired VAP-SCRN1 interaction. N = 2–3, n = 39–62 cells.

C. Quantifications of reticular localization of TagRFP-ER co-expressed with GFP, GFP-SCRN1, GFP-SCRN1-N, GFP-SCRN1-C, GFP-SCRN1-F402A, or GFP-SCRN1-C9A in COS7 cells. Gray bars represent non-reticular localization accompanied with impaired VAP-SCRN1 interaction. Cells with non-reticular ER structures contained < 30% detectable ER tubules in cytoplasm. N = 2–4, n = 58–120.

D. Live COS7 cells co-expressing TagRFP-ER with GFP, GFP-SCRN1, or GFP-SCRN1-F402A. Scale bars: 10 μ m (full size) and 2 μ m (zoom).

E. Pull-down assay of HEK293T cells co-expressing HA-SCRN1-N with BioGFP and BioGFP-SCRN1.

F. Pull-down assay of HEK293T cells co-expressing HA-SCRN1-N with BioGFP, BioGFP-SCRN1-N, BioGFP-SCRN1-C, and BioGFP-SCRN1-F402A.

G. Time-lapse of COS7 cells co-expressing TagRFP-ER and GFP, GFP-SCRN1, or GFP-SCRN1-F402A. Arrowheads mark ER tubule remodeling event, and arrows mark ER remodeling artifacts. Scale bar: 2 μ m.

H. ER nanostructures in somatic structures of hippocampal neurons (DIV18) co-expressing GFP-Sec61 β with pSuper empty vector, SCRN1 shRNA, or VAPA/B shRNAs, and subjected to expansion microscopy. Left panels show maximum intensity projections of all Z-planes. Individual ER tubules and perinuclear sheets are shown in zooms of Z-plane #1 and Z-plane #2, respectively. Scale bars: 5 μ m (full size) and 500 nm (zoom).

I. ER nanostructures visualized with GFP-Sec61 β in dendrites of hippocampal neurons (DIV18) immunostained for α -tubulin and co-expressed with pSuper empty vector, SCRN1 shRNA, or VAPA/B shRNAs, and subjected to expansion microscopy. Scale bars: 5 μ m (full size) and 1 μ m (zoom).

Data information: *P < 0.05; **P < 0.01; ***P < 0.001, by chi-square test (**A–C**) with post hoc analysis including Bonferroni correction (**A, B**). Source data are available online for this Figure.

5.



General discussion

Feline W. Lindhout¹

¹Cell Biology, Neurobiology and Biophysics, Department of Biology, Faculty of Science, Utrecht University, 3584 CH Utrecht, The Netherlands.

Axons are unique structures that are fundamental for information processing in neuronal networks, as they facilitate neurotransmission and maintain neuronal polarity. To carry-out these specialized functions, axons adopt extreme morphologies and characteristic substructures during development. The work in this thesis features new molecular insights in axon formation as well as axon functioning (*Chapter 2, 3 and 4*). To summarize, in *Chapter 2* a new axon developmental stage is identified in human neurons, which reveals that axon formation follows a global distal-to-proximal reorganization in the developing axon. The formation of an axon is driven by extensive remodeling of the microtubule cytoskeleton network, and *Chapter 3* demonstrates that this process critically relies on centrosome function. *Chapter 4* focuses on the functioning of mature axons, and unravels a new molecular interplay between the endoplasmic reticulum (ER) and the synaptic vesicle cycle at presynaptic sites. The implications of these findings are largely discussed in their corresponding chapters. This chapter primarily focuses on discussing the key findings of this thesis in a broader context, and provides future research questions and perspectives.

Novel insights in axon formation from human neurons

Axon development is a highly coordinated multistep process, and the onset of axon development marks the first step in establishing neuronal polarity. Most insights in the molecular processes underlying axon development are obtained from non-human model systems, and in particular from the classical dissociated rodent neuron cultures (Dotti, Sullivan, and Banker 1988). However, it remains to be established to what extent the axon developmental processes identified in non-human species are recapitulated in humans. Moreover, axon development in cultured dissociated rodent neurons likely entails a repolarization event rather than *de novo* polarization, as these dissociated neurons in culture are obtained from yet polarized neurons *in vivo* (Dotti, Sullivan, and Banker 1988). *Chapter 2 and 3* address new biological questions regarding axon development in human neurons, using human induced Pluripotent Stem Cells (iPSC)-derived neuron cultures, which has resulted in new insights and updated views on axon developmental processes (Figure 1) (Lancaster et al. 2013). An important hallmark of human iPSC-derived neurons that significantly contributed in obtaining these new insights, is their profound longer developmental trajectory compared to other species (Dotti, Sullivan, and Banker 1988; Petanjek et al. 2011; Shi, Kirwan, and Livesey 2012; Espuny-Camacho et al. 2013; Nicholas et al. 2013; Otani et al. 2016; Sousa et al. 2017; Linaro et al. 2019) (*Chapter 2*). These species-specific differences in timing of neurodevelopment are consistently observed, also in more closely-related primate species such as humans and macaques (Otani et al. 2016). In fact, this prolonged human-specific developmental timing is even maintained when human neurons are transplanted in rodent brains or when human neurons are co-cultured with macaque neurons (Espuny-Camacho et al. 2013; Nicholas et al. 2013; Otani et al. 2016; Linaro et al. 2019). Together, this implies that neurodevelopmental timing in different species is orchestrated by robust and cell-intrinsic mechanisms. What controls this internal molecular clock in neuronal cells? It would be interesting to direct future studies in addressing this question, as mechanistic insights are still lacking at this point.

The prolonged development of human iPSC-derived neurons makes it a particularly interesting model system to study developmental processes that typically occur at relative fast rates, such as the first steps of axon development. Specifically, the process of axon formation, involving axon specification and axon initial segment (AIS) assembly, occurs after ~24-48 hours in dissociated rodent neurons, whereas this takes ~7-14 days in human iPSC-derived neurons (Dotti, Sullivan, and Banker 1988) (*Chapter 2*). This stretched time window of axon development in human neurons increases the temporal resolution to study this process in more detail. As such, *Chapter 2* uncovers a previously unrecognized intermediate stage during early axon development, revealing that axon formation is first initiated distally in the future axon which is next followed by proximal rearrangements (Fig 1). Specifically, this development in a distal-to-proximal fashion is observed for the reorganization towards the axon-specific microtubule network, as well as the appearance and structural assembly of AIS proteins. It remains to be explored how these distal-to-proximal rearrangements are driven mechanistically over time. As indicated by their name, AIS proteins are originally defined by their collective localization at proximal axons, where they assemble into a highly specialized AIS structure (Letierrier 2018). Thus, their distal appearance at immature axons opens up new discussions, and follow-up studies are necessary to reassess the function of AIS proteins during early axon development. In conclusion, future studies may identify more novel axon developmental processes and dissect its molecular details, and the potential human iPSC-derived neuron cultures to address this is illustrated in *Chapter 2 and 3*.

Centrosomes, as microtubule-organizing organelles, are important for axon formation

Axon formation starts with the by accelerated outgrowth of a single neurite, the future axon. These drastic morphological changes are driven by structural rearrangements of the local microtubule cytoskeleton. *Chapter 3* reveals that this process critically depends on the centrosome, the organelle acting as the main microtubule-organizing center in cells (Figure 1). Depleting neuronal stem cells of centrioles, the core components of centrosomes, results in impaired axon-specific microtubule remodeling at later stages. This is accompanied by additional axon developmental defects, including immature firing of action potentials, mistargeting of the axonal microtubule-associated protein Trim46, suppressed expression of growth cone proteins and impaired growth cone morphologies. Together, these data reveal that centrosomes are indispensable for microtubule remodeling during early axon development, which is important for setting-up the foundation for subsequent axon maturation and functioning. Previous studies reported contradicting results on the interplay between centrosomes and axon formation, resulting in an ongoing debate on the function of centrosomes during this developmental process (Zmuda and Rivas 1998; de Anda et al. 2005; Stiess et al. 2010; Meka, Scharrenberg, and Calderon de Anda 2020). Accumulating evidence revealed that centrosomes are positioned at sites where the new axon emerges, indicating that a possible mechanistic link between localized centrosome

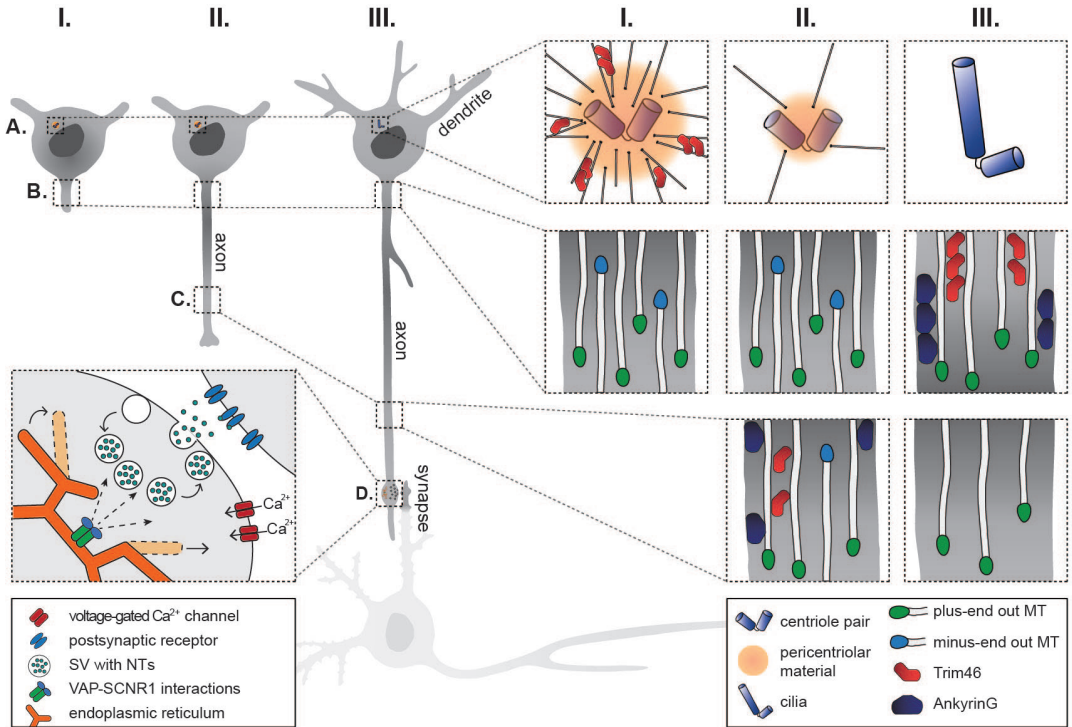


Figure 1.

Updated views on molecular processes underlying axon formation and functioning

A. Centrosomes display microtubule-organizing center (MTOC) functions at early stages 1 and 2, which coincides with local presence of Trim46 proteins (I). The MTOC functions of centrosomes are markedly declined in stage 3a neurons (II), and transform into cilia during further neuronal maturation (III).

B,C. The transformation of a non-polarized neurite in a stage 2 neuron (I) into an axon in a stage 3 neuron (II and III) involves the reorganization of the microtubule (MT) cytoskeleton from a mixed to uniform plus-end out orientation, as well as the accumulation and assembly of axon initial segment (AIS) proteins (e.g. Trim46 and AnkyrinG). All these developmental processes occur first at distal axons (C) in stage 3a neurons (II), followed by rearrangements at proximal axons (B) in stage 3b neurons (III).

D. Neurotransmitter (NT) release at presynaptic sites of mature axons (III) is mediated by the synaptic vesicle cycle, involving the local Ca²⁺-driven exocytosis and subsequent retrieval of synaptic vesicles (SVs). The dynamic ER structure plays an important role in synaptic vesicle recycling, which is mediated by molecular interactions between VAP proteins and VAP-interacting protein Secernin-1 (SCRN1).

functioning and axon development might be at play (Zmuda and Rivas 1998; de Anda et al. 2005). However, depleting centrosomes in young polarized neurons did not affect further outgrowth of the yet formed axon, which supported the idea that centrosomes were not important for axon development (Stiess et al. 2010). These contradicting findings are likely explained by the different functions displayed by centrosomes throughout neurodevelopment, as centrosomes gradually lose their microtubule-organizing ability during the process of ciliogenesis (Stiess et al. 2010; Ishikawa and Marshall 2011). Importantly, this developmental process coincides with the time window in which axon outgrowth occurs (Stiess et al. 2010). Accordingly, microtubule-organizing functions of centrosomes are indispensable for neurodevelopmental processes prior to axon outgrowth, such as neurogenesis and the onset of axon formation (Tsai and Gleeson 2005; Lancaster et al. 2013; Nano and Basto 2017; Meka, Scharrenberg, and Calderon de Anda 2020; Stiess et al. 2010) (*Chapter 3*). These processes critically rely on extensive microtubule remodeling, as this supports the drastic morphological changes of the developing axon and establishes the different microtubule organization in axons and dendrites important for polarized cargo transport (van Beuningen and Hoogenraad 2016). The importance of centrosome function during these early neurodevelopmental processes is further illustrated by a wide range of neurodevelopmental disorders, including microcephaly, that are caused by mutations in centrosome proteins (Nano and Basto 2017). At later developmental stages, when the microtubule organization in axons and dendrites is established, the microtubule-organizing functions of centrosomes become perhaps excessive, as indicated by declining MTOC functions of centrosomes after axon formation.

It remains an open question whether the coincident formation of the axon and gradual loss of microtubule-organizing centrosome functions are also mechanistically linked. To this end, new insights may come from studying proteins that show a developmental translocation from centrosomes to axonal microtubules during early axon development. This re-localization process is observed for NDEL proteins in a previous study and Trim46 proteins in *Chapter 3*, and future studies may identify more candidates following this developmental transition (Kuijpers et al. 2016). The observed relocation of Trim46 and NDEL possibly hints for a common underlying mechanism linking centrosome function and axon development, although the precise function and mechanistic details remain elusive. Speculatively, the translocation of these proteins assists in axon specification, the first step in axon development that marks the important developmental switch from stage 2 to stage 3 neurons. This process of axon specification critically relies on extensive remodeling of the local microtubule network, and perhaps the presence of microtubule-associated proteins such as Trim46 and NDEL at future axons mediates this process. As such, the translocation of microtubule-organizing proteins from centrosomes to the specified axon could thereby guide the neuron through the subsequent developmental stage. It remains unknown how the translocation of these proteins from centrosomes to axons is controlled. Considering that centrosomes are important sites for the recruitment of diverse signaling molecules, it

is plausible that this process is mediated by different local intracellular signaling pathways during the transition from stage 2 to stage 3 neurons (Conduit, Wainman, and Raff 2015). Alternatively, the presence of these proteins at both centrosomes and axons perhaps reflect different isoforms of these proteins, which might be differentially expressed in stage 2 and stage 3 neurons. To this end, it is interesting to highlight that humans contain more Trim46 isoforms with yet unknown functions compared to other species, and that the centrosome location of Trim46 is primarily observed in human cells (*Chapter 3*). In conclusion, the functional relevance of centrosomes during the onset of axon development is emerging, and future studies are necessary to unravel the underlying molecular mechanisms.

Emerging roles of the endoplasmic reticulum for presynaptic function

Presynaptic boutons are crucial sites for neurotransmitter release. This is facilitated by the highly controlled synaptic vesicle cycle, in which neurotransmitter-containing synaptic vesicles proceed through cycles of exocytosis and retrieval at presynaptic sites. Many studies in the past decades focused on investigating this synaptic vesicle cycle, which has greatly advanced our understanding of the underlying molecular mechanisms. However, the contribution of abundant presynaptic organelles, such as the ER and mitochondria, in synaptic vesicle recycling is much less explored. The ER and mitochondria present throughout axons, including presynaptic sites, have adopted unique structures. The axonal ER network is marked by extremely narrow ER tubules, which form local networks of small cisternae at presynaptic boutons (Yalcin et al. 2017; Wu et al. 2017; Terasaki 2018). Axonal mitochondria also display a distinctive morphology marked by short and punctate structures, thereby differing from the long and tubular structures observed in dendrites and most other cell types (Chicurel and Harris 1992; Li et al. 2004; Popov et al. 2005; Dickey and Strack 2011; Kasthuri et al. 2015). Mitochondria at presynaptic sites occupy a large volume, up to one-third, of the presynaptic bouton (Wilhelm et al. 2014). The presence and extreme adaptations of the ER and mitochondria at presynaptic boutons and throughout axons are indicative of their relevance for presynaptic function. Indeed, the findings in *Chapter 4* uncovered the importance of the ER structure and its dynamic remodeling for presynaptic function (Fig 1). Here, a new molecular control mechanism for maintaining ER continuity is identified, mediated by the interaction between ER receptor vesicle-associated membrane protein (VAMP)-associated protein B (VAPB) and VAP-interacting protein Secernin-1 (SCRN1). Perturbing ER structure and dynamics, by interfering with VAP-SCRN1 interactions, largely affected presynaptic function. More specifically, the comprised presynaptic function was marked by a reduction in synaptic vesicle recycling, a decrease in evoked Ca^{2+} responses and an increase in basal Ca^{2+} levels at presynaptic boutons. Together, these data imply that the dynamic ER structures are important to maintain local Ca^{2+} levels and facilitate Ca^{2+} influxes at presynaptic sites, thereby modulating synaptic vesicle recycling. This is consistent with the well-described key function of the ribosome-lacking smooth ER, the primary type of ER present in axons, in controlling Ca^{2+} homeostasis (Yalcin et al. 2017; Wu et al. 2017; Terasaki 2018). The important molecular interplay between ER and presynaptic

sites in mammalian neurons presented in *Chapter 4* is further supported by studies in *Drosophila* neurons, where loss of important ER proteins was accompanied with structural ER perturbations as well as reduced neurotransmitter release (Summerville et al. 2016; De Gregorio et al. 2017). Additionally, in dissociated rodent neurons, intraluminal ER Ca^{2+} levels are reported to be elevated during evoked neurotransmission, thereby highlighting an important interplay between the ER and neurotransmitter release (de Juan-Sanz et al. 2017). Thus, *Chapter 4* provides some first molecular insights in the mechanistic link between ER and presynaptic function, and the results presented in this chapter initiated new discussions regarding the role of ER at the synaptic vesicle cycle (Bezprozvanny and Kavalali 2020; Ozturk, O’Kane, and Perez-Moreno 2020). In addition to the ER, the role of mitochondria for presynaptic function also emerges, as presynaptic mitochondria were found to control Ca^{2+} levels and neurotransmitter release at presynaptic sites (Kwon et al. 2016; Vaccaro et al. 2017; Lewis et al. 2018; Lee et al. 2018). In conclusion, presynaptic organelles such as the ER and mitochondria are emerging as important presynaptic components regulating neurotransmitter release, thereby highlighting the relevance of further studying the role of these organelles in synaptic functioning.

Concluding remarks

Mapping the molecular machineries driving axon formation and functioning is key to gain an advanced understanding in axon biology, as this provides an important basis in understanding and ultimately resolving axonal pathologies (axonopathies). To date, most axonopathies (e.g. spinal cord injuries and spastic paraplegia) remain largely unresolved, despite the many studies focusing on understanding axons in health and disease. What are the main roadblocks preventing resolving these diseases? Although the answer remains elusive, a possible explanation may come from potential discrepancies between the biology of axons from humans and other species. The large majority of neurobiological studies, including those focusing on axons, are performed in non-human species, which is mostly due to the lack of a reproducible and readily accessible human neurobiological model system. This greatly changed with the development of human iPSC-derived neurons, which now for the first time enables addressing neurobiological questions in human neurons. To date, human iPSC-derived neurons are most commonly used by clinical research groups for translational sciences. However, this model system also holds great potential in understanding the fundamentals of axon biology in humans, as illustrated by the discoveries presented in *Chapter 2 and 3*. Generally stated, in the field of life sciences and beyond, important technical developments are often followed by a profound series of new discoveries and impactful insights. It will be exciting to see in the coming years how well the neurobiological processes identified in non-human neurons, including those underlying axon formation and function, can be extrapolated to human neurons, in studies utilizing human iPSC-derived neurons. Moreover, studying neurobiology in a human model system may result in the discovery of human-specific processes that were previously undetectable in other species, such as those described for axon formation in *Chapter 2 and*

3. Thus, human iPSC-derived neurons offers the great advantage of studying neurobiology on a human genetic background, which may contribute to new insights that will perhaps further our understanding of the development of axonal pathologies and other neurological disorders.

Another future challenge in the field of axon biology is to unravel the precise coordination of the different molecular machineries that facilitate neuronal communication. More specifically, it would be interesting to gain an advanced understanding on how the functioning of presynaptic organelles, such as axonal ER and mitochondria, are integrated with neurotransmitter release. To this end, novel insights will likely come from newly developed tools that allow in-depth investigations of the structure and function of axonal organelles. Accordingly, high resolution imaging recently enabled resolving the nanostructures of the axonal ER network, thereby uncovering its unique organization and continuity with the remaining ER network (Yalcin et al. 2017; Wu et al. 2017; Terasaki 2018). What could be the functional implication of this unique axonal ER network? Is perhaps the continuity of the axonal ER with the somatodendritic ER network important for processes underlying axon functioning, such as neurotransmitter release? Future investigations with recently developed tools to measure organelle functions, e.g. by measuring intra-luminal Ca^{2+} levels in ER or mitochondria, will likely address these and other urgent questions (de Juan-Sanz et al. 2017). It will be exciting to learn in the coming years how the well-defined processes of the synaptic vesicle cycle can be mechanistically tweaked by axonal organelles.

Taking together, a combination of multidisciplinary approaches, application of newly developed tools, and the accessibility of different neurobiological model systems, thereby carefully taking into consideration the strengths and limitations of each model system, now allows addressing new questions in the field of axon biology. A thorough understanding of the basic principles of axon formation and function is key, as this might provide an important stepping stone in dissecting and ultimately resolving axonopathies.

ACKNOWLEDGEMENTS

I would like to thank Sybren Portegies for co-producing the illustrations, and Harold MacGillavry and Robbelien Kooistra for their constructive feedback on the text.

REFERENCES

- Bezprozvanny, I., and E. T. Kavalali. 2020. 'Presynaptic endoplasmic reticulum and neurotransmission', *Cell Calcium*, 85: 102133.
- Chicurel, M. E., and K. M. Harris. 1992. 'Three-dimensional analysis of the structure and composition of CA3 branched dendritic spines and their synaptic relationships with mossy fiber boutons in the rat hippocampus', *J Comp Neurol*, 325: 169-82.
- Conduit, P. T., A. Wainman, and J. W. Raff. 2015. 'Centrosome function and assembly in animal cells', *Nat Rev Mol Cell Biol*, 16: 611-24.
- de Anda, F. C., G. Pollarolo, J. S. Da Silva, P. G. Camoletto, F. Feiguin, and C. G. Dotti. 2005. 'Centrosome localization determines neuronal polarity', *Nature*, 436: 704-8.
- De Gregorio, C., R. Delgado, A. Ibacache, J. Sierralta, and A. Couve. 2017. 'Drosophila Atlastin in motor neurons is required for locomotion and presynaptic function', *J Cell Sci*, 130: 3507-16.
- de Juan-Sanz, J., G. T. Holt, E. R. Schreiter, F. de Juan, D. S. Kim, and T. A. Ryan. 2017. 'Axonal Endoplasmic Reticulum Ca(2+) Content Controls Release Probability in CNS Nerve Terminals', *Neuron*, 93: 867-81.e6.
- Dickey, A. S., and S. Strack. 2011. 'PKA/AKAP1 and PP2A/Bbeta2 regulate neuronal morphogenesis via Drp1 phosphorylation and mitochondrial bioenergetics', *J Neurosci*, 31: 15716-26.
- Dotti, C. G., C. A. Sullivan, and G. A. Banker. 1988. 'The establishment of polarity by hippocampal neurons in culture', *J Neurosci*, 8: 1454-68.
- Espuny-Camacho, I., K. A. Michelsen, D. Gall, D. Linaro, A. Hasche, J. Bonnefont, C. Bali, D. Orduz, A. Bilheu, A. Herpoel, N. Lambert, N. Gaspard, S. Peron, S. N. Schiffmann, M. Giugliano, A. Gaillard, and P. Vanderhaeghen. 2013. 'Pyramidal neurons derived from human pluripotent stem cells integrate efficiently into mouse brain circuits in vivo', *Neuron*, 77: 440-56.
- Ishikawa, H., and W. F. Marshall. 2011. 'Ciliogenesis: building the cell's antenna', *Nat Rev Mol Cell Biol*, 12: 222-34.
- Kasthuri, N., K. J. Hayworth, D. R. Berger, R. L. Schalek, J. A. Conchello, S. Knowles-Barley, D. Lee, A. Vazquez-Reina, V. Kaynig, T. R. Jones, M. Roberts, J. L. Morgan, J. C. Tapia, H. S. Seung, W. G. Roncal, J. T. Vogelstein, R. Burns, D. L. Sussman, C. E. Priebe, H. Pfister, and J. W. Lichtman. 2015. 'Saturated Reconstruction of a Volume of Neocortex', *Cell*, 162: 648-61.
- Kuijpers, M., D. van de Willige, A. Freal, A. Chazeau, M. A. Franker, J. Hofenk, R. J. Rodrigues, L. C. Kapitein, A. Akhmanova, D. Jaarsma, and C. C. Hoogenraad. 2016. 'Dynein Regulator NDEL1 Controls Polarized Cargo Transport at the Axon Initial Segment', *Neuron*, 89: 461-71.
- Kwon, S. K., R. Sando, 3rd, T. L. Lewis, Y. Hirabayashi, A. Maximov, and F. Polleux. 2016. 'LKB1 Regulates Mitochondria-Dependent Presynaptic Calcium Clearance and Neurotransmitter Release Properties at Excitatory Synapses along Cortical Axons', *PLoS Biol*, 14: e1002516.
- Lancaster, M. A., M. Renner, C. A. Martin, D. Wenzel, L. S. Bicknell, M. E. Hurler, T. Homfray, J. M. Penninger, A. P. Jackson, and J. A. Knoblich. 2013. 'Cerebral organoids model human brain development and microcephaly', *Nature*, 501: 373-9.

- Lee, A., Y. Hirabayashi, S. K. Kwon, T. L. Lewis, Jr., and F. Polleux. 2018. 'Emerging roles of mitochondria in synaptic transmission and neurodegeneration', *Curr Opin Physiol*, 3: 82-93.
- Leterrier, C. 2018. 'The Axon Initial Segment: An Updated Viewpoint', *J Neurosci*, 38: 2135-45.
- Lewis, T. L., Jr., S. K. Kwon, A. Lee, R. Shaw, and F. Polleux. 2018. 'MFF-dependent mitochondrial fission regulates presynaptic release and axon branching by limiting axonal mitochondria size', *Nat Commun*, 9: 5008.
- Li, Z., K. Okamoto, Y. Hayashi, and M. Sheng. 2004. 'The importance of dendritic mitochondria in the morphogenesis and plasticity of spines and synapses', *Cell*, 119: 873-87.
- Linaro, D., B. Vermaercke, R. Iwata, A. Ramaswamy, B. Libe-Philippot, L. Boubakar, B. A. Davis, K. Wierda, K. Davie, S. Poovathingal, P. A. Penttila, A. Bilheu, L. De Bruyne, D. Gall, K. K. Conzelmann, V. Bonin, and P. Vanderhaeghen. 2019. 'Xenotransplanted Human Cortical Neurons Reveal Species-Specific Development and Functional Integration into Mouse Visual Circuits', *Neuron*, 104: 972-86.e6.
- Meka, D. P., R. Scharrenberg, and F. Calderon de Anda. 2020. 'Emerging roles of the centrosome in neuronal development', *Cytoskeleton (Hoboken)*.
- Nano, M., and R. Basto. 2017. 'Consequences of Centrosome Dysfunction During Brain Development', *Adv Exp Med Biol*, 1002: 19-45.
- Nicholas, C. R., J. Chen, Y. Tang, D. G. Southwell, N. Chalmers, D. Vogt, C. M. Arnold, Y. J. Chen, E. G. Stanley, A. G. Elefanti, Y. Sasai, A. Alvarez-Buylla, J. L. Rubenstein, and A. R. Kriegstein. 2013. 'Functional maturation of hPSC-derived forebrain interneurons requires an extended timeline and mimics human neural development', *Cell Stem Cell*, 12: 573-86.
- Otani, T., M. C. Marchetto, F. H. Gage, B. D. Simons, and F. J. Livesey. 2016. '2D and 3D Stem Cell Models of Primate Cortical Development Identify Species-Specific Differences in Progenitor Behavior Contributing to Brain Size', *Cell Stem Cell*, 18: 467-80.
- Ozturk, Z., C. J. O'Kane, and J. J. Perez-Moreno. 2020. 'Axonal Endoplasmic Reticulum Dynamics and Its Roles in Neurodegeneration', *Front Neurosci*, 14: 48.
- Petanjek, Z., M. Judas, G. Simic, M. R. Rasin, H. B. Uylings, P. Rakic, and I. Kostovic. 2011. 'Extraordinary neoteny of synaptic spines in the human prefrontal cortex', *Proc Natl Acad Sci U S A*, 108: 13281-6.
- Popov, V., N. I. Medvedev, H. A. Davies, and M. G. Stewart. 2005. 'Mitochondria form a filamentous reticular network in hippocampal dendrites but are present as discrete bodies in axons: a three-dimensional ultrastructural study', *J Comp Neurol*, 492: 50-65.
- Shi, Y., P. Kirwan, and F. J. Livesey. 2012. 'Directed differentiation of human pluripotent stem cells to cerebral cortex neurons and neural networks', *Nat Protoc*, 7: 1836-46.
- Sousa, A. M. M., K. A. Meyer, G. Santpere, F. O. Gulden, and N. Sestan. 2017. 'Evolution of the Human Nervous System Function, Structure, and Development', *Cell*, 170: 226-47.
- Stiess, M., N. Maghelli, L. C. Kapitein, S. Gomis-Ruth, M. Wilsch-Brauninger, C. C. Hoogenraad, I. M. Tolic-Norrelykke, and F. Bradke. 2010. 'Axon extension occurs independently of centrosomal microtubule nucleation', *Science*, 327: 704-7.
- Summerville, J. B., J. F. Faust, E. Fan, D. Pendin, A. Daga, J. Formella, M. Stern, and J. A. McNew. 2016. 'The effects of ER morphology on synaptic structure and function in *Drosophila melanogaster*', *J Cell Sci*, 129: 1635-48.
- Terasaki, M. 2018. 'Axonal endoplasmic reticulum is very narrow', *J Cell Sci*, 131.

-
- Tsai, L. H., and J. G. Gleeson. 2005. 'Nucleokinesis in neuronal migration', *Neuron*, 46: 383-8.
- Vaccaro, V., M. J. Devine, N. F. Higgs, and J. T. Kittler. 2017. 'Miro1-dependent mitochondrial positioning drives the rescaling of presynaptic Ca²⁺ signals during homeostatic plasticity', *EMBO Rep*, 18: 231-40.
- van Beuningen, S. F., and C. C. Hoogenraad. 2016. 'Neuronal polarity: remodeling microtubule organization', *Curr Opin Neurobiol*, 39: 1-7.
- Wilhelm, B. G., S. Mandad, S. Truckenbrodt, K. Krohnert, C. Schafer, B. Rammner, S. J. Koo, G. A. Classen, M. Krauss, V. Haucke, H. Urlaub, and S. O. Rizzoli. 2014. 'Composition of isolated synaptic boutons reveals the amounts of vesicle trafficking proteins', *Science*, 344: 1023-8.
- Wu, Y., C. Whiteus, C. S. Xu, K. J. Hayworth, R. J. Weinberg, H. F. Hess, and P. De Camilli. 2017. 'Contacts between the endoplasmic reticulum and other membranes in neurons', *Proc Natl Acad Sci U S A*, 114: E4859-e67.
- Yalcin, B., L. Zhao, M. Stofanko, N. C. O'Sullivan, Z. H. Kang, A. Roost, M. R. Thomas, S. Zaessinger, O. Bhard, A. L. Patto, A. Sohail, V. Baena, M. Terasaki, and C. J. O'Kane. 2017. 'Modeling of axonal endoplasmic reticulum network by spastic paraplegia proteins', *Elife*, 6.
- Zmuda, J. F., and R. J. Rivas. 1998. 'The Golgi apparatus and the centrosome are localized to the sites of newly emerging axons in cerebellar granule neurons in vitro', *Cell Motil Cytoskeleton*, 41: 18-38.

&



Addendum

Nederlandse samenvatting voor non-experts

Curriculum vitae

PhD portfolio

List of publications

Acknowledgements



NEDERLANDSE SAMENVATTING VOOR NON-EXPERTS

Ons brein is één van de meest complexe organen in ons lichaam. Het reguleert hoe we bewegen, welke gedachten zich in ons vormen, de emoties die we voelen en het slaat onze herinneringen op. Het brein is opgebouwd uit biljoenen hersencellen die een complex netwerk met elkaar vormen. Hersencellen bestaan uit twee compartimenten: het cellichaam met enkele relatief korte en zeer vertakte uitlopers, de *dendrieten*, en één hele lange en tevens vertakte uitloper, het *axon* (Fig 1, Hoofdstuk 1). In menselijke hersencellen kan het axon wel tot 1 meter lang worden, terwijl de rest van de hersencel ongeveer duizend keer zo klein blijft. Naast de uitzonderlijke lengte heeft het axon ook de gespecialiseerde functie om efficiënt informatie aan andere hersencellen in het zenuwstelsel door te geven. Het doorgeven van informatie vindt plaats volgens een eenrichtings-principe waarbij het axon van één hersencel signalen stuurt naar dendrieten van andere hersencellen. Deze signaaloverdracht tussen hersencellen vindt plaats via *synapsen*, de gespecialiseerde contacten tussen axonen en dendrieten. De functies van het axon worden gereguleerd door een serie van complexe moleculaire processen. Als het axon echter niet goed werkt doordat deze moleculaire processen verstoord zijn heeft dat grote gevolgen voor de functie van het zenuwstelsel. Tot op heden is er geen goede behandeling mogelijk voor aandoeningen die specifiek geassocieerd zijn met het disfunctioneren van axonen, waaronder hereditaire spastische paraplegias (HSP), Charcot-Marie-Tooth type 2 en dwarslaesies. Een belangrijke stap in het oplossen van deze ziektes is om eerst de basale moleculaire processen van het axon goed in kaart te brengen. Want de unieke vorm alsmede de gespecialiseerde functie van het axon roepen een aantal fundamentele vragen op. Hoe ontstaat een axon eigenlijk in een jonge hersencel? Hoe wordt bepaald welke uitloper het axon wordt en welke de dendrieten? Hoe kan een axon, dat tot duizendmaal langer kan zijn dan de rest van de hersencel, goed functioneren? En in hoeverre zijn alle bevindingen op het gebied van axon onderzoek, dat meestal in ratten- en muizen hersencellen wordt uitgevoerd, te vertalen naar menselijke hersencellen? Dit is een greep uit de vragen die een belangrijke drijfveer hebben gevormd voor het onderzoek beschreven in dit proefschrift. In deze samenvatting wordt verder ingezoomd op de moleculaire processen in het axon en worden de belangrijkste bevindingen van dit proefschrift nader toegelicht.

Historisch gezien is veruit het meeste moleculair en cellulair neurowetenschappelijk onderzoek, door gebrek aan een geschikt menselijk modelsysteem, uitgevoerd in andere diersoorten dan de mens. Onder de klassieke modelsystemen vallen vooral muizen, ratten, vliegen en wormen. Het is echter onbekend in hoeverre de bevindingen die zijn opgedaan in deze klassieke modelsystemen te vertalen zijn naar de mens. Bovendien kunnen mogelijke mens-specifieke processen niet bestudeerd worden in de klassieke modelsystemen. Hier is verandering in gekomen sinds recent onderzoek het nu mogelijk heeft gemaakt om menselijke stamcellen in kweekschalmpjes op het lab te laten uitgroeien tot hersencellen. Met dit nieuwe modelsysteem kan er reproduceerbaar, efficiënt en ethisch verantwoord

onderzoek gedaan worden in menselijke hersencellen. In *hoofdstuk 2 en 3* maken we gebruik van deze menselijke hersencellen om onderzoek te doen naar de ontwikkeling van het axon. In *hoofdstuk 2* wordt dit modelsysteem uitvoerig gekarakteriseerd door gebruik te maken van diverse geavanceerde technieken. Hierbij observeerden we dat de verschillende ontwikkelingsfasen van een groeiend axon, die eerder in klassieke modelsystemen geïdentificeerd waren, ook in menselijke hersencellen terug te vinden zijn. Een opvallende ontdekking was dat we een extra ontwikkelingsfase van het axon konden onderscheiden die nog niet eerder in niet-menselijke hersencellen is gedetecteerd. Het verder karakteriseren van deze unieke ontwikkelingsfase heeft ons nieuwe inzichten gegeven over hoe de ontwikkeling van het axon specifiek plaatsvindt in menselijke hersencellen. Een belangrijke bevinding hierbij was dat het reorganiseren van structuren tijdens axon ontwikkeling eerst in de verste uiteinden van het axon plaatsvindt en pas later in het beginstuk van het axon. Dit is een belangrijke aanwijzing in het veel onderzochte vraagstuk over waar en hoe de identiteit van het axon voor het eerst wordt bepaald.

In het midden van een jonge hersencel bevindt zich een zeer kleine en belangrijke structuur: het *centrosoom*. Het centrosoom is het knooppunt, en ook de voornaamste bron, van de vele *microtubuli* die zich in de cel bevinden (Fig 2, Hoofdstuk 1). Microtubuli zijn sterke bundels die stevigheid aan de cel bieden en eveneens fungeren als een soort snelwegen voor efficiënt transport van bouwstoffen. Er zijn aanwijzingen dat het mogelijk mens-specifieke functies kan vertonen in hersencellen. Gedurende de ontwikkeling van hersencellen maakt het centrosoom plaats voor een andere structuur, het cilium, en daarbij gaan ook de functies van het centrosoom verloren. Dit proces vindt ongeveer tegelijkertijd plaats met het ontstaan van het axon. Een veelgestelde vraag is dan ook of het centrosoom een mogelijke rol speelt bij axon ontwikkeling en specifiek bij het bepalen van de axon identiteit. Eerder onderzoek naar deze vraag dat in verschillende diersoorten is uitgevoerd laat tegenstrijdige resultaten zien. Een mogelijke verklaring hiervoor is dat centrosomen eventueel aangepaste functies in verschillende diersoorten kunnen hebben. Ook is het technisch lastig om de functie van het centrosoom in jonge dierlijke hersencellen te bestuderen, aangezien de ontwikkeling van hersencellen hier een stuk sneller gaat dan in menselijke hersencellen. In *hoofdstuk 3* laten we voor het eerst zien dat het centrosoom een belangrijke rol speelt in de eerste ontwikkelingsfasen van het axon in menselijke hersencellen. Het manipuleren van centrosomale functies leidt tot verstoring van specifieke processen in axonen, waaronder het organiseren van de unieke axon-specifieke organisatie van microtubuli. Bovendien vinden we dat *Trim46*, een belangrijke moleculaire regulator van axon ontwikkeling, zich op centrosomen bevindt in menselijke hersencellen maar niet in niet-menselijke hersencellen. Tijdens axonale ontwikkeling, dat gepaard gaat met het verdwijnen van centrosomen, verplaatst *Trim46* zich van het centrosoom naar het axon. Dit is een belangrijk inzicht voor een mogelijk globaal mechanisme voor het begrijpen van de eerste stappen van axon ontwikkeling, en de rol van het centrosoom hierbij, in menselijke hersencellen.



Wie een ontwikkeld axon ontleedt, vindt structuren terug die zich drastisch hebben aangepast aan de unieke vorm van het axon die vooral gekarakteriseerd wordt door de enorme lengte. Een belangrijke structuur, en tevens de grootste structuur in hersencellen en andere celtypen, is het *endoplasmatisch reticulum* (ER). Het ER heeft dezelfde spanwijdte als de hersencel zelf en loopt door tot in de kleinste en verste vertakkingen van het axon. Structurele defecten van het ER in axonen is specifiek geassocieerd met HSP, een verzamelnaam voor verschillende genetische axonale aandoeningen, maar hoe dit precies op moleculair niveau werkt is nog onbekend. Wat is de rol van het ER voor het functioneren van axonen? In *hoofdstuk 5* is een nieuwe moleculaire interactie ontdekt die cruciaal is voor het organiseren van de speciale ER structuur in axonen. Het blokkeren van deze moleculaire interactie leidt niet alleen tot defecte ER structuren in axonen, maar ook tot verstoring van neuronale communicatie bij de synapsen van het axon. Daarbij is dit een van de eerste onderzoeken die een directe link aantoonst tussen de rol van het ER in axonen en neuronale communicatie.

Samenvattend heeft het onderzoek in dit proefschrift tot nieuwe inzichten geleid in de moleculaire processen die belangrijk zijn voor de ontwikkeling en functie van het axon. Daarbij zijn onder andere nieuwe mens-specifieke ontwikkelingsprocessen in axonen ontdekt. Deze basale fundamentele kennis is van belang om het brein op moleculair niveau goed in kaart te brengen. Dit is een belangrijke stap in het begrijpen en uiteindelijk oplossen van hersenaandoeningen, die worden veroorzaakt door verstoringen van basale moleculaire processen.





CURRICULUM VITAE

Feline Willeke Lindhout was born on the 18th of October 1990 in Tilburg, the Netherlands. In 2009, she finished her secondary education (VWO, Sint Odulphus Lyceum, Tilburg). Because of her broad interest in biology, chemistry and physics she decided to study Biomedical Sciences at Utrecht University that same year. During her studies she was also engaged in extracurricular activities, as she was chairman of an activity committee and member of a female organization of a student association. Additionally, she worked as a teacher assistant at the Utrecht University, gave scientific workshops at high schools and contributed to an outreach project organized by National Genomics Infrastructure. In 2013, she finalized her education with an internship at the department of translational neuroscience at University Medical Center Utrecht and obtained her Bachelor's degree. Motivated by her interest in brain functioning, Feline continued her education that same year at Utrecht University with a master's in Neuroscience and Cognition and with a focus on molecular and cellular neuroscience. During this two-years research Master's program she performed a first research internship in the laboratories of prof. dr. Casper Hoogenraad and dr. Corette Wierenga at the Utrecht University studying the role of molecular motors in synaptic functioning. To broaden her horizon she then left for San Diego to perform a second internship in the laboratory of Gentry Patrick at University of California San Diego, funded by the scholarships Jo Kolk Studiefonds and K.F. Hein Fonds, studying the role of protein turnover at synapses. During her Master's education she was also co-founder of Rise Philippines, a fund-raising event for the damages cost by super typhoon Haiyan in the Philippines. In 2015, she finalized her Master with a writing assignment under supervision of prof. dr. Casper Hoogenraad at Utrecht University and obtained her Master's degree. Driven by her growing fascination for molecular and cellular neuroscience, Feline started her PhD research in 2015 in the laboratory of prof. dr. Casper Hoogenraad at the department of Cell Biology, Neurobiology and Biophysics at Utrecht University which resulted in this current dissertation.



PHD PORTFOLIO

PHD RESEARCH SCHOOL | Institute of Biomembranes (IB)

COURSES & WORKSHOPS

- 2016 - 2019 Various seminars organized by Graduate School of Life Sciences (GSLs), Utrecht University
- 2017 - 2019 PhD retreat of Institute and Graduate School of Biomembranes (IB) (once per 2 years) – *Organized retreat (2017)*
- 2016 - 2018 “Neuron Retreat” organized by the Cell Biology department, Utrecht University (annual) – *Oral presentation (2016, 2017, 2018)*
- 2017 “Art of presenting science” course organized by Artesc
- 2016 “Introduction course” of Institute and Graduate School of Biomembranes (IB)
- 2016 PhD day of Graduate School of Life Sciences (GSLs), Utrecht University

GRANTS & AWARDS


- Award** | Best poster presentation Science for Life Meeting 2018
- Honorable Mention** | Biolmage Of the Day (BIOD) 2018
- Research Grant** | 3R Stimulus Fund appointed by the Animal Welfare Body 2017
- Award/Outreach** | Winner heat Breaking Science pitch competition 2016
- Award/Outreach** | Winner theatre show ScienceBattle (4 out of 8 editions) 2016



TEACHING ACTIVITIES

- 2017 - 2018 Supervised research internship of Rian Stoffelen, student from MSc Molecular and Cellular Life Sciences program (Utrecht University).
- 2016 - 2018 Participated annually in “Meet the Scientist” workshops of the MSc Neuroscience & Cognition program (Utrecht University).
- 2016 - 2017 Teaching assistant Molecular Research course of the BSc Biology program (Utrecht University).
- 2017 Supervised research internship of Michelle Heuvelmans, student from MSc Science & Business Management program (Utrecht University).
- 2016 Supervised BSc thesis of Michelle Heuvelmans, student from BSc Biology program (Utrecht University).
-

SECONDARY ACTIVITIES

- 
- 2017 - 2020 **Science & Society** | *Participant ScienceBattle*
ScienceBattle is a theatre show during which four PhD students from diverse disciplines try to win over the layman’s audience.
- 2015 - 2020 **Organization & Teamwork** | *Member Activity Committee*
Organized various activities for the department, including a two-days team building event for 80+ participants.
- 2017 **Organization** | *Scientific session at Dutch Neuroscience (DN) meeting*
Organized and chaired a parallel session during the DN meeting.
- 2016 - 2017 **Organization & Teamwork** | *Member PhD Committee*
Organized various activities for the PhD graduate school, including a two-days PhD retreat (40+ participants), monthly PhD evenings (15+ participants) and co-organized a two-days conference (150+ participants).

ATTENDANCE & PRESENTATIONS INTERNATIONAL CONFERENCES

- 2020 “ISSCR 2020 Virtual” organized by the International Society for Stem Cell Research (ISSCR)
- 2019 “Stem Cells & Organoids in Development & Disease” organized by the International Society for Stem Cell Research (ISSCR) – *Presented a poster*
- 2018 “Neural Development” organized by Gordon Research Conferences (GRC) – *Presented a poster*
- 2017 “Cell Biology of the Neuron” organized by European Molecular Biology Organization (EMBO)
- 2014 Federation of European Neuroscience Societies (FENS) Meeting
-

ATTENDANCE & PRESENTATIONS NATIONAL CONFERENCES

- 2016 - 2019 Dutch Neuroscience (DN) Meeting (annually) – *Presented poster (2018, 2019), organized and chaired a parallel session (2017)*
- 2016 - 2018 Institute and Graduate School of Biomembranes (IB) Conference (annual) – *Assisted in organizing (2016)*
- 2016 - 2018 Science for Life Conference (annual) – *Presented poster, awarded with best poster prize (2018)*
- 2016 - 2018 Dutch Biophysics organized by the Nederlandse Organisatie voor Wetenschappelijk Onderzoek (NOW) (annually)

List of publications on the next page >





LIST OF PUBLICATIONS

Feline W. Lindhout*, Robbelien Kooistra*, Sybren Portegies*, Lotte J. Herstel, Riccardo Stucchi, Basten L. Snoek, Maarten Altelaar, Harold D. MacGillavry, Corette J. Wierenga, Casper C. Hoogenraad (2020). 'Quantitative mapping of transcriptome and proteome dynamics during polarization of human iPSC-derived neurons', *Elife*, *in press*. Preprint available on *BioRxiv*; doi: 10.1101/2020.04.21.052498

Feline W. Lindhout, Sybren Portegies, Robbelien Kooistra, Riccardo Stucchi, Lotte J. Herstel, Nicky Scheefhals, Maarten Altelaar, Harold D. MacGillavry, Corette J. Wierenga, Casper C. Hoogenraad (2020). 'Centrosome-mediated microtubule remodeling during axon formation in human iPSC-derived neurons', *Submitted, under review*.

Feline W. Lindhout, Yujie Cao*, Josta T. Kevenaar*, Anna Bodzęta*, Riccardo Stucchi, Maria M. Boumpoutsari, Eugene A. Katrukha, Maarten Altelaar, Harold D. MacGillavry, Casper C. Hoogenraad (2019). 'VAP-SCRN1 interaction controls dynamic endoplasmic reticulum remodeling and presynaptic function', *The EMBO J* 38: e101345.

Olga I. Kahn, Philipp Schätzle, Dieudonné van de Willige, Roderick P. Tas, **Feline W. Lindhout**, Sybren Portegies, Lukas C. Kapitein, and Casper C. Hoogenraad (2018). 'APC2 controls dendrite development by promoting microtubule dynamics', *Nature Communications* 9: 2773.

* *Authors contributed equally*



ACKNOWLEDGEMENTS

Het is een dunne scheidslijn van beleven naar herinneren. Aangekomen bij het schrijven van dit dankwoord begin ik aan deze oversteek. Het promoveren was een mooi avontuur. Ik heb veel ervaren, beleefd, geleerd en bovenal een hoop fantastische mensen mogen leren kennen. Een van de belangrijkste lessen die ik tijdens mijn promotietraject heb geleerd is dat wetenschap een teamsport is. Ik neem ik hier dan ook graag de ruimte om iedereen te bedanken die direct of indirect een bijdrage heeft geleverd aan het mede mogelijk maken van dit proefschrift.

Promoveren is pas mogelijk als er iemand is die op de juiste positie zit en in je gelooft. Casper, mijn grootste dank gaat uit naar jou, omdat jij diegene bent geweest die initieel een potentiële wetenschapper in mij heeft gezien. Door mij een PhD positie aan te bieden heb je niet alleen het promoveren voor mij mogelijk gemaakt, maar mij ook het vertrouwen gegeven dat als basis fungeerde voor verdere groei en zelfontplooiing. En wat blijkt ik wetenschap toch leuk te vinden. Tegen het einde van mijn promotietraject hebben we een mooi gesprek gehad over de afslagen die er genomen zijn en de impact die dat met zich mee heeft gebracht. Dankjewel daarvoor, dat gesprek was erg betekenisvol voor mij. Iets wat ik in het bijzonder heb gewaardeerd was de vrijheid die je me gaf om onder jouw supervisie mijn eigen wetenschappelijke ideeën uit te werken. Het opzetten en uitvoeren van zelfbedachte projecten vond ik misschien wel het leukste tijdens mijn PhD. Bedankt dat je dit ruimschoots gestimuleerd en gefaciliteerd hebt. Harold, als copromotor, en misschien bovenal als mentor, heb jij vanaf het tweede jaar een belangrijke rol gespeeld in mijn promotietraject. Ondanks dat onze onderzoeksonderwerpen niet volledig parallel liepen, wist je toch constructieve feedback te geven en moedigde je me vaak aan om mijn eigen ideeën uit te voeren. Als ik je nodig had, voor wetenschap of gerelateerde zaken, stond je paraat. Dat was waardevol, dankjewel. Ons gesprek in het Wilhelminapark over de volgende stap in mijn carrière, daarbij uitgebreid reflecterend over wetenschap en alles eromheen, hebben mij verhelderende inzichten gegeven die mij zeker zullen bijblijven. Bedankt voor de prettige support, openheid en mentorschap. Prof. dr. Lukas Kapitein, prof. dr. Jeroen Pasterkamp, prof. dr. Sander van den Heuvel, prof. dr. ir. Erwin Peterman, dr. Mike Boxem, en dr. Corette Wierenga, de leden van mijn beoordelingscommissie, bedankt voor het uitvoerig lezen van mijn proefschrift en voor de verdediging.

It was such a pleasure to work with all the dear members from the Hoogenraad group. A place filled with science enthusiasts that are always supporting one another, but also a place where the pipette regularly makes place for a beer. A place where I felt at home. Robbelien en Sybren, dat wetenschap een teamsport is heeft ons geslaagde hiPSC clubje mij wel laten inzien. Met zijn drieën was er veel gezamenlijke expertise en kon ieder in haar of zijn eigen kracht staan. Ook was er de ruimte om even een stapje terug te doen als het nodig was of juist om iets extra's op te pakken. Wat hebben we als team veel voor elkaar gekregen

en het resultaat mag er met twee mooie afgeronde projecten dan ook zijn. Robbelien, als jij er bent dan is er voor mij een klankbord aanwezig, iemand om mee te sparren, over wetenschap of andere zaken, iemand om mee te lachen en bovenal iemand bij wie ik onvoorwaardelijke support voel. Bedankt voor het regelen van alle paranormale zaken. Ik weet zeker dat je met jouw doorzettingsvermogen, enthousiasme en empathie niet alleen je PhD fantastisch gaat afronden, maar daarna ook je droombaan gaat vinden. En you know hé, i always got your rug. Sybren, het is meer dan incidenteel voorgekomen dat onze werkrelatie door collega's als een kibbelend getrouwd stel werd samengevat. Het is bijzonder hoe we, met onze uiteenlopende persoonlijkheden, zulke fijne team buddies waren. Inderdaad, er is wat afgekibbeld, want zowel de frustraties als de successen bij het opzetten van het hiPSC lab werden veelal openlijk gedeeld. Stiekem waren we het eigenlijk meestal met elkaar eens, maar vonden we de discussie gewoon te leuk. Dankjewel dat ik zo vaak op je heb kunnen rekenen. Ook voor jou is de finish in zicht, succes met de laatste loodjes en met de volgende stap in je carrière. Amélie, when thinking about the perfect combination of love for science and wine, your name starts to appear. I really enjoyed working with you, hanging out together, and talking about science and life. Not sure if you are aware of this, but I find you a very inspiring person. Having that said, please don't forget to find yourself 'a word of the day' every now and then, oké feesttoeter? Martin, als verkapte mentor heb je mij regelmatig van carrière adviezen voorzien die, erop terugkijkend, enorm waardevol en bepalend voor me zijn geweest. Bij jou is er altijd tijd voor een wetenschappelijke discussie, een goed gesprek of een biertje, en nog een biertje, en nog eentje dan. Ik bewonder je om je veerkracht en ik heb er vertrouwen in dat je jouw carrièrepad gaat vinden. Phebe, de power house van het lab, wat zeg ik, van de hele afdeling. Rotterdamse directheid met een hartje van goud, staat altijd klaar voor diegene die daar een plekje in hebben bemachtigd. En eigenlijk ook voor alle anderen, want dat gaat vanzelf met zo'n enorm verantwoordelijkheidsgevoel. Phebe, ik hou ervan! Bedankt voor de gezelligheid en al het andere. Bart, wat ontvullend om zo'n grapjas als jou tussen dat stelletje serieuze wetenschappers te hebben. In mijn hyperfocus tijdens de maandagochtend kweken had ik de meerderheid van je "pun intended" grappes niet door, maar gelukkig was je niet te beroerd om ze nog even toe te lichten. Robin, wat bijzonder dat we elkaar al sinds het eerste jaar van de bachelor kennen en leuk om elkaar zo te hebben zien groeien en ontwikkelen. Heerlijk hoe lekker jezelf jij bent, met je vrolijke karakter en mooie verhalen. Ik heb er al die jaren erg van genoten. Succes met de laatste loodjes van je PhD en alles wat erna komt. Jessica, de stille kracht in het kantoor en op het lab. Een kauwgompakje verder en ze heeft weer 50 constructen gekloneerd, 10 pull downs gedaan en ook nog even een intensieve frisbee training tussendoor gehad. Wat een ijzeren discipline, ik heb er respect voor. Tijdens een PhD traject leer je veel over wetenschap, maar ook veel over jezelf. Bedankt voor de mooie gesprekken en succes met alles in de toekomst. Xingxiu, my office mate and promotion twin. It has been lovely to see you grow to the person you are today, an enthusiastic scientist with a view of your own. Looking forward to celebrate our promotion on the same day and wish you all the best for the next steps in your career and life. Yujie, my partner in crime when I first started. I hardly caught you without a smile on your face. Always supportive, always enthusiastic. It was really



nice working with you. Keep up the good work and all the best for the future. Eitan, I have always appreciated your love for science and food. Really enjoyed your supportive attitude and feedback, as well as your homemade Israeli dishes. Thanks and all the best! Liu, I will remember you as a positive, kind, hardworking and smart scientist. It was great to be your bench buddy. Good luck with your PhD! Esther, ik bewonder je om je veerkracht, werketos en doorzettingsvermogen. Bedankt dat je altijd zo vriendelijk en oprecht geïnteresseerd bent, al vanaf dat ik hier als masterstudent rondliep. Lena, met fijne herinneringen denk ik terug aan ons avontuur in New York en het congres in Rhode Island. Veel plezier in je functie als docente!

All the lovely people from the MacGillavry group, thanks for adopting me during the early stage of my PhD. Nicky, mijn steun en toeverlaat vanaf vrijwel het eerste uur. Zonder al onze mooie gesprekken, “even-ventileren-hoor”-momentjes, gedeelde enthousiasme voor wetenschap en gezamenlijke voorliefde voor wijn en kaas, had mijn PhD er zeker een stuk minder aantrekkelijk uitgezien. Wat ben je toch een stoere, lieve, slimme en gezellige meid, met talent voor wetenschap en een eigen kijk op de wereld. Ik waardeer je ontzettend om dat alles. Bedankt dat je mijn paranimf wilt zijn en voor het organiseren van alle gerelateerde zaken. Lisa, wat een feest om met jou het kantoor gedeeld te hebben. Heerlijk hoe je af en toe in je hyperfocus bubbel kon opgaan en we op andere momenten weer uitgebreide gesprekken voerden. Veel plezier en succes met je PhD en met alles wat daarna komt! Anna, I admire your passion for science, as well as your perseverance and sense of responsibility. I really enjoyed working together with you on the ER project. Thanks for the great collaboration and all the best for the future! Manon, de vrolijke noot van de groep, ik heb genoten van je altijd aanwezige gezelligheid. Veel plezier en succes met je PhD en voor wat erna komt. Jelmer en Arthur, of ook wel team ORANGE, bedankt voor alle gezelligheid tijdens de lunch en borrels en succes met alle mooie wetenschappelijke projecten. Yolanda, I have really enjoyed your lovely positive attitude, thanks for all the great fun and wish you all the best. Wouter, succes met je PhD!

It's rare to find a place with such rich collaboration and scientific interaction as the Cell Biology, Neurobiology and Biophysics department. At times it felt like the department operated as a single unified research group, which is a win-win not only for the departments' members but also for the scientific progress itself. A big thank you for the department heads Anna, Casper and Lukas, and all the other group leaders, Harold, Corette, Ginny, Paul, Sabrina, Florian, for creating a scientific environment like this. Also thanks to Sander, Mike and the other members from the Developmental Biology department for even further expanding the scientific and social interaction during Monday lunch meetings, Friday afternoon borrels and lab outings. And it goes without saying that the department would not have ran this smooth without the great efforts of Phebe, Bart, Eugene, René, Ilya, Esther, Laurens, Jan-Andries, Marjolein and Lena. Thank you all!

All the great scientists from the Kapitein, Akhmanova, Wierenga, Farias, van Bergen en

Henegouwen and Oliveira groups, it was such a nice experience to work closely with all of you. I have sincerely enjoyed the collaborative atmosphere as well as all the nice social activities. Anna, ik bewonder je om je kennis, je ervaring en je wetenschappelijke inzichten. Bedankt voor alle feedback tijdens de werkdiscussies. Peter Jan, leuk om met jou bijna het hele PhD traject te hebben mogen doorlopen. Ik heb genoten van je vriendelijkheid, je humor en je interessante vragen tijdens werkdiscussies. York, thanks for all the fun and nice chats, wish you all the best for the future. Babet, succes met je toffe stamcelprojecten! Cynthia, bedankt voor alle gezelligheid en succes met je PhD. Dipti, it was great getting to know you, wish you all the best! Ankit, Funso, Joyce, Boris, Kyle, Ruben, Chiung-Yi, Fangrui, Milea, and Emma, good luck with your research and all the best for the future. Lukas, fantastisch om te zien wat je afgelopen jaren allemaal hebt bereikt. Bedankt voor de goede gesprekken en gezelligheid en veel succes met alle onderzoeken. Mithila, I just love the passion you have for science. I really enjoyed the many long and good scientific discussion we have had throughout the years. All the best and hope our paths will cross again in the future. Eugene, your kindness, curiosity, and your willingness to always help others makes it really nice to work with you. Thanks for the lovely collaboration and all the best for the future. Marijn, een lach, een nieuwsgierige blik en nooit te beroerd om iemand iets uit te leggen. Bedankt voor de leuke discussies en gezelligheid. Succes met je PhD en voor wat daarna mag komen! Wilco, aan gezelligheid geen gebrek, want we hebben wat afgekletst tijdens het kweken. Succes met alle mooie projecten! Klara, heerlijk recht door zee, eerlijk, vriendelijk en slim. Bedankt voor de gezelligheid, succes met het afronden van je PhD en met wat erna komt. Daphne, leuk om jou te hebben mogen leren kennen. Succes met het je PhD! HugoMalina, Giel, Josiah, good luck with your research and I wish you all the best. Corette, ooit als masterstudent bij jou begonnen en nu sluiten we af met jou in mijn leescommissie. Bedankt dat je mij als masterstudent een zetje in de goede richting hebt gegeven, dat was waardevol. Veel succes met alles! Lotte, ik heb genoten van onze samenwerking, evenals de gezelligheid aan de lunchtafel en bij borrels. Veel succes met je PhD en alles wat daarna komt, ik weet zeker dat dat helemaal goed gaat komen. Carlijn, goedlachs en vriendelijk, heerlijk om zo'n vrolijke noot te hebben rondlopen in de kweekkamer of bij sociale activiteiten. Veel succes met je PhD! René, bedankt voor alle gezelligheid! Jian and Ate, it was lovely meeting you and I wish you all the best. Ginny, it was great to have another ER enthusiast in the department, even better that you managed to start a research group on this topic. All the best with your research! Nazmiye, my dear office mate, your kindness goes beyond extraordinary. Thanks for all the lovely chats. I wish you all the best for the future and hope our paths will cross again. Mai Dan and Derk, good luck with your PhD! Paul, Sabrina, Katerina, Sara, Thomanai, Vida, Irati, and Bárbara, thanks for the nice scientific discussions during the Monday lunch meetings and for all the fun during social activities. Katerina, it was really nice to start my PhD simultaneously with you. Thanks for all the nice conversations and great fun in the past years. I wish you all the best and hope our paths will cross again in the future. Marjolein, ik heb genoten van al je gezelligheid aan de lunchtafel en bij borrels. Veel succes met je PhD en al je fantastische werk op gebied van onderwijs.



Also a shout out to the many people who moved on by now but were around at some point during my PhD. Dennis, wat leuk dat ik jou in ons eerste jaar al meteen goed leerde kennen tijdens het organiseren van de lab outing. De bromsnor werd een begrip dat nog vele jaren echoden in de gangen van het Kruyt gebouw. Ik heb genoten van de goede gesprekken en gezelligheid, altijd overgoten met een flinke dosis Amsterdamse humor. Succes met je nieuwe baan in Amsterdam, ik ben er van overtuigd dat je het fantastisch gaat doen. Dieudonné, mijn kantoorgenoot, schoenfanaat, en moeder van twee robotdieren, wat heb ik kan ik jou toch ontzettend waarderen. Een uniek talent in wetenschapscommunicatie, fijn dat je zo goed je plek in Maastricht hebt gevonden. Anne, ik heb genoten van je gezelligheid, vrolijkheid en intelligente discussies. Ik kijk er naar uit dat onze paden weer gaan kruisen in Cambridge. Roderick, bij jou kon ik altijd terecht voor een vurige wetenschappelijke discussie, liefst onder het genot van een biertje. Heerlijk! Succes met je postdoc en al het beste voor de toekomst. Marina, Philipp, Elena, Gabriela, Eliana, Olga, Ines, Riccardo, Josta, Mariella, Petra, Joanna, Marleen, Bas, Cátia, Sam, Helma, Marta, Max and Ivar, you have made me feel very welcome when I first started my PhD, thank you all. Josta, het was erg fijn om in de eerste fase van mijn PhD meteen een doorstart te kunnen maken met een goed opgezet project. Ook ons gesprek aan het einde van mijn PhD heeft me mooie inzichten gegeven, bedankt daarvoor. Wie weet kruisen onze paden in de toekomst weer. Cátia, I admire your passion for science. Thanks for supervising me as a master student and all the best for the future. Max, dat je het even weet, de borrels zijn niet meer hetzelfde geweest sinds je weg bent. Fijn om tegen het eind van mijn PhD weer uitgebreid met je gesproken te hebben. Succes met alles!

&

Wat is het fijn om tijdens je promotietraject ook de support te voelen van familie en vrienden. Met de ontnuchterende blik van zoveel lieve mensen om me heen werd promoveren, op de momenten dat dat soms nodig was, even een belangrijke bijzaak. Lieve Roos, Sofie, Vera, Myra, Tosca, Lisa, Laura, Floor, Marlouke, tien jaar vriendschap, tien jaar aan mooie herinneringen, tien jaar hoogtepunten vieren en elkaar tien jaar door dieptepunten heen trekken. Bedankt voor alle mooie momenten. Eva, Lisa, Naomi, Maaïke en Sophie, al vriendinnen vanaf het moment dat je vriendschap voor het eerst foutloos kan spellen, dat is iets om te koesteren. Bedankt dat ik, waar ik ook naar uitvlieg, bij jullie altijd terug naar de roots van Tilburg kan. Lieve Sanne, mijn altijd terugkerende huisgenoot, bedankt dat je altijd paraat staat als er iets gevierd mag, nee, moet worden. Je geduld en support tijdens de laatste loodjes van mijn promotietraject waren fijn, dankjewel! Marina en Karin, terwijl ik dit schrijf zit ik met jullie op een zeilboot in Sicilië. Living the good life, zoals het ons betaamt. Wat is het fijn om jullie als cheerleaders te hebben, altijd oprecht geïnteresseerd in mijn onderzoek en in mijn leven. Hockeytoppers van Phoenix, elke woensdag en zondag een balletje slaan was altijd een heerlijke uitlaatklep voor mij, dankjewel!

Met wie anders kan ik het dankwoord afsluiten dan met mijn lieve familie. José en Roos, onze sterke zussenband koester ik enorm. Zo fijn en waardevol om te weten dat we altijd bijkaar terecht kunnen. Roos, bedankt voor je enorme inzet bij de opmaak van dit proefschrift.

Het is extra speciaal om samen met jou de cover gemaakt te hebben. Maarten en Michiel, het is ontzettend fijn om jullie bij het gezin te hebben. Goed om te zien hoe jullie opgaan in onze bijzondere gezinsdynamiek. Marcel en Maurits, bij jullie vind ik een tweede thuis. Maurits, dankjewel voor alle reflecties, mooie gesprekken en adviezen. Bijzonder dat je altijd zo grenzeloos klaar staat voor dit clubje mensen. Tom, in een korte tijd zo'n berg aan steun kunnen bieden, dat voelt goed. Jij durft mij een duwtje in mijn rug te geven op de momenten dat ik net dat laatste zetje nodig heb en gaat vervolgens vol vertrouwen achter me staan. Dat is betekenisvol en geeft me bijzonder veel vertrouwen. Bedankt voor je dagelijkse steun tijdens de intensieve eindfase van het promotietraject. Oma, ik ben naar u vernoemd en dat is iets om trots op te zijn. Want als ik maar iets van uw avontuurlijke en dappere karakter in mij heb, dan mag ik daar meer dan tevreden mee zijn. Het doet me goed dat u mijn promotie kunt bijwonen. Lieve mama en papa, lieve Anke en Wim, "*niet denken in problemen maar in creatieve oplossingen*" is een van de vele levenslessen die jullie mij hebben mee gegeven. Deze wijsheid heeft mij niet alleen enorm geholpen tijdens mijn promotieonderzoek, maar heeft er bovenal voor gezorgd dat ik het promoveren als een fantastisch avontuur heb mogen ervaren. Ik prijs mijzelf dan ook gelukkig dat ik met deze instelling ben groot gebracht. Daarom, lieve papa, lieve mama, draag ik dit proefschrift op aan jullie.

Hora est!



Feline W. Lindhout

Scan for eBook



